Conférence Internationale sur les Sciences Appliquées et l'Innovation

(CISAI-2023)

Editor :
Dr. Ahmed Rhif (Tunisia)

Proceedings of Engineering & Technology
-PET-

ICID
International Centre for Innovation & Development

Proceedings of Engineering & Technology
-PET-

Conférence Internationale sur les Sciences Appliquées et l'Innovation
(CISAI-2023)

Editor :
Dr. Ahmed Rhif (Tunisia)

PET-Vol. 77
ISSN : 1737-9334

Committees

Committee Chairs:

Afef Khalil (TUN)
Akrouch Soukaina (MAR)
Belatel Mimi (ALG)
Fatima Zohra Boufadi (ALG)
Gherbi Mohamed (ALG)
Georges Descombes (FR)
Hadiza Moussa-Saley (SEN)
Hanaa Benchrifa (MAR)
Haitham Mohamed Ramadan (EGP)
Hayani Mechkouri Meriem (MAR)
Jeru Achyl Hounogbe (SEN)
Mohamad Ramadan (LIB)
Ouardia Laoudj (ALG)
Rahmouni Soumia (ALG)
Rhif Ahmed (TUN)
Sahbeni Kawther (TUN)
Vincent Sambou (SEN)

International Committee:

Abdelkrim Khireddine (ALG)
Abdoulaye Bouya Diop (SEN)
Abdoulaziz Alhassane (SEN)
Afef Trabelsi (TUN)
Ahmed Charif (MAR)
Allé Dioum (SEN)
Amrhar Aicha (MAR)
Barara Mohamed (FR)
Bendifallah Leila (ALG)
Benhabib Lamia (ALG)
Cherkaoui Abdeljzbbar (MAR)
Djalila Boudemagh (ALG)
Faical Mahrek (MAR)
Fateh Mebarek-Oudina (ALG)
Hadja Fatima Mehnane (ALG)
Harrizi Driss (MAR)
Ikhlef Nadia (ALG)
Kheiri Abdelhamid (FR)
Lamia Larioui (MAR)
Madiha Yessari (MAR)
Manal Marzouq (MAR)
Méziane Aïder (ALG)
Mhamed Hammoudi (ALG)
Merdaoui Kamel (ALG)
Mihoub Ouahiba (ALG)
Mor Welle Diop (SEN)
Mounsi Demmouche Nedjoua (ALG)
Nawel Seddiki (ALG)
Ndeye Astou Manel Fall (SEN)
Olfa Kammoun (TUN)
Rachid Benchrifa (MAR)
Rosalie Douyon (FR)
Sara Zatir (ALG)
Sellam Mebrouk (ALG)
Serigne Moussa Dia (SEN)
Sebai Jihane (FR)
Slimane Semghouli (MAR)
Sofiane Amara (ALG)
Souad Elmanssouri (MAR)
Yavo Chaba Estelle Stéphanie (SEN)
Zakaria Ez-Zarzari (MAR)

Summary

Modeling and control of tire pressure for suspension system of Electric vehicle

Rached BEN MEHREZ[1], Abdelkader ABBASSI [2], Nada OUASLI [3]and Lilia EL AMRAOUI[4]
[1,3,4] Research Laboratory on Smart Electricity & ICT, National Engineering School of Carthage, , Tunisia
[2]Institute of Applied Sciences and Technology of Kasserine (ISSATKas), PO Box 471, 1200 Kasserine, Tunisia,
rached.benmehrez@gmail.com, abd_abbassi@yahoo.com, nada.ouasli.esti@gmail.com, lilia.elamraoui@gmail.com

***Abstract*—This research paper focuses on the issue of detecting tire pressure in a vehicle using an indirect method, without the need for pressure sensors. The proposed method aims to determine a decrease in pressure by jointly estimating three parameters: the effective radius of two wheels and the front axle rolling resistance force. To achieve this, an observer based on high-order sliding mode theory is developped, which takes into account the angular velocity values of each wheel and the applied torque. This observer demonstrates robustness against uncertainties and disturbances, ensuring convergence in a finite time. Simulation results are provided to illustrate the effectiveness of this approach.**

***Keywords*— Modeling, Effective radius of wheels, Global rolling resistance, High order sliding mode observer, Tire pressure.**

I. INTRODUCTION

Ensuring adequate tire pressure in vehicles is crucial for passenger safety as it affects directional stability, manoeuvrability, and comfort. Insufficient tire pressure is known to result in increased fuel consumption [1][13].

However, the use of tire pressure sensors located in the tire valves presents drawbacks such as potential failures, the requirement for specialized tires, and additional costs that car manufacturers aim to avoid. Therefore, there is a genuine interest in eliminating these sensors and finding alternative indirect solutions for tire deflation detection [2].

The objective of this paper is to propose online estimation methods for determining the rolling resistance force and effective radius of the wheels. This assessment of variables, along with the application conditions, represents a novel approach. The estimation results could be utilized by a tire pressure monitoring system (TPMS) [3].

To achieve this, the paper considers the longitudinal and rotational dynamics model of two wheels. A variable structure observer, based on high-order sliding mode theory [4], is designed for the online estimation of the tire radius and rolling resistance force. The input signals for this observer are the angular velocity of each wheel in the train and the applied torque [5]. These signals are available through the controller area networks (CANs).

The observer demonstrates robustness against uncertainties and disturbances, ensuring convergence in finite time. Furthermore, it can be applied to a wide range of observable systems [6][7].

The structure of the paper is as follows: Section II introduces the wheel model, providing the main equations for the longitudinal and rotational dynamics of the two tires. Section III elaborates on the design strategies for the observer in the case of overseeing the wheels on the front axle. Additionally, Section IV presents simulation results to illustrate the practicality of the proposed method. Finally, Section V concludes the paper and provides insights into future work.

II. MODEL OF STATEMENT PROBLEM

The main objective of the presented work is to develop a strategy for estimating the effective radius of two wheels and the rolling resistance force of the vehicle's front axle. This estimation is achieved by using only the vehicle speed, angular velocity of each wheel, and the torque applied to the wheels. The strategy requires the following:

ISSN: 1737-93341

- An adapted model that accounts for the dynamics of the two wheels.
- A solution for assessing the unmeasured variables,

Considering that the evolution of these variables cannot be known beforehand. Therefore, a robust estimation solution must be designed, taking into account the unknown effective radius of the two wheels and the rolling resistance force. By applying the second Newton's law to the forces acting on the two wheels of the front axle, their rotational and longitudinal dynamics can be expressed by:

$$J_l \square_l = T_l \square R_l F_{xl} \square C_f \square_l \qquad (1)$$

$$J_r \square_r = T_r \square R_r F_{xr} \square C_f \square_r \qquad (2)$$

$$M_{1/2}\square_x = F_{xr} + F_{xl} - F_{d1/2} - F_{rg} \qquad (3)$$

The subscripts "l" and "r" indicate the front left and right wheels, respectively. The symbol "ω" represents the angular velocity of the left wheel, while "ω" represents the angular velocity of the right wheel. The symbols "Rl" and "Rr" represent the effective radius of the left and right wheels, respectively. The vehicle's linear velocity is denoted by "v." The viscous friction coefficient of the wheel is represented by "γ."

Furthermore, "Jl" and "Jr" are the respective inertias of the left and right wheels, and "m" is half of the vehicle's mass. Additionally, "Tl" and "Tr" denote the torques applied to the left and right wheels, respectively.

The primary forces acting on the two wheels of the front axle are as follows: the traction forces "Fl" and "Fr," the aerodynamic drag forces "Dl" and "Dr," and the overall rolling resistance forces "Rrl" and "Rrr."

1. *Tractive forces*

The tractive forces are generated by the interaction between the tires and the road surface in response to the applied torque on the wheels. These forces are determined by the friction coefficient and the slip ratio. The slip ratio, as defined in reference [8], represents the relative difference between the actual wheel speed and the ideal wheel speed:

$$\square_i = \square\frac{(\square_x \square R_i \square_i)}{R_i \square_i} = \square\frac{\square_x}{R_i \square_i} + 1 \qquad (4)$$

where $i \in \{l,r\}$.

The friction coefficient is typically determined using semi-empirical formulas. A commonly accepted approximation, as mentioned in reference [9], expresses the friction coefficient as a function of the slip ratio:

$$\square_i(\square) = 2\square_0 \frac{\square_0 \square_i}{\square_0^2 + \square_i^2} \qquad (5)$$

where $\square_0$ is the optimal slip ratio, leading to the maximum friction value $\square_0 = \square(\square_0)$.

The tractive forces [8] are then given by :

$$F_{xi} = 2\square_0 \frac{\square_0 \square 1 \square \frac{\square_x}{\square_i R_i}\square}{\square_0^2 + \square 1 \square \frac{\square_x}{\square_i R_i}\square^2} M_{1/2}\, g \qquad (6)$$

2. *Aerodynamic force*

The force mentioned is directly proportional to the square of the vehicle's velocity, as indicated in reference [10].

$$F_{d1/2}(v_x) = \frac{1}{2}(\rho A_{d1/2} C_{d1/2} v_x^2) \qquad (7)$$

with ρ the air density, $A_{d1/2}$ the frontal area of the half-vehicle and $C_{d1/2}$ the drag coefficient.

3. *Global Rolling resistance force*

There exists a linear relationship between the global rolling resistance force and the vehicle's speed, as expressed by the equation:

$$F_{rg}(v_x) = F_{rl}(v_x) + F_{rr}(v_x) = 2M_{1/2} g C_r v_x \qquad (8)$$

with C_r the rolling resistance coefficient. This hypothesis can be made for heavy vehicles and is valid on light vehicles only for low speeds [10].

In the case of light vehicles with higher speeds, another equation must be considered:

$$F_{rg}(v_x) = 2M_{1/2}\, g \left(f_0 + 3.24 f_s \left(3.6 v_x / 100\right)^{2.5} \right) \qquad (9)$$

The rolling resistance coefficient is mainly determined by several factors, including tire inflation pressure, temperature, velocity, and road surface type. These variables collectively impact the magnitude of resistance encountered by the tires as the vehicle travels on the road.

III. NON LINEAR OBSERVER SYNTHESIS FOR PRESSURE DETECTION

The main objective of this task is to monitor the tire pressures of the two wheels located in the front axle of the vehicle. To achieve this, the methodology presented in references [3] and [4] needs to be extended to design an observer that can estimate the radius of the front axle wheels and the global rolling resistance force of the entire axle.

This proposed observer takes into account the coupling between the two wheels, resulting in a more precise estimation of the wheels' radius . By analyzing the increase in rolling resistance caused by a decrease in tire pressure, accurately estimating the radius of each wheel becomes crucial for detecting and locating any pressure drop.

This estimation plays a significant role in determining whether there is a decrease in tire pressure and identifying its location within the front axle.

A. *Observation model*

The observer is designed based on a model that incorporates equations (1), (2), and (3) describing the rotational dynamics of the two wheels in the front axle. The effective radius of the wheels, the rolling resistance force of the front axle, and the variable are initially unknown and can potentially change as a result of pressure loss in both wheels [6]. The goal of the observer is to estimate these unknown parameters and track their changes over time, taking into account the dynamics of the system. By continuously updating the estimates, the observer can provide valuable information about the state of the wheels and the front axle, particularly in relation to tire pressure.

The following equations are therefore used

$$\dot{R}_l = □_l(t),\ \dot{R}_r = □_r(t),\ \dot{F}_{rg} = □_g(t) \qquad (10)$$

with $□_l(t)$, $□_r(t)$ and $□_F(t)$ unknown and bounded. The torques applied to each wheel are, respectively, denoted as $□_l$ and $□_r$.

By denoting $y = [y_1 y_2 y_3]^T = [\Omega_l \Omega_r v_x]^T$, $x = [x_1 x_2 x_3 x_4 x_5 x_6]^T = [\Omega_l \Omega_r v_x F_{rg} R_l R_r]^T$ and $u = [u_1 u_2]^T = [T_l T_r]^T$ the control input, the dynamic behavior of the whole axle is given by

$$\dot{x} = f(x) + □(y,u) + □f \qquad (11)$$

where

$$f(x) = \begin{bmatrix} \frac{1}{J_l} x_5 F_{xl}(x) \\ \frac{1}{J_r} x_6 F_{xr}(x) \\ \frac{1}{M_{1/2}}(F_{xl}(x) + F_{xr}(x) - F_{d1/2}(x) - x_4) \\ 0 \\ 0 \\ 0 \end{bmatrix} \qquad (12)$$

$$□(y,u) = \begin{bmatrix} -\frac{C_f}{J_l} x_1 + \frac{1}{J_l} u_1 & -\frac{C_f}{J_r} x_2 + \frac{1}{J_r} u_2 & 0 & 0 & 0 & 0 \end{bmatrix}^T$$

$$□f = \begin{bmatrix} 0 & 0 & 0 & □_l(t) & □_r(t) & □_F(t) \end{bmatrix}^T$$

Two assumptions are considered [4], [6]:

Assumption 1: The uncertainty term $□f$ does not change the observability of (11). The nonlinear system (11) without any uncertainty ($□f = 0$).

$$\dot{x} = f(x) + □(y,u) \qquad (13)$$

Else, the term $□(y,u)$ only depends on well-known (measured) variable: as shown in [11], [12] this term is not required for the observer design and can be removed thanks to an input-output injection function $□(y,u)$. The term $□□(y,u)$ will be re-injected in the observer.

Assumption 2: The input–output injection function $□□(y,u)$ does not change the observability feature. It yields that the system(13) is transformed into

$$\dot{x} = f(x) \qquad (14)$$

ISSN: 1737-93344

B. Observability analysis

The function $\Phi(x)$ is defined by

$$\Phi(x)=\begin{bmatrix} y_1 \\ \dot{y}_1 \\ y_2 \\ \dot{y}_2 \\ y_3 \\ \dot{y}_3 \end{bmatrix}=\begin{bmatrix} x_1 \\ -\frac{1}{J_l} x_5 F_{xl}(x) \\ x_2 \\ -\frac{1}{J_r} x_5 F_{xr}(x) \\ x_3 \\ \frac{1}{M_{1/2}}\left(F_{xl}(x)+F_{xr}(x)-F_{d1/2}(x)-x_4\right) \end{bmatrix} \tag{15}$$

The measured variables are the wheels' velocities and the vehicle's longitudinal speed $y=\begin{bmatrix} x_1 & x_2 & x_3 \end{bmatrix}^T$. If the determinant of the Jacobian of the function $\Phi(x)$ is in all cases different from 0 on the operating trajectories, this implies that the transformation Φ is invertible and the system (14) is locally observable [3].

TABLE I:
WHEELS AND VEHICULE MODEL PARAMETERS FOR THE AXLE MODEL

Symbol	**Parameter**	**Value**	**Unit**
Left wheel's inertia	J_l	1.6	Kg.m^2
Right wheel's inertia	J_r	1.6	Kg.m^2
Nominal radius	R_{0i}	0.32	M
Half-vehicle mass	$M_{1/2}$	880	Kg
Frontal area	$A_{d1/2}$	0.65	m^2
Air density	ρ	1.205	Kg/m^3
Gravitational constant	g	9.807	m/s^2
Viscous friction coefficient	C_f	0	Kg.m^2/s
Drag coefficient	$C_{d1/2}$	0.25	-
Suspension damping	C_s	7722	Kg/s
Suspension stiffness	K_{si}	19960	Kg/s^2
Peak friction	μ_0	0.9	-
Optimal slip	λ_0	0.25	-

ISSN: 1737-93345

C. Observer design

Theapplication of the inverse input–output injection transformation $\Phi(y, u)$ allows us to get an observer for system(13)

$$\dot{\hat{x}} = f(\hat{x}, y) + \phi(y, x) + \left(\frac{\partial \Phi}{\partial x}\right)^{-1} k(y, \hat{x}) \qquad (16)$$

The function $k(y, \hat{x})$ has to be designed such that the state vector $\hat{x}$ of the previous system is reaching the vicinity of state vector of system(11) in finite time in spite of the uncertain dynamics Δf of R_l , R_r and F_{rg} .

A solution for $k(y, \hat{x})$ [3], [4] is suggested in order to obtain an accurate and robust estimation of $\hat{x}$; it is based on high order sliding mode differentiation. Then, the observer (16) for the system (11) has a correction term defined by :

$$k(y,\hat{x}) = \begin{bmatrix} \kappa_1 \\ \kappa_2 \\ \kappa_3 \\ \kappa_4 \\ \kappa_5 \\ \kappa_6 \end{bmatrix} = \begin{bmatrix} a_1 L_1^{1/2} \left| y_1 - \hat{x}_1 \right|^{1/2} sign(y_1 - \hat{x}_1) \\ a_2 L_1 sign(\kappa_1) \\ a_3 L_2^{1/2} \left| y_2 - \hat{x}_2 \right|^{1/2} sign(y_2 - \hat{x}_2) \\ a_4 L_2 sign(\kappa_3) \\ a_5 L_3^{1/2} \left| y_2 - \hat{x}_2 \right|^{1/2} sign(y_2 - \hat{x}_2) \\ a_6 L_3 sign(\kappa_5) \end{bmatrix} \qquad (17)$$

The parameters used for the axle model are summarized in Table I [3]. The observer coefficients are defined as must be fixed as proposed in [3].

II. SIMULATION AND RESULTS

In this section, we present the results of our solution validation under ideal conditions, where no noise is present. We employed the Matlab/Simulink® software as the tool for constructing the half-vehicle. The torques applied to the two wheels and their angular velocities were obtained from a prototype vehicle, specifically the Renault sedan Laguna II, which was generously provided by Renault [6],[14].

To explore different values for the effective radii and rolling resistance force of the entire axle, we considered two inflation pressure levels. The first pressure value, P1, was set at 2.3 bar, which corresponds to the nominal pressure. For the left front wheel, we used a pressure of 1.9 bar, denoted as P2, while maintaining the right front wheel at its nominal pressure of 2.3 bar. The observer state variables were initialized with the following values.

$$\hat{x}(0) = \begin{bmatrix} \hat{\Omega}_l \\ \hat{\Omega}_r \\ \hat{x} \\ \hat{F}_{rg} \\ \hat{R}_l \\ \hat{R}_r \end{bmatrix} = \begin{bmatrix} 15 / 0.31 \\ 15 / 0.31 \\ 15 \\ 148 \\ 0.305 \\ 0.305 \end{bmatrix} \qquad (18)$$

ISSN: 1737-93346

The gains values of observer are $L_1 = 6$, $L_2 = 5$ and $L_3 = 4$ where as the initial conditions of the complete model are such that

$$x(0) = \begin{bmatrix} \square_l \\ \square_r \\ \square_x \\ d_c \\ d_c \\ \dot{d}_r \\ \bar{d}_r \end{bmatrix} = \begin{bmatrix} 15/0.3 \\ 15/0.3 \\ 15 \\ 0 \\ 0 \\ 0 \\ 0 \end{bmatrix} \qquad (19)$$

Controller design: In order to be as near as possible to real situation, it has been assumed that the effective radii and their dynamics are well-known. A control ensures movement of the vehicle at a slow speed variable in time according to a desired speed v^d [4].

$$v_x^d = v^d \left(1+\square_v \sin(\square t)\right) \qquad (20)$$

with :

v_x^d : Profile to be followed by the speed,
$v^d = 40 km/h$,
$\square_v = 0.01$,
$\square = 0.314 rad/s$.

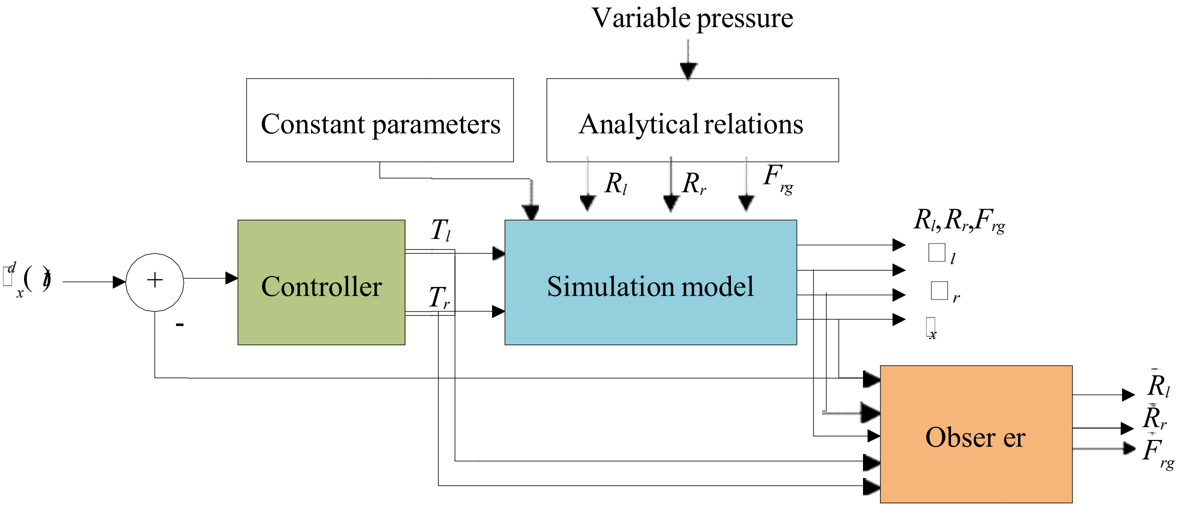

Fig. 1. Schematic diagram for the simulation of the system and the observer effective radusi and the global rolling resistance of front axle of vehicle.

Consider the controller output

$$z = R_i \square_i - \square^d_x(t) \qquad (21)$$

The relative degree of z equals 1, which gives :

ISSN: 1737-93347

$$
\begin{aligned}
z &= \frac{R_i}{J_i}\left(T_i - R_i F_x \square C_f \square_i\right) + R_i \square_i \square\square_x^d \\
&= \underbrace{\square \frac{R_i}{\bar{J}_i}\left(R_i F_x + C_f \square_i\right) + R_i \square_i \square\square_x^d}_{\square(x,t)} + \underbrace{\frac{R_i}{J_i} T_i}_{\square(x,t)} \\
&= \square k z
\end{aligned}
\qquad (22)
$$

where$i \in \{l,r\}$.

There fore the torque applied to each wheels can be written

$$
T_i = \frac{1}{\square_i} \square \square \square_i (x,t) \square k(R_i \square_i \square \square_x^d (t)) \square \qquad (23)
$$

with $k \square 0$ which is set empirically to $k = 1$ in this test.

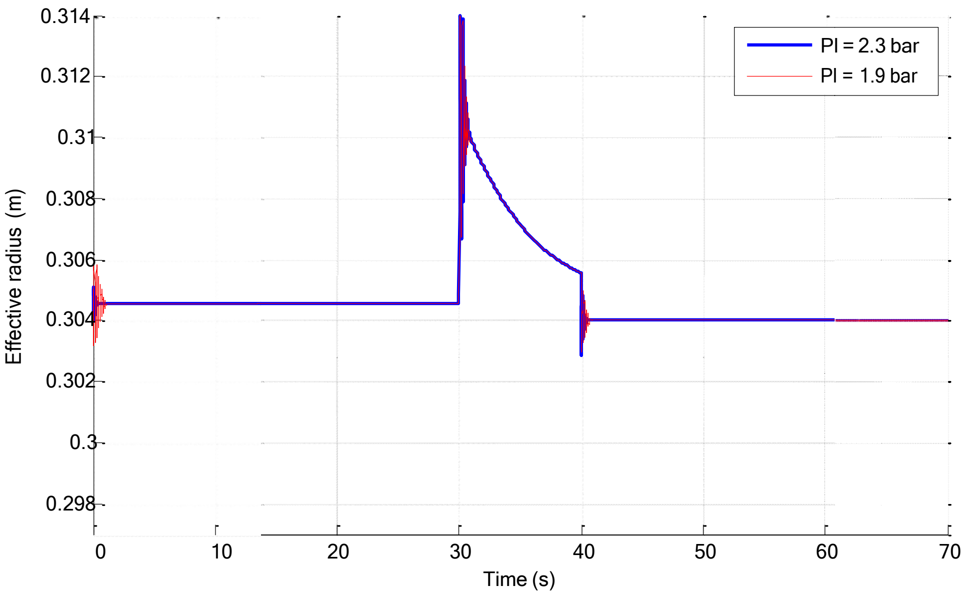

Fig. 3. Estimated right wheel effective radius for two different tire pressures (2.3 and 1.9 bar).

ISSN: 1737-93347

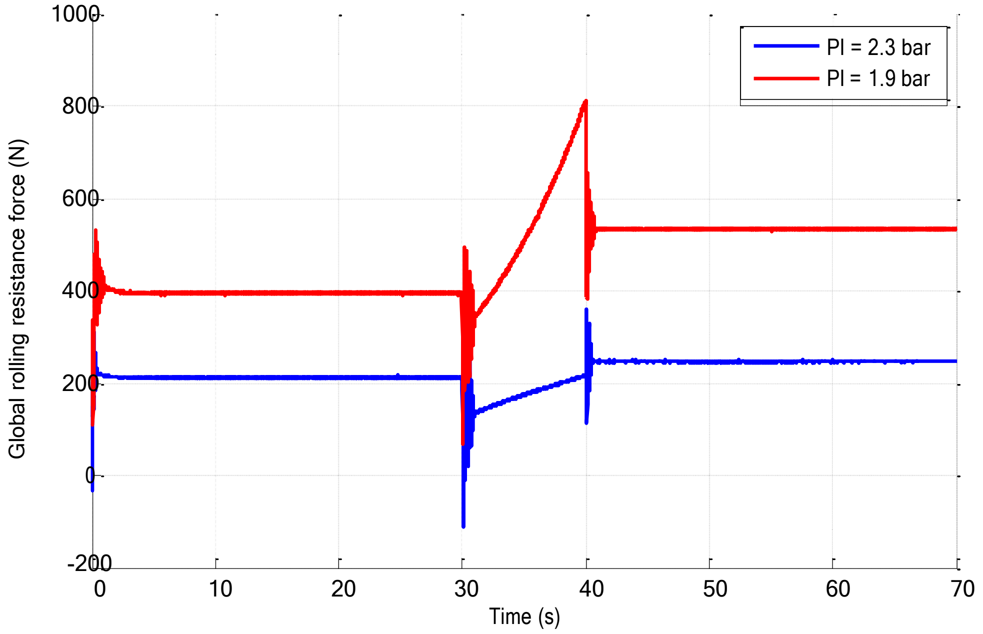

Fig. 4. Estimated global rolling resistance force of the axle for two different tire pressures (2.3 and 1.9 bar).

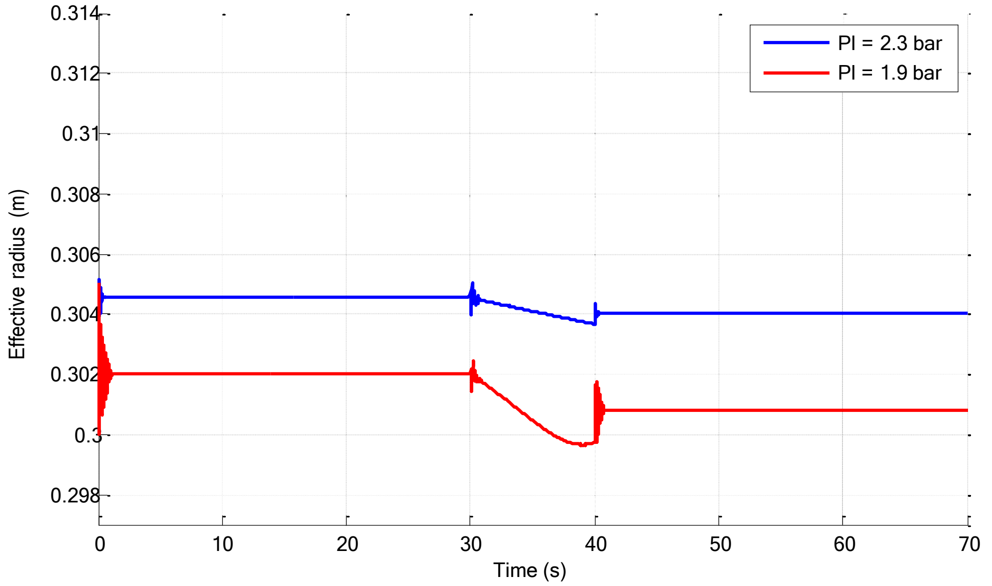

Fig. 2. Estimated left wheel radius for two different tire pressures (2.3 and 1.9 bar).

A simulated scenario involved a 20% decrease in pneumatic pressure from its nominal value of 2.5 bar between specific time intervals $t_1 = 30s$ and $t_2 = 40s$. At the initial time, there was an assumed error of 5 mm between the actual and estimated radii, as well as an error of 1.6 rad/s between the actual and estimated angular velocities for each wheel. Additionally, the two wheels on the front axle of the vehicle had different profiles.

Figures 2, 3, and 4 depict the estimation of the left wheel radius, the right wheel radius, and the global rolling resistance force of the front axle, respectively. It can be observed that when the pressure decreases in the left front wheel's tire, the observer provides a lower value for the wheel radius and a significantly higher value for the global rolling resistance force on the front axle.

The estimated radius of the right front wheel remains constant. The increase in the global rolling resistance force indicates a pressure drop, but it does not alone identify which tire experiences the pressure decrease. The radius of both wheels are directly related to their respective pressures. These graphical representations enable us to deduce that the pressure drop originates fromthe left wheel.

IV. CONCLUSION

This paper focuses on estimating the effective radius and global rolling resistance force of the vehicle's front axle. To address the uncertainty surrounding these parameters, a high-order sliding mode observer is employed, leveraging its robustness and accuracy. The use of this observer is motivated by the lack of prior knowledge regarding the evolution of the effective radius and rolling resistance force. The obtained results demonstrate a satisfactory estimation of the effective radii and rolling resistance force for the vehicle's front axle. This suggests that the sliding mode observer effectively captures the desired non-measurable quantities, providing accurate estimations. The observer's robustness allows it to handle uncertainties and disturbances, while its precision ensures reliable estimations even under challenging conditions. Overall, the application of the sliding mode observer proves to be a viable approach for estimating the essential parameters related to the front axle of the vehicle.

Additionally, extending the study to include the observation model and an observer for the characteristics of all four wheels simultaneously presents an intriguing opportunity. This would involve developing a model of the complete vehicle and incorporating it into the observation framework.

REFERENCES

[1] Egaji O.A., Chakhar S., Brown D.: *An innovative decision rule approach to tyre pressure monitoring. Expert Systems with Applications*. 2019, 124, 252-270, DOI: 10.1016/j.eswa.2019.01.051.

[2] S. Velupillai and L. Guveng, "*Tire pressure monitoring,*" IEEE Control Syst. Mag., vol. 27, no. 6, pp. 22–25, Jun. 2007.

[3] El Tannoury, C "*Développement d'outils de surveillance de la pression dans les pneumatiques d'un véhicule à l'aides des méthodes basées sur l'analyse spectrale et sur la synthèse d'observateurs*,". Diss. Ecole centrale denantes-ECN, 2012.

[4] N. Ouasli, R. Ben Mehrez, L. El Amraoui, " *Parameter estimation of one wheel vehicle using nonlinear observer,*" International Conference on Electrical Sciences and Technologies in Maghreb-CISTEM, Nov. 2014.

[5] T. Boukhobza, "*Observateurs à Modes Glissants et Formes D'observabilité et Analyse et Synthèse Des Commandes Par Ordres Supérieurs,* " Thèse de doctorat, Université de Paris Sud Orsay, 1997.

[6] El Tannoury, C., Moussaoui, S., Plestan, F., Romani, N., & Gil, G. P, "*Synthesis and Application of Nonlinear Observers for the Estimation of Tire Effective Radius and Rolling Resistance of an Automotive Vehicle,*". IEEE Transactions on Control Systems Technology, 21(6), 2408-2416, 2013.

[7] H. Imine, L. Fridman, H. Shraim, and M. Djemai, "*Sliding Mode Based Analysis and Identification of Vehicle Dynamics,*" ser. Lecture Notes in Control and Inf. Sci., New York: Springer-Verlag, 2011, vol. 414.

[8] G. Jazar, "*Vehicle Dynamics: Theory and Applications,*" 1st ed. New York: Springer Verlag, 2008.

[9] W-E.Ting and J-S.Lin, "*Nonlinear control design of anti-lock braking systems combined with active suspensions,"* In 5th Asian control conference, 2004.

[10] T. Gillespie, "*Fundamentals of vehicle dynamics*," SAE International, 1992.

[11] A.J. Krener and A. Isidori, "*Linearization by output injection and nonlinear observers*," Systems & Control Letters, 1983, vol. 3, no 1, p. 47-52.

[12] F. Plestan and A. Glumineau, "*Linearization by generalized input-output injection*," Systems and Control Letters, 31(31):115–128, 1997.

[13] D. Stein, "*Tires and passenger vehicle fuel economy: Informing consumers and improving performances,"* Trans. Res. Board, Washington, DC., TRB Special Rep. 286-78, Aug. 2006.

[14] Žuraulis V., Surblys V., Šabanovič E.: *Technological measures of forefront road identification for vehicle comfort and safety improvement. Transport.* 2019, 34(3), 363-372, DOI: 10.3846/transport.2019.10372.

Conférence Internationale sur les Sciences Appliquées et l'Innovation (CISAI-2023)
Proceedings of Engineering & Technology-PET-Vol 77

Fluid flow and heat transfer around three circulars cylinders in tandem arrangements with variable boundary condition in semi confined media

Farid HACHICHI[*1], Nourdine BELGHAR[*2], Mahfoud KADJA[3], Ridha MEBROUK[#4],
Issam REZAIGUIA[#5], [6]Mohammed LACHI

[*1-2] *Mechanical Engineering, University of Mohamed Khider Biskra*
BP 145 RP, 07000 *Biskra*, Algeria

[3] *Mechanical Engineering, University of Mentouri Brothers University of Constantine 1*
P.O. Box, 325 Ain El Bey Way, Constantine, Algeria, 25017

[#4-5] *Drilling and mechanics of oilfildes, University of Kasdi Merbah*
BP.511, 30,000, Ouargla, Algeria

[6] *University of Reims Champagne Ardenne*
Villa Douce - 9, bd de la Paix - CS 60005 - 51724 Reims Cedex, France
[1]hachichifa@yahoo.fr
[2]n.belghar@univ-biskra.dz
[3]kadja_mahfoud@yahoo.fr
[4]ridhamebrouk@gmail.com
[5]irezaiguia1981@gmail.com
[6]m.lachi@univ-reims.fr

***Abstract*— In this paper, tow dimensional unsteady laminar convective heat transfer from three isothermal cylinders of tandem arrangements with variable boundary condition in semi confined media is numerically investigated. The numerical simulations are carried out by solving continuity, momentum and energy equations using a finite volume method-based commercial solver ANSYS-FLUENT. The present study was conducted using a Prandtl number of 0.7 for air as working fluid, with Reynolds number equal to 100, spacing ratio varying from 2 to 5, and at fixed value of blockage ration β=0.25. The characteristics of the flow such as the totals drag and lift coefficients on these dimensionless parameters has been discussed in detail. The isotherms and vorticity were generated to explain the flow and heat transport visualization. The local and average Nusselt numbers for first, second and third cylinder are also computed. It is found that the force coefficients, the wake structure behind the cylinders and the Nusselt number depend strongly on the value of the spacing ratio. Finally in some cases the behavior of the second cylinder does not follow the overall trend of variations.**

***Keywords*— Forced convection, numerical simulation, circular cylinders in tandem arrangement, vortex shedding patterns, Drag and lift coefficients, Nusselt number.**

I. INTRODUCTION

Fluid flow and heat transfer around cylinders has various applications in engineering systems, such as heat exchangers, gas turbine cooling, electronic cooling, and other thermal applications. Flow dynamics and formation of vortices between two tandem bluff obstacles (circular cylinders, square cylinders, trapezoidal cylinders…..) in unconfined and confined domain are very complex, for these reasons, the fluid flow and heat transfer around tow cylinders in tandem arrangements has received a surge attention in the literature (Igarashi [1-2] and Zdravkovich [3]) and the focus of the most investigation is in vortex formation, vibration, forced and heat transfer. A number of studies have been published on this topic. A comprehensive review is presented by Sumner [4] for understanding the effect of placing tow circular cylinders on the flow field structure, aerodynamics loads, vortices and other parameters, the flow around two identical cylinders in a stable cross flow can be divide into (a) extended-body regime; (b) reattachment regime; (c) coshedding regime. Jiang et al. [5] performed numerical simulation of flow past two tandem cylinders of different diameters and assessed the effects of channel walls on the flow field for

ISSN: 1737-93347

blockage ration ranging from [illegible] to . They showed that the channel width has an important effect on the critical spacing where the flow changes from single body mode to co-shedding mode. Sohanker and Etminan [6] presented numerical results of flow characteristics and heat transfer on two equal square cylinders arranged in series at low Reynolds number ($Re = 1 - 200$). Lin et al [7] carried out numerical investigation of flow past two tandem cylinders that are free to move in the transverse direction in a plane channel with a blockage ration of 15% and singled out that the channel walls play an important role in the computed hydrodynamic forces. In another works, the same authors [8] presented numerical results of the unsteady laminar flow and heat transfer from square cylinders in a channel. The results showed that the cylinder Nusselt and Strouhal numbers decrease as the wall is approached. Rosales [9] performed a numerical study of fluid flow and heat transfer over tow squere cylinders with different sizes and arrangements in a channel for $Re = 500$. Considering channel walls and the upstream cylinder as insulators and the downstream cylinder as a hot obstacle, their results show that the drag coefficient and the Nusselt number decrease when the in-line or offset tandem pair of cylinders is positioned coser to a channel wall.

Unsteady laminar convective heat transfer from two isothermal cylinders in tandem arrangement was studied numerically by mahir and Altac [10]. It was shown from the numerical results that the average Nusselt number of the upstream cylinder approached to heat of a single isothermal cylinder for $L/L > 4$ and the average Nusselt number of the downstream cylinder was about 60% of the upstream cylinder. Ding et al. [11] presented numerical results for flow field around two circular cylinders arranged in side-by-side and tandem configuration ($L/D = 2.5$ and 5) using the mesh-free least square based finite difference method. The flow simulation were carried out for $Re = 100$ and 200. The flow separation and flow state of the trapezoidal cylinder under low Reynolds number ($Re = 1 - 150$) was analyzed by Dhiman and Hasan [12]. The numerical study of Cung and Kang [13] showed that the Strouhal number of the trapezoidal cylinder depends on the Reynolds number and height ratio, wich is thz ratio of height of the rear face to that of the front face (d/D). The flow without heat transfer behavior past a single cylinder as well as tandem square and circular cylinders in vicinity of a wall with low Reynolds number ($Re = 100$ and 200) was studied numerically by Harichandan and Roy [14]. Their analysis focused on the boundary layer growth and the location of the cylinders parameters. Their results are presented for different parameters to visualize vorticities and streamlines. Similarly, the wall effects on flow structure over two tandem cylinders is studied by Jiang and Lin[15] with low Reynolds number ($Re = 20 - 120$). Ajay Raj Dwivedi et al [16] presented numerical results for the fluid flow and mixed convective (thermal cross-buoyancy) heat transfer of incompressible fluid across identical cylinders organized in a confined tandem configuration. For different gap ration ($S/D = 2.5, 3, 3.5, 4, 5,$ and 5.5) with varying Richardson number ($Ri = 0, 0.5$ and 1) at Reynolds number 100 . Prandtl number $Pr = 0.7$ and wall confinement $\beta = 25\%$. It was found that the fluctuations in lift signal shift from zero average value at $Ri = 0$ towards the nonzero negative average value for the tandem cylinders at $Ri > 0$. The local Nusselt number shows the shift in the front stagnation point on both cylinders with increasing thermal cross-buoyancy. The drag coefficient and Nusselt number of the downstream cylinder are always less than the upstream cylinder, but the percentage increment in the physical parameters of the downstream cylinder after critical spacing is much more the its upstream counterpart. A numerical methods was used by Arif Mentese et al [17] to study the effect of distance between cylinders on flow characteristics for tandem and side-by-side two circular cylinders. It was shown from the numerical results that the flow is almost steady with any vortex in the gap when cylinders are in tandem and the gap between them is low. In contrast, the interactions are strong in case of side-by-side arrangement at the lowest gap ratio. When the gap ratio increase, the flow is affected that results in change on the global parameters. Wei Zhang [18] investigated numerically of flow across two tandem cylinders with rounded corners in a channel at $Re = 100$. The cylinder geometry varies from square to circular by rouding all corners, and the partially rounded cylinders were considered. The effects of gap ratio (GR) characterizing the separting distance of two cylinders and the radius (R) was analyzed at dimensionless parameters ($R^+ = 0 - 0.5$) and $GR = 1 - 6$. They showed that the cylinder geometry determines the unsteadiness of the near-wake after the downstream cylinder, the flow is always unsteady for square-like cylinders where the corner radius is small, while the flow can be stabilized by the circular-like cylinders with larger corner radius that the flow fluctuation is greatly weakened or even fully suppressed at small GR

After above investigation, it is clear that there is no reported work on the effect of three tandem cylinders on fluid flow and heat transfer in a confined domain with inlet parabolic velocity, the aim of the present study is to add to our scholarship on the relationship of dynamics fields (C_L, C_D) and thermal fields (Nusselt number) with gap ratio and Reynolds number of the forced convection over three tandem cylinders in confined domain with variable boundary condition. A series of computational is conducted for three tandem cylinders with Reynolds number varying from 100 to 200 and gap ratio varying from 2 to 10 with inlet parabolic velocity profile, analyzed and studied in detail through the flow structures and thermal fields in this configuration.

II. PROBLEM DESCRIPTION

Briefly the description of the problem is shown in Figure 1. Three identical heated circular cylinders of equal diameter D arranged in tandem whose surfaces are fixed temperature T_w and placed in confined duct, with exposed to a fully developed velocity profile with average velocity u_{avg} and T_∞ Tow adiabatic horizontal walls of finite length are placed at a distance of $H/2$ on either side of the center of the cylinders. The outlet of the duct is specified with Neumann condition. The gap ratio r was defined as $r = S/D$, where S represents the spacing between centre to centre of the cylinders, S was selected as 2 to 10. The flow was described in a Cartesian coordinated system (x, y) and . The upstream and downstream distances of computational domain are gives respectively by the values $L_u = 10D$ and $L_d = 48D$. The blockage ratio of the computational domain is given as: $\beta = D/H = 0.25$. It is also considered that the flow unsteady laminar regime with constant thermo-physical proprieties.

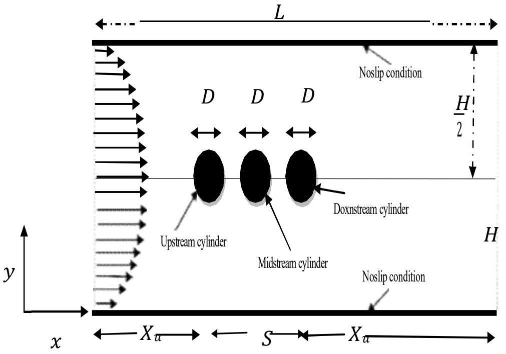

Fig.1 Computational domain and three cylinders configuration.

III. GOVERNING EQUATIONS AND BOUNDARY CONDITIONS

The governing equations, for unsteady incompressible viscous flow with constant thermophysical properties in two-dimensional Cartesian coordinate are expressed as follows:

For continuity

$$\frac{\partial u_x}{\partial x}+\frac{\partial u_y}{\partial y}=0$$

For the momentum

$$\frac{\partial u_x}{\partial t}+u_x\frac{\partial u_x}{\partial x}+u_y\frac{\partial u_x}{\partial y}=-\frac{1}{\rho}\frac{\partial p}{\partial x}+\nu\left(\frac{\partial^2 u_x}{\partial x^2}+\frac{\partial^2 u_x}{\partial y^2}\right)$$

$$\frac{\partial u_y}{\partial t}+u_x\frac{\partial u_y}{\partial x}+u_y\frac{\partial u_y}{\partial y}=-\frac{1}{\rho}\frac{\partial p}{\partial y}+\nu\left(\frac{\partial^2 u_y}{\partial x^2}+\frac{\partial^2 u_y}{\partial y^2}\right)$$

Ffor the energy

$$\frac{\partial T}{\partial t}+u_x\frac{\partial T}{\partial x}+u_y\frac{\partial T}{\partial y}=\alpha\left(\frac{\partial^2 T}{\partial x^2}+\frac{\partial^2 T}{\partial y^2}\right)$$

Where u_x, and u_y are the dimensionless velocity components along $x-$ and y -directions of a Cartesian coordinate system, respectively, p is the dimensionless pressure, ν is the kinematic viscosity, ρ is the density, T is the temperature of the fluid, and α is the thermal diffusivity defined as $k/\rho c$ where is k the thermal conductivity and is the c specific heat of the fluid.

The computational domain and the configuration of the circulars cylinders are illustrated in Fig.1. The boundary conditions for the inlet, outlet, walls and surface of cylinders can be written as:

For the inlet: A fully developed $2-D$ parabolic velocity profile

$$u_x = 1.5u_{avg}\left(1-\left(1-\frac{2Dy}{H}\right)^2\right)$$

Where $0 \le y \le H/D$, $u_y = 0$, $T = T_\infty$

For the outlet: $\frac{\partial u_x}{\partial x} = \frac{\partial u_y}{\partial x} = \frac{\partial T}{\partial x} = 0$

For the Bottom and top: $\frac{\partial T}{\partial y} = 0$, $u_x = u_y = 0$

ISSN: 1737-93347

For thecylinders walls: $u_x = u_y = 0$, $T = T_w$
Were u_{avg}, T_∞ are the average velocity and stream temperature respectively and $T_w$is the cylinder wall temperature.
One of the key parameters in the present study is the Reynolds number, Eq. 9.

$$R_e = \frac{\rho u_{avg} L}{\mu}$$

This numerical study reveals the influence of Reynolds number and the space between the cylinders on lift coefficient (Eq.10), drag coefficient (Eq.11), and Nusselt number (Eq.12) since these coefficients deliver important information about flow characteristic and heat transfer by forced convection.
Overall mean drag and mean lift coefficient was mathematically defined as:

$$C_D = \frac{F_D}{\frac{1}{2}\rho u_{avg}^2 L}$$

$$C_L \quad \frac{F_l}{\frac{1}{2}\rho u_{avg}^2 L}$$

Where, $F_D$and F_L are the force components in the longitudinal and transverse directions respectively.

In the present study, the local Nusselt number is defined based on the cylinder diameter D as the length scale:

$$-k\frac{\partial T}{\partial n}\Big|_w = h_\theta (T_w - T_\infty) \text{ , } Nu_\theta = \frac{h_\theta D}{k}$$

Where, h_θ is the local surface heat transfer coefficient, and n is the direction perpendicular to the cylinder wall. The average Nusselt number at the cylinder wall is calculated by integrated of the local Nusselt number over the cylinder surface.

$$\overline{Nu} = \frac{1}{2\pi}\int_{\theta=0}^{\theta=2\pi} Nu_\theta d\theta$$

IV. NUMERICAL METHODS AND SIMULATION CONDITIONS

In this study, the governing flow and energy equations with its boundary conditions have been solved numerically by the finite volume method using the ANSYS Fluent, the ANSYS work-bench was used to generate structured quadrilateral cells of uniform and no-uniform grid spacing as shown in Fig.1.
The tow-dimensional, unsteady, laminar, segregated solver was used to solve the equations of the incompressible flow on the collocated grid a arrangement. A Semi-Implicit Method for Pressure Linked Equation algorithm (SIMPLE) is used for the velocity-pressure coupling. QUICK (Quadratic Upstream Interpolation for Convective Kinematics) scheme was used to discretize the convective terms in the momentum and energy equations. The second order implicit time-integration scheme was used to solve the evolved transit condition with dimensionless time step Δt of 0.01, which was fixed after a time-dependent study indicates that any decrease in the time step size has negligible effect on the values of the global flow and heat transfer characteristics. The software Fluent uses the Gauss-Seidel point by point iterative method in combination with the algebraic multi-grid method to solve the system of algebraic equations. The inlet velocity input (Eq. 6) is specified by exploiting the by user-defined function (UDF) accessiblein ANSYS Fluent.
In the current computations, we divided the domain into structured mesh with fin clustering distributions in the vicinity of the cylinders surface, top and bottom walls to control the sharp velocity, temperature and pressure gradients near the surfaces of the cylinders and walls and of course these deviations it should not be excessively computationally intensive. Therefore, a grid independency test has been performed using the gap ratio GR=4 and 10 for R_e=100 and three quadrilateral grid which are differentiated by the number of points on the surface of cylinders (N_i), the value of (δD) near the surface of the cylinders. we was found that the N_i=200 and (δD=0.005) is sufficient to conduct the following numerical simulations with conditions used in this work.
In unsteady flow numerical simulations results also depend on the time interval. In this study, three different dimensionless time intervals: Δt=0.1, 0.01 and 0.005 is used to determine an optimum value which resulted in less computational time, yet sufficiently accurate solutions. Finally a dimensionless time step size of 0.01 which was adapted in this study.

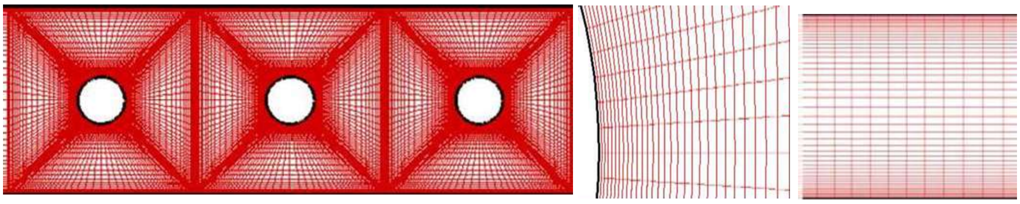

Fig.2 Magnified view of a grid structure around the three tandem cylinders ($GR = 4$)

V. RESULTS AND DISCUSSION

This section starts with presentation and discussion of the validation study, before systematize the results obtained by this numerical simulation in the form of streamline, vorticity and isotherm contours along with drag coefficient, lift coefficient and Nusselt number (local and surface average).

A. *Validation study*

A validation is performed before solving the present problem to demonstrate and confirm the precision of the results reported in this study. For this purpose figure 2 and Table 1 compares the numerical results of Ajay Raj Dwivedi and Amit Kumar Dhiman [16] to our numerical results for for two identical circular cylinders in the case of parabolic inlet velocity at gap ration GR=4 for Re=100 and Pr=0.7, the comparison of the results through the values of mean drag and lift coefficients and average Nusselt numbers for both upstreamand downstream cylinders. Figure 2 and Table 1 shows excellent agreement between the findings, confirming the veracity of our numerical results.

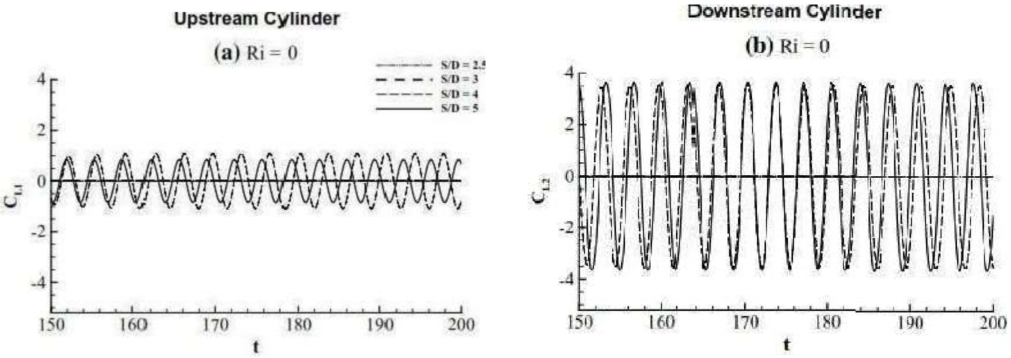

Ajay Raj Dwivedi and Amit Kumar Dhiman [16]

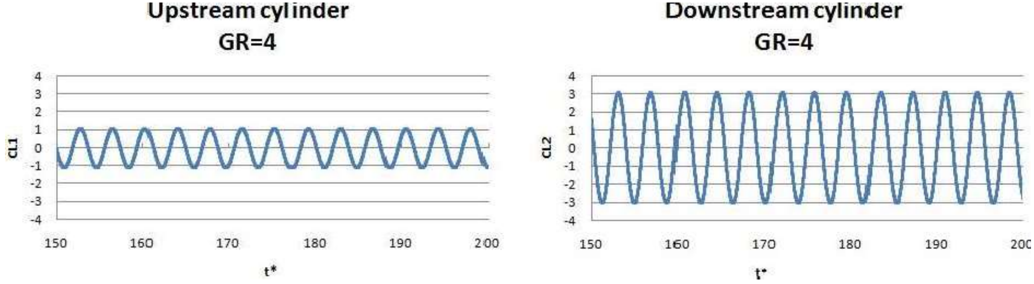

Present study

Fig.3 Comparison between the present and literature values of the time histories of lift coefficients and for a two tandem confined cylinders at $Re = 100$, GR=4 and $Pr = 0.7$.

Table 1 Comparison between the present and literature values of the mean drag coefficients and average Nusselt number for a two tandem confined cylinders at $Re = 100$, GR=4 and $Pr = 0.7$.

References	***Present study***	***Ajay Raj Dwivedi and Amit Kumar Dhiman [16]***
C_{D1}	*2.9684*	[illegible] *2.97*
C_{D2}	*2.4832*	[illegible] *2.49*

ISSN: 1737-93347

Nu_2	*6.368*	≈ *6.38*
Nu_3	*5.260*	≈ *5.53*

B. Streamlines, vorticity and isotherms contours

Streamline and vorticity contours it is one of the keys to understanding the flow regimes, this flow regimes it is divided into three regimes depending on the gap ratio G (a) the extended-body regime ($G < 1.2 - 1.8$) in this range the free shear layers separated from the upstream cylinder overshot the downstream cylinder. (b) reattachment regime, ($1.2 - 1.8 < G < 3.4 - 3.8$) in this range the shear layers reattached on the downstream cylinder, and (c) the co-shedding regime ($G > 4$) and the shear layers rolled up alternately, forming a vortex street in the gap between, as well as behind, the cylinders, like's reported by Zdravkovich (1977).

Figure 4, figure 5 and figure 6 show streamlines, vorticity and isotherms in the computational domain respectively, both figures reveal that the gap ratio between cylinders has significant great impact of the mechanism of flow and thermal patterns evolution around tandem circular cylinders. The dependence of instantaneous streamlines near the cylinders for different spacing ratios at Re=100 obtained at dimensionless time t*=225 are shown in Figure.4. It can be assessed that the flow behaves as steady for GR<4 and the flow filed obtained is symmetric about the mid-plane with formation of twin vortices are observed. For GR=3 the flow remains steady, whereas the centers of symmetric recirculation zones in gap region move toward inside slightly due to the increasing driven effect from the free stream flow. With increasing the gap ratio (GR≥4) The shear layer from the front cylinder reattaches on the rear cylinder at some point. After impinging on the rear cylinder, this shear layer is divided into two parts and transported away and detaches from the lower and upper part of the rear cylinder. The detached layer once again impinged on the lower part of the rear cylinder. The flow patterns in the gap and around the cylinders strongly depend on the cylinder spacing and this is confirmed by figure 5.

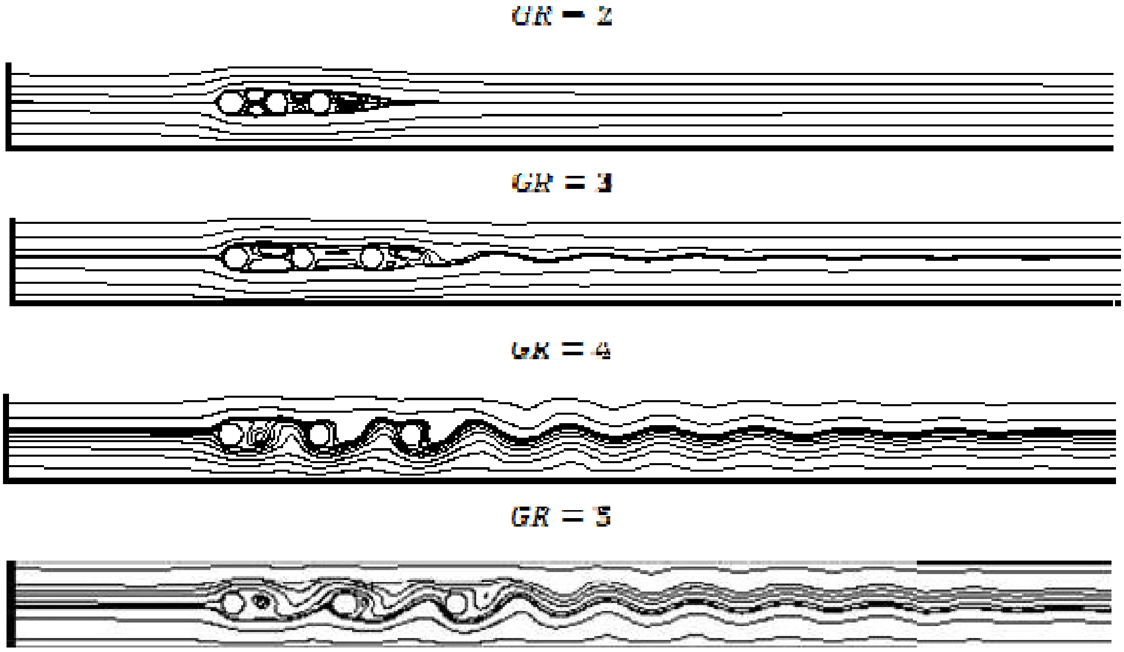

Fig.4 Streamlines around three cylinders in tandem arrangement for different spacing ratios at $Re = 100$ with $t^* = 225$.

The instantaneous vorticity contours around three tandem cylinders are shown in Figure.5, these contours are plotted for different spacing ratios at Re=100 and at dimensionless time t*=225. As can be seen in this figure, the vorticity contours become more complex with increasing the spacing. The wake structure behind the cylinders strongly depends on the spacing ratio. There is no vortex shedding from the cylinders at GR=2 and GR=3. It is observed that for GR ≥ 4, the generated vortices are more obvious. For small gap ratio (Gr<4) the flow is steady and shear layers detached from the first and second cylinder do not form vortex shedding upstream of the second and third cylinders respectively. Vortices are formed in between the cylinders and behind the third cylinder and the formation of vortex shedding for both cylinders occurs only after GR ≥ 4. We can observed that the flow remains steady until GR <4, but at GR ≥ 4 the flow becomes unsteady and at this gap ratio the fluid separates from the first, second and third cylinder and it is seen that in this instability, a couple of eddies is developed, and is shed alternately in the downstream direction with two row vortex street. These results mean that at high gap ratios ($G \geq 4$) the shear layer from the first cylinder top surface reattaches on the surface of the second cylinder and is divided

ISSN: 1737-93347

into two parts as well the shear layer from the second cylinder top surface reattaches on the surface of the third cylinder and is divided into two parts , where one will be moving through the gap between the cylinders and the other over the third cylinder. Overall, the flow is characterized by the formation of the Ka´rma´n vortex street behind the third cylinder.

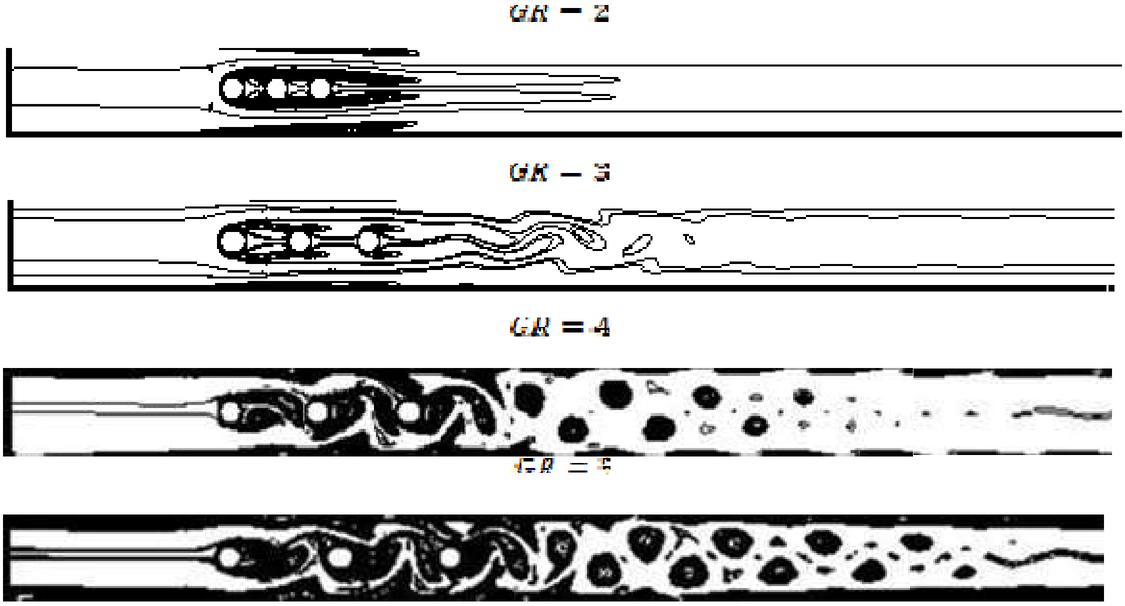

Fig.5 Vorticiy around three cylinders in tandem arrangement for different spacing ratios at $Re =$ [illegible] and [illegible].

Figure 5 shows the temperature contours gap ratio. The vorticity transport characteristics are indicative of the thermal transport. Accordingly, it is seen from figure 5 that the characteristic feature of the isotherms are similar to the vorticities evolving. Most of the isotherms are clustered around both the cylinder surfaces resulting in maximum heat transfer on the front stagnation point for first, second and for third cylinder maximum heat transfer location are at two points where thermal and hydrodynamic boundary layer thickness becomes thin for GR=2, 3 and for GR>3 (after reattachment), maximum heat transfer (cluster of isotherms) for first cylinder also shifts to its front stagnation point. There is a uniform temperature field between the cylinders for lower gap spacing. However, when the spacing increases, an unsteadytemperature pattern is observed between the cylinders.

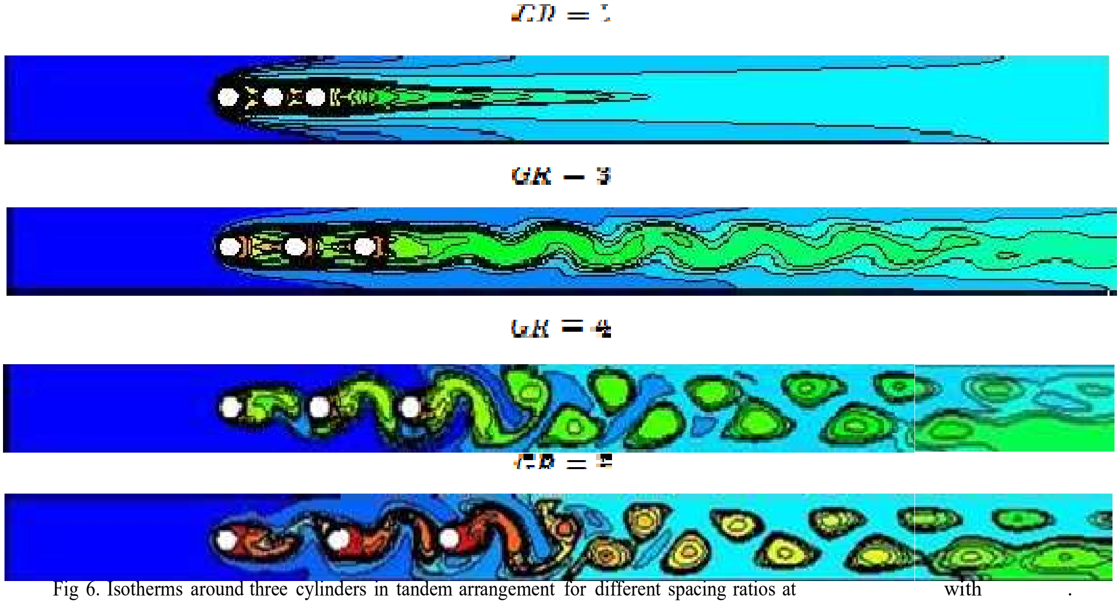

Fig 6. Isotherms around three cylinders in tandem arrangement for different spacing ratios at $Re = 100$ with [illegible].

B. Variation of lift and drag coefficients with gap ratio

Figure 7 and 8 shows results for time histories of the lift and Drag coefficient of three circular cylinders in the range of GR= 2 to 5 at Re =100 respectively. The amplitudes of time histories of CL and CD at GR=2 are quite small because the vortex street behind the cylinders is not formed as seen in figure 5.

The CL and CD amplitudes of the first cylinder is small relative to that of the second and third cylinder. No vortices are shed from the first and second cylinder, and the CL fluctuation of the first and second cylinder is induced by the movement of the first and second cylinder shear layers. The CL fluctuation of the second and third cylinder is caused by the alternate reattachment of the first cylinder shear layers, as well as by the vortex shedding fromthe first and second cylinder.

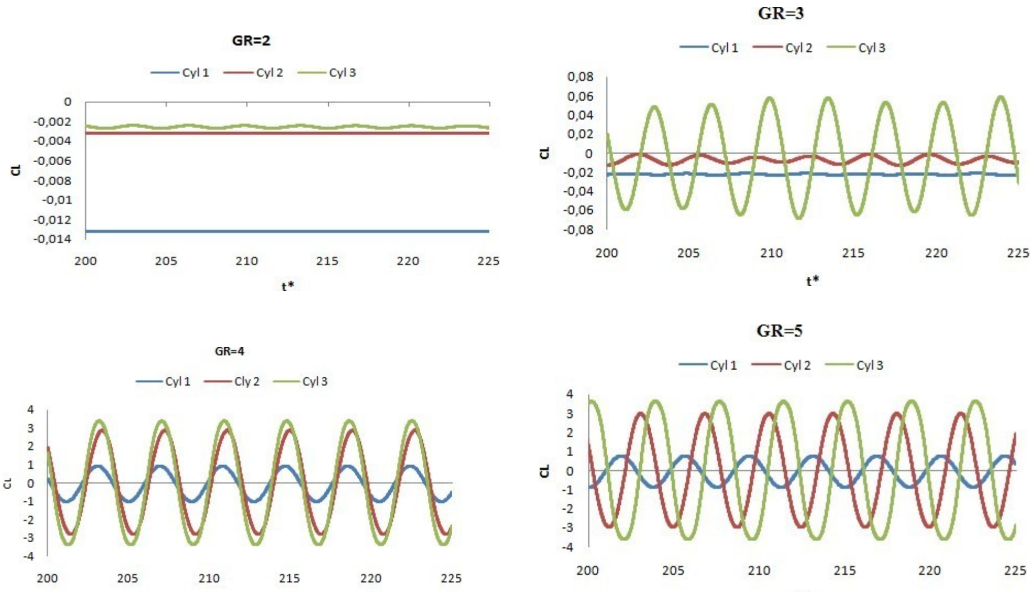

Fig.7 Time histories of lift for first, second and third cylinders at different gap ratios.

However, in the range of GR>3, it is observed that fluid forces of the third cylinder which is located in the wake of the first and second cylinder are very much larger than those of the windward cylinder because the vortex shedding behind two cylinders has a strong influence on the amplitudes of CD and CL. It is possible to clearly catch the phenomena that the flow patterns behind the windward cylinder and the fluid forces of three circular cylinders change suddenly at the spacing ratio of approximately GR=4 which is well known as the critical spacing ratio.

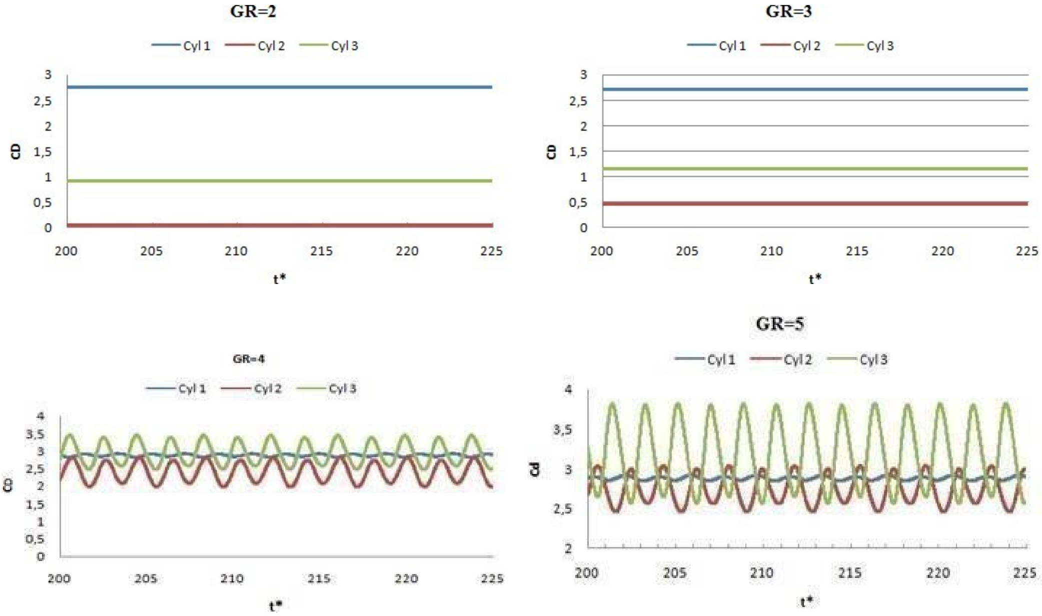

Fig.8 Time histories of Drag force acting on the cylinders for different gap ratios at Re=100.

C. *Local Nusselt number variations*

The local Nusselt number on the first, second and third cylinder surface is plotted as a function of circumferential direction ð for different gap ratios are shown in Figure.5. It can be deduced from this figure that the local Nusselt number is greatest at the front portions of the cylinders. Since heat transfer rate is closely related to flow structure, the minima of the local heat transfer rates appear in the front and back stagnation points of the second and third cylinder where the velocity magnitudes are relatively small for Gr=2 and 3. The local Nusselt number distribution of the second and third cylinder resembles to that of first cylinder typified for Gr=4 and 5. The maximum heat transfer from first cylinder occurring at θ=45 and 360 of the cylinder wall for all values of gap ratios. The maximum heat transfer fro second and third cylinder exhibits itself with a double hump occurring at θ=115 and 240 of the cylinder wall at GR=2 and 3 where the thermal and hydrodynamic boundary layers become the thinnest.

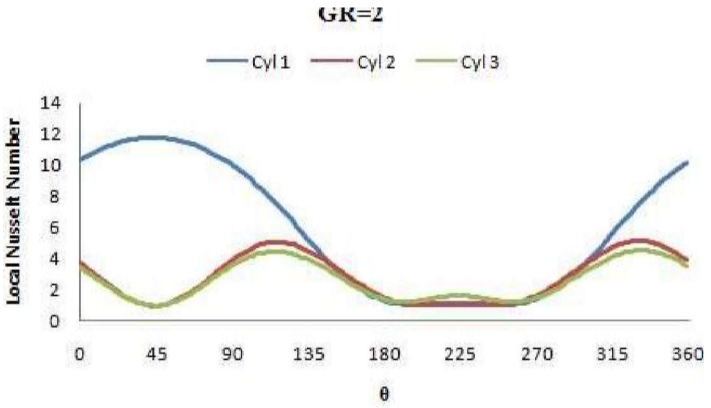

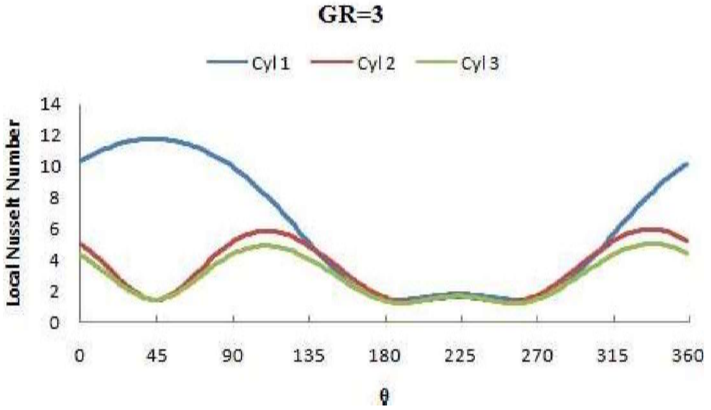

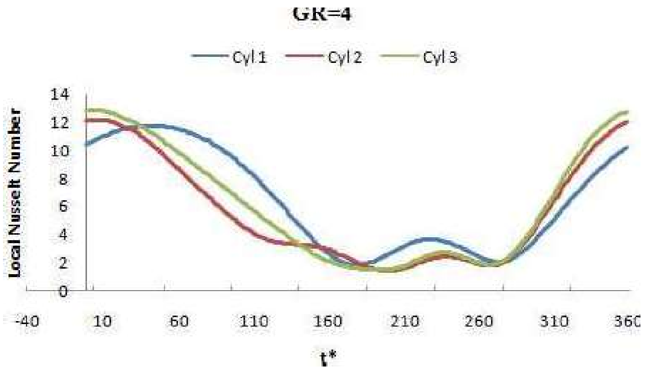

Copyright © 2023
ISSN: 1737-93347

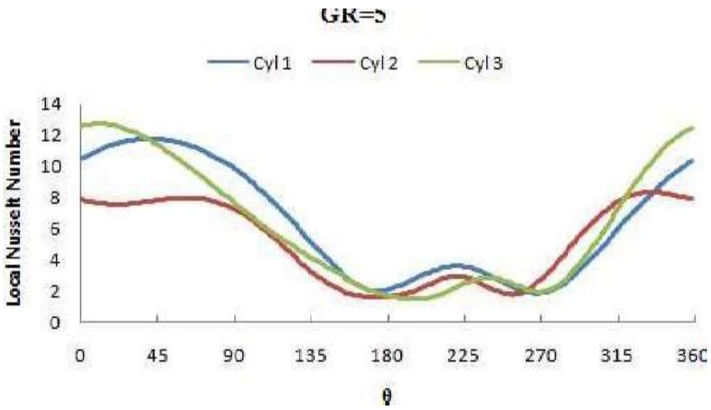

Fig 10. The local Nusselt number distribution on the first, second and third cylinder at $Re = 100$ and $t^* = 225$.

D. *Average Nusselt numbers*

Figure 11 shows the variation of the mean Nusselt number of the three whole cylinders with the spacing ratio at Re=100. It can be deduced from this figure that the level of Nusselt number for first cylinder is higher than the corresponding value for the second and third cylinder. The heat transfer from the second and third cylinder increases with increase in the gap ratio for 2 to 3 and it decreases for GR> 4. It can also be pointed out that the mean Nusselt number for the third cylinder is always less than its second counterpart for Gr<4. In general, the global transport of heat quantities have larger values for the fiest cylinder compared to the second and third cylinder, and at lower cylinder spacing the difference is more; however, at larger spacing this discrepancy is substantially reduced.

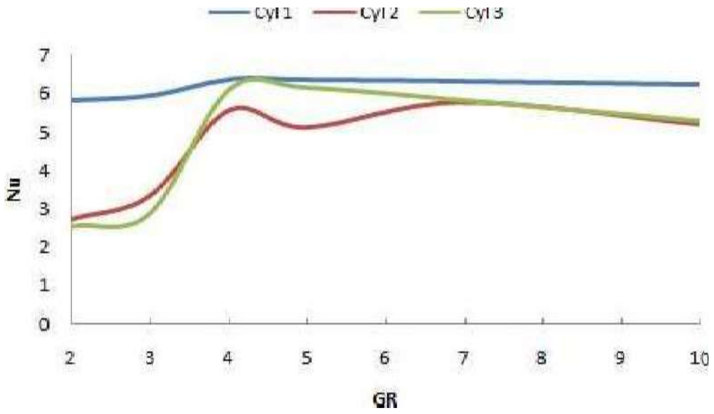

Fig.11 Mean Nusselt number of the first, second and third cylinder for different gap ratio.

VI. CONCLUSIONS

A two-dimensional numerical study is reported addressing the laminar flow and heat transfer around three circulars cylinders in tandem arrangements with variable boundary condition in semi confined media. Three identical heated circular cylinders of equal diameter D arranged in tandem whose surfaces are fixed temperature T_w and placed in confined duct, with exposed to a fully developed velocity profile with average velocity u_{max} and T_∞ at Reynolds number equal to 100. Tow adiabatic horizontal walls of finite length are placed at a distance of $H/2$ on either side of the center of the cylinders. The outlet of the duct is specified with Neumann condition. The gap ratio GR was selected as 2 to 5. One of the objectives is to understand the critical gap ratio at which the unsteady flow and thermal fields are transformed into a steady pattern. The results of simulation show that beyond the critical gap ratio (GRcr) there is a stabilization in the flow and thermal fields. The main findings are summarized below:

The gap between cylinders has crucial impact on flow patterns, when cylinders are very close to each other, the flow regime is steady in gap area and no vortex shedding occurs. After the critical gap (GR=4), a vortex shedding forms in the gap while double row vortex streets are observed behind the third cylinder as the gap increases.

The vorticity and isotherms were obtained to understand and interpret the flow and heat transport. For $GR \geq 4$, the vortices and isotherms are in unsteady behaviour irrespective of the gap spacing.

It is observed that fluid forces of the third cylinder which is located in the wake of the second cylinder are very much larger than those of the first cylinder.

The local Nusselt number is greatest at the front portions of the cylinders. The heat transfer from the second and third cylinder increases $GR < 4$ and it decreases for $GR \geq 4$. The heat transfer rate from the second and third cylinder is about 80% and 90% of that of the first cylinder respectively.

REFERENCES

[1] Igarashi, T. (1981). Characteristics of the flow around two circular cylinders arranged in tandem: 1st report. Bulletin of JSME 24(188),323–331.
[2] Igarashi, T. (1984). Characteristics of the flow around two circular cylinders arranged in tandem: 2nd report, unique phenomenon at small spacing. Bulletin of JSME 27(233), 23802387.
[3] Zdravkovich, M. (1987). The effects of interference between circular cylinders in cross flow. Journal of fluids and structures 1(2), 239-261.
[4] D. Sumner, “Two circular cylinders in cross-flow: a review,” Journal of Fluids and Structures, vol. 26, no. 6, pp. 849–899, 2010
[5] Jiang, R.J., Lin, J.Z.: Wall effects on flows past two tandem cylinders of different diameters. J. Hydrodyn. 24, 1–10 (2012)
[6] A. Sohankar and A. Etminan, “Forced-convection heat transfer from tandem square cylinders in cross flow at low Reynolds numbers,” International Journal for Numerical Methods in Fluids, vol. 60, no. 7, pp. 733–751, 2009.
[7] Lin, J., Jiang, R., Chen, Z., Ku, X.: Poiseuille flow-induced vibrations of two cylinders in tandem. J. Fluid Struct. 40, 70–85(2013)
[8] [8] J. L. Rosales, A. Ortega, and J. A. C. Humphrey, A Numerical Simulation of the Convective Heat Transfer in Confined Channel Flow Past Square Cylinders: Comparison of Inline and Offset Tandem Pairs, Numer. Heat Transfer A, vol. 38, pp. 443–465, 2000.
[9] J. L. Rosales, A. Ortega, and J. A. C. Humphrey, A Numerical Simulation of the Convective Heat Transfer in Confined Channel Flow Past Square Cylinders: Comparison of Inline and Offset Tandem Pairs, Int. J. Heat Mass Transfer, vol. 44, pp. 587–603, 2001.
[10] N. Mahir, Z. Altac, Numerical investigation of convective heat transfer in unsteady flow past two cylinders in tandem arrangements, Int. J. Heat Fluid Flow 29 (2008) 1309-1318.
[11] Ding, H., Shu, C., Yeo, Y.O., Xu, D., 2007. Numerical simulation of flows around two circular cylinders by mesh-free least square-based finite difference methods, Int. J. Numer. Meth. Fluids 53, 305–332.
[12] A. Dhiman and M. Hasan, “Flow and heat transfer over a trapezoidal cylinder: steady and unsteady regimes,” AsiaPacific Journal of Chemical Engineering, vol. 8, no. 3, pp. 433–446, 2013.
[13] Y. J. Chung and S.-H. Kang, “Laminar vortex shedding from a trapezoidal cylinder with different height ratios,” Physics of Fluids, vol. 12, no. 5, pp. 1251–1254, 2000.
[14] A. Harichandan, and A. Roy, "Numerical investigation of flow past a single and tandem cylindrical bodies in the vicinity of a plane wall", Journal of Fluids and Structures, vol. 33, pp. 19–43, 2012.doi: 10.1016/j.jfluidstructs.2012.04.006.
[15] R.J. Jiang, and J.Z. Lin, "Wall effects on flows past two tandem cylinders of different diameters", Journal of Hydrodynamics, vol. 24, pp. 1-10, 2012. doi: 10.1016/s1001-6058(11)60212-6.
[16] Ajay Raj Dwivedi and Amit Kumar Dhiman. Flow and heat transfer analysis around tandem cylinders: critical gap ratio and thermal cross-buoyancy. Journal of the Brazilian Society of Mechanical Sciences and Engineering (2019) 41:487
[17] Arif MENTEŞE , Seyfettin BAYRAKTAR. Numerical investigation of flow over tandem and side-by-side cylinders. Seatific 2021;1:1:15–25.
[18] Wei Zhang et al. Forced convection for flow across two tandem cylinders with rounded corners in a channel. International Journal of Heat and Mass Transfer 130 (2019) 1053–1069.
[19] Zdravkovich, M.M., 1977. Review of flow interference between two circular cylinders in various arrangements. Trans. ASME J. Fluids Eng. 99, 618–633.

ISSN: 1737-93347

USE of LICHENS for the QUALITATIVE and QUANTITATIVE ASSESSMENT of AIR QUALITY in the Annaba REGION

Amina CHAKER#1, Kheireddine FEKROUNE#2, Sameh BOUKHDIR#3, Labiba ZERARI#4, Khaoula Abdelli#5

1, 3, 4, 5 *Department of Biology, Faculty of Sciences, University of Badji Mokhtar of Annaba, Algeria*

1amina.fekrounechaker@yahoo.fr
3samehboukhdir@gmail.com
4hortansia23@gmail.com
5khawlabdelli66@gmail.com

2 *Department of Biology, Faculty of Nature and Life Sciences, University of Chadli BenDjeddid of El Tarf, Algeria*

2kfekroune@gmail.com

Abstract— ***It is possible to assess air quality using measuring apparatus, but physical collectors remain expensive equipment. Lichens were recognised as potential indicators of air pollution as early as the 1860s in Great Britain and the rest of Europe, so they were used for qualitative or quantitative assessment of the air quality of a given area. Hence, qualitative methods (the method of Van Haluwyn and Lerond (1986) [1], the illustrated scale of Dalby (1981)[2] and the scale adapted by Tiévant (2001)[3]) and a quantitative method (atmospheric purity index) of Leblanc and De Sloover (1970)[4] were used for the estimation of the air quality of the Annaba region, which allowed us to classify the stations studied according to the evaluation of the SO_2 rate ($\mu g/m^3$). From the most polluted stations (such as the city centre) to the least polluted stations (the reference station, the Edough mountain or Edough Peninsula). This montain abounds in fruticose species (Ramalina sp.) and foliose species, particularly those that are toxiphobic such as Lobaria pulmonaria. It is possible to monitor the evolution of the air quality of a region by following the evolution of its lichenic flora.***

Keywords— ***Lichens, qualitative methods, quantitative method, pollution, assessment, Annaba.***

I. INTRODUCTION

Lichens are made up of fungi and algae living in true symbiosis: one cannot live without the other [3]. This lichenic symbiosis is a permanent and harmonious association from the structural point of view, balanced and beneficial from the nutritional point of view for both partners: algae and fungi [5]. Because sulphur dioxide (SO_2) pollution is the easiest to detect and study, it is considered the main "tracer" of atmospheric and urban pollution [6]. Reference [7] lists certain characteristics of lichens that have led authors ([8] or [9]) to recognise lichens as good bioindicators of air quality, such as their particular sensitivity to certain pollutants or an easily observable way of reacting, etc. Thus, lichens make it possible to establish an extensive and inexpensive observation network in both space and time [7]. It is in this context that we proposed to use lichen species as biological indicators of air pollution in the Annaba region. To do so, we have different qualitative and quantitative methods.

II. THE STUDY AREA

The city of Annaba is located in the east of Algeria, between latitudes 36°30' North and 37°30' North, and longitudes 07°20' East and 08°40' East, with 12 communes with a total area of 1,411.98 km^2. It is delimited by the Mediterranean Sea to the North, the wilaya of Skikda to the West, Guelma to the south and El-Tarf to the east [10]. It is the industrial capital of eastern Algeria and has long been subjected to various types of pollutants that spare neither humans nor animals, let alone plants ([11], [12], [13], [14]).

Five stations were the subject of our study in the Annaba region (Fig. 1):

ISSN: 1737-933422

Station 1: Fertial (Algerian Fertiliser Company), which is located in the immediate vicinity of the Fertial Annaba complex (road of the salt flats W56). This phosphate and nitrogen fertiliser complex is the main source of fluorinated atmospheric emissions (latitude: 36.866058° longitude: 7.767669°)

Station 2: Boukhadra, EL-Bouni, which is located at the entrance of the city Boukhadra, EL-Bouni, and is exposed to the north-east wind coming fromFertial (latitude: 36.871220°, longitude: 7.74801°)

Station 3: (city centre)

Sub-station 1: The Edough Square (north) in the centre of Annaba (latitude: 36.909359°, longitude: 7.756934°),

Sub-station 2: The Christian Cemetery (latitude: 36.970322°, longitude: 7.756702°)

Station 4: Bouhdid Cemetery (latitude : 36.88934°, longitude : 7.712582°)

Station 5: Cork oak forests (northern slopes) of the Edough mountain (latitude: 36.551164°, 7.41555468°).

III. MATERIAL AND METHODS

Sampling was carried out on 6 trees, diversifying the tree species according to the trees available in the selected stations), in order to optimise the representativeness of lichen diversity [15]. The survey is carried out on the four sides of each tree using an observation grid consisting of five 10×10 cm meshes superimposed vertically. The grid is placed at least 1m high to avoid any disturbance of the ground (Fig. 2). To determine the frequency of each lichen species, their possible presence in the different grid cells of the observation grid is noted, i.e. a frequency ranging from 0 (species absent) to 5 (species present in all grid cells).

These frequencies are indicated for each side of the tree on a field sheet, which also mentions the geographical coordinates of the phorophytes

The Air quality of the Annaba region was assessed using qualitative and quantitative methods by means of lichen flora.

In the field, lichens are collected by hand or with the help of a knife to gently remove a piece of bark that supports the thallus (Van Haluwyn et al, 2013). The collected lichens will be individually wrapped in absorbent paper and placed in small plastic boxes on which we note the date, station, as well as phorophyte (Tiévant, 2001; Van Haluwyn et al., 2013; Asta et al., 2016).

The identification of lichens is carried out in the field and continued in the laboratory using a binocular magnifying glass and the usual thallin reactions.

The following references (guidebooks and websites) were used for the identification of lichens:

Guide des Lichens de France, Lichens des arbres [16], Guide des Lichens, 350 espèces de lichens d'Europe [3], Images of British Lichens [17], and specialised websites ([18], [19]).

The lichens identified follow the nomenclature of reference [20].

Qualitative methods:

The scale for estimating air quality in northern France according to the Method of Van Haluwyn et Lerond (1986) [1]

The Illustrated Scale of Dalby (1981) [2]

The scale adapted by Tiévant (2001) [3]

Quantitative methods:

The method of I.A.P. (Index of Atmospheric Purity) of Leblanc et De Sloover (1970) [4].

The method for calculating Lichenic Diversity per Station (LDS). It is a quantitative method that consists of calculating the lichen diversity in each station (DLS) and to do this it is first necessary to calculate the lichen diversity in each tree (DLA). To carry out these calculations, it is first necessary to

ISSN: 1737-933422

identify each species present in the grid and then count the number of cells in which the lichen species is present. A frequency score ranging from 0 to 5 is then obtained [21].

Lichen diversity per tree:
LDT = SFnorth + SFeast + SFsouth + SFwest where SF: sum of frequencies
Lichenic diversity per station:
LDS = (DLA1 + DLA2 + DLA3 + DLA4 + DLA5 + DLA6) / 6

Fig. 1 Study stations in the region of Annaba

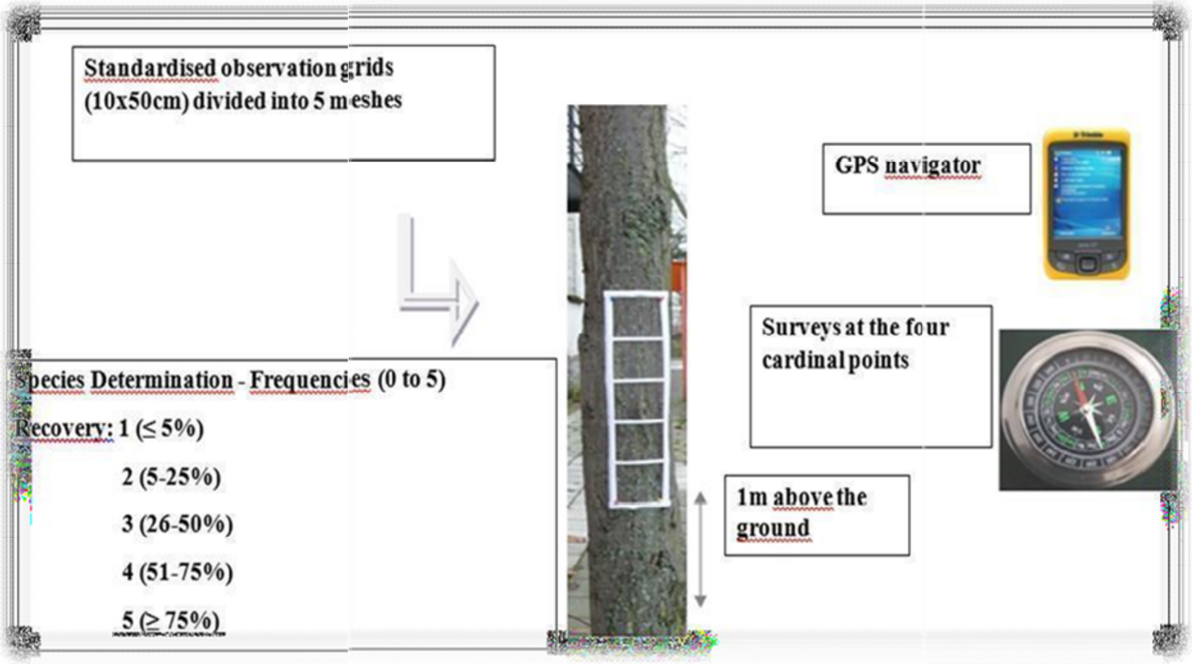

Fig. 2 Experimental protocol (according to [22])

IV. RESULTS AND DISCUSSION

The results relating to the lichenic flora of the stations studied in the Annaba region are expressed according to the physiognomy (type of thallus: foliose, crustose.. etc (Fig. 3)) and according to the systematic classification (orders, families and genera (Fig. 4)).

The first station is poor in lichens. We note the presence of the green alga Pleurococcus viridis and Nostoc ssp., the absence of fruticulous lichens and the codominance of the crustose lichen Lecanora conizaeoides and the foliose lichen, *Xanthoria parientina*, a nitrophilic lichen (roadside as is the case of station 1). These two lichenic species still belong to two different orders and families (Tab. 1).

TABLE 1
THE LICHENIC FLORA OF STATION 1

n°	Name of species	Order	Family	Type of thallus	Substratum
1	*Xanthoria parietina* (L.) Th. Fr.	Teloschistales	Teloschistaceae	Foliose	*Cupressus sempervirens*
2	*Lecanora conizaeoides* Nyl. ex Cromb.	Lecanorales	Lecanoraceae	Crustose	*Cupressus sempervirens*

Unlike green plants, lichens have no cuticle and therefore no stomata and therefore no means of regulating their exchanges with the atmosphere. Thus, in the event of atmospheric pollution, however slight, they absorb the pollutants, which may even cause them to disappear. This is why lichens can be used as bio-indicators of air quality [24].

In the second station, a low number of lichens (4 species) and the dominance of the foliaceous thallus type was observed: *Xanthoria parientina*, *Physconia grisea*, *Physcia adscendes* being all nitrophilic lichens, quite toxic-tolerant (very common in urban areas as the case of station 2). On the other hand, the fourth species *Parmeliopsis ambigua*, which is a nitrophobic lichen, was only encountered once (a single specimen on an olive tree very far from the roadside). The lichens recorded in station 2 (Boukhadra) are grouped into 2 orders only: Teloschistales (75%) and Lecanorales (25%), and two families: Teloschistaceae and Parmeliaceae (Tab. 2).

TABLE 2
THE LICHENIC FLORA OF STATION 2

n°	Name of species	Order	Family	Type of thallus	Substratum
1	*Physcia adscendens* (Fr.) H. Olivier	Caliciales	Physciaceae	Foliose	*Olea europea*
2	*Xanthoria parietina* (L.) Th. Fr.	Teloschistales	Teloschistaceae	Foliose	*Olea europea*
3	*Physconia grisea* (Lam.) Poelt	Caliciales	Physciaceae	Foliose	*Olea europea*
4	*Parmeliopsis ambigua* (Wulf.) Nyl.	Lecanorales	Parmeliaceae	Foliose	*Olea europea*

The Station 3 is split into two sub-stations (1 and 2) located side by side: Christian Cemetery and Edough Square (North). In this station, foliose lichens dominate (74%) followed by crustose lichens (21%) and finally leprose lichens (5%). The 12 species recorded in this station are quite diverse, divided into four orders: Teloschistales, Lecanorales, Candelariales and Peltigerales; and six families: Teloschistaceae, Physciaceae, Lecanoraceae, Candelariaceae, Cladoniaceae and Collemataceae.

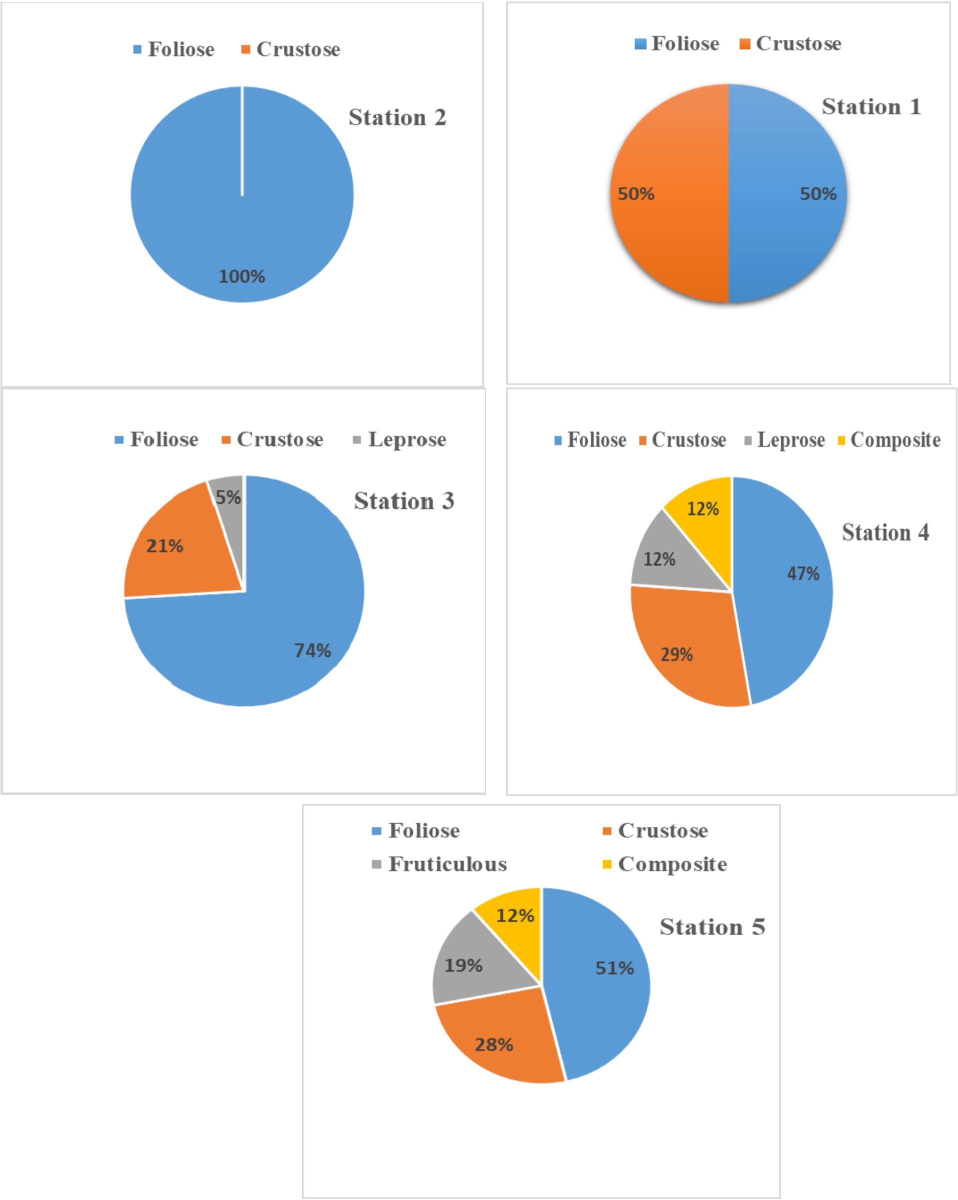

Fig. 3 Physiognomic spectra by thallus type of stations (station1, station 2, station 3, station 4)

TABLE 3

THE LICHENIC FLORA OF STATION 3 (SUB-STATIONS 1 AND 2)

n°	Name of species	Order	Family	Typeof thallus	Substratum	Sub-station
1	*Candelariella reflexa* (Nyl.) Lettau	Candelariales	Candelariaceae	Crustose	*Cercis siliquastrum*	2
2	*Cladonia chlorophaea* (Flörke ex Sommerf.) Spreng.	Lecanorales	Cladoniaceae	Composite	*Cupressus sempervirens* and *Cercis siliquastrum*	1 and 2
3	*Collema nigrescens* (Huds.) DC	Peltigerales	Collemataceae	Foliose	*Cercis siliquastrum*	2
4	*Lecanora argentata* (Ach.) Malm.	Lecanorales	Lecanoraceae	Crustose	*Cercis siliquastrum*	2

5	*Lecanora chlarotera* Nyl.	Lecanorales	Lecanoraceae	Crustose	*Cercis siliquastrum*	2
6	*Lecanora conizaeoides* Nyl. ex Cromb.	Lecanorales	Lecanoraceae	Crustose	Cercis siliquastrum	2
7	*Lepraria incana* (L.) Ach	Lecanorales	Lecanoraceae	Crustose	Cercis siliquastrum	2
8	*Physcia adscendens* (Fr.) H. Olivier	Teloschistales	Physciaceae	Foliose	Cercis siliquastrum	2
9	*Physcia biziana* (A. Massal.) Zahlbr.	Teloschistales	Physciaceae	Foliose	*Cercis siliquastrum* and *Cercis siliquastrum*	1 and 2
10	*Physconia grisea* (Lam.) Poelt	Teloschistales	Physciaceae	Foliose	*Cupressus sempervirens* and *Cercis siliquastrum*	1 and 2
11	*Scytinium lichenoides* (L.) Otálora, P. M. Jørg. et Wedin.	Peltigerales	Collemataceae	Foliose	*Cupressus sempervirens*	1
12	*Xanthoria parietina* (L.) Th. Fr.	Teloschistales	Teloschistaceae	Foliose	*Cercis siliquastrum*	2

In general, the types of thallus represented in the station number 4 are given by the following values: foliose thallus 47%, crustose thallus 29%, composite and leprose thallus each giving a value of 12%.

TABLE 4

THE LICHENIC FLORA OF STATION 4

n°	**Name of species**	**Order**	**Family**	**Typeof thallus**	**Substratum**
1	*Amandina punctata* (Ach.) Frydayet L. Arcadia	Caliciales	Caliciaceae	Crustose	*Fraxinus excelsior*
2	*Candelariella reflexa* (Nyl.) Lettau	Candelariales	Candelariaceae	Crustose	*Fraxinus excelsior*
3	*Collema furfuraceum* (Arnold) Du Rietz	Peltigerales	Collemataceae	Foliose	*Fraxinus excelsior*
4	*Collema subflaccidum* Degel.	Peltigerales	Collemataceae	Foliose	*Fraxinus excelsior*
5	*Collema subnigrescens* Degel. f.	Peltigerales	Collemataceae	Foliose	*Fraxinus excelsior*
6	*Collema nigrescens* (Huds.) DC	Peltigerales	Collemataceae	Foliose	*Fraxinus excelsior*
7	*Hypogymnia physodes* (L.) Nyl.	Lecanorales	Parmeliaceae	Foliose	*Fraxinus excelsior*
8	*Physcia adscendens* (Fr.) H. Olivier	Teloschistales	Physciaceae	Foliose	*Fraxinus excelsior*
9	*Physcia biziana* (A. Massal.) Zahlbr.	Teloschistales	Physciaceae	Foliose	*Fraxinus excelsior*
10	*Physcia leptalea* (Ach.) DC.	Caliciales	Physciaceae	Foliose	*Fraxinus excelsior*
11	*Physcia stellaris* (L.) Nyl.	Caliciales	Physciaceae	Foliose	*Fraxinus excelsior*
12	*Physconia grisea* (Lam.) Poelt	Caliciales	Physciaceae	Foliose	*Fraxinus excelsior*
13	*Physconia distorta* (With.) Laundon	Caliciales	Physciaceae	Foliose	*Fraxinus excelsior*
14	*Physconia venusta* (Ach.) Poelt	Caliciales	Physciaceae	Foliose	*Fraxinus excelsior*
15	*Lecanora chlarotera* Nyl.	Lecanorales	Lecanoraceae	Crustose	*Fraxinus excelsior*

16	*Lepraria incana* (L.) Ach	Lecanorales	Lecanoraceae	Crustose	*Fraxinus excelsior*
17	*Lecanora conizaeoides* Nyl. ex Cromb.	Lecanorales	Lecanoraceae	Crustose	*Fraxinus excelsior*
18	*Scytinium lichenoides* (L.) Otálora, P. M. Jørg. et Wedin.	Peltigerales	Collemataceae	Foliose	*Fraxinus excelsior*
19	*Xanthoria parietina* (L.) Th. Fr.	Teloschistales	Teloschistaceae	Foliose	*Fraxinus excelsior*

Regarding the last station (station 5), the corticolous populations of lichens of the foliose thallus type (*Flavoparmelia caperata*, *Parmotrema perlatum*, *Parmelia borreri*), and especially fruticulose ones (the abondant *Ramalina farinacea* or *Ramalina fastigiata*, *Evernia prunastri*, and *Teloschistes Chrisophtalmus*), seem to be the best indicators of good air quality in this station. We note the presence of *Usnea ceratina*, which seems to grow well on *Erica arborea* (better than on *Quercus suber* on which it was also found), since a few pendulous specimens of about ten centimetres long were found. For the crustose thallus we find mainly: *Lepra amara*, *Pertusaria pertusa* and also *Diploicia canescens*, *Gyalolechia flavorubescens*, in addition to the abundance of *Lecanora chlarotera*, *Bacidia rubella* is present on almost the entire surface of the bark of trees.

The lichenic specimens found in the Edough station are grouped into six orders: Teloschistales, Lecanorales, Peltigerales, Verrucariales, Pertusariales, Ortospales, comprising twelve families: Physciaceae, Lecanoraceae, Ramalinaceae, Collemataceae, Cladoniaceae, Teloschistaceae, Parmeliaceae, Lobariaceae, Verrucariaceae, Pertusariaceae, Pannariaceae, Phlyctidaceae and 26 genera.

TABLE 5

The lichenic flora of station 5. (*) and writing in bold are a new records (under press) for the study area (Edough Peninsula)

n°	**Name of species**	**Order**	**Family**	**Type of thallus**	**Substratum**
1	**Amandina punctata* Hoffm.	Caliciales	Caliciaceae	Crustose	*Quercus suber*
2	*Anaptychia cilliaris* (L.) Körb. ex A. Massal.	Caliciales	Physciaceae	Fruticulose	*Quercus suber*
3	*Bacidia rubella* (Hoffm.) A. Massal	Lecanorales	Ramalinaceae	Crustose	*Quercus suber*
4	**Blastenia ferruginea* (Huds.) A. Massal.	Teloschistales	Teloschistaceae	Crustose	*Quercus suber*
5	**Collema furfuraceum* (Arnold) Du Rietz	Peltigerales	Collemataceae	Foliose	*Quercus suber*
6	*Collema nigrescens* (Huds.) DC	Peltigerales	Collemataceae	Foliose	*Quercus suber*
7	**Cladonia chlorophaea* (Flörke ex Sommerf.) Spreng	Lecanorales	Cladoniaceae	Composite	*Quercus suber*
8	*Evernia prunastri* (L.) Ach	Lecanorales	Parmeliaceae	Fruticulose	*Quercus suber*
9	*Flavoparmelia caperata* (L.) Hale	Lecanorales	Parmeliaceae	Foliose	*Quercus suber*
10	**Fuscopannaria leucosticta* (Tuck. ex E. Michener) P.M. Jørg	Peltigerales	Pannariacea	Foliose	*Quercus suber*
11	**Gyalolechia flavorubescens* (Huds.) Søchting, Frödén & Arup	Teloschistales	Teloschistaceae	Crustose	*Quercus suber*
12	**Lecanora chlarotera* Nyl	Lecanorales	Lecanoraceae	Crustose	*Quercus suber*
13	**Lecidella elaeochroma* (Ach.) M. Choisy	Lecanorales	Lecanoraceae	Crustose	*Quercus suber*
14	**Lepra albescens* (Huds.) Hafellner	Pertusariales	Pertusariaceae	Crustose	*Quercus suber*
15	*Lepra amara* (Ach.) Hafellner	Pertusariales	Pertusariaceae	Crustose	*Quercus suber*
16	*Lobaria amplissima* (Scop.) Forssell.	Peltigerales	Lobariaceae	Foliose	*Quercus suber*
17	*Lobaria pulmonaria* (L.) Hoffm.	Peltigerales	Lobariaceae	Foliose	*Quercus suber*

18	*Nephroma laevigatum* (Ach.) Ach.	Peltigerales	Peltigeraceae	Foliose	*Quercus suber*
19	**Normandina pulchella* (Borrer.) Nyl.	Verrucariales	Verrucariaceae	Squamulose	*Quercus suber*
20	**Ochrolechia androgyna* (Hoffm.) Arnold	Pertusariales	Ochrolechiaceae	Crustose	*Quercus suber*
21	*Parmelia sulcata* Taylor	Lecanorales	Parmeliaceae	Foliose	*Quercus suber*
22	*Parmelina pastillifera* (Harm.) Hale	Lecanorales	Parmeliaceae	Foliose	*Quercus suber*
23	**Parmotrema perlatum* (Huds.) M. Choisy	Lecanorales	Parmeliaceae	Foliose	*Quercus suber*
24	*Parmotrema reticulatum (*Taylor) M. Choisy	Lecanorales	Parmeliaceae	Foliose	*Quercus suber*
25	**Pectenia plumbea* (Lightf.)	Peltigerales	Pannariacea	Foliose	*Quercus suber*
26	**Pertusaria coccodes* (Ach.) Nyl	Pertusariales	Pertusariaceae	Crustose	*Quercus suber*
27	*Pertusaria pertusa* (Weigel) Tuck.	Pertusariales	Pertusariaceae	Crustose	*Quercus suber*
28	*Phaeophyscia orbicularis* (Neck.) Moberg	Caliciales	Physciaceae	Foliose	*Quercus suber*
29	*Physcia aipolia* (Ehrh. ex Humb.) Fürnr .	Caliciales	Physciaceae	Foliose	*Quercus suber*
30	*Physcia leptalea* (Ach.) DC.	Caliciales	Physciaceae	Foliose	*Quercus suber*
31	*Physconia distorta* (With.) Laundon	Caliciales	Physciaceae	Foliose	*Quercus suber*
32	*Physconia perisidiosa* (Erichsen) Moberg	Caliciales	Physciaceae	Foliose	*Quercus suber*
33	*Physconia venusta* (Ach.) Poelt.	Caliciales	Physciaceae	Foliose	*Quercus suber*
34	*Pleurostitca acetabulum* (Neck.) Elix & Lumbsch	Lecanorales	Parmeliaceae	Foliose	*Quercus suber*
35	*Punctelia subrudecta* (Nyl.) Krog	Lecanorales	Parmeliaceae	Foliose	*Quercus suber*
36	*Ramalina canariens* J. Steiner	Lecanorales	Ramalinaceae	Fruticulose	*Quercus suber*
37	*Ramalina farinacea* (L.) Ach	Lecanorales	Ramalinaceae	Fruticulose	*Quercus suber*
38	*Ramalinafastigiata* (Pers.) Ach	Lecanorales	Ramalinaceae	Fruticulose	*Quercus suber*
39	**Ramalinafraxinea* (L.) Ach.	Lecanorales	Ramalinaceae	Fruticulose	*Quercus suber*
40	**Ramalina pollinaria* (Westr.) Ach.	Lecanorales	Ramalinaceae	Fruticulose	*Quercus suber*
41	**Scytiniumlichenoides* (L.) Otálora	Peltigerales	Collemataceae	Foliose	*Quercus suber*
42	**Teloschistes chrysophthalmos* (L.) Th.Fr	Teloschistales	Teloschistaceae	Fruticulose	*Quercus suber*
43	**Usnea ceratina* Ach.	Lecanorales	Parmeliaceae	Fruticulose	*Quercus suber*
44	*Xanthoria parietina* (L.) Th.Fr.	Teloschistales	Teloschistaceae	Foliose	*Quercus suber*

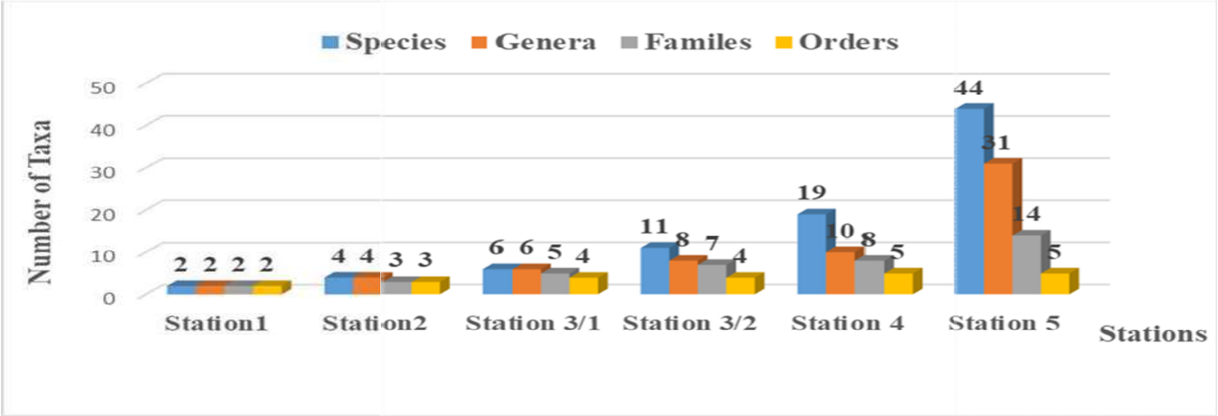

Fig. 4 Systematic spectra of the five surveyed stations

Air quality assessment using qualitative and quantitative methods

❖ Qualitative methods

- ***The scale for estimating air quality in northern France according to the Method of Van Haluwyn et Lerond (1986)*****[1]**

SO_2 is considered the main "tracer" of industrial and urban air pollution. Therefore, SO_2 pollution is the easiest to track and study.

The air quality assessment of our study area (station 1: Fertial (Algerian Fertiliser Company), station 2: Boukhadra (a municipality next to Fertial); station 3: Christian Cemetery (City centre of Annaba)and Square de l'Edough Nord (In front of the Christian Cemetery), station 4: Bouhdid Cemetery (at the foothills of the Edough mountain), station 5: which is the reference station, Edough Montain or Edough Peninsula) according to the method of Van Halwyun and Lerond [1] is given in Table 6. A variation in air quality was observed between the five stations studied:

Station 1 (Fertial) was considered to be a very heavily polluted station, which places it in class "B".

The 2nd station (Boukhadra) has been classified in zone "E" because its air pollution is estimated to be medium.

Station 3, subdivided into two juxtaposed substations (Christian Cemetery, Square de l'Edough "North"), is estimated as a station with moderately low pollution, placing it between two classes "E-F". The same observation was made for the Bouhdid station (station 4) even though the number of lichens recorded in the latter is higher (19 taxa) than that of station 3.

The reference station (Edough Peninsula) has low to very low pollution; placing this station between classes F and G.

TABLE 6

ESTIMATION OF THE AIR QUALITY OF THE STATIONS ACCORDING TO THE METHOD OF VAN HALUWYN AND LEROND [1]

Class	**SO_2 Pollution**	**Station**	**Lichen species present according to the air quality assessment scale of Van Haluwyn and Lerond [1]**
B	Veryheavy pollution	1	*Pleurococccus virdis* ;*Leanora conzaeiodes*; *Xanthori parietina*
E	Moderate pollution	2	*Physcia adscendens*; *Xanthoria parietina*
E-F	Moderately low pollution	3	*Physconia grisea*, *Lepraria incana* *Physconia grisea*, *Lepraria incana*, *Xanthoria parietina*, *Lecanora conizaeoides*, *Physcia adscendens*
E-F	Moderately low pollution	4	*Physcia adscendens*; *Xanthoria parietina*; *Physconia grisea*; *Lepraria incana*

F-G	Low to verylow pollution	5	*Anaptychia cilliaris*, *Parmotrema perlatum*; *Ramalina farinacea*, *Ramalina fraxinea*, *Physcia aipolia*, *Flavoparmelia caperata*, *Ramalina fastigiata*

- **Dalby's Illustrated Scale [2]**

The results of the estimation of air quality in our five study stations, according to the scale of Dalby [2]are recorded in Table 7.

According to the lichen species identified in station 1 (Fertial), the rate of atmospheric pollution is estimated between 150 and 70 µg/m^3 of SO$_2$.

In the station 2 (Boukhadra), the rate of atmospheric pollution is estimated between 70 and 60 µg/m^3 de SO$_2$.

According to the resenced lichen specimens in the station 3, the rate of atmospheric pollution varied between 50 and 150 µg/m^3 de SO$_2$

In the fourth station (Bouhdid), the SO$_2$ level is estimated at more than 50 µg/m^3.

Thanks to the presence of lichen species sensitive to pollution according to the air quality estimation scale of Van haluwyn and Lerond (1986), such as: *Usnea ssp.*, *Lobaria ssp.* or *Pectenia plumbea* (previously known as), the estimated SO$_2$ level at reference station 5 (Edough Penninsula) is [30-35] to 5 µg/m^3.

TABLE 7

ESTIMATION OF STATION AIR QUALITY ACCORDING TO THE ILLUSTRATED SCALE OF DALBY [2]

SO$_2$ µg/m^3	**Station**	**Lichen species present according to Dalby's Air Quality Assessment Scale [2]**
150-70	1	*Pleurococccus virdis ; Leanora conzaeiodes; Xanthoria parietina*
70-60	2	*Physcia adscendens; Xanthoria parietina, Parmeliopsis ambigua,*
150- ≥50	3	*Physconia grisea, Physcia biziana*
		Physconia grisea, Xanthoria parietina, Lecanora chlarotera; Physcia adscendes
≥50	4	*Xanthoria parietina, Lecanora chlarotera; Physcia adscendes, Lepraria incana*
35-30 to 5	5	*Parmotrema perlatum, Lobaria pulmonaria, Ramalina fraxinea, Ramalina calicaris,Ramalina fastigiata ,Physcia aipolia, Degelia plumbea*

- **The scale adapted by Tiévant (2001) [3]**

According to the air quality assessment scale adapted by Tiévant [3], which classifies areas (ranging from 1 to 10) according to the estimated SO$_2$ level based on the presence of specific lichen species, we estimate the air quality of our 5 study stations as follows (Table 8):

- ✓ The 1st station (Fertial) corresponds to the 4th zone of the adapted Tiévant scale [3] with an estimated SO$_2$ value of about 70 µg/m^3.
- ✓ Depending on the lichen species$_3$ growing in s$_3$tation 2 (Boukhadra), the SO$_2$ level is estimated to be between 50 µg/m and 60 µg/m , which corresponds to zones 5 and 6 respectively, of the adapted scale of Tiévant [3]. The same estimate is noted for station 4 (Bouhdid Cemetery).
- ✓ Concerning station 3 (Christian Cemetery and Square de l'Edough Nord) and according to the lichenic species recorded, it corresponds to zone 4 with an estimate of SO$_2$ of approximately 70µg/m^3.
- ✓ The reference station 5 (Edough Peninsula) is classified in the 9th zone (on a scale of 10 zones) with a SO$_2$ value of about 30µg/m^3 according to the lichen species recorded.

Table 8

The scale adapted by Tiévant (2001) [3]

zone	SO_2 µg/m^3	station	**Lichen species present according to the scale adopted for estimating air quality by Tiévant [3]**
4	70 approximately	1	*Pleurococccus virdis ; Leanora conzaeiodes; Xanthoria parietina*
5 and 6	(50-60)	2	*Physcia adscendens; Xanthoria parietina, Parmeliopsis ambigua, Physconia grisea*
4	70 approximately	3	*Physconia grisea, Physcia biziana, Lepraria incana*
			Lepraria incana, Xanthoria parietina, Lecanorachlarotera; Physcia adscendes
5 and 6	(50-60)	4	*Xanthoria parietina, Lepraria incana,Lecanora chlarotera, Physconia grisea,Physcia adscendens*
9	30 approximately	5	*Pertusaria albescens, Lobaria pulmonaria, Ramalina fraxinea, Ramalina calicaris,Ramalina fastigiata, Physcia aipolia, Anaptychia ciliaris; Physcia leptalea*

In general, the comparison of the three qualitative methods (Van Haluwyn and Lerond's method [1], Dalby's illustrated scale [2] and Tiévant's adapted method [3]) shows that:

- Station 1 (Fertial): is classified as a very heavily polluted area up to a SO_2 value of 150µg/m^3.
- Station 2 (Boukhadra): is considered as a medium pollution zone around SO_2 of 60µg/m^3.
- Station 3 (Christian Cemetery and Square de l'Edough Nord) as well as station 4 (Bouhdid Cemetery): is considered as a "medium" low pollution area around an SO_2 value of 70-50µg/m^3.
- Station 5 (Edough Park): this station is classified as a low to very low pollution zone with the presence of *Anaptychia cilliaris*, *Permotrema perlatum*, *Physcia aipolia*, *Ramalina fraxinae*, *Lobaria pulmonaria*, *Ramalina calicaris*, which according to Dalby's scale [2] grows in zones below 5µg/m^3 as well as the presence of *Usnea ceratina* and *Pectenia plumbea*, which testify to the good air quality of the Edough mountain.

❖ Quantitative methods

In order to estimate the air quality in the studied stations, two quantitative methods were used: the first one is based on the calculation of the *index of atmospheric purity* (I.A.P.) of each station which aims to evaluate the air quality according to a scale, the second method consists in calculating the index of Lichenic Diversity per Station (LDS).

- ***The method of I.A.P. (index of atmospheric purity) of Leblanc et De Sloover*** **[4]**

The results of the atmospheric purity index (A.P.I.) obtained respectively for each station and which are recorded in table 9 (Tab. 9), show in a global way, the air quality of each of them (Fig. 5).

According to the scale established by reference [25] or [26], it appears that :

- Station 1 (Fertial) and station 2 (Boukhadra) have a low I.A.P. which translates into a very high atmospheric pollution (7.4 and 8.6 between [0-15]), hence a limited presence of the number of lichen species.
- On the other hand, station 3 (sub-station 1: Square de l'Edough Nord, sub-station 2: Christian Cemetery) is subject to a moderately polluted atmosphere due to their moderately

ISSN: 1737-933432

high I.A.P. values (27.7 and 34.7, i.e. an average of : 31.2, thus an I.A.P. between [30-45] classifying this station in a mediumair pollution area (Tab.20).

- As for station 4, its I.A.P. value is quite high at 85.9 (≥ 60 according to the scale) which shows that the pollution is very low translating the good air quality of this station.
- Similarly for station 5 (Edough National Park) whose I.A.P. is ≥ 100, which translates into an important number of lichenic specimens compared to the other stations studied but also by the presence of lichens typically indicative of good air quality.

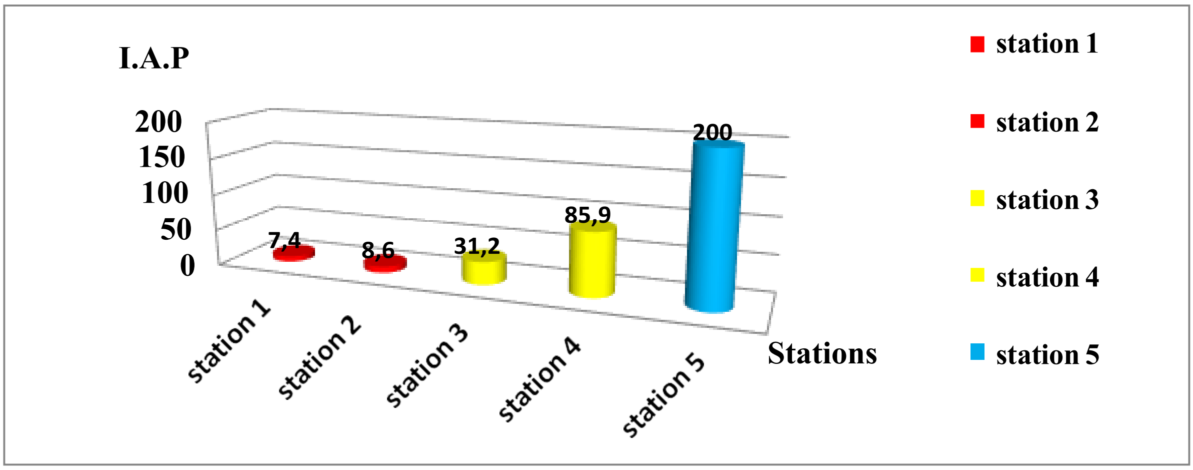

Fig. 5 Results of the air quality assessment using the quantitative method (Index of Air Purity I.A.P.)

TABLE 9

SCALE OF CORRESPONDENCE BETWEEN THE I.A.P. AND AIR POLLUTION

Atmospheric pollution	I.A.P. (Index of the air purity)	Station
Extremelyhigh	0-15	S1 and S2
Medium	30-45	S3
Verylow	≥ 60	S3 and S4

- ***The method for calculating lichen diversity per station (LDS)***

The indices of lichenic diversity per station, are recorded in the figure 6 and compared between them. Although the number of species seems to differ from one station to another, the index of lichenic diversity of certain stations (S1: Fertial, S2: Boukhadra) is identical, but remains much lower than that of the reference station, in this case the Edough station (S5): more than 13 times lower. This leads us to say that the stations of Fertial and Boukhadra (S1 and S2) are the most polluted and the poorest in terms of lichen diversity, followed by station S3 and S4 which are respectively 6 and 3 times less diverse in lichens than station 5 (Edough).

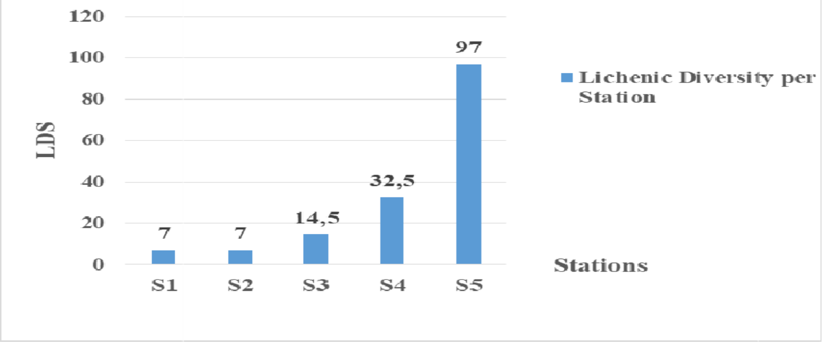

Fig. 6 Results of the air quality assessment using the quantitative method The index of Lichenic Diversity per Station (LDS)

As reported by the reference [27], the better the air quality of the environment, the more species will be able to thrive and the higher the lichenic diversity per station; and conversely, the more limiting the environmental conditions, the fewer species will be able to survive and the lower the lichenic diversity.

V. CONCLUSION

It appears from the use of lichens as an indicator of abiotic stress, in this case air pollution, in the stations studied (station1 Fertial; station2 Boukhadra, station3 Edough North Square and Christian Cemetery, station4 Bouhdid Cemetery and station5 Edough Peninsula):

Significant reduction in the number of species in station 1 (Fertial) which is considered to be polluted (source of fluorinated and plumbed air pollution) and where the SO_2 level is estimated at 150 $\mu g/m^3$.

Stations 2 and 3 are intermediate (average pollution) between stations 1 and 4, as they are more exposed to north-east winds, especially as station 3 is only separated from Fertial (Algerian Fertiliser Company) by the Mediterranean Sea

The Bouhdid cemetery station is considered to be a moderately polluted place located between the reference station (Edough) and the most polluted station, namely station 1 (Fertial)

The abundance of fruticulous and foliaceous lichens in station 5 (Edough) gives an idea about the good air quality of the station and especially the presence of some specimens:

Usnea ceratina, *Teloschistes chrysophtalmus*, *Lobaria pulmonaria Pectenia plumbea* (a new species in the study area) and *Fuscopannania leucosticta* (a species rediscovered in Algeria), which are particularly sensitive to pollution.

REFERENCES

[1] C. Van Haluwyn et M. Lerond, “Les lichens et la qualité de l’air. Evaluation méthodologique et lmites”. Rapport final au Ministère de l’Environnement (SRETIE), 1986.

[2] C. Dalby, “LICHENS AND AIR POLLUTION”, British Museum (Natural History), BP Educational Service, London, England, 1981.

[3] P. Tiévant, “Guide des Lichens, 350 espèces de lichens d’Europe”. Paris, France, Edition Delachaux et Niestlé, 2001.

[4] F. LeBlanc and J. De Sloover, “Relation between industrialization and the distribution and growth of epiphytic lichens and mosses in Montreal”. Canadian Journal of Botany, vol.48, pp. 1485–1496, 1970.

[5] G. Gooet et J. Ferguson, “Nature et science”, Paris, France: Edition. Casteilla, 1987.

[6] J.P. Gavériaux, “Les lichens et la bio-indication de la qualité de l’air Guide technique à l’usage des professeurs des Collèges et des Lycées”. *Bull. Soc. Bot. N. Fr.*, vol. 49, pp. 1–52, 1996.

[7] A-M. Fiore-Donno, “Les lichens épiphytes comme bioindicateurs de la pollution atmosphérique dans la région genevoise = Epiphytic lichens as bioindicators of atmospheric pollution in Geneva (Switzerland)”. Saussurea, vol 28, pp.189–218, 1997.

[8] T.H.Nash III and C. Gries, “The response of lichens to atmospheric deposition with an emphasis on the Arctic”. Science of The Total Environment, vol. 160–161, pp 737–747, 1995.

[9] C. Van Haluwyn et M. Lerond, “Guide des lichens”, France, Edition Lechevalier, 1993.

[10] N. Maizi, A. Alouia et A. Tahar, “Jumelage des bio-indicateurs et d’un réseau de surveillance de la qualité de l’air pour la détection de la pollution par le SO2 dans la région de Annaba (Algérie)”, Biotechnol. Agron.

Soc. Environ., vol. 16, pp.149–158, 2012.

[11] A. Semadi, “Effet de la pollution atmosphérique (pollution globale, fluorée et plombique) sur la végétation dans la région de Annaba”. Thèse de Doctorat d’état en sciences naturelles. Université Pierre et Marie Curie, Paris VI, France, 1989.

[12] A. Alioua “Détection de la pollution mercurielle dans la région de Azzaba à l'aide de bio-accumulateurs (*Xanthoria parietina*, *Olea europea*, *Cupressus sempervirens*, *Casuarina equisetifolia* et *Triticum durum*) ”. Thèse de Magister, Université d’Annaba, Algérie, 1995.

[13] A. Alioua “Détection de la pollution plombique d'origine automobile à l'aide de bio-accumulateurs végétaux dans l'agglomération de Skikda (N. E. Algérie) ”, Thèse de Doctorat, Université Joseph Fourier, Grenoble, France, 2001.

[14] A. Alioua, N. Maizi, A. Semadi, A. Tahar et M. Kahoul “Détection et Etude de la Pollution Mercurielle à l’Aide des Bioindicateurs Dans la Région de Azzaba (Algérie Orientale)”, *European Journal of Scientific Reasearch*,vol. 23, pp.187–196, Nov. 2008.

[15] H. Poličnik, P. Simoncic and F. Batic, “Monitoring air quality with lichens : a comparison between mapping in forest and in open areas”, Environmental pollution, vol. 151, pp. 395– 400, 2008.

[16] C. Van Haluwyn, J. Asta, J.P. Gavériaux, “Guide des Lichens de France, Lichens des arbres”. Paris, France Edition Belin, 2013.

[17] A.J. Silverside (2013) “Images of British Lichens”. [Online]. Available: lastdragon.org

[18] (2023) The AFL website. [Online]. Available: http:// www.afl-lichenologie.fr

[19] (2023) The irishlichens website. [Online]. Available: http:// www.irishlichens.ie

[20] C. Roux et coll., “Catalogue des lichens et champignons lichénicoles de France métropolitaine”. 2e édition revue et augmentée. Association française de lichénologie (A.F.L.). Fontainebleau, France, 2017.

[21] C. Boucheron et N. Martin, “Estimation de la qualité de l’air par l’étude des lichens épiphytes bio-indicateurs sur le Pays du Bocage Vendéen”. CPIE Sèvre et Bocage, 2019.

[22] (2023) The SIGLES website. [Online]. Available: http://www.sigles-sante-environnement.fr/?page_id=14303

[23] A. Chaker, K. Fekroune, A. Hassaine, A. slimani, L. Zerari and R. Moulaï, “New data on lichen flora of the Edough Peninsula in north-eastern Algeria”, Botanica, vol. 29, pp. 9–20, 2023.

[24] J.C. Masson. (2014) Les lichens, bio-indicateurs de la qualité de l'air. IFE, [Online]. Available: http://www.attiredailes.be/pdf/botanique/bota_lichens_bio-indicateurs.pdf

[25] R.H. Herzig, J.D. Hines, G.P. Herzig, S.N. Wolff, P.A. Cassileth, H.M. Lazarus, D.J. Adelstein, R.A. Brown, P.F. Coccia and S. Strandjord, “Cerebellar toxicity with high-dose cytosine arabinoside”. J Clin Oncol. Vol. 5, pp.927–32, 1987.

[26] R. Kricke and S. Loppi, “Bioindication: the I.A.P. approach”. In: P.L. Nimis, C. Scheidegger, P.A. Wolseley, Ed. “Monitoring with lichens”. Monitoring lichens, Kluwer Academic Publishers, NATO Science Series, pp. 21–37, 2002.

[27] C. Boucheron et N. Martin, Estimation de la qualité de l’air par l’étude des lichens épiphytes bio-indicateurs sur le Pays du Bocage Vendéen. France: CPIE Sèvre et Bocage, 2019.

Conférence Internationale sur les Sciences Appliquées et l'Innovation (CISAI-2023)
Proceedings of Engineering & Technology-PET-Vol 77

Characterisation of a Carreau-Yassuda Fluid Flow Within a Circular Pipe

Labsi Nabila[1], Melki Rafik[2], Benkahla Youb Khaled[3]

Equipe Rhéologie et Simulation Numérique des Ecoulements, Laboratoire des Phénomènes de Transfert,
Faculté de Génie Mécanique et de Génie des Procédés,
Université des Sciences et de la Technologie Houari Boumediene
BP. 32 El Allia, Bab Ezzouar, Alger, Algérie
[1]nabilalabsi@yahoo.fr ; nlabsi@usthb.dz
[2]melki.rafik@hotmail.com
[3]youbenkahla@yahoo.fr

***Abstract*— The study considers the laminar steady axisymmetric flow of an incompressible Carreau fluid in a circular pipe, maintained at a constant and uniform wall temperature. The dimensionless governing equations, i.e. continuity, momentum and energy equations, are discretized using the Finite Volume Method and resolved by means of a homemade computer code. The study focuses on the effect, on heat transfer, of both viscous dissipation and temperature-dependency of the fluid's viscosity. The results show that neglecting viscous dissipation for both isoviscous and thermodependent fluid leads to underestimate heat transfer.**

***Keywords*— Carreau fluid, thermodependent viscosity, viscous dissipation, finite volume method, circular pipe.**

I. INTRODUCTION

Some fluids such as polymers are well described by the rheological model of Carreau-Yasuda. Thus, many studies have been undertaken considering the flow of this non Newtonian fluid within various geometries.

Khellaf and Lauriat [1] studied the forced, mixed and natural convection of a Carreau fluid within a short annulus with a heated and rotating inner cylinder and a cooled and fixed outer cylinder. Their results show that the shear thinning effect decreases the friction factor at the rotating cylinder and increases the heat transfer through the annular.

Abbasi et *al.* [2] undertook a numerical study on the effect of applied magnetic field on the peristaltic transport of a Carreau-Yasuda fluid in a curved duct. They found that the fluid velocity is not symmetric about the centreline for small values of curvature parameter and that the increase of the Hall parameter value balances the magnetic effect of applied magnetic field.

Rousset et *al.* [3] analyzed the temporal stability of a Carreau fluid flow along a tilted plate plane. They highlighted the effect of shear-thinning fluid's properties on the definition of the stability kind. They found also that the critical Reynolds number for this fluid is smaller than the one corresponding to Newtonian fluids.

Lounis et *al.* [4] studied numerically, the thermosolutal convection of a Carreau-Yasuda fluid within an inclined square cavity by considering Soret and Dufour effects. The active walls are subject to constant and uniform concentrations and temperatures whereas the other walls are impermeable and adiabatic. The results show that the increase of the time constant parameter as well as the decrease of the ratio of infinite-to zero-shear-rate viscosities enhance thermal and mass exchange for various values of the flow index. In addition, the rise of the orientation angel from 0° to 90° increases heat and mass transfer rates.

Bilal et *al.* [5] analyzed the magnetic dipole and heat transmission through ternary hybrid $Al_2O_3/SiO_2/TiO_2$-Carreau-Yasuda nanofluid flow across a vertical stretching sheet. The heat transfer and velocity were analysed by considering the effect of heat source/sink and Darcy Forchhemier. Among the results, they found that the increase of the flow index increases the skin friction and the Nusselt number. Also, the rising effect of Darcy Forchheimer's term and porosity constant decreases the velocity outlines and finally, the ternary hybrid nanofluid have a greater tendency to increase the energy transmission across a vertical plate in comparison to the base fluid.

It can be seen that there is few studies regarding the Carreau-Yasuda or Carreau fluid flow within a pipe and moreover, by considering the effect of viscous dissipation. For this purpose, the present numerical study deals with the analysis of thermal exchange through the flow of a temperature-dependent Carreau fluid within a pipe, by considering viscous dissipation.

II. MATHEMATICAL FORMULATION AND NUMERICAL MODELLING

Let's consider the laminar steady axisymmetric flow of an incompressible Carreau fluid in a pipe of a circular cross section. The pipe is of length L and radius r_w and is maintained at a constant and uniform wall temperature T_w. The fluid is assumed to be of constant physical and rheological properties except for the apparent viscosity which is considered thermodependent. Viscous dissipation will be considered, by taking both cases of wall heating and wall cooling.

A. Mathematical Formulation

The dimensionless governing equations, i.e. continuity, momentum and energy equations are, respectively, given in cylindrical coordinates by:

$$\frac{1}{R}\frac{\partial (RV)}{\partial R}+\frac{\partial U}{\partial X}=0 \quad (1)$$

$$\frac{1}{R}\frac{\partial (RVV)}{\partial R}+\frac{\partial (UV)}{\partial X}=-\frac{\partial P^*}{\partial R}+\frac{1}{\mathrm{Re}}\left[\frac{1}{R}\frac{\partial}{\partial R}\left(\eta_{app}R\frac{\partial V}{\partial R}\right)+\frac{\partial}{\partial X}\left(\eta_{app}\frac{\partial V}{\partial X}\right)\right]$$
$$+\frac{1}{\mathrm{Re}}\left[\frac{\partial V}{\partial R}\left(\frac{\partial \eta_{app}}{\partial R}\right)+\frac{\partial U}{\partial R}\left(\frac{\partial \eta_{app}}{\partial X}\right)\right]-\frac{2\eta_{app}V}{\mathrm{Re}\,R^2} \quad (2)$$

$$\frac{1}{R}\frac{\partial (RVU)}{\partial R}+\frac{\partial (UU)}{\partial X}=-\frac{\partial P^*}{\partial X}+\frac{1}{\mathrm{Re}}\left[\frac{1}{R}\frac{\partial}{\partial R}\left(R\,\eta_{app}\frac{\partial U}{\partial R}\right)+\frac{\partial}{\partial X}\left(\eta_{app}\frac{\partial U}{\partial X}\right)\right]$$
$$+\frac{1}{\mathrm{Re}}\left[\left(\frac{\partial \eta_{app}}{\partial R}\right)\frac{\partial V}{\partial X}+\left(\frac{\partial \eta_{app}}{\partial X}\right)\frac{\partial U}{\partial X}\right] \quad (3)$$

$$\frac{1}{R}\frac{\partial (RV\theta)}{\partial R}+\frac{\partial (U\theta)}{\partial X}=\frac{1}{\mathrm{Pr}\,\mathrm{Re}}\left[\frac{1}{R}\frac{\partial}{\partial R}\left(R\frac{\partial \theta}{\partial R}\right)+\frac{\partial^2\theta}{\partial X^2}\right]+\frac{\mathrm{Br}}{\mathrm{Pr}\,\mathrm{Re}}\eta_{app}\dot{\gamma}^{*2} \quad (4)$$

Where the dimensionless second invariant in Equation (4) is given by:

$$\dot{\gamma}^{*2}=2\left[\left(\frac{\partial V}{\partial R}\right)^2+\left(\frac{\partial U}{\partial X}\right)^2+\left(\frac{V}{R}\right)^2\right]+\left(\frac{\partial U}{\partial R}+\frac{\partial V}{\partial X}\right)^2 \quad (5)$$

The apparent viscosity of Carreau fluid is given, in its dimensionless form by the following law, proposed by Bird at al. [6]:

$$\eta_{app}=\left(1+\mathrm{We}^2\dot{\gamma}^{*2}\right)^{\frac{n-1}{2}} \quad (6)$$

Where We represents the Weissenberg number and n is the flow index.

To complete the system of governing equations, we consider as steady boundary conditions, a uniform axial velocity and temperature at the inlet ($U=\theta=1$, $V=0$), no-slip conditions are applied at the wall along the pipe where a uniform wall temperature is assumed ($U=V=\theta=0$) and finally, at the symmetry plan ($R=0$), we consider: $\frac{\partial U}{\partial X}=\frac{\partial V}{\partial X}=\frac{\partial \theta}{\partial X}=0$.

B. Numerical Modelling and validation of the computer code

The governing equations with the corresponding boundary conditions are solved numerically using the finite volume method proposed by Patankar [7]. Thus, these differential equations are transformed in algebraic equations which are solved by means of the line by line method.

The grid adopted in the present study is non-uniform and consists, after studying the sensitivity of the results to the mesh, of 250 nodes in the X direction and 50 nodes in the R direction. The convergence criterion, which is based on the residual, is set to 10^{-5} for both velocity components and temperature and to 10^{-6} for pressure.

Since there is few works regarding the Carreau fluid's flow within a pipe, to validate our computer code, we considered the limit case of a Newtonian fluid (n = 1). Thus, our results, concerning the axial evolution of the Nusselt number, were compared to those of Min et *al.* [8]. The comparison, illustrated in Fig. 1, shows a good agreement between both results since the relative gap does not exceed 1.8%.

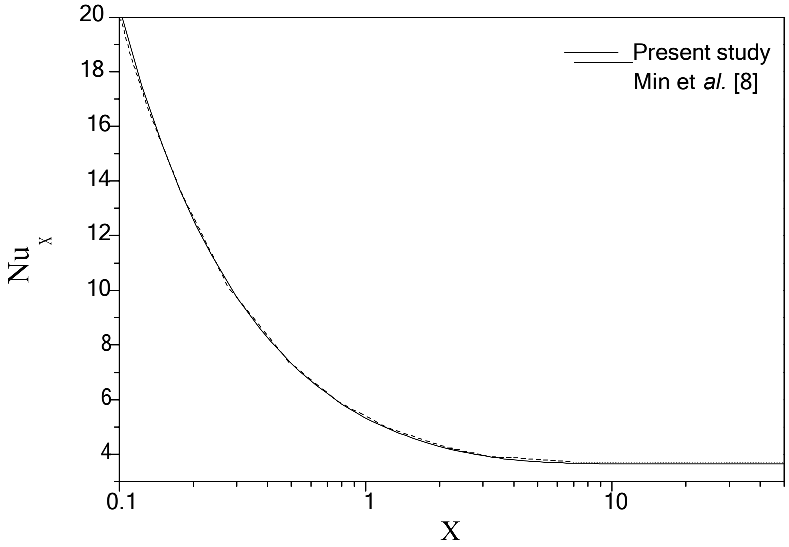

Fig. 1 Axial evolution of the local Nusselt number. Re = 50, Pr = 1, n = 1.

III. RESULTS AND DISCUSSION

The present study focuses on the analysis of the effect of neglecting viscous dissipation when the Carreau fluid is considered isoviscous and thermodependent.

Viscous dissipation is an energy source, represented by the Brinkman number (Br). Taking this function into account in the energy equation, leads to significant modifications on heat transfer behaviour, especially for viscous Newtonian and non Newtonian fluids.

A. Case of a Isoviscous Fluid

Fig. 2 represents the effect of the Brinkman number on the axial evolution of the Nusselt number, by considering both cases of wall heating (Br < 0) and wall cooling (Br > 0).

The figure shows a pronounced decrease of the Nusselt number from the inlet until reaching an asymptotic value which corresponds to the fully developed flow. For both heating and cooling, this value is single and is equal to 11.07, which is greater than the one obtained when viscous dissipation is neglected (Br = 0), i.e. 3.79.

Heat transfer is improved by the increase of the Brinkman number. Thus, neglecting viscous dissipation leads to undervalue heat transfer about 192% comparing to the case where viscous dissipation is neglected.

Note that in the case of wall heating (Br < 0), the curves present a discontinuity, with the existence of negative values of the Nusselt number due to the change in heat direction.

ISSN: 1737-38

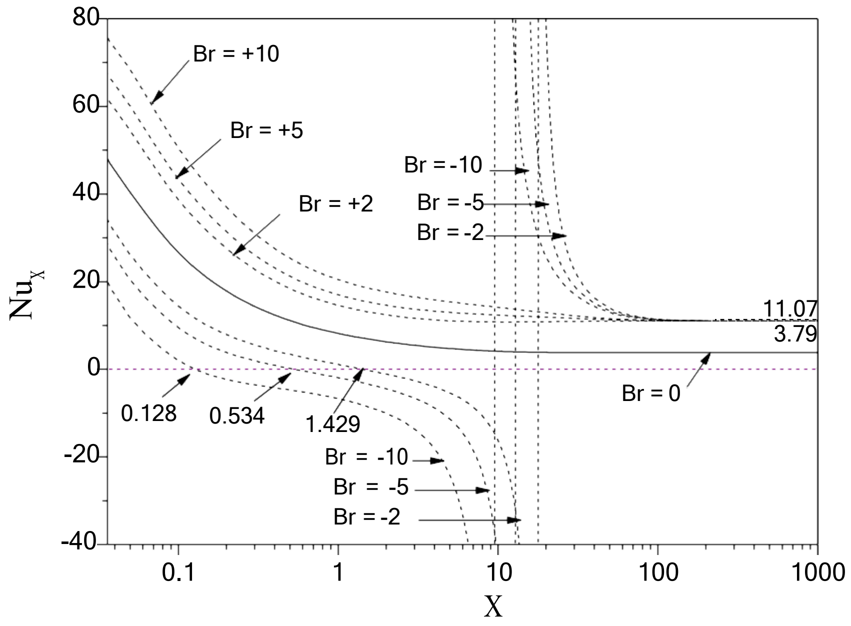

Fig. 2 Axial evolution of the local Nusselt number for various values of the Brinkman number. Re = 40, Pr = 10, n = 0.7, We = 20.

B. *Case of a Thermodependent Fluid*

The curves of Fig. 3 which represent the axial evolution of the Nusselt number when the fluid's apparent viscosity is thermodependent, show a decrease of the Nusselt number to reach different asymptotic values according to heating (Br < 0 ; a* > 0) or cooling (Br > 0 ; a* < 0) cases. Indeed, contrary to the case of a constant viscosity, an asymptotic value of the Nusselt number is obtained for each value of the Brinkman number as the fluid is temperature-dependent.

It is interesting to note also that in the developing region, the increase of the Brinkman number enhances heat transfer in the cooling case and worsens it in the heating case. However, in the fully developed region, heat transfer is improved when the Brinkman number decreases in absolute value, for both heating and cooling cases.

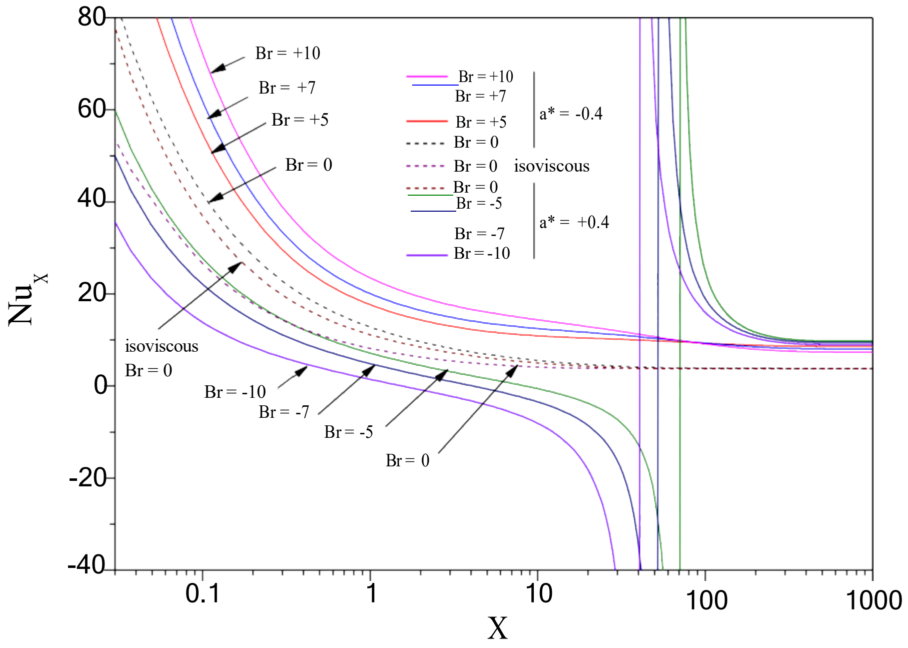

Fig. 3 Axial evolution of a temperature-dependent Carreau-Yasuda fluid's Nusselt number via the Brinkman number. n = 0.7, Re = 40, Pr = 10, We = 20.

IV. CONCLUSIONS

A numerical study based on the finite volume method was undertaken for a steady laminar forced convection flow of a Carreau fluid within a circular pipe maintained at a uniform wall temperature.

The study focused on the effect of viscous dissipation on heat transfer rate in the pipe, by considering an isoviscous fluid and a thermodependent one. The results show that heat transfer is strongly affected by viscous dissipation for both cases.

Thus, it is not rigorous to neglect viscous dissipation in calculation especially, when dealing with viscous fluids such as those obeying the rheological model of Carreau.

REFERENCES

[1] K. Khellaf, G. Lauriat, "Numerical study of heat transfer in a non-Newtonian Carreau-fluid between rotating concentric vertical cylinders," *J. Non-Newtonian Fluid Mech.*, vol. 89, pp. 45-61, 2000.

[2] F.M. Abbasi, T. Hayat, A. Alsaedi, "Numerical analysis for MHD peristaltic transport of Carreau–Yasuda fluid in a curved channel with hall effects," *J. Magnetism and Magnetic Materials*, vol. 382, pp. 104-110, 2015.

[3] F. Rousset, S. Millet, V. Botton, H. Ben Hadid, "Temporal stability of Carreau fluid flow down an incline," *J. Fluids Eng.*, vol. 129, pp. 913-920, 2007.

[4] S. Lounis, R. Rebhi, N. Hadidi, G. Lorenzini, Y. Menni, H. Ameur, N.A. Che Sidik, "Thermo-Solutal Convection of Carreau-Yasuda Non-Newtonian Fluids in Inclined Square Cavities Under Dufour and Soret Impacts," *CFD Letters*, vol. 14 (3), pp. 96-118 (2022).

[5] M. Bilal, I. Ullah, M.M. Alam, S.I. Shah, S.M. Eldin, "Energy transfer in Carreau Yasuda liquid influenced by engine oil with Magnetic dipole using tri-hybrid nanoparticles," *Scientific Reports*, vol. 13, Article number 5432, 2023.

[6] R.B. Bird, R.C. Armstrong, O. Hassager, *Dynamics of Polymeric Liquids*, Vol. 1 Fluid Mechanics, 2nd edtion, Wiley and sons, New York, 1978.

[7] S.V. Patankar, *Numerical heat transfer and fluid flow*, Hemisphere, New York, 1980.

[8] T. Min, H.G. Choi, J.Y. Yoo, H. Choi, "Laminar convective heat transfer of a Bingham plastic in a circular pipe-II. Numerical approach-hydrodynamically developing flow and simultaneously developing flow," *Int. J. Heat Mass Trans*, vol. 40, pp. 3689-3701, 1997.

NOMENCLATURE

Br Brinkman number, $= \square_0 V_0^2 / k(T_0 \square T_w)$
C_p specific heat at constant pressure, $J.kg^{-1}.K^{-1}$
D pipe diameter, m
k fluid thermal conductivity, $W.m^{-2}.K^{-1}$
L pipe length, m
n flow index
Nu Nusselt number, $= \square \frac{1}{\square_m} \square \square R \big|_{R=0.5}$
Pr Prandtl number, $= \square_{à} C_p V_0 k / D$
P^* dimensionless pressure, $= p^* / \square V_0^2$
p^* pressure, Pa
r radial coordinate, m
R dimensionless radial coordinate, $= r / D$
Re Reynolds number, $= \square V_0 D / \square_0$
T temperature, K
T_m dimensional bulk temperature, K
T_0 inlet and reference temperature, K
T_w wall temperature, K
U dimensionless x-component velocity, $= V_x / V_0$
V dimensionless r-component velocity, $= V_r / V_0$
V_x x-component velocity, $m.s^{-1}$
V_r r-component velocity, $m.s^{-1}$
V_0 inlet velocity, $m.s^{-1}$
We Weissenberg number, $= \square D / V_0$
x axial coordinate, m
X dimensionless axial coordinate, $= x / D$

Greek symbols:
$\square$ density of the fluid, $kg.m^{-3}$
$\square$ shear rate, s^{-1}
$\square^*$ dimensionless shear rate, $= \square D / V_0$
$\square$ effective viscosity, $Pa.s^n$
$\square_{app}$ dimensionless effective viscosity, $= \square / K_0$
$\square_0$ viscosity at zero shear, Pa.s
$\square$ the relaxation time, s
$\square$ dimensionless temperature, $= (T - T_w) / (T_0 - T_w)$
$\square_m$ dimensionless mean temperature, $= (T_m - T_w)/(T_0 - T_w)$

ISSN: 1737-40

Numerical investigation of double diffusive mixed convection in vertical channel with a porous medium

Karima SELLAMI[#1], M'barek FEDDAOUI[2], Monssif NAJIM[2], Nabila LABSI[1], and Youb Khaled BENKAHLA[1]

[#1]*Laboratoire de phénomènes de transfert, RSNE, Faculté de Génie Mécanique et de Génie des Procédés, USTHB, Alger, Algérie*

[2]*Laboratoire Génie de l'Energie, Matériaux et Systèmes, ENSA Agadir, Maroc*

`Email 1 - sellami_karima@yahoo.fr`

Abstract:

The present paper concerns a new mathematical approach to analyse the influence of the effective parameters on the performance of direct evaporation from a porous layer. The ambient air flows over a porous material, fed with water. The evaporation of an amount of water into the air reduces its temperature and, at the same time, raises the air's humidity. A mathematical model that accounts for simultaneous heat and mass transfer characteristics in the ambient air and water flow in corporating non-Darcian model in the porous region within vertical parallel walls is presented. The solution of the mathematical model is based on the finite volume method and the velocity-pressure coupling is treated with the SIMPLE algorithm. The results showed that the porous evaporative cooler could meet the cooling requirements in arid climates. An average drop of 15 °C of air temperature below the ambient temperature can be reached at the considered conditions. Therefore, the ambient air is satisfactorily cooled. Furthermore, the better cooling performance can be achieved for a high porositywith a thick porous medium and lower air velocity at the entrance.

Key words: evaporative cooling, non-Darcian Model, porous ceramic, vertical walls, mixed convection.

Nomenclature

A	area, m^2
C	inertia parameter.
Cp	specific heat of the fluid at constant pressure, (J.kg^{-1}.K^{-1})
d	porous layer thickness, (m)
D_h	hydraulic diameter, (m)
D	mass diffusivity, (m^2.s^{-1})
g	gravitational acceleration, (m.s^{-2})
H	channel width, (m)
h_{fg}	latent heat of vaporization, (J.kg^{-1})
K	permeability of the porous layer, (m^2)
k	thermal conductivity, (W.m^{-1}.K^{-1})
L	channel length, (m).
m_L	liquid mass flow rate, (kg.m^{-1}.s^{-1})
$\dot{m}_I$	evaporative mass flux, (kg.m^{-2}.s^{-1})
Mr	evaporation rate of mixture
P	pressure, (Pa)
Q_l	latent heat flux density (W.m^{-2})
Q_s	sensible heat flux density (W.m^{-2})
Q_t	total heat flux density (W.m^{-2})
Re	Reynolds number
T	temperature, (K)
U_0	gas inlet velocity, (m.$^{-1}$)
V_x	longitudinal velocity, (m.s^{-1})
V_y	transverse velocity, (m.s^{-1})
W	mass vapour fraction,
x	longitudinal coordinate, (m)
y	transverse coordinate, (m)

Greek symbols

□	coefficient of thermal expansion, (K^{-1})
□	density, (kg.m^{-3})
□	relative humidity of the air-vapour mixture.
□	porosity
□	dynamic viscosity, (kg.m^{-1}.s^{-1}).
□	cooling efficiency.

Indices and exponents

0	inlet
a	air
e	effective
I	interface
L	liquid
m	mixture
out	channel outlet
S	solid
v	vapour
w	wall

Introduction :

- The Double-diffusive convection in porous media are attracting increasing interest for several decades, where the fluid flow is induced by the simultaneous presence of heat and mass transfer. A considerable amount of research has been reported on double-diffusive convection since of its many engineering and technology applications. To enhance the heat and mass transfer, researchers have developed a diversity of effective strengthening heat transfer technologies, such as changing the surface structure using the corrugated wall to increase the heat exchange surface; introducing nanoparticle to change fluid characteristics; and so on. Porous media, as an efficient tool, is also used commonly to enhance heat transfer in many engineering applications because of its high thermal conductivity.

Wan et al. (2018) developed a new method to determine the heat and mass transfer coefficients in the counter-flow dew point evaporative cooler under diverse climatic. The authors investigated the effects of the various conditions on the heat and mass transfer coefficients, including climatic, operating and geometric conditions. Their results showed the capabilityof the dew point evaporative cooler to achieve higher cooling effectiveness. In addition, the new method provide the accurate data to realize optimum design of the dew point evaporative cooler.

Recently, Sohani et al. (2018) presented a comparative analysis of various kinds of heat and mass exchangers to determine the best design of dew point evaporative coolers at diverse climatic conditions. It was found that the counter regenerative configuration was the ideal choice in very hot and dryareas, while in other investigated climates; the cross configuration was the better alternative.

Dai and Sumathy (2002) investigated a cross-flow direct evaporative cooler with wet honeycomb paper as the packing material. The system was expected to act as both humidifier and evaporative cooler that can create a comfortable indoor environment in arid regions. They presented a mathematical model, which was validated experimentally for theoretical prediction of the system performance. Later, a simplified mathematical model was developed by Fouda and Melikyan (2011) to describe the heat and mass transfer between air and water in a direct evaporative cooler. The relationship between the cooling efficiency and its influence factors for the direct evaporative cooler with porous, durable honeycomb papers as a pad material was considered. The effectiveness of evaporative cooling has been proved in different climatic situations, not only in hot and dry regions where it was initially applied (Dabaieh et al., 2015; Kharrufa and Adil, 2012) but also in hot and humid regions (Zhang et al., 2015, 2016).

In addition, several passive evaporative cooling systems such as intermittent evaporative roof cooling (Alturki and Zaki, 1991; Wang et al., 2008) and two-stage indirect/direct evaporative cooling (Al-Juwayhel et al., 2004; Jain, 2007) have been investigated in order to enhance the cooling effect in an evaporative cooling system and to reduce the dissipated energy caused by the inherent heat and mass transfer resistance need to be achieved in all these systems. Therefore, some physical quantities are necessary to be defined to estimate the cooling ability of the evaporative system and to measure the endothermic abilitydissipation during the process. Veryrecently, Zhang et al. (2017)

presented a novel approach for modelling and analysing the influence of evaporation on roof thermal performance. A multivariate nonlinear model was developed for the prediction of the evaporation rate from a porous tile. Their studyfocused on a numerical method rather than heat and mass transfer model itself, and a complete discussion about mathematical models was avoided.

A theoretical analysis to free evaporating cooling in unsaturated porous packed bed in houses or buildings was presented by Liu et al. (1995). The simultaneous heat and mass transfer in the porous media unsaturated with liquid was numerically simulated. He et al. (2009, 2010) constructed a passive evaporative cooling wall out of moist void bricks, and Chen et al. (2015) for a pipe-shaped porous ceramics that were capable to absorb water and allowed wind penetration, which consequently reduced their surface temperature via water evaporation. Other authors used ceramic as porous materials. Indeed, Riffat and Zhu (2004) combined porous ceramic and heat pipe into an indirect evaporative cooler. Ibrahim et al. (2003) have built several prototypes of wet porous ceramic materials for building cooling. Achievement of this indirect evaporative cooling has been affected bypassing air through a wet porous medium plate.

The main objective of this work is to investigate the heat and mass transfer during the evaporation of liquid film by mixed convection of humid air in a vertical channel with porous wet wall. The liquid and air streams are modeled as two coupled laminar boundary layers incorporating non-Darcian models of the inertia and boundary effects. The governing equations and the associated boundary conditions are discretized by means of the finite volume method implemented on a staggered mesh and the velocitypressure coupling is processed bythe SIMPLE algorithm.

Problem Formulation.

Our model consists of a vertical channel formed by two plates of length L = 3 m, spaced by a distance H = 0.04 m (Fig. 1). The internal left wall is assumed adiabatic and covered with a porous material of thickness d, permeability K, and porosity □. The plate is wetted by a falling water film with an inlet temperature $T_{0;L}$and inlet mass flow rate $m_{0;L}$, used as a porous evaporative plate. The second plate is adiabatic and dry. A laminar ambient air flows along the channel with a uniform velocityU_0, temperature T_0, and relative humidity $□_0$.

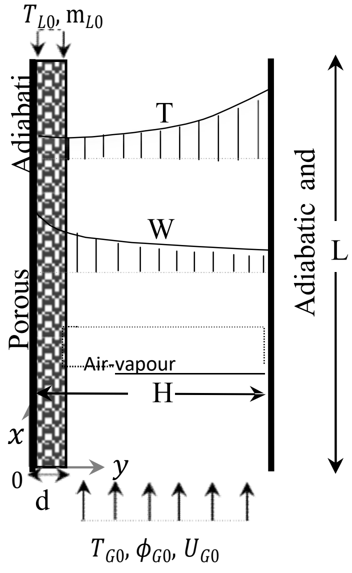

Figure 1: *Schematization of the physical problem and boundary conditions*

- Basic equations for the liquid film

$$0 = \square\square_L g + \frac{\square}{\square y}\left(\square_L \frac{\square V_x}{\square y}\right) - \frac{\square_L}{K} V_x - \frac{\square_L C_2}{\sqrt{K}} V_x^2 \qquad (1)$$

$$\square_L C_{p,L} V_x \frac{\square T}{\square x} = \frac{\square}{\square y}\left(k_e \frac{\square T}{\square y}\right) \qquad (2)$$

- **Basic equations for gas flow**

$$\frac{\square(\square_m V_x)}{\square x} + \frac{\square(\square_m V_y)}{\square y} = 0 \qquad (3)$$

$$\frac{\square(\square_m V_x^2)}{\square x} + \frac{\square(\square_m V_x V_y)}{\square y} = -\frac{\square p}{\square x} + \square_m g + \frac{\square}{\square x}\left(\square_m \frac{\square V_x}{\square x}\right) + \frac{\square}{\square y}\left(\square_m \frac{\square V_x}{\square y}\right) \qquad (4)$$

$$\frac{\square(\square_m V_y V_x)}{\square x} + \frac{\square(\square_m V_y^2)}{\square y} = -\frac{\square p}{\square y} + \frac{\square}{\square x}\left(\square_m \frac{\square V_y}{\square x}\right) + \frac{\square}{\square y}\left(\square_m \frac{\square V_y}{\square y}\right) \qquad (5)$$

$$\frac{\square(\square_m V_x C_p T)}{\square x} + \frac{\square(\square_m V_y C_p T)}{\square y} = \frac{\square}{\square x}\left(k_m \frac{\square T}{\square x}\right) + \frac{\square}{\square y}\left(k_m \frac{\square T}{\square y}\right) \qquad (6)$$

$$\frac{\square(\square_m V_x W)}{\square x} + \frac{\square(\square_m V_y W)}{\square y} = \frac{\square}{\square x}\left(\square_m D_m \frac{\square W}{\square x}\right) + \frac{\square}{\square y}\left(\square_m D_m \frac{\square W}{\square y}\right) \qquad (7)$$

Boundary conditions and used expressions

The boundaryconditions associated with this problem, are given as follow:

At the inlet: $x = 0$

For the liquid $0 < y < d$: $T = T_{0,L}$ $m_L = m_{0,L}$ (8)

For the gas $d < y < H$: $V_{x,m} = U_{0,m}$ $V_{y,m} = 0$ $T = T_{0,m}$ $\square = \square_{0,m}$ (9)

At the walls:

$y = 0$: $V_{x,L} = 0$ $\left.\frac{\square T}{\square y}\right|_{y=0} = 0$ (10)

$y = H$: $V_{x,m} = V_{y,m} = 0$ $\left.\frac{\square T}{\square y}\right|_{y=H} = 0$, $\left.\frac{\square W}{\square y}\right|_{y=H} = 0$ (11)

At the outlet: $x = L \ \ and \ \ d < y < H$

$$\frac{\square V_x}{\square x} = \frac{\square V_y}{\square x} = \frac{\square T}{\square x} = \frac{\square W}{\square x} = 0 \qquad (12)$$

At the interface: $y = d$

The solution fromthe liquid side and gas side satisfies the following interfacial matching conditions:

- Continuities of velocityand temperature

$$V_{x,I} = V_{x,I,m} = V_{x,I,L} \qquad T_I = T_{I,m} = T_{I,L} \qquad (13)$$

- Continuityof shear stress

$$\square_I = \square\square\left(\frac{\square V_x}{\square y}\right)_{I,L} = \square\square\left(\frac{\square V}{\square y}\right)_{I,m} \tag{14}$$

- The transverse velocity component of the air-vapour mixture at the interface is calculated by:

$$V_e = \square\frac{D_m}{1\ \square W_I}\frac{\square W}{\square y}\Bigg|_I \tag{15}$$

Résultats :

This study investigates the characteristics of heat and mass transfer process between two vertical parallel walls with a wetted porous wall used as an evaporative cooler, with particular emphasis on studying the factors affecting the thermal and mass performances. Evaporative cooling is a heat and mass transfer process that uses water evaporation for air-cooling, in which a large amount of heat is transferred from air to water, involving consequently, a decrease of ambient air temperature and a rises of its relative humidity.

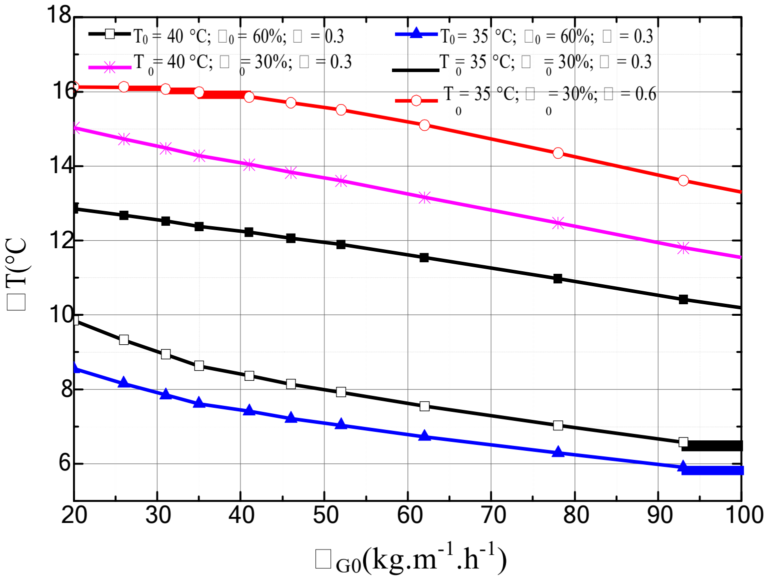

Figure 2 : *Variation of the temperature drop as a function of the inlet airflow for various considered parameters*

Figure 2 shows the variation of the temperature deference between the inlet and the outlet of the channel, as a function of the airflow at the inlet, and this, for different values of the temperature and humidityof the air at the entrance as well as the thickness of the porous layer.

This figure shows that the increase of the inlet air mass flow induces the decrease of the temperature deference. Indeed, at high airflow at the entrance, the required contact time between the air and the surface decreases. As a result, the gas temperature on the channel axis decreases due to evaporation. The most intense decrease is observed for low values of the airflow at the entrance. Indeed, for a flow of air mG0 < 70 kg.m-1.h-1, the difference in temperature decreases slightly. It is also noted that for fixed moisture and porosity, the air-cooling is improved for high values of inlet air temperature and porosity. Regarding the effect of air humidity at the inlet, we note that its increase deteriorates the performance of cooling, since a small differences in temperature are noted.

The effect of the inlet air parameters as well as the characteristics of the porous layer on the evolution of the difference of the relative humidity of the ambient air between the inlet and the outlet of the evaporative cooler are represented in Figures 5 and 6.

The figures show that the difference in the humidity of the air decreases as a function of the air flow at the inlet. This decrease is more important as the air flow at the entrance is large. It should be noted in Figure 5 that the effect of the parameters considered, namely: temperature and porosity, is small on the relative humidity however, the relative humidity of the air is more important.

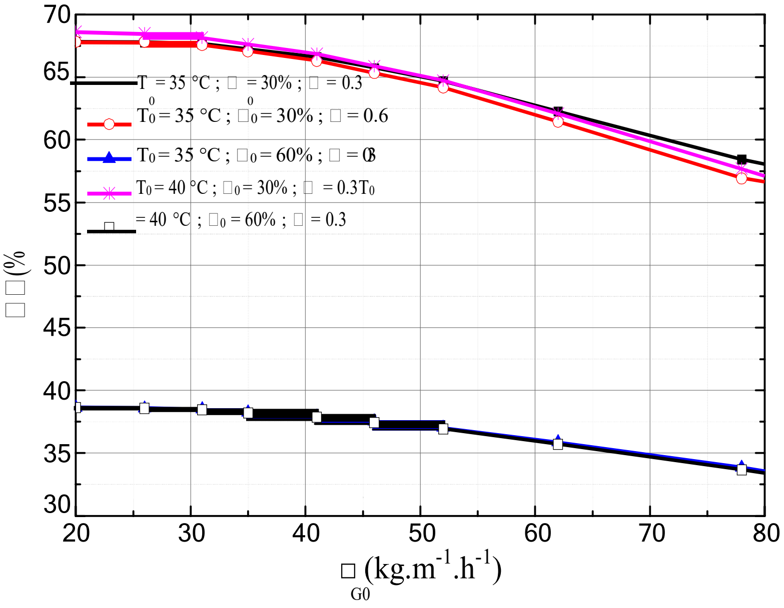

Figure 3 : Variation of the air relative humiditydrop as a function of the airflow.

Conclusion:

- This paper presents a two dimensional numerical study to describe heat and mass transfer during the evaporative cooling process from porous media. This article has reported the investigation of the effect of the imposed inlet air mass flow, porous layer thickness and porosity on the evaporative cooling performance.

The results show a drop in the temperature of air proportional to the sensible heat and an increase in humidity proportional to the latent heat drop. The lower ambient relative humidity causes a high evaporation rate in the porous evaporative cooling plate. Moreover, the increase in the thickness of the porous layer causes the increase of the temperature difference between the porous media and the ambient air.

Reference:

1. Al-Juwayhel, F., El-Dessouky, H., Ettouney, H., Al-Qattan, M., 2004, Experimental evaluation of one, two, and three stage evaporative cooling systems. Heat Transfer Eng. 25(6), 72-86.

2. Alturki AM, Zaki GM. Energy saving through intermittent evaporative roof cooling. Energy Build. 17(1), 35–42.

3. Chen, W., Liu, S. and J. Lin, 2015, Analysis on the passive evaporative cooling wall constructed of porous ceramic pipes with water sucking ability, EnergyBuild. 86, 541–549.

4. Dabaieh, M., Wanas, O., Hegazy, M.A., Johansson, E., 2015, Reducing cooling demands in a hot dry climate: a simulation study for non-insulated passive cool roof thermal performance in residential buildings, EnergyBuild. 89, 142–152.

5. Dai, Y.J., Sumathy, K., 2002, Theoretical study on a cross-flow direct evaporative cooler using honeycomb paper as packing material, Applied Thermal Engineering. 22, 1417–1430.

6. Fouda, A., Melikyan, Z., 2011, A simplified model for analysis of heat and mass transfer in a direct evaporative cooler, Applied Thermal Engineering. 31, 932-936.

7. He, J. and Hoyano, A., 2009, A 3D CAD-based simulation tool for prediction and evaluation of the thermal improvement effect of passive cooling walls in the developed urban locations, Sol. Energy. 83 (7), 1064–1075.

8. He, J., and Hoyano, A., 2010, Experimental study of cooling effects of a passive evaporative cooling wall constructed of porous ceramics with high water soaking-up ability, Build. Environ. 45 (2), 461–472.

9. Ibrahim, E., Shao, L., Riffat, S.B., 2003, Performance of porous ceramic evaporators for building cooling application. EnergyBuild. 35(9), 941-9.

10. Kharrufa, S.N. and Adil, Y., 22012, Upgrading the building envelope to reduce cooling loads, EnergyBuild. 55, 389–396.

11. Liu, W., Peng, S. W., Mizukami, K., 1995, A general mathematical modelling for heat and mass transfer in unsaturated porous media: an application to free evaporative cooling, Heat and Mass Transfer. 31, 49-55.

12. Patankar S.V, 1980, Numerical heat transfer and fluid flow, Hemisphere.

13. Riffat, S.B. and Zhu, J., 2004, Mathematical model of indirect evaporative cooler using porous ceramic and heat pipe. Appl Therm Eng 24(4), 457-70.

14. Sohani A, Sayyaadi H, Mohammadhosseini N., 2018, Comparative study of the conventional types of heat and mass exchangers to achieve the best design of dew point evaporative coolers at diverse climatic conditions, EnergyConversion and Management 158, 327–345.

15. Wang, XC, Niu, JL, Van Paassen, AHC, 2008, Raising evaporative cooling potentials using combined cooled ceiling and MPCM slurrystorage. EnergyBuild. 40, 1691–8.

16. Zhang, L., Feng, Y., Meng, Q., Zhang, Y., 2015, Experimental studyon the building evaporative cooling byusing the Climatic Wind Tunnel, EnergyBuild. 104, 360–368.

17. Zhang, L., Liu, X., Meng, Q., Zhang, Y., 2016, Experimental study on the impact of mass moisture content on the evaporative cooling effect of porous face brick, Energy Effic. 9 (2), 511–523.

18. Zhang, L., Zhang, R., Zhang, Y., Hong, T., Meng, Q., Feng, Y., 2017, The impact of evaporation from porous tile on roof thermal performance: A case study of Guangzhou's climatic conditions, Energyand Buildings. 136, 161–172.

Optimization of surface roughness by the tribofinishing process with the use of Box-Behnken experimental designs

D. SAIDI[1], **M.A. DJEMA2**, **K. HAMOUDA**[2],**M. BOUAZIZ**[1]

1. Ecole Nationale Polytechnique, Alger, Algérie
2. Université des Sciences et de la Technologie Houari Boumediene, Alger, Algérie
e-mail: djamel.saidi@g.enp.edu.dz

Abstract

This work presents an experimental research of the influence of the three important parameters (frequency, amplitude, abrasive size) on surface roughness during tribofinishing treatment.

The process of tribofinishing is investigated as a means to reach a state of quality for the surface treated, this work consists in treatment on cylindrical samples of AA 2017 aluminium alloys in order to improve the surface state, using Box-Behnken design which is a power full tool for experimental design is used to optimize the process parameters. Box-Behnken design method as well as analysis of variance (ANOVA) is used to analyze the influence of parameters of treatment on surface roughness Ra.

The optimum process parameters for minimum surface roughness in tribofinishig process have been obtained and validated with the experiments and found highlysatisfactoryresults.

Keywords: Box–Behnken design, tribofinishing, roughness, frequency, amplitude, abrasive size

---

1. Introduction

The tribofinishing process is a mechanical-chemical process which aims to remove small particles of metal and its oxides by micro blows that the surface receives, which generates plastic deformation while causing surface hardening.

This method was inspired by nature where the constant flow of water transforms rough stones into perfectlypolished pebbles.

Tribofinishing is a process to improve the surface state of mechanical parts that includes: elimination of rough edges, burrs, also to round off angles, to polish, with a technologythat uses unguided cutting tools **(**abrasive particles)[1, 2]
The ability of mechanical parts to insure a particular function depends on some parameters, such as microstructure, superficial geometrical and mechanical characteristics
[3, 4].

To obtain such a surface state, many methods such grinding, superfinishing, lapping, etc… are used [5, 6].

Some of these processes are relatively expensive and cannot be adapted perfectly to complex geometries of the specimen used. Tribofinishing is a suitable process used to improve complex geometries characteristics. It acts by removing small metal particles and oxides from the treated surface [7, 8, 9].

Achievement of surface quality is obtained by continuous friction between the work pieces and the particles (generally porcelain balls) acting as abrasives [10].

ISSN: 1737-48

This study focuses on the application of tribofinishing treatment (porcelain balls) on aluminium alloy(AlCu4MgSi) AA 2017, and parameters optimization oftreatment regime.

The process parameters that were taken into consideration are: frequency, amplitude and abrasive size, using Box-Behnken design.

In 1960, Box and Behnken proposed designs that allow us to directly implement seconddegreemodels. All the factors have three levels: –1, 0, and 1.

These designs are easy to carry out and have the property of sequentiality.

The Box-Behnken design for three factors is constructed on a cube.

The experimental points are placed not at the corners of the cube, but in the middle of the edges. This arrangement means that all experimental points are placed equidistant from the center ofthe studydomain. Center points are added to the studydomain [11,12].

The Box-Behnken design for three factors is shown in Figure 1. The cube has 12 edges. Traditionally, three experimental points are placed at the center of the study. Box-Behnken designs for three factors therefore have 12 +3 = 15 trials [13, 14].

We have developed an empirical mathematical model to illustrate the relationship between these three parameters and the response roughness “Ra”.
In this study, the design and analysis have been carried using Design-Expert version 10.

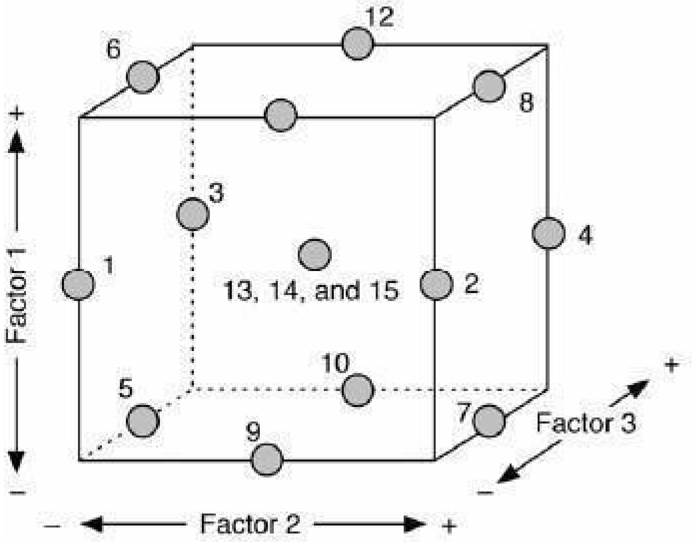

Figure 1 Illustration of the Box-Behnken design for three factors. There are twelve experimental points at the center of each edge, and three points at the center of the cube.

2. Surface roughness measurement

Surface roughness is one of the important parameters toassess the product quality or surface quality. This factor has asignificant effect on functionality as well as esthetic aspects ofthe product.

The most commonly used parameter to quantifythe surface roughness is arithmetic mean surface roughnessvalue (Ra). $Ra$is the arithmetic average of the absolute valuesof the roughness profile ordinates or the integral of the absolute value of the roughness profile height over the evaluationlength. Mathematically this can be described bythe following relation [8].

$$Ra = \frac{1}{L}\int_0^L |z(x)|dx \qquad (1)$$

3. Experimental setup

The experimental tests were carried out on AA 2017 using a brand type (УВГ 4 x 10)linear vibrator (Figure 2). The total duration of tribofinishing treatment is 240 minutes, with a variation of parameters (frequency, Amplitude, Abrasive size).

The work pieces are put into the working chamber of the vibrator which is filled with porcelain balls and chemical additives. The vibrator receives a low frequency vibration and can move freely in the space three directions.

The working chamber is ring shape with a flat bottom which ensures a perfect immersion of the parts in the abrasive charges.

The treated parts are usually removed manually.

Machine Features

- Working chamber capacity: 10 dm^3
- Number of working chamber: 4
- Engine power (KW) 1
- Dimensions (mm) 1300 X 952 X 1370
- Type pumpПА-22
- Power (KW)0.12
- Flow rate (l/min) 22
- Particle nature: Porcelain balls
- Net weight of particles: 5 kg.
- Chemical Additive: Lauryl Ether Sulfate ($C_{12}H_{25}O_4S$) in one liter of water.
- Treatment time: 60min.

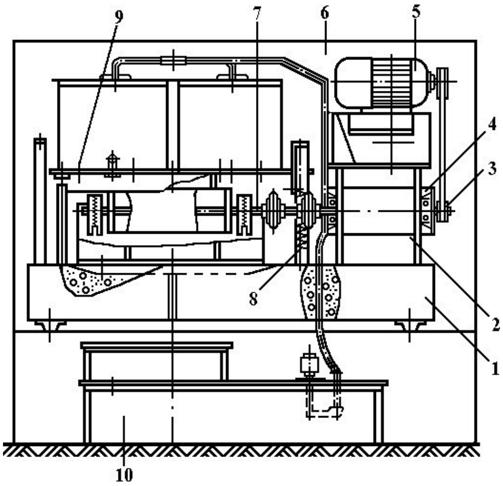

Figure 2 Schematic of the experimental linear vibrator.

1- Foundation
2- Intermediate shaft
3- System belt transmission
4- Maine shaft
5- Electric motor
6- Lubricating system
7- Elastic sleeve
8- Unbalance
9- Working chamber
10- Ferry reservoir**.**

Process parameters and experimental design

The summary of the parameters used for this study are in the table 1.

Table 1 Process parameters and their levels

Parameters	Variation Levels		
	Low (-1)	Medium (0)	High (+1)
Frequency(Hz)	15	33	50
Amplitude (mm)	1.5	3	5
Abrasive size (mm)	6	8	10

This study evokes a Box-Behnken design which requires 3-levels of each factor coded as -1, 0 and 1.

In order to observe parameter effects on surface state, testing scheme are shown in figure 3.

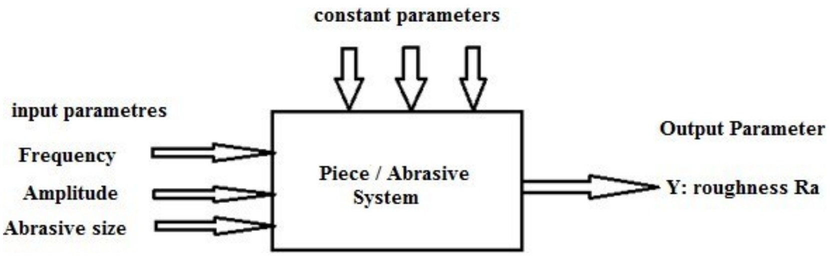

Figure 3Testing scheme

Experimentations

The design matrix, including the recorded experimental values for the roughness, is presented in table 2.

Table 2 Design matrix with their experimental values of roughness (Ra)

Test Number	Independent Variables			Response
	Frequency(Hz)	Amplitude (mm)	Abrasive size (mm)	Roughness Ra (µm)
1	15	1.5	8	1.610
2	50	1.5	8	1.488
3	15	5	8	1.600
4	50	5	8	1.358
5	15	3	6	1.592
6	15	3	10	1.606
7	50	3	6	1.412
8	50	3	10	1.454
9	33	1.5	6	1.570
10	33	5	6	1.516
11	33	1.5	10	1.582
12	33	5	10	1.538
13	33	3	8	1.556
14	33	3	8	1.556
15	33	3	8	1.556

The dimensions and the roughness measured samples are presented in figure 4.

Figure 4 Roughness measured samples.

Chemical composition of the work piece was 86.15% Al and 5.51% Cu, as confirmed by SEM image (shown in figure 5).

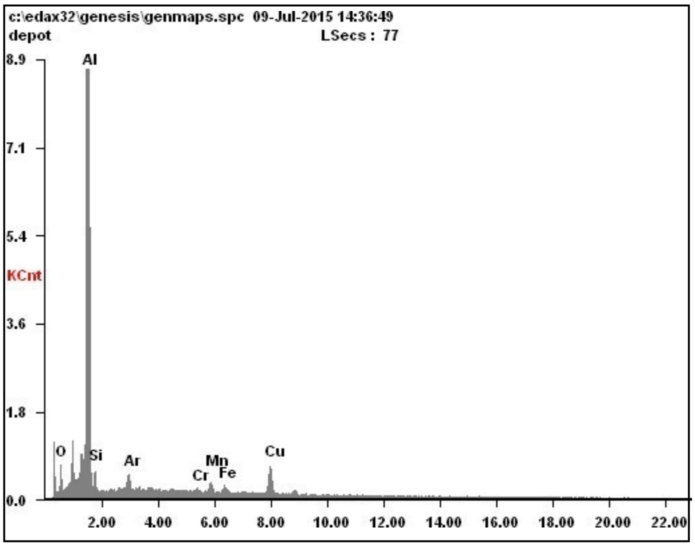

Figure 5 SEM image

4. Results and discussion

The general equation for the proposed second order regression model to predict the response Y can be written as:

$$Y = a_0 + a_1x_1 + a_2x_2 + a_3x_3 + a_{12}x_1x_2 + a_{13}x_1x_3 + a_{23}x_2x_3 + a_{11}x_1^2 + a_{22}x_2^2 + a_{33}x_3^2 + e \quad (2)$$

Where:

- Y: Response
- a: Coefficient
- x: variable
- e: Prediction error.

To formulate the effect of selected process parameters on surface roughness, the modeller software was given inputs of measured responses (Ra values) for all experimental runs. The surface roughness was modelled in terms of frequency, amplitude and abrasive size as follows:

- **Final Equation in Terms of Coded Factors:**

$$Ra = +1.56 - 0.088 * A - 0.030 * B + 0.010 * \mathrm{C} - 0.030 * \mathrm{AB} + 9.500\mathrm{E} - 003 * \mathrm{AC} + 2.500\mathrm{E} - 003 * \mathrm{BC} - 0.038 * \mathrm{A}^2 - 4.500\mathrm{E} - 003 * \mathrm{B}^2 + 0.000 * \mathrm{C}^2 \quad (3)$$

ISSN: 1737-52

Statistical results

Using analysis of variance (ANOVA), the effects of frequency, amplitude, abrasive size and their second order interactions on surface roughness were calculated. (See table 3)

Table 3 Analysis of variance (ANOVA) for Response Surface Quadratic model

Source	DF	SS	MS	F	P
Model	9	0.080	8.91E-003	208.86	<0.0001 significant
A Frequency	1	0.062	0.062	1458.63	<0.0001
B Amplitude	1	7.080E-003	7.080E-003	165.76	<0.0001
C Abrasive size	1	8.000E-004	8.000E-004	18.73	0.0034
AB	1	3.600E-003	3.600E-003	84.28	<0.0001
AC	1	3.610E-004	3.610E-004	8 .45	0.0228
BC	1	2.500E-005	2.500E-005	0.59	0.4693
A^2	1	5.921E-00	5.921E-003	138.62	<0.0001
$B^2$1	8.526E-005	8.526E-0052.00	0.2006		
C^2	1	0.000	0.000 0.000	1.0000Residual	7
2.990E-004	4.271E-005				
Lack of Fit	3	2.990E-004	9.967E-005		
Pure Error	4	0.000	0.000		
Cor Total	16	0.081			

R-Squared 0.9963, The "Pred R-Squared" of 0.9406 is in reasonable agreement with the "Adj R-Squared" of 0.9915; i.e. the difference is less than 0.2.
Values of "Prob> F" less than 0.0500 indicate model terms are significant.
In this case A, B, C, AB, AC, A^2 are significant model terms.

Graphical results

Figure 6 show the perturbation plot of surface roughness. This perturbation plot compares the effect of every factor at a particular point in the design space (Design Expert, 10)
The roughness decreases when increasing the frequency and amplitude and the abrasive size decreases.

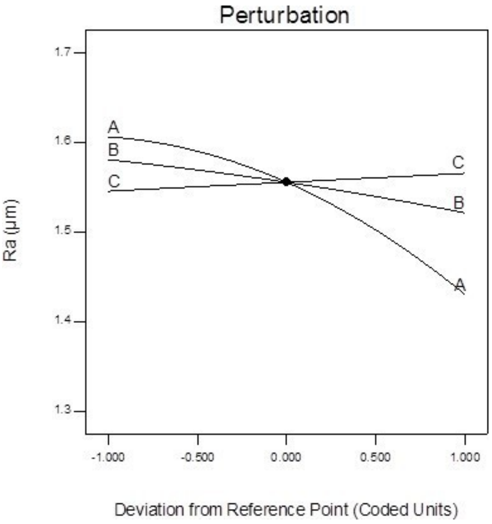

Figure 6 Perturbation plot for surface roughness.

ISSN: 1737-53

Response Surface Plot

In order to gain a better understanding of the interactioneffects of variables on surface roughness, three-dimensional (3D)plots for the measured responses were formed based on themodel equation (4). Also the relationship between thevariables and responses can be further understood by theseplots. Since model has three variables, one variable is held constant at medium level; therefore, a total of 6 responsesurface plots were produced for responses.

The relationship between variables and their influence onthe response, the surface roughness, is shown in Figure 7which showsthe influence of frequency and amplitude onthe surface roughness.

It indicates that surface roughnessdecreases.

In others words, Figures 7, 8 and 9indicate that frequency, amplitude, and abrasive size have considerable influence on the surface roughness.

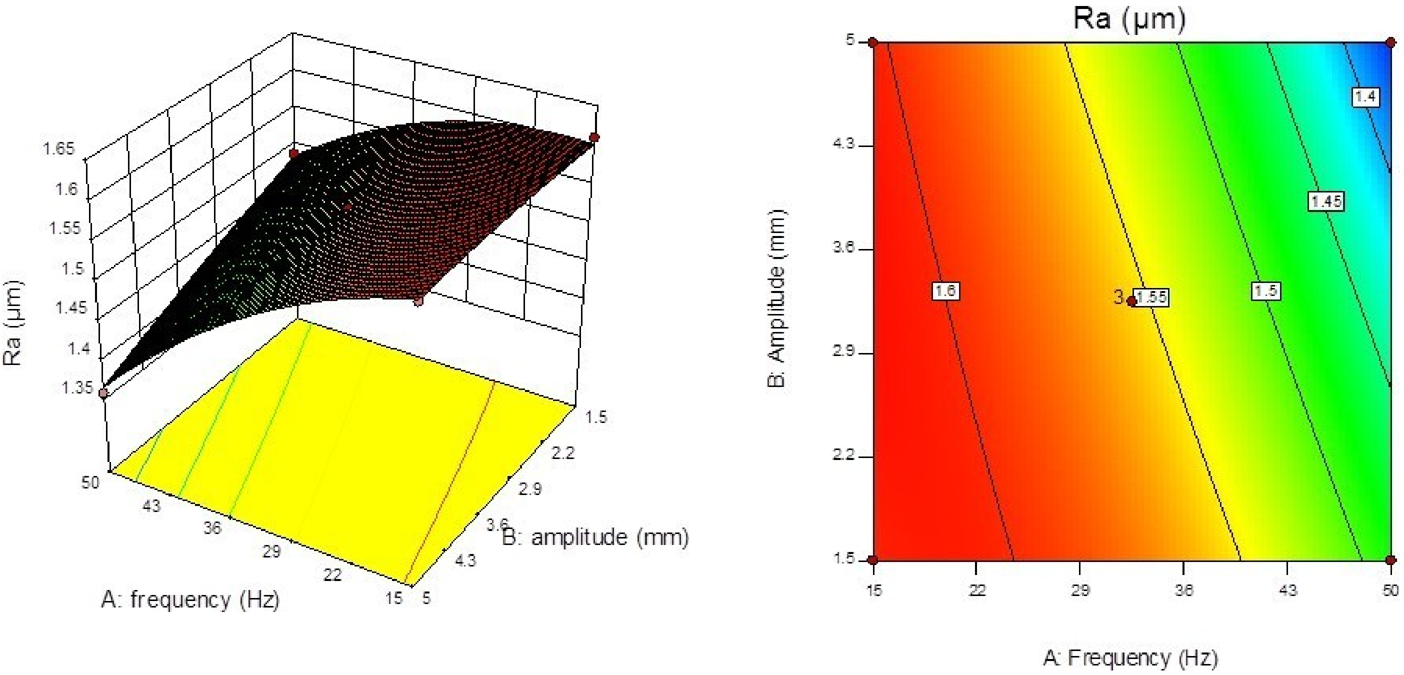

Figure 7Response surface plots showing effect oftwo variables (frequency, amplitude) on surface roughness

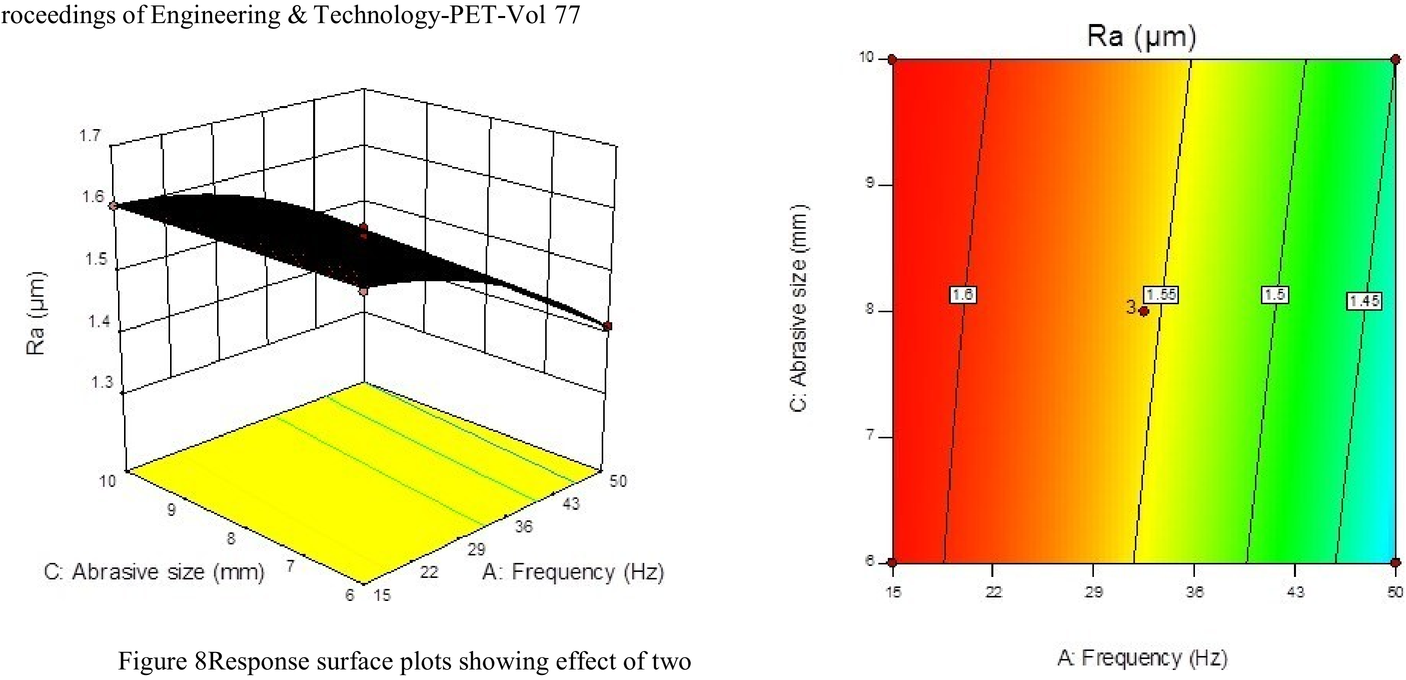

Figure 8Response surface plots showing effect of two variables (frequency, abrasive size) on surface roughness

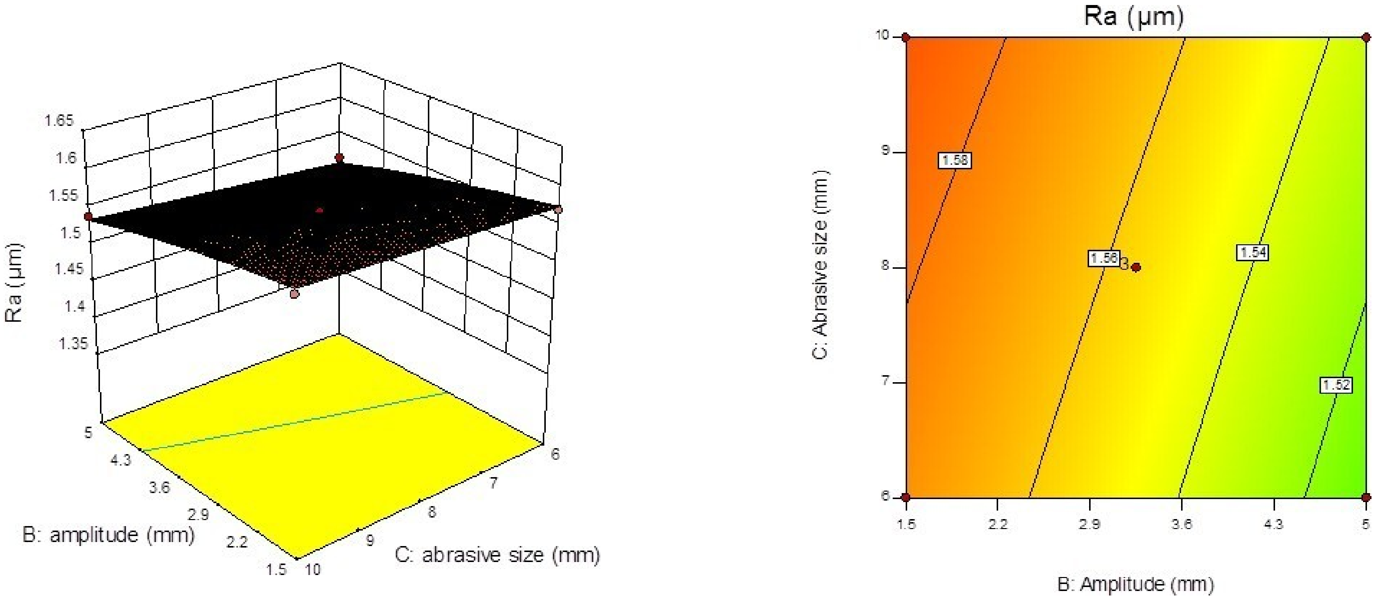

Figure 9Response surface plots showing effect of two variables (amplitude, abrasive size) on surface roughness

Figure 9a and figure 9b shows a comparison between predicted and actual values of the response and confirms that the results obtained are in a good agreement with the predicted values.

Additionally, the developed response surface model for Ra has been checked by using residual analysis.

The residual plots for Ra are shown in Figures. 10a-10b. In normal probability plot, the data are spread approximately in a straight line, which show a good correlation between experimentaland predicted values for the response (Figure 10a).

Figure 10b is the plot of the residuals calculated against the order of experimentation. It is asserted that a tendency to have runs of positive and negative residuals indicate the existence of correlation. From the above analysis of residual plots for Ra, the model does not reveal inadequacy.

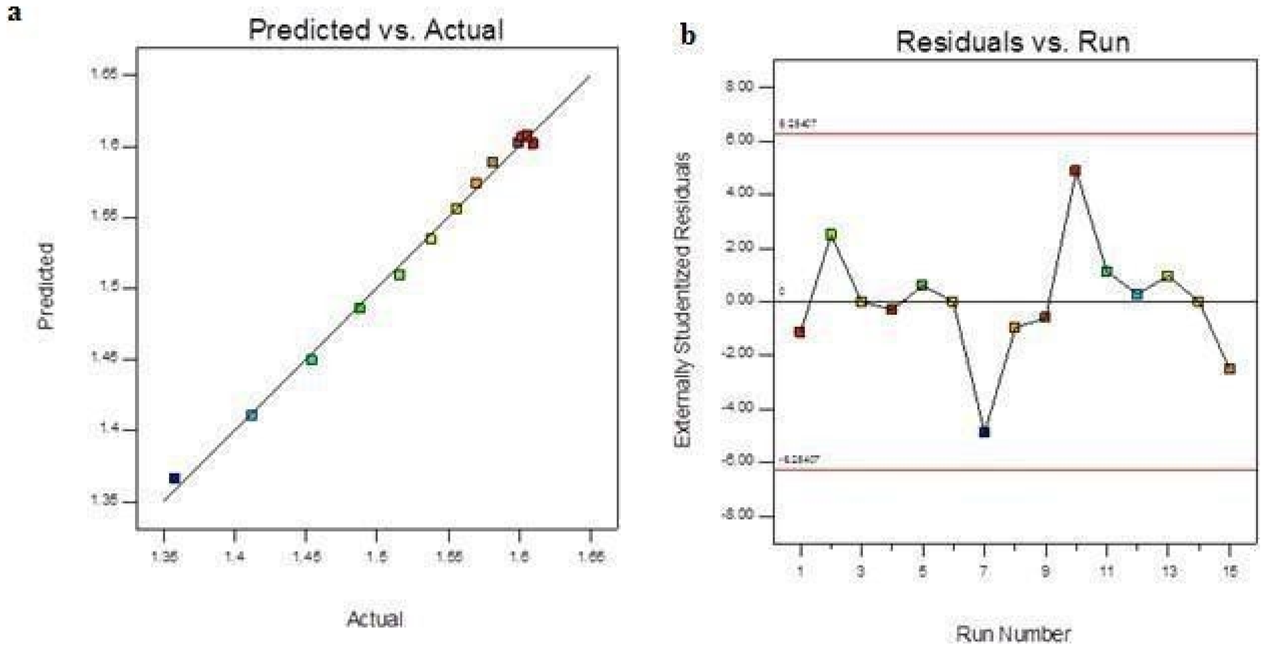

Figure 10 Relation between experimental and predicted values (a), Residual analysis (b)

Hardened layer

Figure 11 illustrates the hardened layer that appears on the SEM image, in light graycolor in the order of 100 microns with an X350 magnification, observed by a scanning electron microscope (SEM) JEOL JSM-type 6360

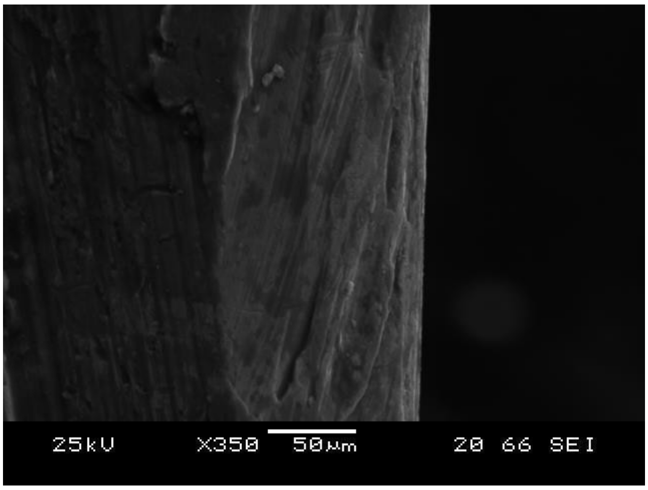

Figure 11 Hardened layer

Conclusions

In this study, optimization of parameters (frequency, amplitude, abrasive size)during tribofinishing process has been carried out.

The surface roughness response Ra has been modeled and analyzed through response surface methodology (RSM).

A Box-Behnken design was used to carryout the experimental study.

Analysis of variance (ANOVA) was used to analyze the effect of the parameters on the response.

In summary, the following conclusions can be drawn:

1. The frequency is found to be the most importantparameter effecting Ra, followed by amplitudewhile abrasive size has the least effect.
2. The predicted value of Ra matches the experimentalvalues reasonably well, with high value of coefficientof determination (R2 = 0.9963) for Ra.
3. The variation in percentage error for Ra is between 1 to5%, which shows that the model developed for Ra isaccurate, and can be used for predicting the surfaceroughness.

Acknowledgements

The authors gratefully acknowledge VIBROTECH laboratory for the cooperation and help. The authors are also thankful toVIBROTECH laboratory for providing the linear vibrator to achieve the experimental testing.

References

[1] M. A. Tamarkin, Theoretical principles of optimization processing of mechanical parts in free abrasive particles, as PhD thesis, 1995 Russia.
[2] Surface treatments and coatings for tribological purposes, CETIM, GAMI, 1994 ISBN 2-85400-333-0
[3] A. P. Babichev, P.D. Motrenko, Using the Vibration technology for improving the surface qualityand the mechanical characteristics, 2006, ISBN 5-7890-0390-7
[4] A. P. Babichev, improving the fatigue strength of non-ferrous materials by tribofinishing process, 2010.
[5] A. P. Babichev, I. A. Babichev, Principles of vibration technology, 2008, ISBN 978-5-7890-0472-2
[6] Jacques Goupy, Lee Creighton, Introduction to design of experiments, SAS Publishing, 2007
[7] Jacques Goupy, Pratiquer les plans d'expériences, Dunod, 2005
[8] Alain Cornet, Jean-Paul Deville, Physics and surface engineering, 1998, ISBN 2-86883-352-7
[9] [2] F. Hashimoto, Modeling and Optimization of Vibratory Finishing Process, CIRP Ann. Manuf. Technol. 45 (1) (1996) 303–306.
[10] Mohammad Reza Baghbanan, Akihiro Yabuki, Roland S. Timsit, Jan K. Spelt, Tribologicalbehavior of aluminum alloys in a vibratory finishing process, Wear, 255 (2003), 1369-1379.
[11] VOLKER SCHULZE, Modern Mechanical Surface Treatment, Edition WILEY-VCH, 2006.
[12] DOUGLAS C. MONTGOMERY, Design and analysis of experiments, Publisher: JOHN WILEY & SONS, 5th Edition, 2001.
[13] LAROUX. K. GILLESPIE, Mass Finishing Handbook, Edition Industrial Press New York, 2007.
[14] LAROUX. K. GILLESPIE, Deburring and Edge Finishing, Handbook, Edition SME, 1999

Conférence Internationale sur les Sciences Appliquées et l'Innovation (CISAI-2023)
Proceedings of Engineering & Technology-PET-Vol 77

Evaluating the Efficiency of Municipal Solid Waste Collection in Tunisian's Municipalities using Data Envelopment Analysis

Sabrine Ismail[#1], Habib Chabchoub[*2], SoulefSmaoui[#3]

[#] *Quantitative Methods, Faculty of Economics and Management, Sfax, Tunisia*
* *College of Business, Al Ain University, Abu Dhabi,UAE*

Email 1 - sabrineismail9@gmail.com
Email 2 - habib.chabchoub@aau.ac.ae

Email 3 - soulef.smaoui@gmail.com

Abstract

Municipal solid waste (MSW) collection plays a crucial role in achieving sustainability goals within municipalities.Systems for collecting waste that are efficient are crucial for protecting the environment, encouraging resource conservation, and enhancing public health.In this paper, we study the efficiency of 23 municipalities in Sfax City, Tunisia in order to evaluate their performance and identify the sources of inefficiencies.The Data Envelopment Analysis (DEA) method has been chosen to address our objective.

Keywords: MunicipalSolid Waste Collection, Sustainability, Data Envelopment Analysis.

1 Introduction

Municipal Solid Waste Management, including Municipal Solid Waste Collection, has been garnering growing attention from scholars, economists, technical staff, and other stakeholders [15].Proper disposal of MSW is vital to safeguard environmental quality, human health, and natural resources. By adopting sustainable waste management strategies, communities can address the economic, environmental, and social impacts of waste while working towards achieving long-term sustainability goals [9].This study primarily aims to pinpoint best practices for MSW collection and establish performance targets by identifying areas of excessive resource consumption and areas that require improvement. To accomplish these objectives, DEA will be utilized as a suitable method.

The remainder of this paper is structured as follows:Section 2 is dedicated to the literature review, while Section 3 elaborates on the DEA methodology. In Section 4, the case study is presented, and Section 5 focuses on the discussion of the results. Lastly, the conclusion is presented.

2 Literature review

The DEA methodology has been widely employed in numerous studies to address MSW-related issues. Among these studies, some notable examples includeSánchez (2006) [13] whoconducted an analysis of the waste collection schemes in 34 municipalities in Spain. For this study, he considered the total staff as an input and two outputs, namely tonnage collected and collection points.In 2011, De Jaeger *et al.* [6] examined the state of Municipal Solid Waste Management (MSWM) in 299 municipalities in Belgium. The inputs selected for the study were costs, and the five outputs analyzed were residual waste, packaging waste, paper and cardboard waste, glass, and other separately collected waste.The following year, Rogger and De Jaeger [11] implemented the shared input DEA approach in 293 municipalities of Belgium. For this analysis, waste costs were chosen as the input, and six outputs were considered: residual waste, other municipal waste, packaging waste, other EPR-waste, green waste, and bulky waste.In his study encompassing 103 municipalities in Italy, Lo Storto [8] utilized annual expenditures as inputs, while urban infrastructure development, urban ecosystem quality, nursery schools, municipality area extension, and resident population were considered as outputs.Struk *et al.* [16] employed a one-stage DEA approach to assess the efficiency of 400 municipalities in Czech Republic. For this evaluation, expenditures were taken as the input indicator, while population, number of dwellings, and serviced area served as the output indicators.In 2017, Sarra *et al.* [14] conducted an analysis of 289 municipalities in Italy, focusing on waste-related factors. For their study, they chose waste costs as the input, and two outputs were considered, one being desirable and the other undesirable.Yang *et al.* [17] utilized a three-stage DEA methodology to evaluate 34 cities in China. The selected inputs for the analysis were the number of Vehicles and Equipment Designated for Municipal Environmental Sanitation and Fixed Assets Investment in the Public Facilities of Municipal Environmental Sanitation. The output indicators considered were the Quantity of MSW Collected and Transported and the MSW Harmless Treatment Rate.

3 Data Envelopment Analysis method

An effective method utilized to assess the performance of Sfax's municipalities is DEA. It is proposed byCharnes et *al*. [5] in 1978. Employing a non-parametric approach, DEA evaluates the efficiency and productivity of entities known as decision-making units (DMUs) [10].DEA finds application in a wide array of settings, encompassing financial institutions, hospitals, the US Air Force, airports, schools, rates departments, and courts, among others [1].The relative efficiency of homogenous decision-making units (DMUs) is evaluated using DEA. In this context, inputs are the resources that a DMU uses, and outputs are the products the DMU produces or measures in terms of performance [2]. The efficiency score when dealing with multiple inputs and outputs is determined by calculating the weighted sum of outputs divided by the weighted sum of inputs [4]. DEA employs two fundamental models, resulting in the identification of two distinct efficiency frontiers. The first one is known as the Charnes, Cooper, and Rhodes (CCR) model [5] and the second model is referred to Banker, Charnes, and Cooper (BCC) model under both Constant Returns to Scale (CRS) assumption and Variable Returns to Scale (VRS) assumption, respectively[3]. Model orientation can be whether input or output orientation. The selection depends on whether the goal is to minimize inputs or maximize outputs.DEA's strength lies in its ability to handle multiple inputs and outputs when evaluating the relative efficiencies of a groupof homogeneous DMUs [12].

4 Case study

The DEA method is applied to assess the efficiency of MSW management in Sfax City.Sfax, situated in the Republic of Tunisia in North Africa, is the second-largest city in the country. Notably, it faces environmental challenges due to pollution levels. In 2019, the population of Sfax was approximately 1,007,592 inhabitants, leading to the production of 233,982 tons of municipal solid waste during that year, which is equivalent to 0.1795 kg per person per day. Sfax City is composed of a total of 23 municipalities presented in Figure1.

Figure1: Sfax Municipalities

Our objective is to assess the performance of Sfax municipalities, examine their efficiencies, and pinpoint the origins of inefficiencies in both inputs and outputs for each municipality. By identifying benchmark members of the efficient set, we can conduct a comprehensive evaluation and discern the specific sources of inefficiency in the process. So, the most appropriate tool to deal with our objective is DEA. First, inputs and outputs must be determined. The first input selected is the number of working hours in order to enhance work-life balance and prioritize employee well-being. By carefully selecting and managing this aspect, we aim to create an environment that fosters a harmonious integration of work and personal life, leading to increased job satisfaction and overall contentment among employees.As part of our strategy to achieve economic sustainability and cost reduction, the second input chosen pertains to the quantity of fuel. By optimizing fuel consumption, we aim to minimize expenses and improve the overall financial efficiency of the operations, ensuring a sustainable and economically viable approach. The output selected was the quantity of waste collected. By effectively managing waste disposal, we aim to curb pollution and mitigate the impact on the environment. This environmentally responsible approach aligns with our commitment to fostering a greener and cleaner future for our municipalities.This metric is widely employed as the primary means of assessing the effectiveness of waste-collecting operations [7]. Next, the model as well as the orientation must be fixed. We have opted for a Variable Returns to Scale (VRS) model with an input orientation since we have to minimize inputs for a fixed quantityof output.

5 Results and interpretations

As previously stated, a Variable Returns to Scale (VRS) model with an input orientation is chosen for the analysis.The efficiency of all municipalities is evaluated using the DEA method, utilizing the DEAP Software as the primary tool for conducting the analysis.The software gives efficiency details for each municipality, empowering local governments to make data-driven decisions and optimize resource allocation for better service delivery and citizen satisfaction.

The first example of a benchmark unit is shown in Figure 2. This benchmark unit serves as a valuable foundation for assessing and improving the overall efficiencyof similar entities.

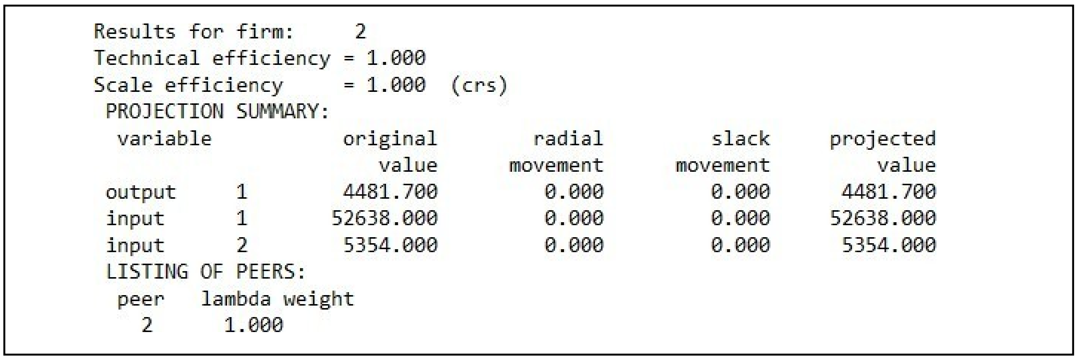

```
Results for firm:     2
Technical efficiency = 1.000
Scale efficiency     = 1.000  (crs)
 PROJECTION SUMMARY:
  variable           original        radial         slack     projected
                        value      movement      movement         value
 output     1        4481.700         0.000         0.000      4481.700
 input      1       52638.000         0.000         0.000     52638.000
 input      2        5354.000         0.000         0.000      5354.000
 LISTING OF PEERS:
  peer   lambda weight
    2      1.000
```

Figure2: Municipality2 EfficiencyResults

Figure 2 shows that municipality 2 isa benchmark; ithas a technical efficiency and a scale efficiency of 100%.The remarkable feat of achieving 100% in both these aspects makes it a shining example for other municipalities to aspire to.

Asecond result example is presented in Figure 3.

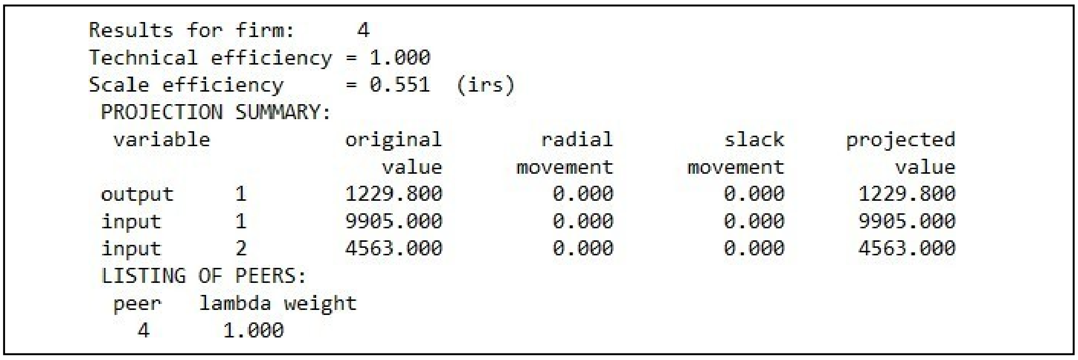

```
Results for firm:     4
Technical efficiency = 1.000
Scale efficiency     = 0.551  (irs)
 PROJECTION SUMMARY:
  variable           original        radial         slack     projected
                        value      movement      movement         value
 output     1        1229.800         0.000         0.000      1229.800
 input      1        9905.000         0.000         0.000      9905.000
 input      2        4563.000         0.000         0.000      4563.000
 LISTING OF PEERS:
  peer   lambda weight
    4      1.000
```

Figure3: Municipality4 EfficiencyResults

Municipality 4 currently exhibits a technical efficiency of 100%, indicating optimal performance and effective resource management and operational practices. However, there is room for improvement by adjusting its size, which has the potential to lead to significant input savings. If properly optimized, it could potentially reduce inputs by 44.9% (100% - 55.1%), further enhancing its overall efficiency.

A third example concerning municipality5 is presented in Figure 4.

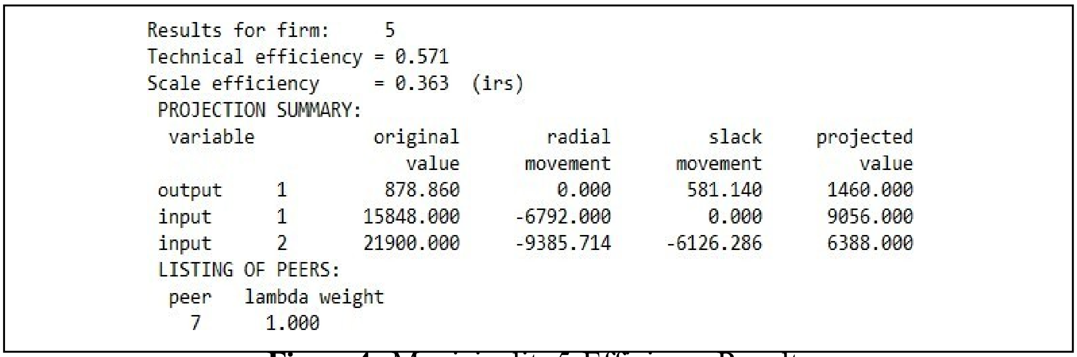

```
Results for firm:     5
Technical efficiency = 0.571
Scale efficiency     = 0.363  (irs)
 PROJECTION SUMMARY:
  variable          original       radial        slack     projected
                       value     movement     movement         value
 output     1        878.860        0.000      581.140      1460.000
 input      1      15848.000    -6792.000        0.000      9056.000
 input      2      21900.000    -9385.714    -6126.286      6388.000
 LISTING OF PEERS:
  peer   lambda weight
    7      1.000
```

Figure4: Municipality5 EfficiencyResults

According to Figure 3, municipality 5 demonstrates a technical efficiency of 0.571 and a scale efficiency of 0.363. This indicates that it has the potential to save 42.9% (100% - 57.1%) of inputs through management improvements and 63.7% (100% - 36.3%)by minimizing its size. To enhance its efficiency, municipality 5 can seek guidance from municipality 7, which serves as a benchmark for comparison. The reduced input quantities required by municipality 5, in contrast to the original values, are presented in the last column.As an example, the initial value of "input1" was 15,848, and for "input2," it was 21,900. However, after projecting, the values for "input1" and "input2" became 9,056 and 6,388, respectively.

6 Conclusion:

This study aimed to assess the efficiency of MSW collection in all 23 municipalities of Sfax City using the DEA method. The analysis enabled the identification of efficiency and inefficiency sources, offering valuable managerial insights. For inefficient municipalities, peers were identified, and revised input quantities were determined. As a part of future work, we plan to extend this evaluation to assess the efficiency of municipalities in other cities across Tunisia.

References:

[1] N. K Avkiran. “Productivity analysis in the service sector with data envelopment analysis”. In: *Available at SSRN 2627576* (2006).

[2] H. Bal, H H. Örkcü, and S. Çelebioğlu. “Improving the discrimination power and weights dispersion in the data envelopment analysis”. In: *Computers & operations research* 37.1 (2010), pp. 99–107.

[3] Banker, R. D., Charnes, A., and Cooper, W. W. “Some models for estimating technical and scale inefficiencies in data envelopment analysis”. *Management science30* (1984), 1078–1092.

[4] D. S. Chang et al. “A novel approach for evaluating the risk of health care failure modes”. In: *Journal of medical systems* 36 (2012), pp. 3967–3974.

[5] Charnes, A., Cooper, W. W., and Rhodes, E. Measuring the efficiency of decision-making units. *European journal of operational research* 2 (1978), 429–444.

[6] S. De Jaeger et al. “Wasteful waste-reducing policies? The impact of waste reduction policy instruments on collection and processing costs of municipal solid waste”. In: *Waste Management* 31.7 (2011), pp. 1429–1440.

[7] Garc´ıa-Sanchez, I. M. “The performance of spanish solid waste collection”. *Waste Management &Research* 26 (2008), 327–336.

[8] C. Lo Storto. “Evaluating technical efficiency of Italian major municipalities: a Data Envelopment Analysis model”. In: *Procedia-Social and Behavioral Sciences* 81 (2013), pp. 346–350.

[9] Menikpura, S. N. M., et al. “Evaluation of the effect of recycling on sustainability of municipal solid waste management in Thailand”. *Waste and Biomass Valorization* 4 (2013): 237-257.

[10] H. Najadat, Q. Althebyan, and Y. Al-Omary. “Higher Education Units Assessment Based on Data Envelopment Analysis and Clustering Techniques”. In: *2019 International Arab Conference on Information Technology (ACIT).* IEEE. 2019, pp. 171–17.

[11] . Rogge and S. De Jaeger. “Evaluating the efficiency of municipalities in collecting and processing municipal solid waste: A shared input DEA-model”. In: *Waste management* 32.10 (2012), pp. 1968–1978.

[12] P. Rouse. “Data envelopment analysis in the public sector”. In: *Socio-economic planning sciences* 48 (2014), 2e3.

[13] IM G. Sánchez. “Efficiency of solid waste collection in Spain”. In: WIT *Transactions on Ecology and the Environment* 92 (2006).

[14] A. Sarra, M. Mazzocchitti, and A. Rapposelli. “Evaluating joint environmental and cost performance in municipal waste management systems through data envelopment analysis: Scale effects and policy implications”. In: *Ecological Indicators* 73 (2017), pp. 756–771.

[15] P. Simões, P. Carvalho, and R. C. Marques. “Performance assessment of refuse collection services using robust efficiency measures”. In: *Resources, Conservation and Recycling* 67 (2012), pp. 56–66.

[16] M. Struk et al. “The application of two-stage data envelopment analysis on municipal solid waste management in the Czech Republic”. 2016.

[17] Q. Yang et al. “Evaluating the efficiency of municipal solid waste management in China”. In: *International journal of environmental research and public health* 15.11 (2018), p. 2448.

Effect of Surfactants on double diffusive natural convection of CNT water-based micropolar nanofluids

Awatef Abidi[a,b,c], , NessrinManaa[b], Patrice Estellé[d], Mohammed NaceurBorjini[b]

[a] *Physics Department, College of Sciences Abha , King Khalid University, Saudi Arabia.*
[b] *Research Laboratory of Metrology and Energy Systems, National Engineering School, Energy Engineering Department, Monastir University , Monastir City, Tunisia.*
[d]*Higher school of Scienecs and Technology of Hammam Sousse, Sousse University, Tunisia.*
[d]*Univ Rennes, LGCGM, F-35000, Rennes, France.*
Email1 : abidiawatef@yahoo.fr
Email 2 : manaa_nessrin@outlook.com
Email3 : patrice.estelle@univ-rennes1.fr
Email 4 : borjinimn@yahoo.com

Abstract :**The present study deals withthe influence of surfactants which are one of the most important factors affecting the process of energy transport during the preparation ofnanofluids. In fact, these additives modify the transport properties of nanofluids such as viscosity and thermal conductivity. This highlights the modeling and study of the impact of surfactant on heat and mass transfer rates in a cubic cavity containing a micropolar nanofluid. The objective of this work is therefore to perform an analysis of the three-dimensional natural convection with double diffusion in the multi-walled CNT/water micropolar nanofluid stabilized with two types of surfactants “lignin” and “sodium polycarboxylate”. We have discussed the effects of surfactants used to stabilize the micropolar nanofluid, the microrotation parameter, the nanoparticle volume fraction, the buoyancy ratio, and the Rayleigh number on heat and mass transfer rates and flow behavior.**

I. INTRODUCTION

Utilizing nanofluid is one of the new methods for conservation energy during natural convection. These fluids are manufactured by the dispersion of nanoparticles in conventional heat transfer fluids.It exists many types of nanoparticles used in nanofluids that differ in nature, such as metallic (Al, Cu, Ag...), oxide (Al_2O_3, TiO_2, CuO…) and carbon-based materials.

Putra et al. [1] investigated experimentally the natural convection of nanofluid in a horizontal cylinder filled with two types of nanoparticles CuO and Al_2O_3. They obtained a decrease in heat transfer rate with the enhancement in nanoparticles’ concentrations. Khanafer et al. [2] carried out a numerical investigation on natural convection with Cu nanofluid and noticed heat transfer increase with an increase in nanoparticles’ volume fraction. Enhancement in heat transfer was shown to be more efficient with nanofluid than with pure fluid. Abu Nada et al. [3] carried out numerical investigations considering different nanofluids based on Al_2O_3, TiO_2, Cu and Ag, in horizontal annuli. They reported the dependence of heat transfer performance following the type of nanofluid used.

Among all nanoparticles available for producing nanofluids, carbon nanotubes (CNT) are more recommending than other traditional nanoparticles because of their relatively low density and very high thermal conductivity.Wen and Ding [4] studied the effective thermal conductivity of aqueous suspensions of MWCNTs.They used the sodium polycarboxylate as surfactant to stabilize the nanofluids. They obtained an enhancement of thermal conductivity when the nanoparticles volume concentrationincreases, and the dependence was nonlinear even at very low concentrations. They founded

ISSN: 1737-933465

that an enhancement in temperature increases the effective thermal conductivity of nanofluid. A study of the effect of lignin as surfactant on viscosity and thermal conductivity of CNT/water-based nanofluids was investigated by Estellé et al. [5]. They compared the effect of lignin on the viscosity and thermal conductivity of CNT/water nanofluid with the effect of sodium polycarboxylate. They noticed that the thermal conductivity of nanofluid increase with the nanoparticles volume concentration. Estellé et al. [6] investigated theoreticallythe natural convection in a square cavity partially heated filled with CNT water-based nanofluids. They analyzed the effect of the average temperature and the nanoparticles volume fraction, driving temperature between hot and cold walls and role of surfactant. They founded that the Nusselt number of nanofluids is decreased with the increase of the volume fraction of nanofluid, which is related to non-Newtonian behavior of nanofluids.

The theory of Enrigen [7] can be used to elucidate fluid particles' micro-motions which cannot be explained by the classical models. In fact, physically, fluid particles may expand, contract, rotate about their own axis or may even change their shape due to the shear stress applied on them. So, the micropolar fluid theory can be valuable to explore fluid behavior of polymer fluids, solidification of liquid crystals, cooling of a metallic plate in a bath, exotic lubricants, colloidal systems, and biological fluids, for which the theory of Navier–Stokes is inadequate to describe the impacts of the microstructures on fluid motion.

The rotating micro-constituents 'effects in nanofluids should be judiciously exploited to understand the behavior of fluid flow effectively. Abidi et al. [8] carried out the 3D numerical simulation of both heat and mass transfer rates and fluid flow in a cubic cavity filled with an Al_2O_3/water micropolar fluid. The simulations are conducted under a uniform magnetic field. The results reveal that heat and mass transfer rates and three-dimensional characters of the flow are weaker when the micropolar nanofluid model was used compared to the pure nanofluid model. Manaa et al. [9] investigated the thermo-solutal natural convection of a micropolar nanofluid filled 3D enclosure with different types of nanoparticles (Al_2O_3, TiO_2, Cu and Ag) considering the effect of relevant parameters on heat and mass transfer characteristics. They obtained that both heat and mass transfer rates and the three-dimensional character of the flow for the micropolar nanofluid model are smaller compared with that of a pure nanofluid model. Their results show that the rates of heat and mass transfer decrease with an enhancement in micropolar parameter as well as nanoparticlesvolume fractions.The main aim of thisworkis to perform a computation analysis on the three-dimensional double-diffusive natural convection in multi-walled CNT/water micropolar nanofluid stabilized with two types of surfactants lignin and sodium polycarboxylate. In this work, experimental thermophysical properties determined in previous works were used. The effect of the type of used surfactant to stabilize the micropolar nanofluid, micropolar parameter, nanoparticles' volume fraction, buoyancy ratio, and the Rayleigh number on heat and mass transfer rates and flow behavior are meticulously elucidated.

II. MATHEMATICAL MODELING

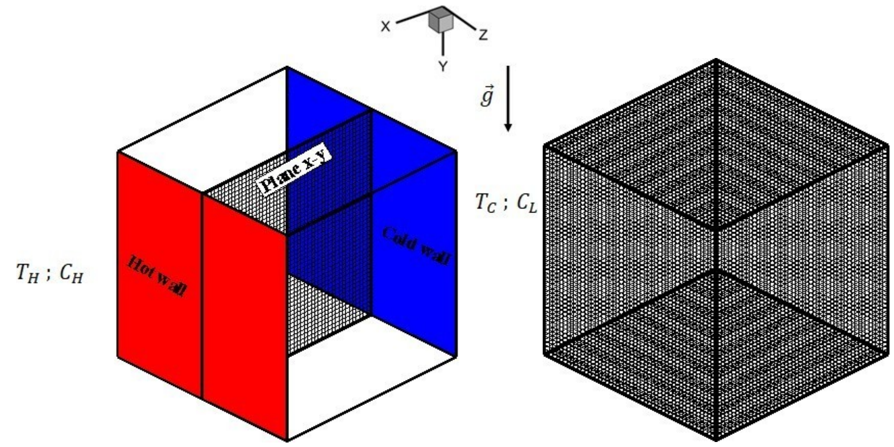

(a) (b)

Fig.1 (a) Schematic of theconsidered problem, **(b)** Mesh surfaces

A simple schematic view of the thermo-solutal natural convection problem under study is described inFig. 1. The cube is filled with multi-walled CNT water-based micropolar nanofluid stabilized with two types of surfactants lignin and sodium polycarboxylate respectively. The two vertical walls parallel to the plane (y-z) are subject to constant temperatures ($T_H>T_C$) and constant concentrations ($C_H>C_L$). The other walls are supposed to be impermeable and adiabatic. The dynamic and thermal slips between nanoparticles and the base fluid are negligible. During the process of the natural convection, all the properties of the base fluid and nanoparticles are unchangeable except the density in the buoyancy term in momentum equation, its variations being modeled using Boussinesq approximation. The effects of Soret and Dufour are assumed to be negligible.

The vorticity–vector potential formulation is used in the present study to eliminate the pressure term and makes easier the numerical treatment. The vorticity and vector potential are respectively defined by the following two relations: $\vec{U} = \nabla\times\vec{\psi}$ and $\vec{\omega} = \nabla\times\vec{U}$.

The system of governing equationsof the phenomenonis:

$$\nabla^2\vec{\psi} = -\vec{\omega} \tag{7}$$

$$\frac{\partial\vec{\omega}}{\partial t} + (\vec{U}.\nabla)\vec{\omega} - (\vec{\omega}.\nabla)\vec{U} = Pr\left(\frac{\mu_{nf}}{\mu_f}+K\right)\left(\frac{\rho_f}{\rho_{nf}}\right)\nabla^2\vec{\omega} - PrK\left(\frac{\rho_f}{\rho_{nf}}\right)\nabla^2\vec{H} + RaPr\left(\frac{(\rho\beta_T)_{nf}}{(\rho\beta_T)_f}\right)\left(\frac{\rho_f}{\rho_{nf}}\right)\left(\left[\frac{\partial T}{\partial z},0,-\frac{\partial T}{\partial x}\right] - N\left[\frac{\partial C}{\partial z},0,-\frac{\partial C}{\partial x}\right]\right) \tag{8}$$

$$\left(\frac{\partial\vec{H}}{\partial t} + (\vec{U}.\nabla)\vec{H}\right) = Pr\left(\frac{\mu_{nf}}{\mu_f}+\frac{K}{2}\right)\left(\frac{\rho_f}{\rho_{nf}}\right)\nabla^2\vec{H} + PrK\left(\frac{\rho_f}{\rho_{nf}}\right)(\vec{\omega} - 2\vec{H}) \tag{9}$$

$$\frac{\partial T}{\partial t} + (\vec{U}.\nabla)T = \left(\frac{(\rho C_P)_f}{(\rho C_P)_{nf}}\right)\left(\frac{k_{nf}}{k_f}\right)\nabla^2 T \tag{10}$$

$$\frac{\partial C}{\partial t} + (\vec{U}.\nabla)C = \frac{1}{Le}\left(\frac{(\rho C_P)_{nf}}{(\rho C_P)_f}\right)\left(\frac{k_f}{k_{nf}}\right)\nabla^2 C \tag{11}$$

The local Nusselt and Sherwood numbers on the isothermal walls are defined by:

$$Nu = \left.\frac{k_{nf}\frac{\partial T^F}{\partial x^F}}{k_f\frac{T^F_H - T^F_C}{L}}\right)_{x^F=0,1} = -\left.\frac{k_{nf}}{k_f}\frac{\partial T}{\partial x}\right)_{x=0,1} \tag{12}$$

$$Sh = \left.\frac{D\frac{\partial C^F}{\partial x^F}}{D\frac{C^F_H - C^F_L}{L}}\right)_{x^F=0,1} = \left.\frac{\partial C}{\partial x}\right)_{x=0,1} \tag{13}$$

The average Nusselt and Sherwoood numbers, on the isothermal walls of the enclosure are defined as follows:

$$\overline{Nu} = \int_0^1\int_0^1 Nu\,dy\,dz \tag{14}$$

$$\overline{Sh} = \int_0^1\int_0^1 Sh\,dy\,dz \tag{15}$$

For each time step, the following convergence criterionissatisfied:

$$\sum_{1,2,3} \frac{\max|\psi^n - \psi^{n+1}|}{\max|\psi^n|} + \max|T^n - T^{n+1}| + \max|C^n - C^{n+1}| \leq 10^{-5} \tag{16}$$

III. RESULTS AND DISCUSSION:

For comparison purpose with nanofluids, water which is the base fluid of nanofluids was takenas a reference. Thethermo-physical properties of water used for the simulations are reported in [1].

In this study, it is considered carbon nanotubes with density of 1800 kg m^{-3} and purity of 90% and 9.2 nm and 1.5 µm in average diameter and length, respectively, dispersed in a mixture of water and surfactant. To improve the dispersion and stability of multi-walled CNT within water and to reduce clogging and the sedimentation with time, it was used two types of surfactants lignin and sodium polycarboxylate. The preparation of nanofluid was reported in [5, 6, 11]. The volume fraction of carbon nanotubes under consideration ranges from 0.0055 to 0.557%. Density, thermal conductivity, viscosity at 20°C were experimentally determined in [5, 6, 11] from well-designed procedures while heat capacity was theoretically determined neglecting heat capacity of surfactants. All these results are shown in Fig. 2and used in the present numerical simulations.

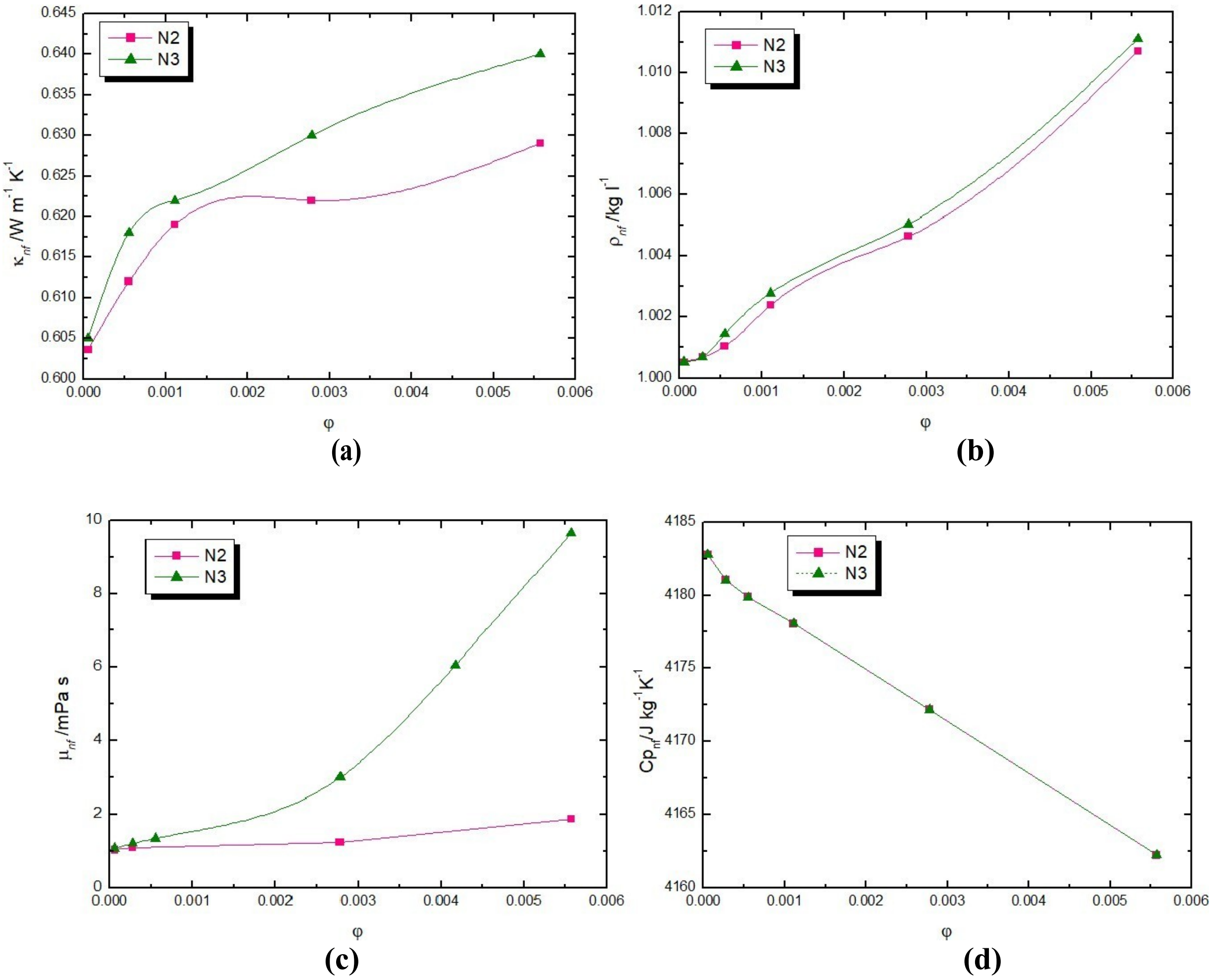

(a) (b)

(c) (d)

Fig. 2 Thermophysical properties of CNT nanofluids at 20°C with two types of surfactants: **(a)** thermal conductivity, **(b)** density, **(c)** dynamic viscosity and **(d)** heat capacity

Figure 3shows the variations of maximum transverse velocity with the nanoparticle's volume fraction for micropolar/non-micropolar nanofluid stabilized with Lignin (N2) and sodium polycarboxylate (N3). Thus, the effects of nanoparticles' volume fraction on the three-dimensional flow are explored. This figure shows, irrespective of the model used,that the maximum transverse velocity is improved by increasing φ to the critical value then the velocity tends to decrease. Also, it is clearly noted that N2 have higher transverse velocity compared to N3. For example, for φ=0.0055% it exists a 27.63 % difference between the two cases. In addition, it isinteresting to note that the non-micropolar nanofluid ($K=0$) has the highest maximum transverse velocity compared to the micropolar nanofluids ($K\neq0$) for all the considered values of nanoparticles volume fraction.

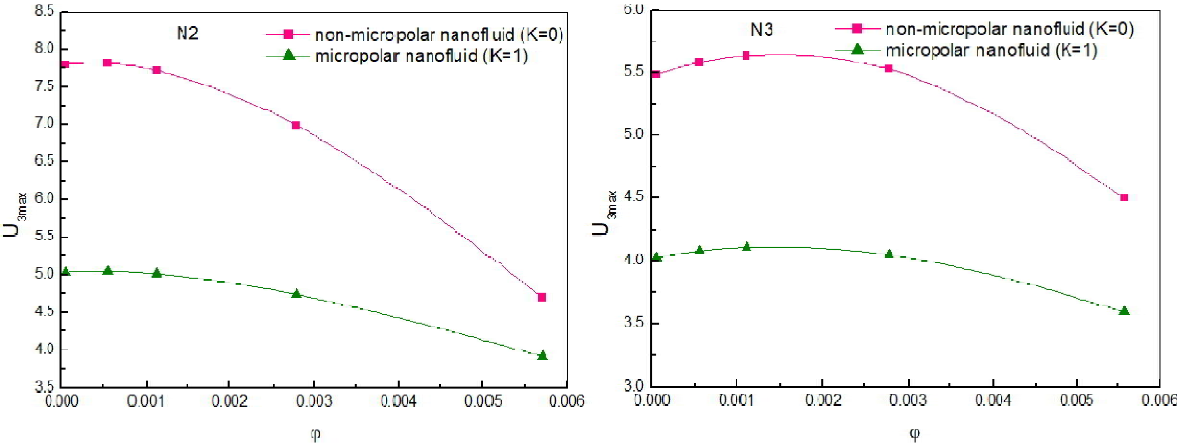

Fig. 3: Variation of maximum of transversal velocity U_{3max} according to the nanoparticles volume fraction for N2 and N3 micropolar/non-micropolar nanofluid for $Ra=10^5$ and $N=-0.2$.

Figure 4 shows the variations of average Nusselt number $\overline{Nu}$ and Sherwood number $\overline{Sh}$ with nanoparticles' volume fraction for micropolar/non-micropolar nanofluid stabilized with Lignin (N2) and sodium polycarboxylate (N3). Irrespective to the considered type of nanofluids, $\overline{Nu}$ and $\overline{Sh}$ are lower when the micropolar nanofluid model is under consideration, and are increased when the non-micropolar fluid model is under consideration irrespective of the values of nanoparticles volume fraction. It is noticed that for the two types of surfactants used, the average Nusselt and Sherwood numbers increase in the area where the value of the volume fraction of nanoparticles is less than its critical value. This is because the thermal performance of water solution is improved by the addition of nanoparticles. Afterwards, the heat and mass transfer rates decrease in the area where the value of the nanoparticles volume fraction is greater than its critical value due to the predominant influence of viscosity over thermal properties. It can be seen also from Fig.3, for the case where the surfactant lignin is used, the average Nusselt and Sherwood numbers are greater than in the case of the surfactant sodiumpolycarboxylate is employed.

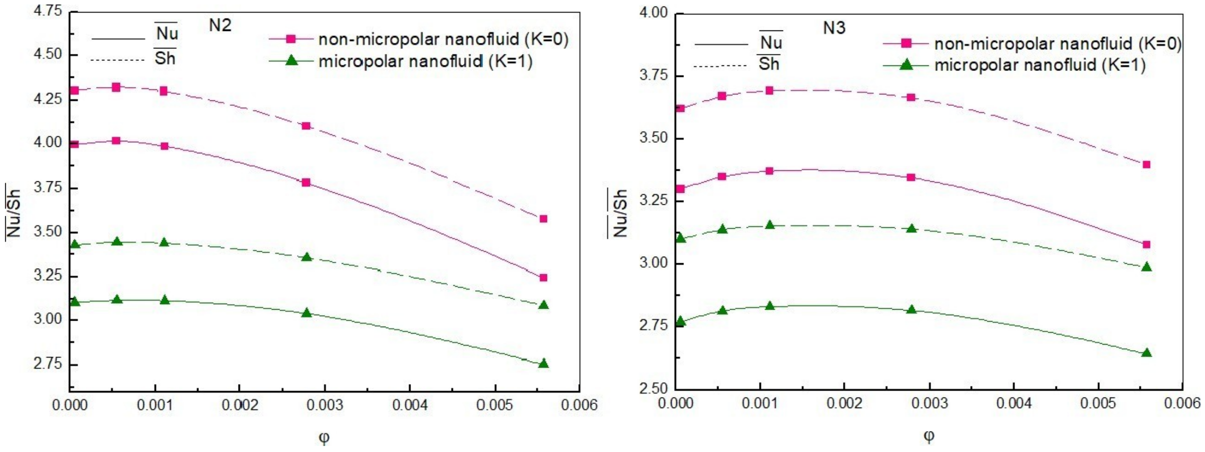

Fig. 4: Variation of $\overline{Nu}$ and $\overline{Sh}$ on the hot wall with nanoparticles volume fraction for both micropolar and non-micropolar N2/N3 nanofluid models for $Ra=10^5$ and $N=-0.2$.

IV. CONCLUSION:

It is observed that the heat and mass transfer rates are lower for a micropolar nanofluid model when compared to the pure nanofluid model. In fact, the enhancement of micropolar parameter results a decrease of average Nusselt and Sherwood numbers. The use of lignin as a surfactant ameliorates heat and mass transfer rate and nanofluid flow better than the use of sodium polycarboxylate as a surfactant. The nanoparticles volume fraction can be used as a control element for heat rate and fluid flow. Thus, for a nanoparticles volume concentration less than the critical value, the flow intensity is ameliorated and is deteriorated when it exceeds this value.

REFERENCES :

[1] Putra N, Roetzel W, Das SK. Natural convection of nano-fluids.Heat Mass Transf. 2002; 39:775-784.

[2] Khanafer K, Vafai K, Lightstone M. Buoyancy-driven heat transfer enhancement in a two-dimensional enclosure utilizing nanofluids. Int J Heat Mass Trans. 2003; 46: 3639–3653.

[3] Abu-Nada E, Masoud Z, Hijazi A. Natural convection heat transfer enhancement in horizontal concentric annuli using nanofluids. IntComm Heat Mass Transf. 2008; 35: 657–665.

[4] Wen D, Ding Y. Effective thermal conductivity of aqueous suspensions of carbon nanotubes (carbon nanotube nanofluids). J Thermal Heat Transf. 2004; 18: 481-485.

[5] Estellé P, Halelfadl S, Maré T. Lignin as dispersant for water-based carbon nanotubes nanofluids:Impact on viscosityand thermal conductivity. Int Com Heat Mass Transf. 2014; 57: 8-12.

[6] Estellé P, Mahian O, Maré T, Öztop HF. Natural convection of CNT water-based nanofluids in a differentially heated square cavity. J Thermal Anal Calorim. 2017; 28: 1765–1770.

[7] Eringen AC. Theoryof micropolar fluids, J MathMech. 1966; 16: 1–18.

[8] Abidi A, Raizah Z, Madiouli J. Magnetic Field Effect on the Double Diffusive Natural Convection in Three-Dimensional CavityFilled with Micropolar Nanofluid. App Sci. 2018; 8: 2342–2367.

Manaa N, Abidi A, Saleel CA, Al Makwash SM, Borjini MN. On Simulation of Double-Diffusive Natural Convection in a Micropolar Nanofluid Filled Cubic Cavity. Heat Transf Eng. 2020;https://doi.org/10.1080/01457632.2020.1756074.

[9] Therme-Excel: Physical characteristics of water at the atmospheric pressure. Last update: 2003.http://www.thermexcel.com/english/tables/eau_atm.htm.

[10] Estellé P, Halelfadl S, Maré T. Thermal conductivity of CNT water based nanofluids: Experimental trends and models overview. J Thermal Eng. 2015; 1: 381-390

Vortex characteristics of two rotating immiscible fluids

Kenza Brahma*[1], Rachid Saci[2], Kacem Mansouri[3]
*[1]*Mechanical Engineering Department, Energy and Mechanical Engineering Laboratory, Boumerdes University*
Frantz fanon City, Boumerdes, Algeria
[2]*Physics Department, Boumerdes University*
[3]*Mechanical Engineering Department, Boumerdes University*

*k.brahma@univ-boumerdes.dz
r.saci@univ-boumerdes.dz
manskac@yahoo.fr

Abstract

Hydrodynamic and behavior of laminar confined axisymmetric flows driven by the rotating top disk in cylindrical cavity have been studied numerically. The vertical cavity, is filled with two superposed immiscible incompressible fluids. The top more viscous liquid drives the lower heavier fluid via the interface shear. The study, identified and highlighted a flow topology of types of axisymmetric recirculation regions; depending upon the effects of the disk rotation rate. This work confirms partly previous experimental observations and provides additional quantitative findings; particularly in the vicinity of the interface. The findings are in good accord with the experiments and show that vortex size increases with increasing rotation rate. The basic flow is made up of two clockwise circulation cells, separated by a thin layer of anticlockwise circulation (TCL). The gap thickness of TCL decreases with increasing rotation rate however, the interface high increases as rotation rate increases

Introduction:

The vortex breakdown phenomenon may be observed in several industrial applications involving rotating fluid flows (bioreactors, hydro-cyclones, chemical reactors etc) as well as in the natural environment (atmospheric vortices, hurricanes, tornadoes etc). The physical mechanisms of this structure are still not fully highlighted; which motivated numerous attempts to develop strategies to control the conditions of its onset and development [1], [2], [3]. Unlike the case of a single fluid configuration, relatively few studies were devoted to the conditions of occurrence and development of the vortex breakdown within two a layer of two immiscible rotating fluids [4], [5]. In this context, the present work explores numerically means of controlling the vortex pattern which develops in a vertical cylinder under differential rotation of its boundaries.

Physical problem:

A schematic description of confined axisymmetric flow considered in the present work is reported in Fig. 1. The physical problem consists of a cylindrical cavity filled with “glycerin-water mixture”of density $\rho_g = 1208\ kg/m^3$ and kinematic viscosity$u_g = 42.82 \times 10^{-6} m^2/s$ till h_g. The sunflower oil is of density$\rho_o = 920\ kg/m^3$ and viscosity $u_o = 54.86 \times 10^{-6} m^2/s$ The surface tension at theinterface is σ = 0.0315 N/m [5].The radius of the cylindrical cavity is 0.045m while the height is 0.1125m.The aspect ratio ofthe cylinder is fixed at Ah=H/R=2.5.

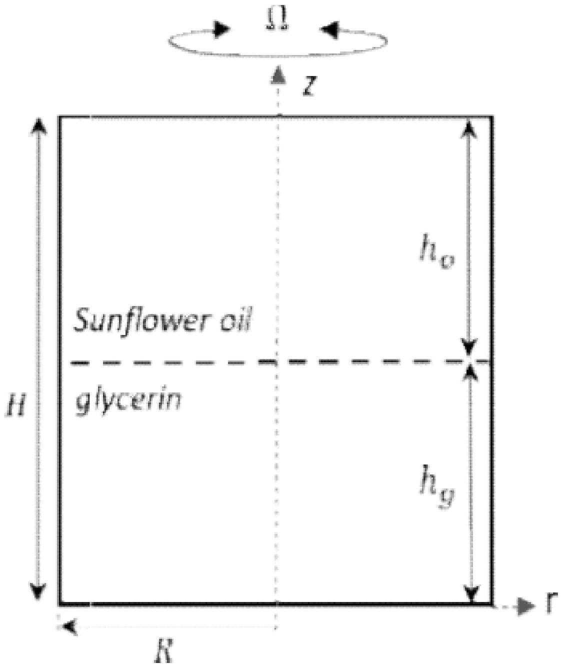

Fig. 1Schematic ofthe model flows under consideration

The flow is driven by the top part with constant angular velocity Ω. Thenon-dimensional numbers which govern the problem is Reynolds number $Re = \Omega R^2/\nu_o$Here, subscripts "o" and "g" denote oil and glycerin respectively.

Results:

The induced flow topology is mainly presented in terms of streamlines and circulation zones for Reynolds number Re = 900 (Fig.2 (a)). In order to confirm the numerical method, our results were partly validated by comparing the mean axial velocity distribution against experimental measurement (Fig.2 (b)).

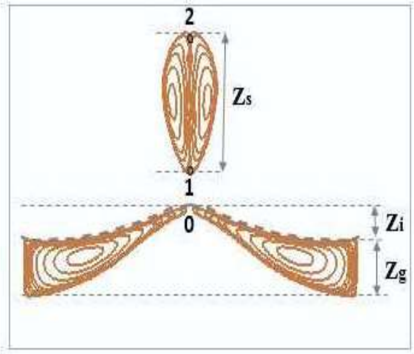

(a)

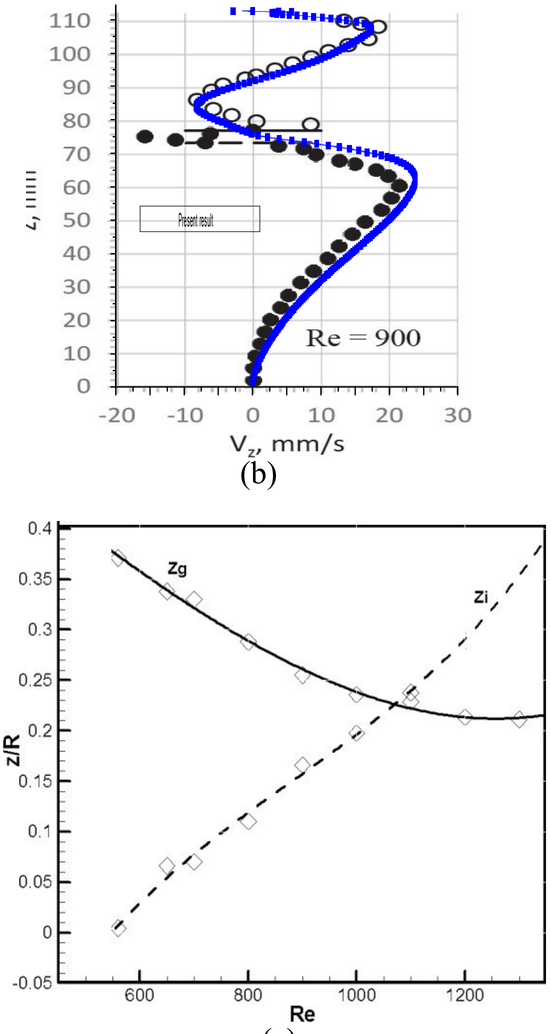

(b)

(c)

Fig. 2(a) schematic of selected vortex and associated thin circulation layer characteristics, (b) comparison of the mean axial velocity with experiments (black and withe circles), (c) dependence of interface height and gap width on the rotation rate

The top more viscous liquid drives the lower heavier fluid viathe interface shear.The basic flow is made up of two clockwise circulationcells, separated by a thin layer of anticlockwise circulation (TCL) and Vortex Breakdown Bubble (VBB) occurs in the oil flow, as Re increases.

The vortex types and characteristics, are identified and analyzed. The gap thickness of TCLdecreases with increasing rotation rate however, the interface high increases as rotation rate increases (Fig.2 (b)).

The effect of Reynolds number on VVB size is also well illustrated in Fig.3which is in good accord of experimental finding of [5]

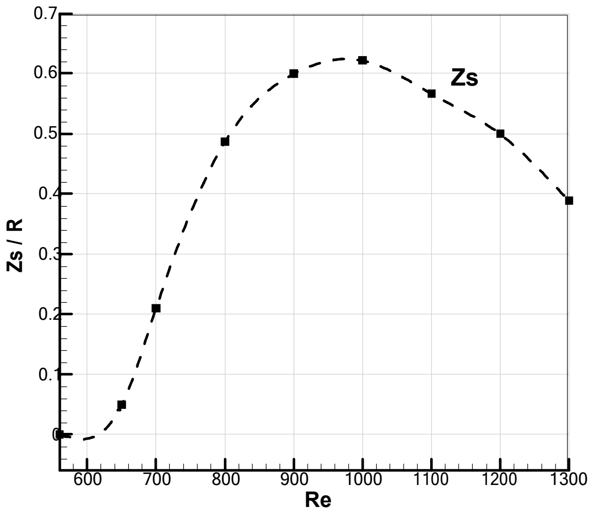

Fig. 3 Dependence of VBB size on Reynolds number

Conclusion:

The swirling axisymmetric laminar flow of two fluids has been numerically investigated.the TCL has been detectedby numerical simulations, because it has not been experimentally observed.This work compliments and confirm previous prediction of[5].

The study of vortex flows characteristics is relevant for both industrial and natural applications, in particular, this type of flow can provide efficient mixing in aerial vortex bioreactors for tissue growth in chemical applications.

References:

[1] Escudier, M. (1988). Vortex breakdown: observations and explanations. Progress in Aerospace Sciences, 25(2), 189-229.

[2] Fujimura, K., Yoshizawa, H., Iwatsu, R., Koyama, H. S., & Hyun, J. M. (2001). Velocity measurements of vortex breakdown in an enclosed cylinder. J. Fluids Eng., 123(3), 604-611.

[3] Fekhar, M., Rachid, S. A. C. I., & Gatignol, R. (2021). Swirling Flows Characteristics in a Cylinder Under Effect of Buoyancy. Mechanics, 27(3), 201-208.

[4] Naumov, I. V., Sharifullin, B. R., Tsoy, M. A., & Shtern, V. N. (2020). Dual vortex breakdown in a two-fluid confined flow. Physics of Fluids, 32(6), 061706.

[5] Naumov, I. V., Glavny, V. G., Sharifullin, B. R., & Shtern, V. N. (2019). Formation of a thin circulation layer in a two-fluid rotating flow. Physical Review Fluids, 4(5), 054702.

Recent Trends in Signal Processing

Tamrabet Chaima[#1], Hadjadj Aoul Elias[*2], Dekhmouche Med Tahar[#3]

[#] *Department of Electromechanical, Badji Moukhtar- Annaba, Algeria*

Email 1 - chaima.tamrabet@univ-annaba.org
Email 2 - Hadjadj.elias@yahoo.fr
Email 3 - dekhmouchemed@gmail.com

Abstract:

Using signal processing techniques for fault diagnosis of rotating machines become increasingly important. Advanced digital technology started to accelerate the theoretical signal processing techniques over academia. Despite this interest, no one to the best of our knowledge studied so deeply the possibility of making all of these innovations feasible on real or not. The aim of our work is the theory understanding and verification of basic signal processing techniques for practical problems such as bearings faults with the help of MATLAB. FFT, EMD, and HT are done in order to extract features from signals for fault detection and identification with the help of MATLAB code. These tests reveal that strong evidence of FFT is found on filtering signals based on the frequency information. EMD also reflected as a self-adaptive and an automatic filter. Finally, Hilbert transform extract time-frequencydomain features from the IMFs.

Keywords— signal processing, bearing diagnosis, fast fourier transform, empirical mode decomposition, Hilbert transform

Introduction:

In recent years, signal processing has many applications in the field of machine condition monitoring and diagnosis of typical rotating machine. Being one of the most fragile elements of rotating machinery, rolling bearings are a must-have.

In the literature, there are a surprising number of examples showing the application of signal processing for bearing fault detection. In particular, combining decomposition-based methods with traditional or artificial intelligence-based methods. Singh et al. have been proved that by adding white noise to EMD, the mode mixing problem can be removed and got a signal with effectively reduced noise [1]. Sher et al. conducted a satisfying hybrid signal processing approach for fault diagnosis of bearing using discrete wavelet transform (DWT), empirical mode decomposition (EMD), and One-way ANOVA and Kruskal Wallis in MATLAB for feature extraction and selection. DWT is used to split the raw vibration signal into certain frequency sub-bands, and EMD is used to decompose the selected frequency band into a number of intrinsic mode functions (IMFs) and a residue. Finally compared to SVM and ANN. The results were quite satisfying [2]. Another research that proved an effective approach for bearing monitoring, based on (EMD) and the Hilbert transform (HT). The proposed approach using EMD to extract the temporal components of oscillating vibration signals called intrinsic mode functions (IMFs). Combined with the HT, the EMD allows an estimate of the instantaneous frequency of each IMF. The Hilbert marginal spectrum density is then extracted as a health indicator in order to detect and diagnose the degradation of bearings. This approach was validated on two test benches with variable speeds and loads [3]. Weng et al. have been combining time-varying filtered empirical modal decomposition and the singular value decomposition (TVF-EMD-SVD) with deep belief neural network show that the fault identification of rolling bearing reaches more than 95 % [4]. C. Zhou et al. have been proposed a parameter-adaptive time-varying filtering empirical mode decomposition (TVF-EMD) feature extraction method based on the improved grasshopper optimization algorithm (IGOA), In order to separate the sub-signals and extract the feature frequency in the signal accurately. At last, the result was Compared with ensemble empirical mode decomposition (EEMD), variational mode decomposition (VMD), TVF-EMD-GOA have been achieved high performance [5]. Faysal et al. have been applied empirical mode decomposition (EMD) to the raw vibration signal. Intrinsic mode function (IMF) containing the characteristics of vibration data was analysed to obtain 90 statistical features. principal components analysis (PCA) and binary particle swarm optimiser (BPSO) were applied individually for feature reduction. The reduced feature subsets were 12 and 35 for PCA and BPSO, respectively. -NN was applied to the entire feature set and individually on the selected feature subset of PCA and BPSO. The reduced feature subset with PCA performed the finest in all the measurements taken [6].

After reviewing the literature, it can be concluded that there is always some error associated with the results when working with a single domain analysis. So, in this work, a hybrid of Empirical Mode Decomposition (EMD), Hilbert Transform (HT) and condition indicators (kurtosis, mean…) are used to collect and analyze features imbedded in the data provided by the case Western Reserve University Bearing Data Center Website (CWRU).

Signal processing techniques using MATLAB:

Methods and Results:

Signal processing techniques are widely used to improve the effectiveness of fault detection and identification approaches. Signal processing techniques extract the hidden properties of the signal using various analyses, such as time-domain analysis, frequency-domain analysis, and time–frequency analysis.[7, p. 5]

I. Data acquisition:

The case Western Reserve University Bearing Data Center Website:

https://engineering.case.edu/bearingdatacenter

II. Feature extraction:

✓ Time-domain:

a. Kurtosis:

Figure 1. representes signal processing in the time domain, no useful information about the state of the bearing.In order to quantify the infromation contained in the signal. The use of certain statistical indicator (RMS, mean, variance, kurtosis,…etc) could provide a precise information about the state.As mentioned in [3]. For bearing that operates in normal state, the value of kurtosis is close to 3 and increases dramatically as soon as pulses occur due to defect.

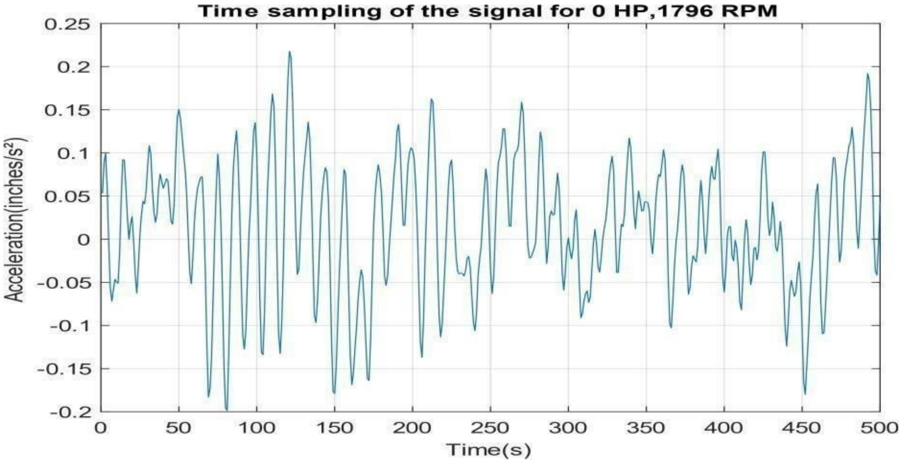

Figure1. Time sampling of healthy rolling bearing for 0 HP, 1796 RPM

Byusing MATLAB we get the following results:

- **a)** The Kurtosis value for healthy state (0HP, 1796 RPM) is: **2.7642**
- **b)** The Kurtosis value for abnormal state (inner race, fault depth 0.007, 0HP, 1796 RPM) is: **6.0272**
- **c)** The Kurtosis value for abnormal state (inner race, fault depth 0.021, 0HP, 1796 RPM) is: **4.1681**

The result indicates the existance of fault byusing the statistical quantitykurtosis.

b. Other condition indicators:

The following statistical indicators (min, max, mean, median, peak to peak, RMS) obtained by Signal Analyzer application on MATLAB, provide a precise information about the state. The value increases dramatically for each indicator due to the existence of defect.

Name	Line	ROI - Min	ROI - Max	Min - Value	Min - Time	Max - Value	Max - Time	Mean	Median	Peak to P...	RMS
X097_DE...	🟦	0	243937	-2.8664e-01	28964	3.1125e-01	49841	1.2558e-02	1.2517e-02	5.9789e-01	7.3764e-02

ISSN: 1737-933477

Name	Line	ROI - Min	ROI - Max	Min - Value	Min - Time	Max - Value	Max - Time	Mean	Median	Peak to P...	RMS
X213_DE...	🟥	0	244338	-3.0276e+00	147895	3.0750e+00	147848	1.1167e-02	9.3877e-03	6.1026e+00	5.8507e-01

✓ Frequency-domain: Fast Fourier Transform:

Table 1. Defect frequencies**:** (multiple of running speed **in Hz**). [8]

Inner Ring	Outer Ring	Cage Train	Rolling Element
5.4152	3.5848	0.39828	4.7135

For: F_r 0HP (1796 RPM) → $=\frac{1796}{60}$=**29.93 Hz**

BPFI=5.4152*F_r= 5.4152*29.93≈ **162.0769 Hz.**

2BPFI=324.15 Hz.

3BPFI=486.23 Hz.

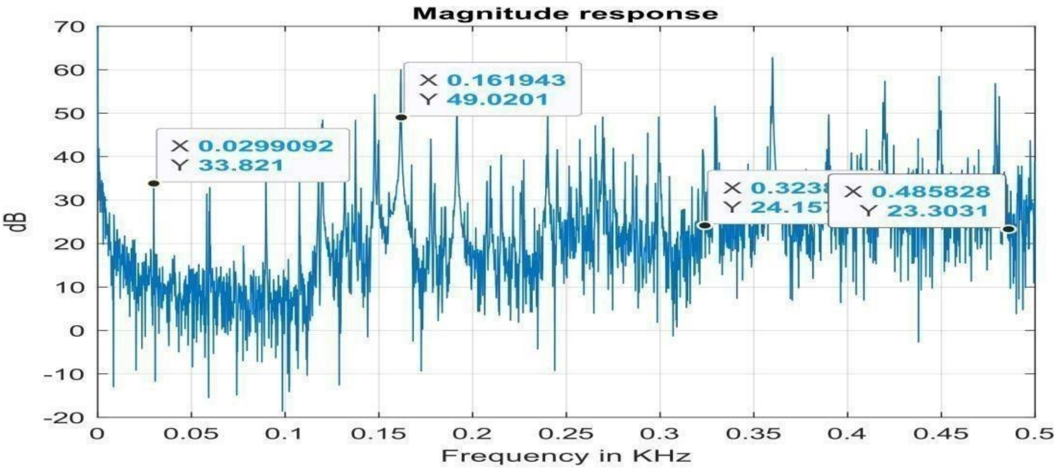

Figure2. Frequencysampling of healthyrolling bearing for 0 HP, 1796 RPM.

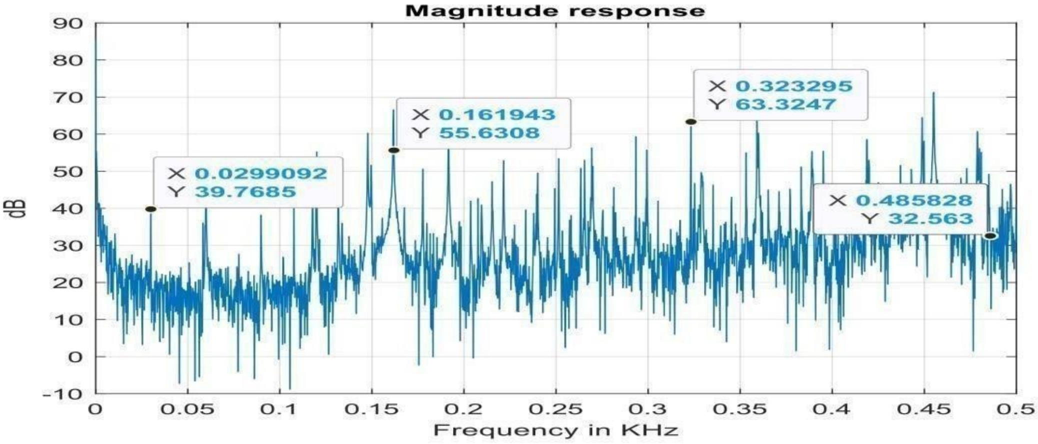

Figure3. Frequency sampling of faulty inner race for 0.007 in depth, 0 HP, 1796 RPM.

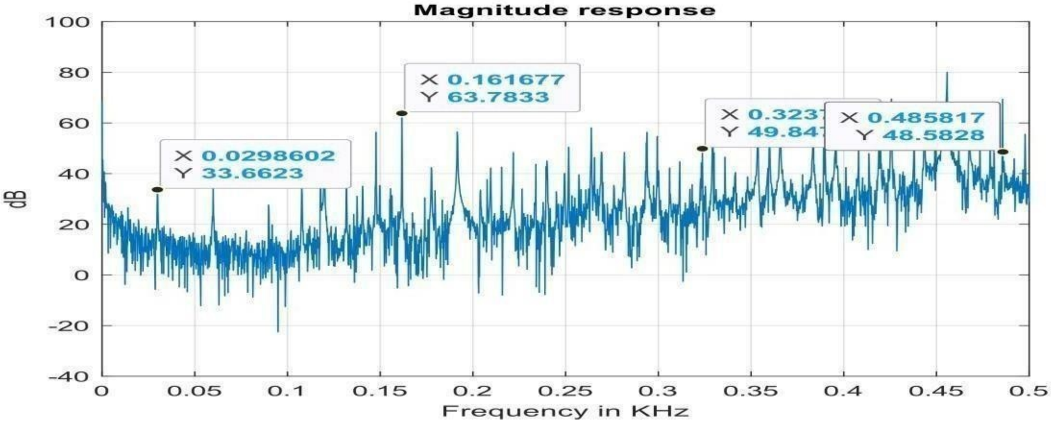

Figure 4. Frequency sampling of faulty inner race for 0.021 in depth, 0 HP, 1796 RPM.

We can notice from figures (figure 2-4), that the acceleration exceeded at the fault frequency characteristic for bearing with 0.021 in depth more than the bearing with 0.007. So, the existence of the fault effects the magnitude at the peak of inner fault frequency and its harmonics, 2BPFI, 3BPFI, …etc. In addition, there was no visible periodicity between the acceleration peaks giving an indication of its fault frequency. Which implies further analysis.

✓ Emperical Mode Decomposition for feature extraction:

As we mentioned before, our approach was based on filtering the vibration signals around the characteristic frequencies. Knowing that the signal of the bearing contains sinusoidal waves with different amplitude and frequency values. For such nonstationary signals, EMD approach is used by dividing the signal into intrinsic mode functions (IMF), that helps in finding crucial machine failure data for processing purposes. Sifting is the process of breaking down a signal into an IMF function. According to frequency, the EMD approach ranks the IMF from highest to lowest.

In order to determine the intrinsic mode functions (IMFs), we performed an empirical mode decomposition to the healthy and defective bearing signals using MATLAB. The table generated in the command window indicates the number of sifting iterations, the relative tolerance, and the sift stop criterion for each generated IMF.

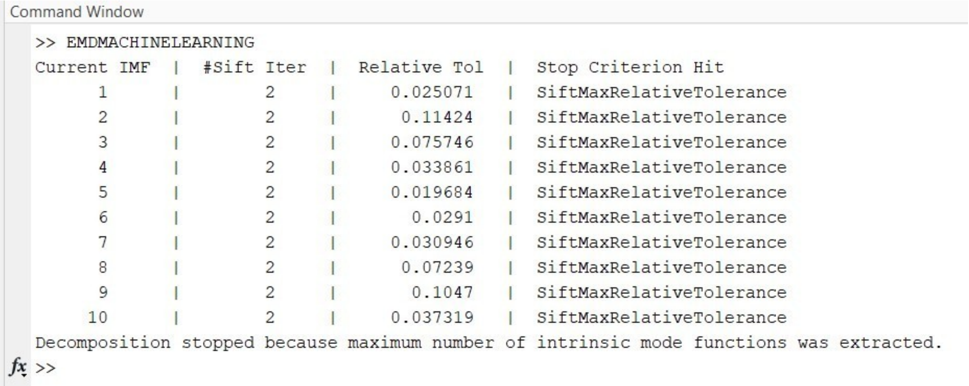

```
>> EMDMACHINELEARNING
Current IMF  |  #Sift Iter  |  Relative Tol  |  Stop Criterion Hit
      1      |        2     |     0.025071   |  SiftMaxRelativeTolerance
      2      |        2     |      0.11424   |  SiftMaxRelativeTolerance
      3      |        2     |     0.075746   |  SiftMaxRelativeTolerance
      4      |        2     |     0.033861   |  SiftMaxRelativeTolerance
      5      |        2     |     0.019684   |  SiftMaxRelativeTolerance
      6      |        2     |       0.0291   |  SiftMaxRelativeTolerance
      7      |        2     |     0.030946   |  SiftMaxRelativeTolerance
      8      |        2     |      0.07239   |  SiftMaxRelativeTolerance
      9      |        2     |       0.1047   |  SiftMaxRelativeTolerance
     10      |        2     |     0.037319   |  SiftMaxRelativeTolerance
Decomposition stopped because maximum number of intrinsic mode functions was extracted.
fx >>
```

Table 2. The number of sift iterations, the relative tolerance, and the sift stop criterion for each generated IMF for the healthy bearing (0HP,1796 RPM).

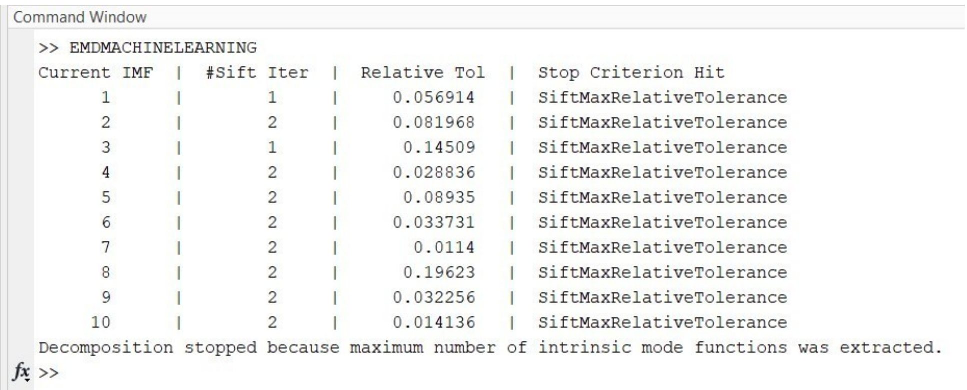

```
>> EMDMACHINELEARNING
Current IMF  |  #Sift Iter  |  Relative Tol  |  Stop Criterion Hit
      1      |        1     |     0.056914   |  SiftMaxRelativeTolerance
      2      |        2     |     0.081968   |  SiftMaxRelativeTolerance
      3      |        1     |      0.14509   |  SiftMaxRelativeTolerance
      4      |        2     |     0.028836   |  SiftMaxRelativeTolerance
      5      |        2     |      0.08935   |  SiftMaxRelativeTolerance
      6      |        2     |     0.033731   |  SiftMaxRelativeTolerance
      7      |        2     |       0.0114   |  SiftMaxRelativeTolerance
      8      |        2     |      0.19623   |  SiftMaxRelativeTolerance
      9      |        2     |     0.032256   |  SiftMaxRelativeTolerance
     10      |        2     |     0.014136   |  SiftMaxRelativeTolerance
Decomposition stopped because maximum number of intrinsic mode functions was extracted.
fx >>
```

Table 3. The number of sift iterations, the relative tolerance, and the sift stop criterion for each generated IMF of inner race faulty bearing with 0.021 in depth (0HP,17976 RPM).

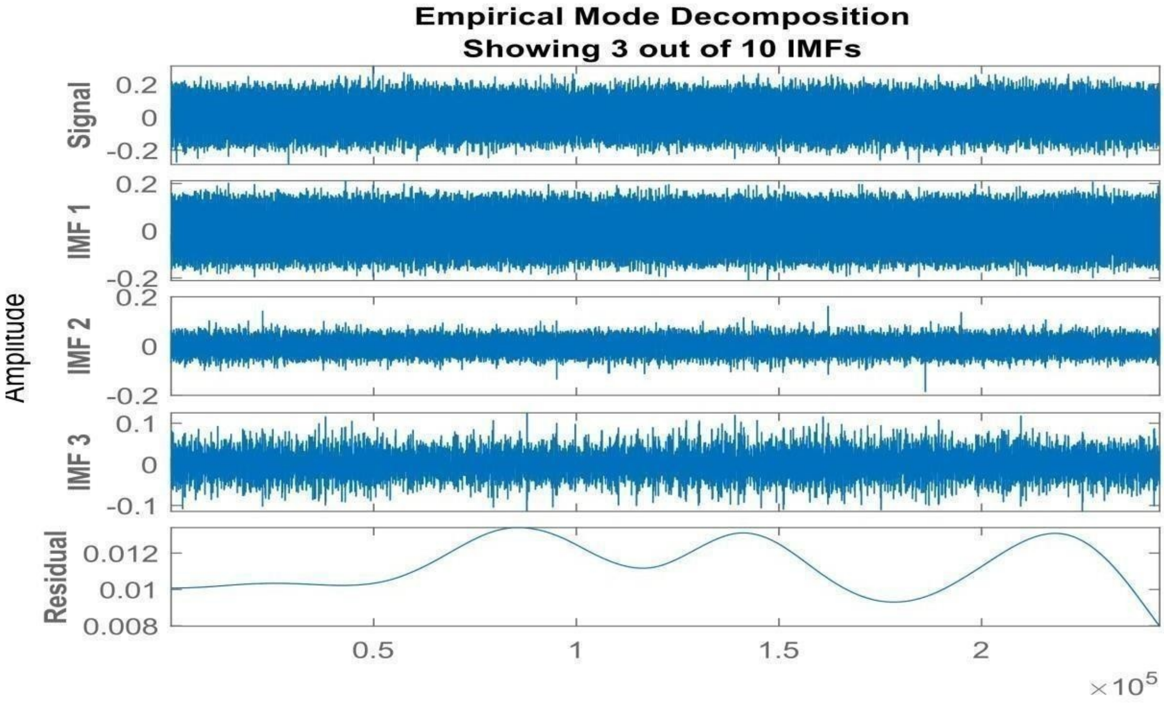

Figure 5. EMD of the healthy bearing 0HP, 1796RPM.

As the figure indicates, the visualization of the IMFs of the healthy or for the defective bearing. The first empirical mode reveals the high-frequency impacts. This high-frequency mode increases in energy as the inner race fault progresses. The third mode shows the resonance in the vibration signal. The residue generated has not been used for further analysis due to the fact that it does not contain any rich information for a fault diagnosis. The resultant IMFs contain meaningful data, and it can be used for a varietyof purposes.

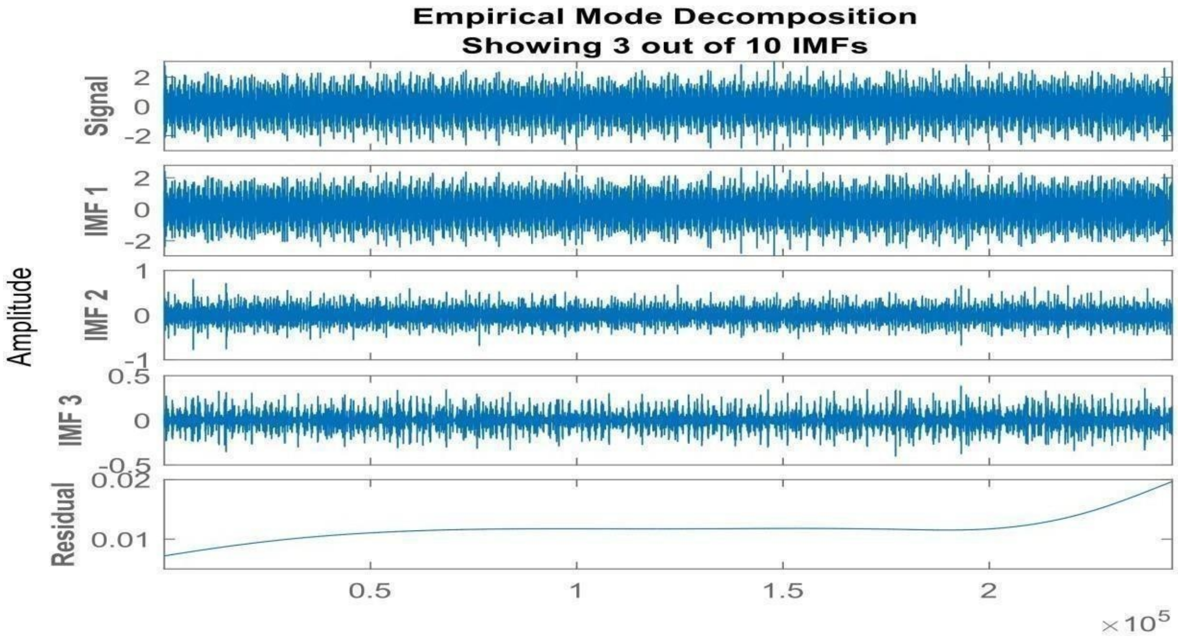

Figure 6. EMD of faulty inner race for 0.021in depth, 0HP, 1796RPM.

According to previous studies, EMD has a sudden change by a huge noise in the time-scaled decomposed signal called mixing mode. So, each IMF has a large number of frequency components (figure 5, figure 6).

To eliminate these phenomena, we perform Hilbert spectrum that could help for reaching the ultimate goal of data analysis for extracting the true signals.

✓ Time-frequency domain: Hilbert Huang Transform

To create the Hilbert spectrum plot, we need the intrinsic mode functions (IMFs) of the signal obtained bythe empirical decomposition method of the previous analysis.

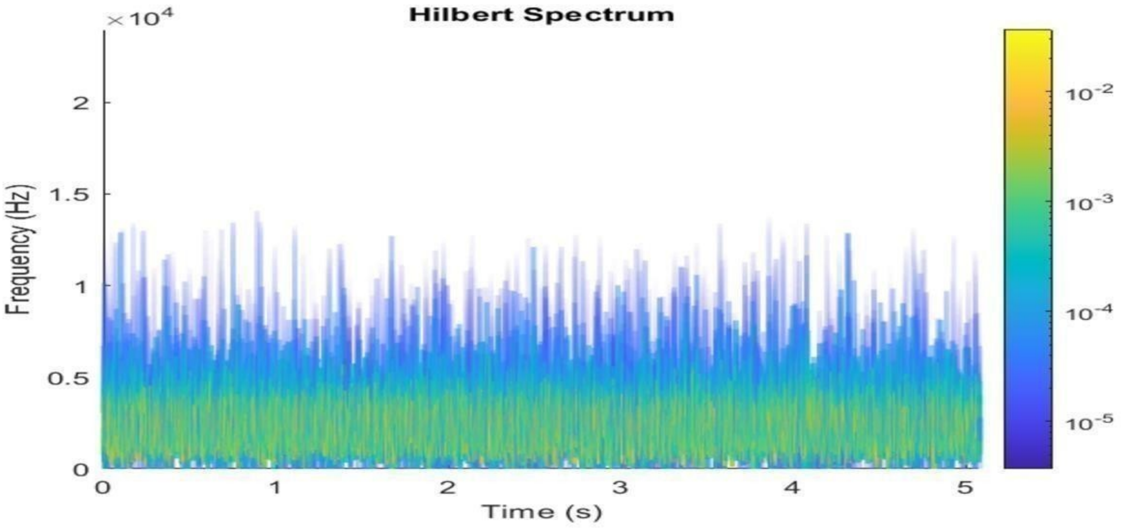

Figure 7. Hilbert spectrumofthe healthy bearing (0HP, 1796RPM).

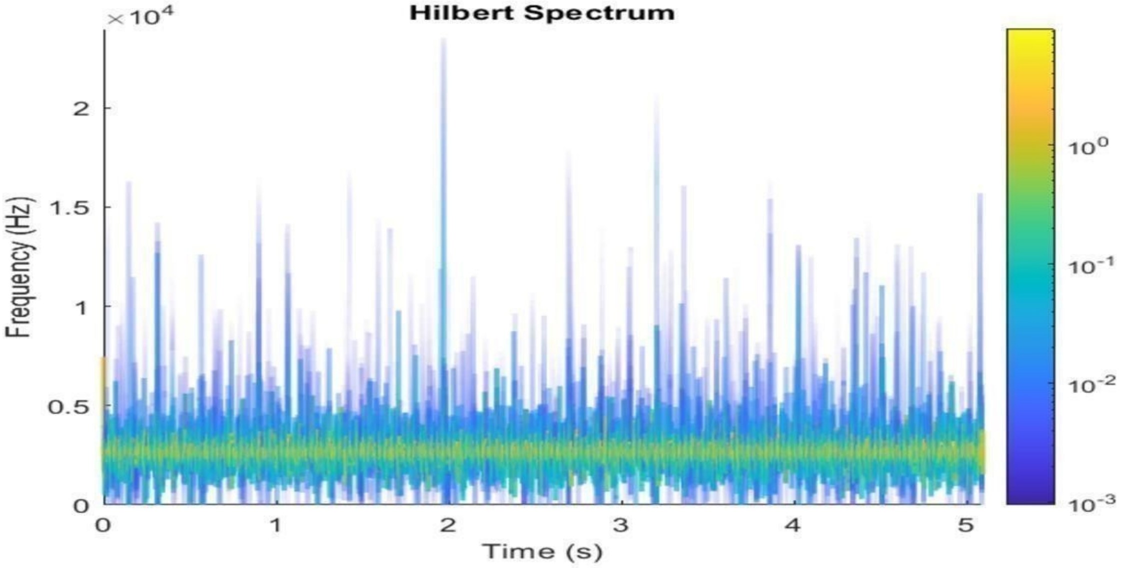

Figure 8. Hilbert spectrum ofthe inner race bearing fault (0HP,1796RPM).

In Figure. 8, The frequency versus time plot is a sparse plot with a vertical color bar representing the instantaneous energy at each point in the IMF. The plot represents the instantaneous frequency spectrum of each component decomposed from the original mixed signal.

The Hilbert spectrum of IMFs 1, 3 (figure 7, figure 8) allow us to identify the frequency corresponding to the inner race fault. However, IMFs 2, 4,5,6,7,8,9,10 do not show significant anomalies (the amplitude ofthe defect is embedded in the noise).

The HT of the IMF 3, indicates high peaks around a harmonic of the frequency characteristic of inner race bearing fault. With an increase of the energy, which confirm that the signal is contain inner race bearing fault. We can conclude that, EMD and HT allows detecting and quantifying the fault for a given speed and load.

Conclusion:

Our research underlined the effectiveness of signal processing methods implemented in MATLAB for understanding real-time machine status. We start by extracting time-domain features from machine data using kurtosis. Then, extracting frequency-domain features using FFT, since the filter is designed based on the frequency information. EMD reflected as a self-adaptive and an automatic filter, by decomposing the signals into IMFs. These IMFs were classified locally from the highest frequencies to the lowest frequencies. Finally, extracting time-frequency domain features from the IMFs using Hilbert transform. The findings of this study indicate how powerful is signal processing-based techniques on detecting, locating, and quantifying the severity of degradation for a given speed and load. Our work clearly has some limitations related to the elimination of background noise that affects the quality of diagnosis. Like The need to choose the appropriate IMF, which will be used for further incorporation with other methods for extraction purposes or classification purposes using Artificial Intelligence. Time-frequency domains methods generally suffer from a need for strong expertise both for their application and for their interpretation. Despite this we believe our work could be a starting point for beginners on this field. We are currently in the process of investigating on how we implement more indicators in a machine learning for an automatic analysis.

References:

[1] A. Singh, K. R. Satyajit, and P. Ray, “A Computational Intelligence-Based Novel Bearing Defect Detection Method,” in *Recent Advances in Power Electronics and Drives*, S. Kumar, B. Singh, and A. K. Singh, Eds., in Lecture Notes in Electrical Engineering. Singapore: Springer Nature, 2022, pp. 645–659. doi: 10.1007/978-981-16-9239-0_49.

[2] M. A. Sher, X. Yu, and Q. Hu, “A Novel Fault Diagnosis of Bearing Approach using a Hybrid of Empirical Mode Decomposition and Discrete Wavelet Transform,” in *2021 IEEE Asia-Pacific Conference on Image Processing, Electronics and Computers (IPEC)*, Apr. 2021, pp. 865–870. doi: 10.1109/IPEC51340.2021.9421273.

[3] A. Soualhi, B. El Yousfi, H. Razik, and T. Wang, “A Novel Feature Extraction Method for the Condition Monitoring of Bearings,” *Energies*, vol. 14, no. 8, p. 2322, Apr. 2021, doi: 10.3390/en14082322.

[4] J. Weng, H. Sun, and B. Li, “Fault Identification of Rolling Bearing Based on Improved EMD-Kurtosis Criterion and DBN,” in *2022 4th International Conference on Artificial Intelligence and Advanced Manufacturing (AIAM)*, Oct. 2022, pp. 879–883. doi: 10.1109/AIAM57466.2022.00177.

[5] C. Zhou, Z. Xiong, H. Bai, L. Xing, Y. Jia, and X. Yuan, “Parameter-Adaptive TVF-EMD Feature Extraction Method Based on Improved GOA,” *Sensors*, vol. 22, no. 19, Art. no. 19, Jan. 2022, doi: 10.3390/s22197195.

[6] A. Faysal, N. W. Keng, and M. H. Lim, “Performance Evaluation of BPSO & PCA as Feature Reduction Techniques for Bearing Fault Diagnosis,” in *Recent Trends in Mechatronics Towards Industry 4.0*, A. F. Ab. Nasir, A. N. Ibrahim, I. Ishak, N. Mat Yahya, M. A. Zakaria, and A. P. P. Abdul Majeed, Eds., in Lecture Notes in Electrical Engineering. Singapore: Springer, 2022, pp. 605–615. doi: 10.1007/978-981-33-4597-3_55.

[7] R. Varghese P, M. S. P. Subathra, S. T. George, N. M. Kumar, E. S. Suviseshamuthu, and S. Deb, “Application of signal processing techniques and intelligent classifiers for high-impedance fault detection in ensuring the reliable operation of power distribution systems,” *Front. Energy Res.*, vol. 11, 2023, Accessed: May 14, 2023. [Online]. Available: https://www.frontiersin.org/articles/10.3389/fenrg.2023.1114230

[8] “https://csegroups.case.edu/ bearing datacenter/pages/download-,” *Bing*. https://www.bing.com/search?q=https%3A%2F%2Fcsegroups.case.edu%2F+bearing+datacenter%2Fpages%2Fdownload-&form=ANSPH1&refig=90d99c40b95f4e17b16669ec110ba786&pc=U531 (accessed Jul. 09, 2023).

Investigation of power flow calculation methods and analysis of computing efficiency

Fateh Ouali[#1], Narimen A. Lahaçani[*2],

[#]*Laboratoire de Maitrise des Energies Renouvelables, Faculté de Technologie,*
Université de Bejaia, 06000 Bejaia, Algeria
[1]`fateh.ouali@univ-bejaia.dz`
[*] *Laboratoire de Maitrise des Energies Renouvelables, Faculté de Technologie,*
Université de Bejaia, 06000 Bejaia, Algeria
[2]`narimen.lahacani@univ-bejaia.dz`

Abstract— **In this article, a comparison is made in the first place between the stability of the methods of calculating the power flow in terms of accuracy as well as the calculation time to show the characteristics of convergence or divergence of the three numerical methods most used in scientific research; therefore, they can be used in the case of the unavailability or temporary interruption of power measuring devices in some substations. Second, the analysis of the complexity of the execution time makes it possible to determine and compare the efficiency of algorithms to solve the same problem, as well as to study the impact of electric load modeling on power flow calculation algorithms, i.e., the evaluated power calculation methods such as the direct approach (DA), the front-back method (BFS), and the Newton-Raphson method (NR). Suitable methods are evaluated on a test and real IEEE HTA distribution network of 33, 69, and 155 buses. Satisfactory results are obtained by comparing the degree of uncertainty of the methods, the calculation time, and the number of iterations performed in the calculated power flow with other advantages.**

Keywords— **Power flow analysis; Newton Raphson; Backward/Forward Sweep, Approach direct, Execution time**

I. INTRODUCTION

The importance of power flow in the analysis and operation of the electrical system lies in its ability to determine steady-state voltage profiles and to provide information on the general operation of the system [1], [2]. It helps to assess the suitability of the nominal characteristics of the equipment, determine possible violations of voltage and current, and optimize the operation of the power system [3], [4]. In addition, the analysis of the power flow is considered fundamental data for the protective elements of the electrical system. It allows the coordination and proper functioning of relays and protective devices to ensure the safety and reliability of the electrical network. As a result, it ensures the safe and efficient operation of radial distribution systems and keeps them in good working order.

This type of analysis confronts the determination of the characteristics and performance of each method, which are evaluated on three radial distribution networks of different sizes, allowing weak areas for improvement to be identified. The analysis of power flow in RDN is based on solving a set of nonlinear algebraic equations with numerical methods such as the direct approach (DA)[5], Newton-Raphson (NR), and backward forward sweep (BFS) [6], [7]. Power flow equations are directly solved using matrix manipulation in DA, while an iterative technique based on power mismatches is employed by the NR method [8]–[10]. Power flow equations are solved iteratively from the load end to the source end in the BFS. The results of this analysis can be used to optimize the grid and manage distribution, including reconfiguration, fault detection, distributed generation placement (DG) and placement of flexible AC transmission Systems (FACTS) [11], [12]. The study of energy flow data has multiple objectives, such as optimizing energy production, identifying technical problems in electrical systems, planning preventive maintenance, monitoring the quality of the electrical wave, reducing costs associated with energy production and transmission, and improving the safety and reliability of electricity distribution. In addition, network design is a sizable combinatorial optimization problem with a difficult-to-find optimal solution [13], [14]. This makes computational time, rapid convergence of these methods, and load modeling important in load flow analysis, as they affect the accuracy, efficiency, and reliability of results [15], [16]. Despite extensive research on computation optimization, convergence analysis, and load modeling for power flow methods, there are still gaps that need attention. Further exploration is needed to develop advanced parallel processing techniques and machine learning to improve power flow calculations in large-scale systems [5], [17].

Studying convergence challenges in complex scenarios, such as renewable energy integration and voltage stability issues, is essential to ensuring accurate load flow solutions. Improving the accuracy of load modeling by taking dynamic and stochastic load behaviors into account and integrating uncertainty analysis to manage prediction errors and measurement uncertainties will further improve the reliability and accuracy of power calculation results.

II. METHODOLOGY

Power flow analysis is typically performed in an experimental configuration involving a simulated radial network, such as IEEE systems or the real 155-bus Bejaia radial network. In this configuration, the mathematical expression of the power flow problem can be formulated as a system of nonlinear equations that model the relationships between voltages, currents, and active and reactive powers in an electrical system [18]. The amplitude of the voltages at the buses of the network and the currents in the branches are generally the variables to be determined.

The equations describing the system can be derived from Kirchhoff's equations for loads and power equilibria, as well as Ohm's and Faraday's laws governing the relations between currents and voltages. Solving the problem can be done using the power flow methods listed in Section I. The convergence is measured by monitoring certain criteria, such as the maximum mismatch of tension between successive iterations for a tolerance defined at one Pico, which are considered estimation performance measures of these methods. In addition, the number of iterations required and the execution time, the accuracy of the power flow analysis is evaluated by comparing the calculated maximum error values of voltage amplitudes, phase shifts. Performance measures, such as mean square error (RMS) and maximum deviation from predicted values, are used to quantify the accuracy of these algorithms.

A range of charge modeling approaches are examined in this work by integrating mathematical models that represent the distinct characteristics and behaviors of different types of electric charges. In order to evaluate the influence of these load modeling techniques on the analysis and optimization of power systems, load models are integrated with load flow analysis algorithms to assess the impact on the functionality and stability of these algorithms.

A. Selected Methods

In this section, we describe the methods that will be used as references in our study: These methods of calculating power flow were chosen for their reliability and accuracy, as well as for their relevance and importance in the field of electrical engineering and for their ability to achieve computational objectives.

1. Direct approach

The power flow calculation method called the direct approach is used to solve PF equations directly to determine voltages and currents. The solution is achieved through an iterative approach, using input data such as active and reactive power consumption at each network node and line data.

S_i The expression for the complex load at the node level is provided:

$$S_i = P_i + jQ_i \tag{1}$$

At iteration k of the solution, the corresponding equivalent current injection is calculated.

$$I^k_i =)I^{\$}_i + I^{i*}_i = +\frac{S_i}{V_i^{k-}}^{*} \tag{2}$$

The bus voltage V and the equivalent current injection I of the bus at iteration k are represented, where the real and imaginary parts of the current injection equivalent to the k-th iteration are indicated as I^r and I^i, respectively.

The relationship between the branch current and the nodal currents of the bus is expressed by the following equation.

$$[B] = [BIBC][I] \tag{3}$$

The variable vectors [B], [*I*] and matrix variables [BIBC] are concerned, where represents the branch current, represents the bus current, and refers to a matrix known as the branch current node injection matrix defined in [17]. The constant matrix is an upper triangular matrix composed of only 0 and +1 values. It applies to different power system analysis techniques, including load rate analysis, failure analysis, and stability analysis. This technique is used to examine the performance of power systems under various operating conditions.

2. *Backward/Forward Sweep*

The Backward/Forward Sweep (BFS) method is an iterative method that involves performing a backward swipe and a forward swipe through the power grid. It is an iterative approach that can solve equations at different nodes in the network. The principle of this method is during the backward scanning, the knot currents are calculated using the voltages of the nodes and the injected apparent power using the equations 2 and 3.

The first step in initialization is to select one of the nodes as the voltage reference node. Then, the system voltage of each node is initialized to 1 pu. The tolerance value for the voltage loop is set at 10^{-12}.

The calculation is performed using the backward/forward scan method. During the backward phase, the node currents are determined from the nodes furthest from the reference node using the Kirchhoff current equations for each node. These node currents are then summed to determine the branch currents associated with each row in the system. During the forward phase, the knot voltages are determined from the reference node using the Kirchhoff voltage equations for each node. These knot voltages are used to determine the voltages at the ends of the branches.

$$S_i^* = V_i^* \sum_{k=1}^{n} Y_{ik} V_k \tag{4}$$

where * denotes the complex conjugate.

3. *Newton–Raphson Methods*

The Newton-Raphson (NR) method is a commonly used method for calculating power flow. The objective of this method is to iteratively solve nonlinear equations in order to determine the voltages at each node of the network. Active and reactive power equations for each branch of the network are used, as are input data such as loads, generators, and line configuration. The NR method relies on deriving equations to find a solution that gradually approaches reality with each iteration, until a convergent solution is reached. Details of the NR method are provided in references [7], [19].

The formulation of the power flow problem by the Newton-Raphson method makes it possible to use the expressions of active and reactive power in the following ways:

$$S_i = P_i + jQ_i = V_i \sum_{k=1}^{n} Y_{ik}^* V_k^* \tag{5}$$

$$S_i = \sum_{k=1}^{n} (V_i V_k Y_{ik}) \angle(\delta_i - \delta_k - \theta_{ik}) \tag{6}$$

$$P_i = V_i V_k Y_{ik} \cos\theta_{ii} + \sum_{\substack{k=1 \\ k \neq i}}^{n} (V_i V_k Y_{ik}) \cos(\delta_i - \delta_k - \theta_{ik}) \tag{7}$$

$$Q_i = V_i V_k Y_{ik} \cos\theta_{ii} + \sum_{\substack{k=1 \\ k \neq i}}^{n} (V_i V_k Y_{ik}) \sin(\delta_i - \delta_k - \theta_{ik}) \tag{8}$$

In each iteration, a Jacobian matrix is constructed and then solved. This matrix equation offers a linearized correlation between alterations in voltage angle (δ) and voltage magnitude (V), represented as follows:

$$\begin{bmatrix} \Delta P \\ \Delta Q \end{bmatrix} = J \begin{bmatrix} \Delta\delta \\ \Delta|V| \end{bmatrix} \tag{9}$$

Elements of the Jacobian matrix are the partial derivatives which are given as:

$$J = \begin{bmatrix} \frac{\partial P}{\partial \delta} & \frac{\partial P}{\partial |V|} \\ \frac{\partial Q}{\partial \delta} & \frac{\partial Q_i}{\partial |V_i|} \end{bmatrix} \quad (10)$$

The system of equations is solved to determine the next iteration of the voltage amplitude and angles, as shown in the following equations:

$$\delta_i^{(k\text{-}O)} = \delta_i^{(k)} + \Delta\delta_i^{(k)} \quad (11)$$

$$|V_i^{(k\text{-}O)}| = |V_i^{(k)}| + \Delta |V_i^{(k)}| \quad (12)$$

The calculations are repeated as many times as necessary until the specified tolerance is reached.

Where; ΔP and ΔQ are the difference between the planned and calculated values. k and (k+1) indicate the previous and next iterations, respectively.

$\delta_i^{(k\text{-}O)}$ and $\Delta\delta_i^{(k)}$ are the calculated angle and the variation of the calculated angle, respectively;

$|V_i^{(k\text{-}O)}|$ and $|V_i^{(k)}|$ are the voltage magnitude at iteration k at node i.

The total real and reactive power losses for each method are calculated as follows:

$$\begin{cases} P_{total_{loss}} = 5_i^{nb} \frac{Pl_i^3 + Ql_i^3}{|V_i|^3} R_i \\ Q_{total_{loss}} = 5_i^{nb} \frac{Pl_i^3 + Ql_i^3}{|V_i|^3} X_i \end{cases} \quad (13)$$

R_i and X_i are the resistance and reactance of the line i-th.

B. Modeling the voltage dependency of system loads

Load modeling describes how electrical power is used by consumers in an electrical system. This anticipates the demand for electrical energy through an analysis as a function of weather conditions and consumption habits at different times of the day or year, which is important for producers and suppliers of electrical energy to plan and size their production and distribution capacity.

The dependence on load constraints is modeled by a mathematical function for more accurate analysis and planning and to see its influence on power flow calculation algorithms. These loads are modeled using the variable load model, where the power absorbed by the load varies according to the amplitude of the voltage [20], [21]. A composite model of loads is considered.

The modeling of voltage-dependent loads $Pl_{,i}$ and $Ql_{,i}$ is adapted from [10]. The active and reactive power loads of node 'i' are given as follows:

$$W\begin{cases} Pl_{,i} = P_n\,[\,a_5 + a_(V_i + a_3 V_i^3\,] \\ Ql_{,i} = Q_n\,[\,b_5 + b_(V_i + b_3 V_i^3\,] \end{cases} \quad (14)$$

Where P_n and Q_n are the nominal active and reactive loads, respectively. The other load coefficients (a_5, $a_($, a_3) and (b_5, $b_($, b_3) must satisfy the following equations:

$$Z\begin{cases} a_5 + a_(+ a_3 = 1 \\ b_5 + b_(+ b_3 = 1 \end{cases} \quad (15)$$

Exponential load modeling is essential to understanding the behavior of electrical systems. It refers to a load profile that shows rapid growth or decrease in energy consumption over time. The modeling equations for exponential load

ISSN: 1737-933484

use parameters k1 and k2, which determine the magnitude of the change in energy consumption relative to a reference voltage V_{ref} using “(16)”. Typical values of k1 range from 0.6 to 1.8, while values of k2 range from 1.6 to 6. These models help simulate and analyze the effects of exponential charging on electrical systems [20], [22].

$$\begin{cases} Pl_{,i} = P_{n_i}\left(\frac{V_i}{V_{re9}}\right)^{k1} \\ Ql_{,i} = Q_{ni}\left(\frac{V_i}{V_{re9}}\right)^{k2} \end{cases} \tag{16}$$

The heating and charging systems of electric vehicles (EVs) often have exponential electrical load profiles due to the nature of their active energy requirements. In this case, we will review the minimum k1 and the maximum k2.

III. RIGOROUS VALIDATION OF POWER FLOW ANALYSIS

The proposed methods were validated by a series of rigorous simulations and comparisons. These attempts were aimed at evaluating the performance, accuracy, and reliability of algorithms in various scenarios. The validation process involved the use of reference datasets and numerical simulation studies performed on the MATLAB_R2023a software version using a 3.3 GHz Intel Core i7 processor with 16 GB of RAM. And these three systems, namely IEEE 33-bus, 69-bus, and 155-bus of the Bejaia region, as shown in the appendix, are considered cases of small and medium-scale networks. Each of these systems is used as a relatively small- and medium-scale network case for the purposes of this comparative study. The effectiveness of each proposed method is verified using the complete data from these systems, which start from a specific initial point of 1 pu.

To ensure consistency, fairness, and that all methods are implemented and executed under similar conditions in this comparison. The size and nature of the radial network, as well as the hardware and software used, have been selected to provide a fair basis for evaluating the performance of these methods.

A. Statistical analysis of results

By comparing these proposed methods based on iterative processes on several critical factors in order to eliminate bias and provide a fair comparison, a consistent set of input data, system parameters, and computing resources is used for all three methods. This comparison provided valuable information on the efficiency of the calculation. The evaluation of the execution time of these algorithms is performed using tools provided by MATLAB, such as tic toc and timeit, both of which are used as parameters to assess the calculation time of these algorithms. MAE (Average Absolute Error) is employed by the first function, and RMSE (Root Mean Square Error) is employed by the second function, respectively.

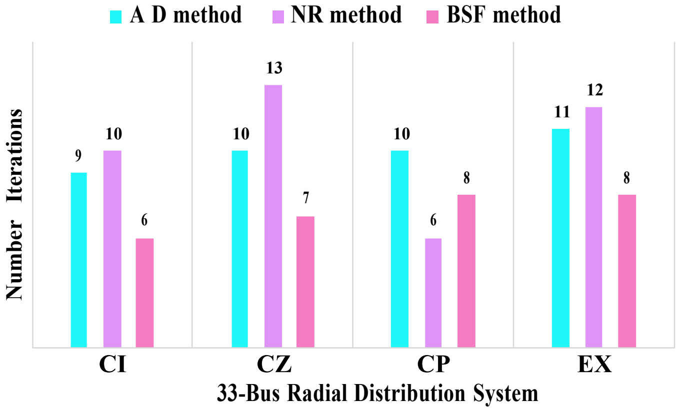

Fig. 1 Comparison of the performance in terms of the number of iterations of load flow methods

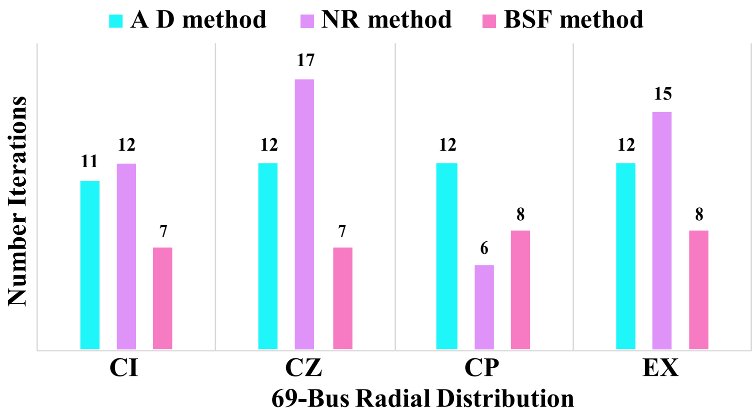

Fig. 2 Comparison of the performance in terms of the number of iterations of load flow methods

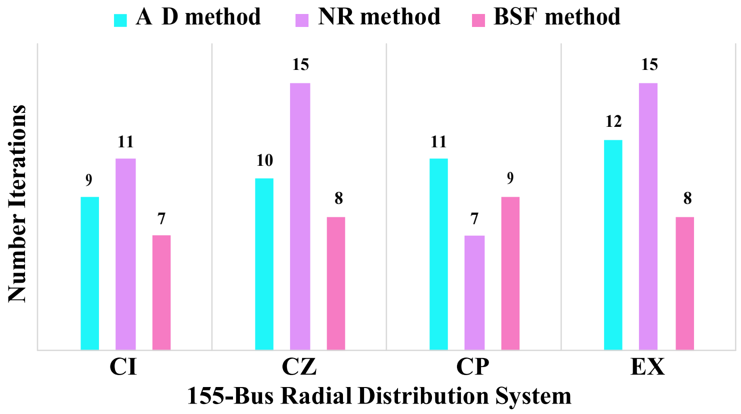

Fig. 3 Comparison of the performance in terms of the number of iterations of load flow methods

Figures 1, 2, and 3 illustrate the comparison of the number of iterations of the different methods of calculating the power flow. The direct approach (DA) and the BFS (Backward/Forward Sweep) method differ in their stability in terms of number of iterations, regardless of network size and load types. On the other hand, the Newton-Raphson (NR) method shows a significant variation in the number of iterations according to the types of loads. This suggests that the NR method may be more sensitive to variations in electrical loads and require more frequent iteration adjustments to achieve convergence.

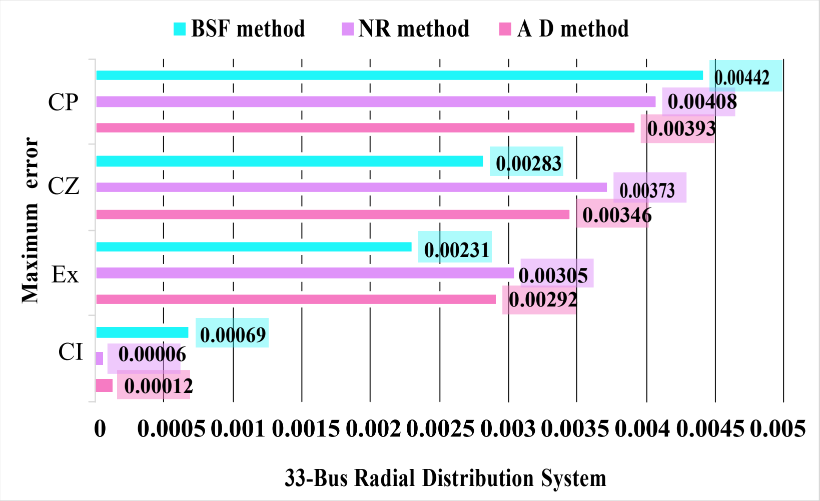

Fig. 4 Maximum error between two successive iterations

ISSN: 1737-933484

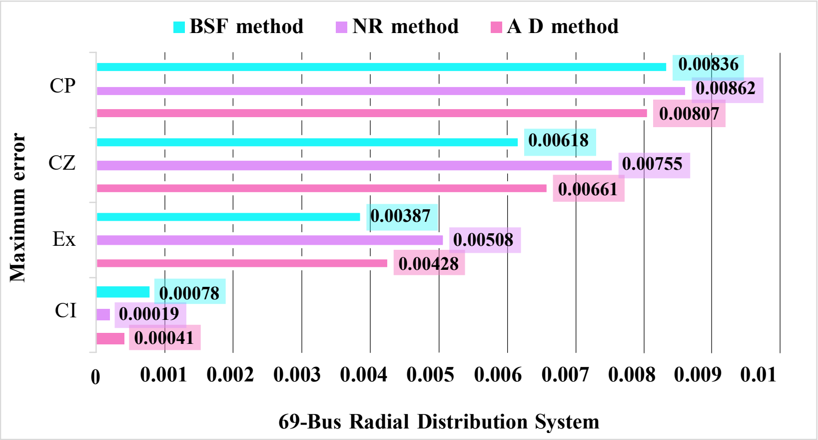

Fig. 5 Maximum error between two successive iterations

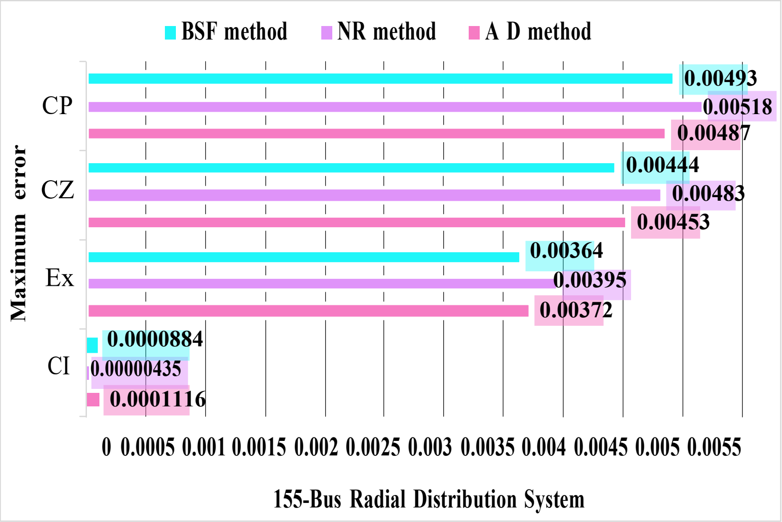

Fig. 6 Maximum error between two successive iterations

Figures 4, 5, and 6 show the stability of the maximum error between two successive iterations for each method. These figures show the results for the three radial networks, as a function of load type. We see a similar pattern across all figures. The DA and BFS approaches continue to show maximum error stability between successive iterations, regardless of network size or load type. These methods maintain weak and almost stable errors, demonstrating their ability to converge effectively in radial networks.

The figures 7, 8, and 9 highlights the differences in run time between the three approaches for the different radial network systems and the four load modeling scenarios. The DA and BFS approaches show quasi-stable run times, while the NR approach shows increased run time with larger networks and different load modeling. These findings allow us to assess the computer efficiency of each approach and suggest that the DA and BFS approaches are the most appropriate for the radial network, regardless of the type of load selected.

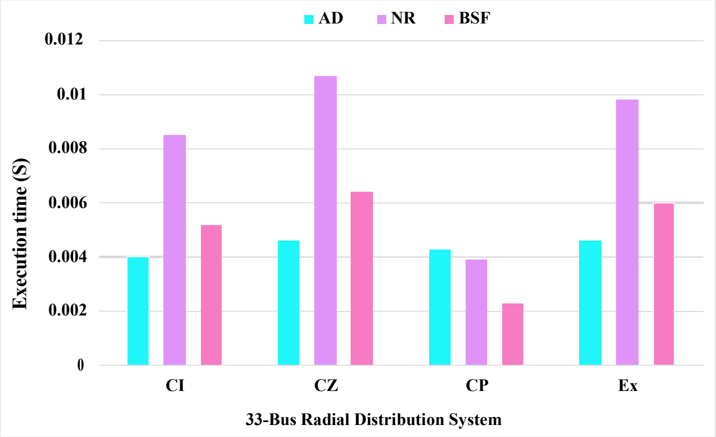

Fig. 7 Comparison of the performance in terms of the execution time

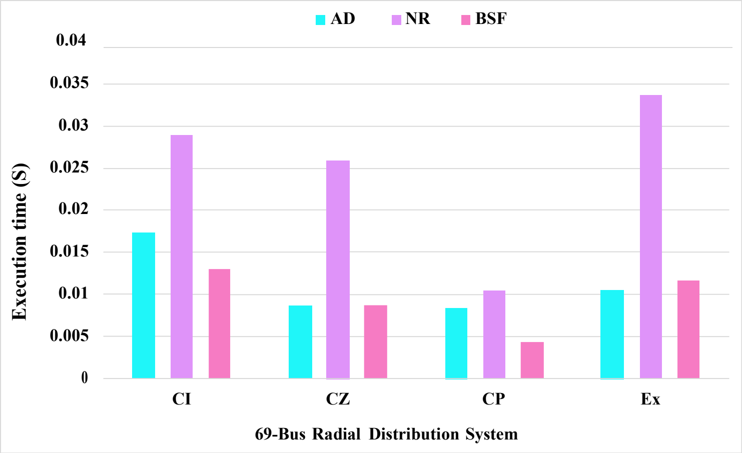

Fig. 8 Comparison of the performance in terms of the execution time

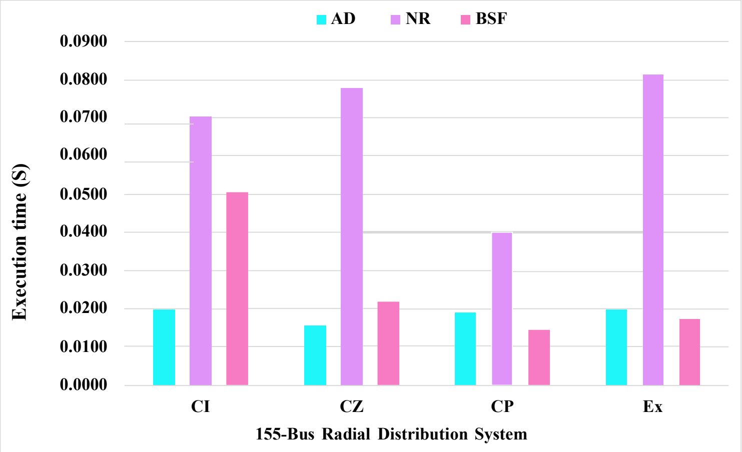

Fig. 9 Comparison of the performance in terms of the execution time

B. Comparative analysis

This section presents the results of our analysis on the computational efficiency, execution time taken by each algorithm, number of iterations, power losses, convergence characteristics, and performance of these power flow calculation methods, which sheds light on their ability to analyze and know the state of the power system.

Throughout the validation process, extensive analyses were conducted to ensure that the proposed methods met the required criteria. Statistical analyses, error assessments, and sensitivity studies were conducted to thoroughly assess the efficiency of these methods. The results provide valuable information on the strengths and limitations of each method, helping to select the most appropriate load flow method for specific applications. The test results demonstrate the flexibility and accuracy of the proposed algorithms for the intended applications.

Overall, the validation process provided comprehensive evidence of the ability of the proposed methods to provide reliable and accurate results in the analysis of power systems. It demonstrated their strengths, highlighted their limitations, and identified areas for improvement. The results of the validation provided coherence in the practical implementation of these methods and supported their integration into power system analysis and operational workflows.

C. Discussion

Based on the analysis performed, significant differences were observed in the results of the comparative tests, including run time, number of iterations, and total power losses. The behavior of these algorithms and their iterative approach to the solution have been observed; in this instance, the reference relates to the voltage rather than the power because using the Newton-Raphson method caused the algorithm to become unstable and diverge. These differences are crucial for ensuring the protection of the power system and effective long-range planning, where accuracy holds importance.

IV. CONCLUSIONS

In conclusion, these methods demonstrated their ability to maintain consistently low and stable errors, showcasing reliable and robust convergence across various radial network sizes. However, further analysis is recommended to ascertain the simulation's reliability and validate the baseline assumptions.

Furthermore, the algorithms' behavior, especially their iterative approach to the solution, was closely monitored during the study. Notably, using the Newton-Raphson method with power as the reference parameter led to instability and divergence.

Additionally, it is crucial to consider the influence of Electronic Control Unit (ECU) technology and the relative robustness of the algorithms in the analysis. These factors can significantly impact the execution time and the concordance required to achieve convergence and find solutions to the systems under study. Careful consideration of these aspects can enhance the accuracy and efficiency of power flow calculations in practical applications.

ACKNOWLEDGMENT

We would like to thank the DGRSDT of Algeria for providing necessary subventions to our laboratory.

REFERENCES

[1] A. Kumar, B. K. Jha, D. K. Dheer, D. Singh, and R. K. Misra, 'Nested backward/forward sweep algorithm for power flow analysis of droop regulated islanded microgrids', *IET Gener. Transm. Distrib.*, vol. 13, no. 14, pp. 3086–3095, Jul. 2019, doi: 10.1049/iet-gtd.2019.0388.

[2] M. Gao, J. Yu, Z. Yang, and J. Zhao, 'A Physics-Guided Graph Convolution Neural Network for Optimal Power Flow', *IEEE Trans. Power Syst.*, vol. PP, pp. 1–11, 2023, doi: 10.1109/TPWRS.2023.3238377.

[3] A. Pandey, M. Jereminov, M. R. Wagner, D. M. Bromberg, G. Hug, and L. Pileggi, 'Robust Power Flow and Three-Phase Power Flow Analyses', *IEEE Trans. Power Syst.*, vol. 34, no. 1, pp. 616–626, Jan. 2019, doi: 10.1109/TPWRS.2018.2863042.

[4] S. Venkatasivanagaraju and M. V. Rao, 'Loss Minimization and Optimal Power flow for long term and short-term Real-Time Forecasting System using Cuckoo Search Algorithm', in *2022 Second International Conference on Artificial Intelligence and Smart Energy (ICAIS)*, Feb. 2022, pp. 805–810, doi: 10.1109/ICAIS53314.2022.9742990.

[5] U. H. Ramadhani, M. Shepero, J. Munkhammar, J. Widén, and N. Etherden, 'Review of probabilistic load flow approaches for power distribution systems with photovoltaic generation and electric vehicle charging', *Int. J. Electr. Power Energy Syst.*, vol. 120, no. December 2019, p. 106003, Sep. 2020, doi: 10.1016/j.ijepes.2020.106003.

[6] M. Balasubbareddy, D. Dwivedi, G. V. K. Murthy, and K. S. Kumar, 'Optimal power flow solution with current injection model of generalized interline power flow controller using ameliorated ant lion optimization', *Int. J. Electr. Comput. Eng.*, vol. 13, no. 1, p. 1060, Feb. 2023, doi: 10.11591/ijece.v13i1.pp1060-1077.

[7] J. Dancker and M. Wolter, 'Improved quasi-steady-state power flow calculation for district heating systems: A coupled Newton-Raphson approach', *Appl. Energy*, vol. 295, p. 116930, Aug. 2021, doi: 10.1016/j.apenergy.2021.116930.

[8] Y. Venkatesan, K. Srilakshmi, and A. Palanivelu, 'Modified soccer game optimization and its application on power flow and distribution generation placement problems of distribution systems', *Evol. Intell.*, vol. 16, no. 2, pp. 539–552, Apr. 2023, doi: 10.1007/s12065-021-00677-9.

[9] Z. Shao, Q. Zhai, Y. Mao, and X. Guan, 'A method for evaluating and improving linear power flow models in system with large fluctuations', *Int. J. Electr. Power Energy Syst.*, vol. 145, no. August 2022, p. 108635, Feb. 2023, doi: 10.1016/j.ijepes.2022.108635.

[10] S. Bhalla, S. Kumar, and S. K. Aggarwal, 'Comparative Analysis of Newton's Higher Order Methods for Load Flow Problem', in *2019 Amity International Conference on Artificial Intelligence (AICAI)*, Feb. 2019, no. 1, pp. 334–339, doi: 10.1109/AICAI.2019.8701346.

[11] P. P. Biswas, P. Arora, R. Mallipeddi, P. N. Suganthan, and B. K. Panigrahi, 'Optimal placement and sizing of FACTS devices for optimal power flow in a wind power integrated electrical network', *Neural Comput. Appl.*, vol. 33, no. 12, pp. 6753–6774, Jun. 2021, doi: 10.1007/s00521-020-05453-x.

[12] J. Zhang, J. Cai, S. Wang, and P. Li, 'Many-objective optimal power flow problems based on distributed power flow calculations for hierarchical partition-managed power systems', *Int. J. Electr. Power Energy Syst.*, vol. 148, no. January, p. 108945, Jun. 2023, doi: 10.1016/j.ijepes.2023.108945.

[13] M. Zheng, R. Zhou, S. Liu, F. Liu, and X. Guo, 'Route Design Model of Multiple Feeder Bus Service Based on Existing Bus Lines', *J. Adv. Transp.*, vol. 2020, pp. 1–12, Dec. 2020, doi: 10.1155/2020/8853872.

[14] Z. Wu, D. Fan, and F. Zou, 'Traction Load Modeling and Parameter Identification Based on Improved Sparrow Search Algorithm', *Energies*, vol. 15, no. 14, p. 5034, Jul. 2022, doi: 10.3390/en15145034.

[15] M. S. Shahriar, 'Load-flowdependent twofold technique of tolerance selection for robust estimation of power system states', *Adv. Eng. Softw.*, vol. 176, no. August 2022, p. 103376, Feb. 2023, doi: 10.1016/j.advengsoft.2022.103376.

[16] F. D. Freitas and L. Neves de Oliveira, 'Conditioning step on the initial estimate when solving ill-conditioned power flow problems', *Int. J. Electr. Power Energy Syst.*, vol. 146, no. October 2022, p. 108772, Mar. 2023, doi: 10.1016/j.ijepes.2022.108772.

[17] H. Bennani, A. Chebak, and A. El Ouafi, ‘A generic power flow formulation for flexible modeling and fast solving for large-scale unbalanced networks’, *Int. J. Electr. Power Energy Syst.*, vol. 148, no. January, p. 108956, Jun. 2023, doi: 10.1016/j.ijepes.2023.108956.

[18] L. H. T. Bandória, M. C. Almeida, and T. R. Fernandes, ‘A phasor rotation-based approach to represent PV buses on the current injection power flow’, *Electr. Power Syst. Res.*, vol. 216, no. October 2022, p. 108999, Mar. 2023, doi: 10.1016/j.epsr.2022.108999.

[19] R. G. Wasley, B. S. Tech, M. Sc, D. Ph, M. A. Shlash, and M. Sc, ‘Newton-Raphson algorithm for 3-phase load flow’, vol. 121, no. 7, 1974.

[20] J. Yang *et al.*, ‘Identification and Stabilization of Constant Power Loads in AC Microgrids’, *IEEE Trans. Ind. Electron.*, vol. PP, pp. 1–10, 2023, doi: 10.1109/TIE.2023.3257386.

[21] S. Nikkhah, A. Rabiee, A. Soroudi, A. Allahham, P. C. Taylor, and D. Giaouris, ‘Distributed flexibility to maintain security margin through decentralised TSO–DSO coordination’, *Int. J. Electr. Power Energy Syst.*, vol. 146, no. June 2022, p. 108735, Mar. 2023, doi: 10.1016/j.ijepes.2022.108735.

[22] J. S. Bhadoriya, A. R. Gupta, and B. Khan, ‘Analysis of Pre- and during COVID-19 Mixed Load Models on Unbalanced Radial Distribution System Using a New Metaphor-Less Rao Optimization’, *Int. Trans. Electr. Energy Syst.*, vol. 2023, pp. 1–21, Mar. 2023, doi: 10.1155/2023/6777135.

APPENDIX

Bejaia Radial Distribution Network 155 buses.

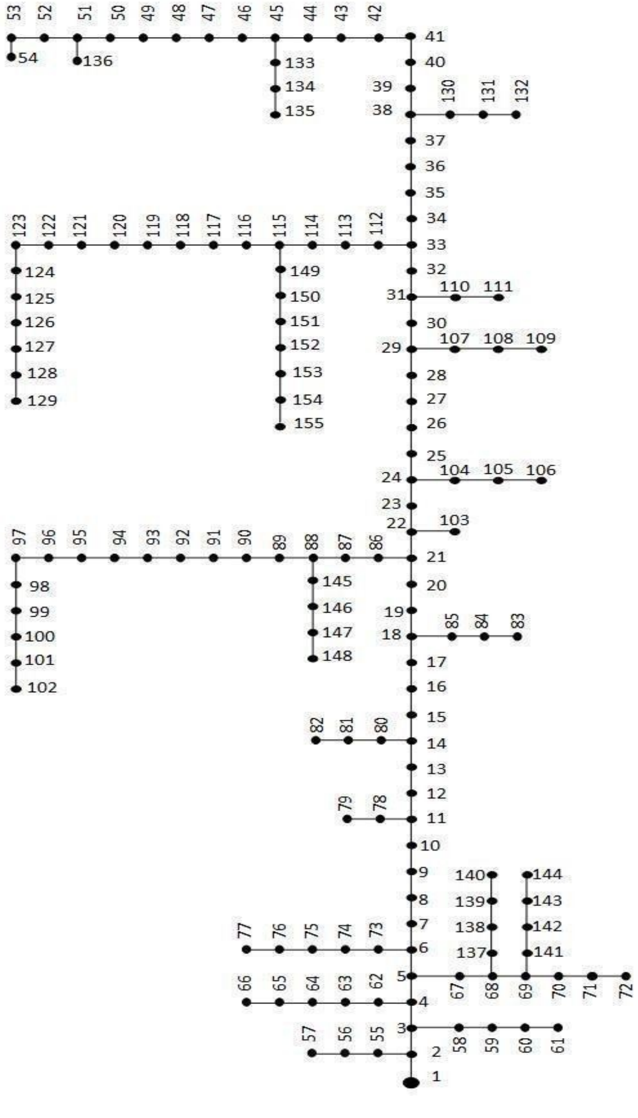

Characterisation of a Carreau-Yassuda Fluid Flow Within a Circular Pipe

Labsi Nabila[1], Melki Rafik[2], Benkahla Youb Khaled[3]

Equipe Rhéologie et Simulation Numérique des Ecoulements, Laboratoire des Phénomènes de Transfert,
Faculté de Génie Mécanique et de Génie des Procédés,
Université des Sciences et de la Technologie Houari Boumediene
BP. 32 El Allia, Bab Ezzouar, Alger, Algérie
[1]nabilalabsi@yahoo.fr ; nlabsi@usthb.dz
[2]melki.rafik@hotmail.com
[3]youbenkahla@yahoo.fr

***Abstract*— The study considers the laminar steady axisymmetric flow of an incompressible Carreau fluid in a circular pipe, maintained at a constant and uniform wall temperature. The dimensionless governing equations, i.e. continuity, momentum and energy equations, are discretized using the Finite Volume Method and resolved by means of a homemade computer code. The study focuses on the effect, on heat transfer, of both viscous dissipation and temperature-dependency of the fluid's viscosity. The results show that neglecting viscous dissipation for both isoviscous and thermodependent fluid leads to underestimate heat transfer.**

Keywords— **Carreau fluid, thermodependent viscosity, viscous dissipation, finite volume method, circular pipe.**

I. INTRODUCTION

Some fluids such as polymers are well described by the rheological model of Carreau-Yasuda. Thus, many studies have been undertaken considering the flow of this non Newtonian fluid within various geometries.

Khellaf and Lauriat [1] studied the forced, mixed and natural convection of a Carreau fluid within a short annulus with a heated and rotating inner cylinder and a cooled and fixed outer cylinder. Their results show that the shear thinning effect decreases the friction factor at the rotating cylinder and increases the heat transfer through the annular.

Abbasi et *al.* [2] undertook a numerical study on the effect of applied magnetic field on the peristaltic transport of a Carreau-Yasuda fluid in a curved duct. They found that the fluid velocity is not symmetric about the centreline for small values of curvature parameter and that the increase of the Hall parameter value balances the magnetic effect of applied magnetic field.

Rousset et *al.* [3] analyzed the temporal stability of a Carreau fluid flow along a tilted plate plane. They highlighted the effect of shear-thinning fluid's properties on the definition of the stability kind. They found also that the critical Reynolds number for this fluid is smaller than the one corresponding to Newtonian fluids.

Lounis et *al.* [4] studied numerically, the thermosolutal convection of a Carreau-Yasuda fluid within an inclined square cavity by considering Soret and Dufour effects. The active walls are subject to constant and uniform concentrations and temperatures whereas the other walls are impermeable and adiabatic. The results show that the increase of the time constant parameter as well as the decrease of the ratio of infinite-to zero-shear-rate viscosities enhance thermal and mass exchange for various values of the flow index. In addition, the rise of the orientation angel from 0° to 90° increases heat and mass transfer rates.

Bilal et *al.* [5] analyzed the magnetic dipole and heat transmission through ternary hybrid $Al_2O_3/SiO_2/TiO_2$-Carreau-Yasuda nanofluid flow across a vertical stretching sheet. The heat transfer and velocity were analysed by considering the effect of heat source/sink and Darcy Forchhemier. Among the results, they found that the increase of the flow index increases the skin friction and the Nusselt number. Also, the rising effect of Darcy Forchheimer's term and porosity constant decreases the velocity outlines and finally, the ternary hybrid nanofluid have a greater tendency to increase the energy transmission across a vertical plate in comparison to the base fluid.

It can be seen that there is few studies regarding the Carreau-Yasuda or Carreau fluid flow within a pipe and moreover, by considering the effect of viscous dissipation. For this purpose, the present numerical study deals with

ISSN: 1737-933484

the analysis of thermal exchange through the flow of a temperature-dependent Carreau fluid within a pipe, by considering viscous dissipation.

II. MATHEMATICAL FORMULATION AND NUMERICAL MODELLING

Let’s consider the laminar steady axisymmetric flow of an incompressible Carreau fluid in a pipe of a circular cross section. The pipe is of length L and radius r_w and is maintained at a constant and uniform wall temperature T_w. The fluid is assumed to be of constant physical and rheological properties except for the apparent viscosity which is considered thermodependent. Viscous dissipation will be considered, by taking both cases of wall heating and wall cooling.

A. *Mathematical Formulation*

The dimensionless governing equations, i.e. continuity, momentum and energy equations are, respectively, given in cylindrical coordinates by:

$$\frac{1}{R}\frac{\partial(RV)}{\partial R}+\frac{\partial U}{\partial X}=0 \tag{1}$$

$$\frac{1}{R}\frac{\partial(RVV)}{\partial R}+\frac{\partial(UV)}{\partial X}=-\frac{\partial P^*}{\partial R}+\frac{1}{Re}\left[\frac{1}{R}\frac{\partial}{\partial R}\left(\eta_{app}R\frac{\partial V}{\partial R}\right)+\frac{\partial}{\partial X}\left(\eta_{app}\frac{\partial V}{\partial X}\right)\right]+\frac{1}{Re}\left[\frac{\partial V}{\partial R}\frac{\partial}{\partial R}\left(\eta_{app}\right)-\eta_{eff}\frac{V}{R^2}+\frac{\partial}{\partial X}\left(\eta_{app}\right)\frac{\partial U}{\partial R}+R\frac{\partial}{\partial R}\left(\eta_{app}\right)\frac{\partial}{\partial R}\left(\frac{V}{R}\right)\right] \tag{2}$$

$$\frac{1}{R}\frac{\partial(RVU)}{\partial R}+\frac{\partial(UU)}{\partial X}=-\frac{\partial P^*}{\partial X}+\frac{1}{Re}\left[\frac{1}{R}\frac{\partial}{\partial R}\left(\eta_{app}R\frac{\partial U}{\partial R}\right)+\frac{\partial}{\partial X}\left(\eta_{app}\frac{\partial U}{\partial X}\right)\right]+\frac{1}{Re}\left[\frac{\partial}{\partial R}\left(\eta_{app}\right)\frac{\partial V}{\partial X}+\frac{\partial}{\partial X}\left(\eta_{app}\right)\frac{\partial U}{\partial X}\right] \tag{3}$$

$$\frac{1}{R}\frac{\partial(RV\theta)}{\partial R}+\frac{\partial(U\theta)}{\partial X}=\frac{1}{Pr\,Re}\left[\frac{1}{R}\frac{\partial}{\partial R}\left(R\frac{\partial\theta}{\partial R}\right)+\frac{\partial^2\theta}{\partial X^2}\right]+\frac{Br}{Pr\,Re}\eta_{app}\dot{\gamma}^{*2} \tag{4}$$

Where the dimensionless second invariant in Equation (4) is given by:

$$\dot{\gamma}^{*2}=2\left[\left(\frac{\partial V}{\partial R}\right)^2+\left(\frac{\partial U}{\partial X}\right)^2+\left(\frac{V}{R}\right)^2\right]+\left(\frac{\partial U}{\partial R}+\frac{\partial V}{\partial X}\right)^2 \tag{5}$$

The apparent viscosity of Carreau fluid is given, in its dimensionless form by the following law, proposed by Bird at al. [6]:

$$\eta_{app}=\left(1+We^2\dot{\gamma}^{*2}\right)^{\frac{n-1}{2}} \tag{6}$$

Where We represents the Weissenberg number and n is the flow index.

To complete the system of governing equations, we consider as steady boundary conditions, a uniform axial velocity and temperature at the inlet ($U = \theta = 1$, $V = 0$), no-slip conditions are applied at the wall along the pipe where a uniform wall temperature is assumed ($U = V = \theta = 0$) and finally, at the symmetry plan ($\theta = 0$), we consider: $(\partial U/\partial X) = (\partial V/\partial X) = (\partial\theta/\partial X) = 0$.

B. *Numerical Modelling and validation of the computer code*

The governing equations with the corresponding boundary conditions are solved numerically using the finite volume method proposed by Patankar [7]. Thus, these differential equations are transformed in algebraic equations which are solved by means of the line by line method.

The grid adopted in the present study is non-uniform and consists, after studying the sensitivity of the results to the mesh, of 250 nodes in the X direction and 50 nodes in the R direction. The convergence criterion, which is based on the residual, is set to 10^{-5} for both velocity components and temperature and to 10^{-6} for pressure.

Since there is few works regarding the Carreau fluid's flow within a pipe, to validate our computer code, we considered the limit case of a Newtonian fluid (n = 1). Thus, our results, concerning the axial evolution of the Nusselt number, were compared to those of Min et *al.* [8]. The comparison, illustrated in Fig. 1, shows a good agreement between both results since the relative gap does not exceed 1.8%.

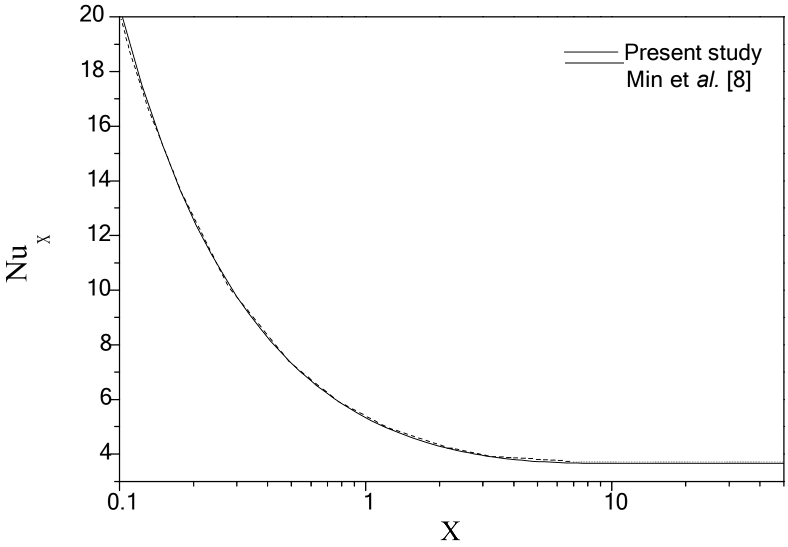

Fig. 1 Axial evolution of the local Nusselt number. Re = 50, Pr = 1, n = 1.

III. RESULTS AND DISCUSSION

The present study focuses on the analysis of the effect of neglecting viscous dissipation when the Carreau fluid is considered isoviscous and thermodependent.

Viscous dissipation is an energy source, represented by the Brinkman number (Br). Taking this function into account in the energy equation, leads to significant modifications on heat transfer behaviour, especially for viscous Newtonian and non Newtonian fluids.

A. *Case of a Isoviscous Fluid*

Fig. 2 represents the effect of the Brinkman number on the axial evolution of the Nusselt number, by considering both cases of wall heating (Br < 0) and wall cooling (Br > 0).

The figure shows a pronounced decrease of the Nusselt number from the inlet until reaching an asymptotic value which corresponds to the fully developed flow. For both heating and cooling, this value is single and is equal to 11.07, which is greater than the one obtained when viscous dissipation is neglected (Br = 0), i.e. 3.79.

Heat transfer is improved by the increase of the Brinkman number. Thus, neglecting viscous dissipation leads to undervalue heat transfer about 192% comparing to the case where viscous dissipation is neglected.

Note that in the case of wall heating (Br < 0), the curves present a discontinuity, with the existence of negative values of the Nusselt number due to the change in heat direction.

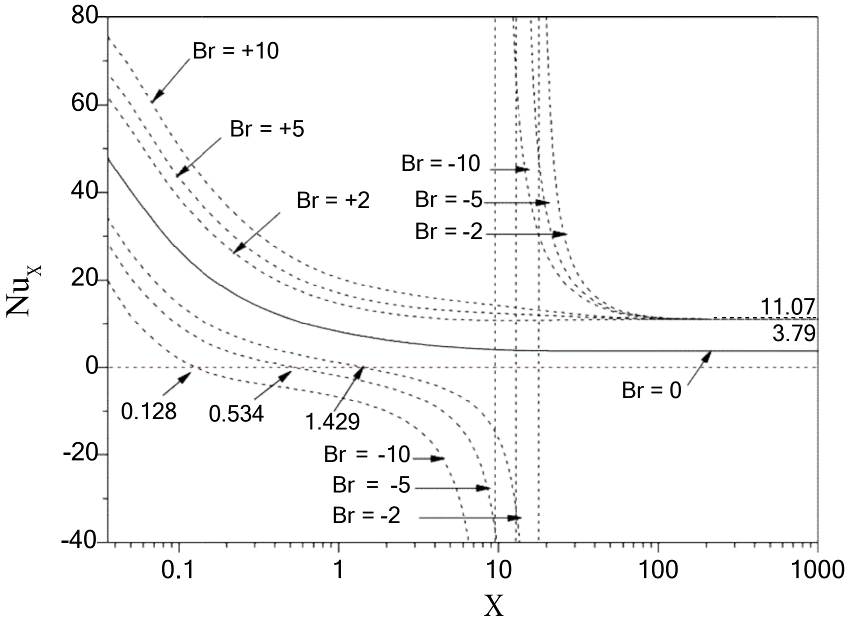

Fig. 2 Axial evolution of the local Nusselt number for various values of the Brinkman number. Re = 40, Pr = 10, n = 0.7, We = 20.

B. *Case of a Thermodependent Fluid*

The curves of Fig. 3 which represent the axial evolution of the Nusselt number when the fluid's apparent viscosity is thermodependent, show a decrease of the Nusselt number to reach different asymptotic values according to heating (Br < 0 ; a* > 0) or cooling (Br > 0 ; a* < 0) cases. Indeed, contrary to the case of a constant viscosity, an asymptotic value of the Nusselt number is obtained for each value of the Brinkman number as the fluid is temperature-dependent.

It is interesting to note also that in the developing region, the increase of the Brinkman number enhances heat transfer in the cooling case and worsens it in the heating case. However, in the fully developed region, heat transfer is improved when the Brinkman number decreases in absolute value, for both heating and cooling cases.

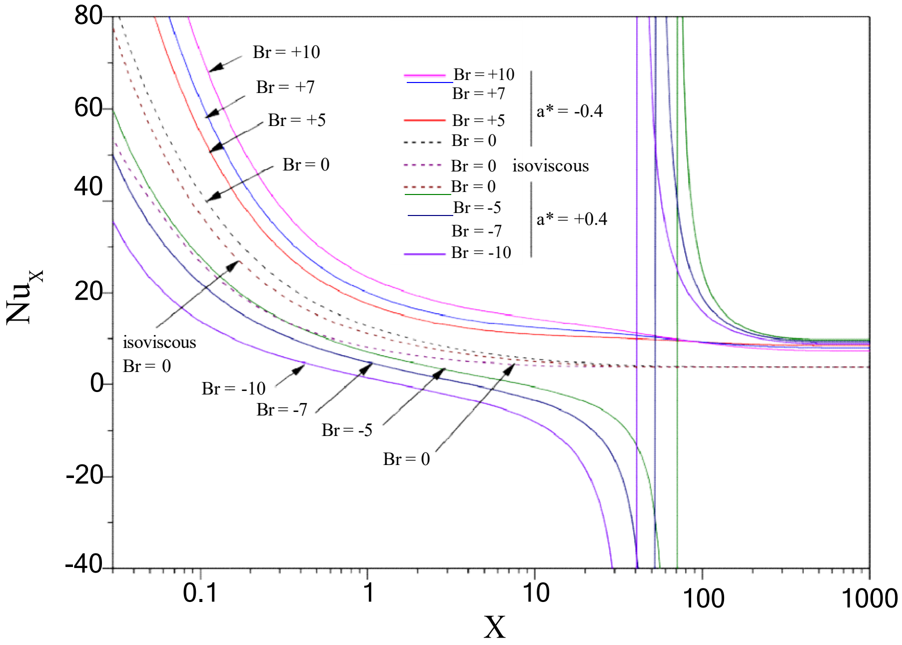

Fig. 3 Axial evolution of a temperature-dependent Carreau-Yasuda fluid's Nusselt number via the Brinkman number. n = 0.7, Re = 40, Pr = 10, We = 20.

IV. CONCLUSIONS

A numerical study based on the finite volume method was undertaken for a steady laminar forced convection flow of a Carreau fluid within a circular pipe maintained at a uniform wall temperature.

The study focused on the effect of viscous dissipation on heat transfer rate in the pipe, by considering an isoviscous fluid and a thermodependent one. The results show that heat transfer is strongly affected by viscous dissipation for both cases.

Thus, it is not rigorous to neglect viscous dissipation in calculation especially, when dealing with viscous fluids such as those obeying the rheological model of Carreau.

REFERENCES

[1] K. Khellaf, G. Lauriat, "Numerical study of heat transfer in a non-Newtonian Carreau-fluid between rotating concentric vertical cylinders," *J. Non-Newtonian Fluid Mech.*, vol. 89, pp. 45-61, 2000.

[2] F.M. Abbasi, T. Hayat, A. Alsaedi, "Numerical analysis for MHD peristaltic transport of Carreau–Yasuda fluid in a curved channel with hall effects," *J. Magnetism and Magnetic Materials*, vol. 382, pp. 104-110, 2015.

[3] F. Rousset, S. Millet, V. Botton, H. Ben Hadid, "Temporal stability of Carreau fluid flow down an incline," *J. Fluids Eng.*, vol. 129, pp. 913-920, 2007.

[4] S. Lounis, R. Rebhi, N. Hadidi, G. Lorenzini, Y. Menni, H. Ameur, N.A. Che Sidik, "Thermo-Solutal Convection of Carreau-Yasuda Non-Newtonian Fluids in Inclined Square Cavities Under Dufour and Soret Impacts," *CFD Letters*, vol. 14 (3), pp. 96-118 (2022).

[5] M. Bilal, I. Ullah, M.M. Alam, S.I. Shah, S.M. Eldin, "Energy transfer in Carreau Yasuda liquid influenced by engine oil with Magnetic dipole using tri-hybrid nanoparticles," *Scientific Reports*, vol. 13, Article number 5432, 2023.

[6] R.B. Bird, R.C. Armstrong, O. Hassager, *Dynamics of Polymeric Liquids*, Vol. 1 Fluid Mechanics, 2nd edtion, Wiley and sons, New York, 1978.

[7] S.V. Patankar, *Numerical heat transfer and fluid flow*, Hemisphere, New York, 1980.

[8] T. Min, H.G. Choi, J.Y. Yoo, H. Choi, "Laminar convective heat transfer of a Bingham plastic in a circular pipe-II. Numerical approach-hydrodynamically developing flow and simultaneously developing flow," *Int. J. Heat Mass Trans*, vol. 40, pp. 3689-3701, 1997.

NOMENCLATURE

Br	Brinkman number, $= \square_0 V_0^2 / k(T_0 \square T_w)$
C_p	specific heat at constant pressure, $J.kg^{-1}.K^{-1}$
D	pipe diameter, m
k	fluid thermal conductivity, $W.m^{-2}.K^{-1}$
L	pipe length, m
n	flow index
Nu	Nusselt number, $= \square \frac{1}{\square_m} \frac{\square\square}{\square R}\Big\|_{R=0.5}$
Pr	Prandtl number, $= \square_à C_p V_0 k D$
P^*	dimensionless pressure, $= p^* / \square V_0^2$
p^*	pressure, Pa
r	radial coordinate, m
R	dimensionless radial coordinate, $= r / D$
Re	Reynolds number, $= \square V_0 D / \square_0$
T	temperature, K
T_m	dimensional bulk temperature, K
T_0	inlet and reference temperature, K
T_w	wall temperature, K
U	dimensionless x-component velocity, $= V_x / V_0$
V	dimensionless r-component velocity, $= V_r / V_0$
V_x	x-component velocity, $m.s^{-1}$
V_r	r-component velocity, $m.s^{-1}$
V_0	inlet velocity, $m.s^{-1}$
We	Weissenberg number, $= \square D / V_0$
x	axial coordinate, m
X	dimensionless axial coordinate, $= x / D$

Greek symbols:

$\square$	density of the fluid, $kg.m^{-3}$
$\square$	shear rate, s^{-1}
$\square^*$	dimensionless shear rate, $= \square D / V_0$
$\square$	effective viscosity, $Pa.s^n$
$\square_{app}$	dimensionless effective viscosity, $= \square / K_0$
$\square_0$	viscosity at zero shear, Pa.s
$\square$	the relaxation time, s
$\square$	dimensionless temperature, $= (T - T_w) / (T_0 - T_w)$
$\square_m$	dimensionless mean temperature, $= (T_m - T_w)/(T_0 - T_w)$

ISSN: 1737-933484

Effect of Traffic Volume Variability on Road Noise Level Under Continuous and Heterogeneous Traffic Conditions

Abdessalem Jbara[#*1], Ahmed Komti[*2], Najah Kechiche[#3], Khalifa Slimi[*4]

[#]*Department of Transportation Technology, ISTLS, University of Sousse*
Riadh city, Sousse 4023, Tunisia

[1]j.abdesslem@yahoo.fr
[3]kechiche2000@gmail.com

[*]*LESTE laboratory, Department of Energy, ENIM, University of Monastir*
Ibn El Jazzar Street, Monastir 5035, Tunisia

[2]ahmedkomti568@gmail.com
[4]khalifa_slimi@yahoo.fr

Abstract— **Traffic noise disturbance was classified among the major transportation negative externalities since road traffic is the most prevalent source of urban noise. In general, this annoyance is strongly correlated with some traffic parameters, such as traffic volume, which remains the dominant factor that influences road noise levels in metropolitan areas. This paper reports a theoretical investigation to assess and analyze the effect of traffic volume variability on road noise levels under continuous and heterogeneous traffic flow conditions. At the first stage, a comparative study will be presented to select the most suitable traffic noise predictive model. In the second stage, the selected model will be coupled with the macroscopic first-order traffic model to investigate the effect of traffic volume variability on road noise levels. The main results indicated that the French NMPB-Roads-2008 model outperforms the German RLS-90 and the Italian CNR models in terms of noise level prediction. Therefore, compared to some experimental measurements, the NMPB-Roads-2008 model gives the lowest value of the root mean squared error (RMSE) and the highest values of the coefficient of determination (R^2) and the accuracy (Acc). Furthermore, the numerical simulation showed that the road traffic noise level increases with traffic volume until reaching a threshold value, beyond which the noise level remains almost stable. In this study, the threshold traffic volume was found to be equal to 1650 vehicles per hour, which corresponds to an average fleet velocity of 47.25 kilometers per hour and a road traffic density of 35 vehicles per kilometer.**

Keywords— **Road traffic, Noise level, Numerical simulation**

I. INTRODUCTION

In modern planning, noise protection is one of the fundamental requirements that should be respected before performing any kind of project aiming to install new infrastructure (roads, railroads, airports, and seaports). Besides, in environmental studies, noise impact assessment is an essential key for risk evaluation, identification of noise sources, simulation of mitigation measures, evaluation of the exposed population, and urban planning ([1], [2], [3], [4], [5], [6], [7], [8]). For all these reasons and according to the European Directive 2002/EC/49, noise impact studies are mandatory for all agglomerations with more than 250 000 inhabitants and for all major airports, roads, and railways [9].

Currently, noise assessment is commonly done in two ways. The first is based on direct measurements of noise level, while the second is based on simulation tools. When dealing with simulation tools, useful data for noise assessment is obtained by using noise prediction methods. In the case of road noise studies, applying these methods requires, in general, the knowledge of road traffic variables (i.e., average fleet velocity, vehicular density, and flow rate). Usually, these variables are measured on the roadside or calculated by using road traffic flow models.

Macroscopic road traffic flow models are frequently employed by traffic managers in order to get a more realistic estimation of the real-time traffic states on networks. These simple and robust models allow for solutions at a low computational cost [10]. Typically, the literature classifies these models into two main classes: the first and the higher order traffic flow models [11]. A first-order traffic model, commonly named the LWR model ([12], [13]), is more

ISSN: 1737-933484

adapted to continuous road traffic cases under equilibrium conditions, while higher-order traffic models are more efficient to model non-equilibrium traffic states observed mainly in congested situations [10]. It is worth noting that when applied to a hypothetical mid-block section, the LWR model and higher-order traffic models give similar results [11]. Furthermore, the LWR model is robust, simple, does not require too much input data, and guarantees that vehicular density and traffic volume remain consistent with the physical limits of the network at all points and at all times [14]. Along with these advantages, it generally provides satisfactory results in the case of continuous and balanced road traffic flow.

As road noise prediction models are of concern, there are several available ones to predict the sound levels from road traffic ([15], [16]). The early basic models are simple, and they need some traffic variables, including vehicular flow rate, average speed, heavy vehicle percentage, and distance between source and receptor. Among these models, we can quote those developed by Burgess [17], Griffiths and Langdon [18], Fagotti and Poggi [19], French C.S.T.B. [20], and Quartieri et al. [16].

Through the last few years and following even more extensive research, more developed and comprehensive models have appeared. Most of these noise level calculation models are regional and specific to countries such as ASJ in Japan [21], GIS in China [22], CORTN in the UK [23], CNR in Italy [24], RLS-90 in Germany [25], FHWA in the USA [26] Nord 2000 in the Nordic countries [27], StL-86 and SonRoad in Switzerland [28], ERTC in Thailand [29] and NMPB-roads in France [30]. Besides these models, others have been developed for the European Union, such as Harmonoise [31] and the most recent model, CNOSSOS-EU [32]. It is worth noting that the aspects related to sound propagation in CNOSSOS-EU are the same as those in NMBP-roads method. A more detailed comparison between several of these models can be found in [33], [34], [35], [36], [37], [38], and [39].

Traffic factors, road factors, vehicle factors, and human factors are the four main categories of variables that affect traffic noise levels [40]. Among traffic factors, on can cite traffic volume, traffic speed, traffic mix, traffic jams and bottle necks. The most important determining factor is the traffic volume, since the other factors are considered to be a result of the traffic volume fluctuations. Despite the strong dependency, the relationship between traffic volume and road noise level is non-linear and is controlled by a number of factors that are mostly related to road traffic conditions.

The current work aims to compare the most available road noise prediction models in the literature. The more accurate model will be coupled, thereafter, with the macroscopic first-order traffic model to investigate the effect of traffic volume variability on the road noise levels. The manuscript is organized as follows: Section 2 presents the adopted methodology. Section 3 displays the obtained results and discussion. Finally, Section 4 deals with some concluding remarks.

II. METHODOLOGY

A. *Comparative Analysis and Traffic Noise Model Selection*

The selection of a predictive model is essentially based on its accuracy. In this subsection, a comparative study was carried out in order to select the most suitable model for traffic noise prediction. To perform this task, 12 traffic noise models have been tested. It is worth noting that, for the sake of brevity, we have not exposed the mathematical formulation of each model. A more detailed review of these predictive models can be found in [15], [35], [38], [41] and [42].

The adopted procedure is to fix some control parameters, such as the distance from the lane axis (d), the heavy vehicle percentage, the free flow speed, the jam density, and the road capacity and then to plot the equivalent sound level (Leq) given by each model versus the traffic volume (Q). Moreover, some corrective factors, which usually strongly influence the behavior of the prediction in some particular conditions, are also neglected.

Fig. 1 shows a quantitative comparison between the results obtained by several road traffic noise predictive models as a function of traffic volume. As shown, the evolutions of the acoustic levels predicted by these models show almost the same shape, with a very notable increase for traffic volumes up to around 500 veh/h. Beyond this value, the evolutions show slower growth with respect to the traffic volume. On the same graph, it is easy to see that the higher acoustic levels are obtained by the ERTC and CSTB models, however, the lowest values are obtained by the model of Fagotti et al.

Table 1 provides some field measurements relative to the road traffic volumes (Q(veh/h)), heavy vehicle percentages (P(%)), as well as related equivalent noise levels (Leq). It should be noted that all of these measurements have been collected from Tunisian urban streets at different times of the day. Besides, the sound level measurements have been conducted in the vicinity of the same streets, at a distance of 5 mfrom the road's axes. Traffic measurements (i.e., traffic volumes and heavy vehicle percentages) will also be used by all the above-mentioned models in order to compare and select the most adequate model for traffic noise level prediction. According to a preliminary analysis, the noise levels estimated by the NMPB-2008, RLS90 and CNR models are the most suitable compared to those recorded in the field.

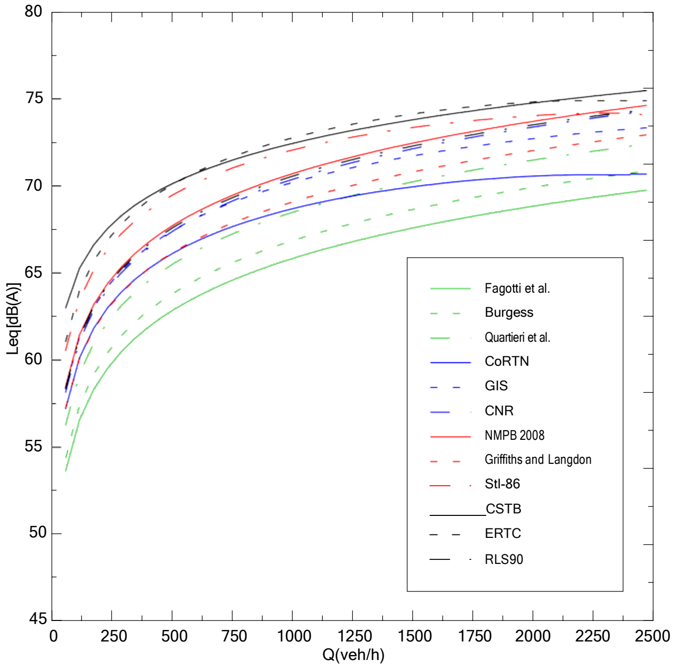

Fig. 1 Comparison between various traffic noise predictive models

TABLE I
COMPARISON BETWEEN MEASURED AND PREDICTED NOISE LEVELS BY NMPB-2008, CNR AND RLS90 MODELS

Q(veh/h)	P(%)	L_{eq}(dB(A))			
		Measurements	**NMPB-2008**	**CNR**	**RLS90**
660	1,6	74,98	71,75	70,11	71,95
480	0,8	69,5	68,56	68,57	69,54
690	11 ,3	73,96	72,30	71,92	71,37
510	10,6	68,79	69,27	70,51	70,04
830	23,4	78,65	76,25	74,39	75,45
640	19,3	70,92	71,90	72,58	71,23
740	18,7	70,92	71,39	73,14	71,84
580	15,4	70,13	71,08	71,70	70,71

In this step, we will select only one model among the three above models to predict, thereafter, the traffic noise level. Indeed, to perform this task, three statistical metrics including, the root mean squared error (RMSE), the coefficient of determination (R^2), and the accuracy (Acc) were employed to evaluate the performance of each model. These metrics are expressed as [43]:

$$\mathrm{RMSE} = \sqrt{\frac{1}{n}\sum_{i=1}^{n}\left(L_{eqi} - \hat{L}_{eqi}\right)^2} \quad (1)$$

$$R^2 = 1 - \frac{\sum_{i=1}^{n}\left(L_{eqi} - \hat{L}_{eqi}\right)^2}{\sum_{i=1}^{n}\left(L_{eqi} - \bar{L}_{eq}\right)^2} \quad (2)$$

$$\mathrm{Acc} = \frac{100}{n}\sum_{i=1}^{n} c_i \quad (3)$$

$$c_i = \begin{cases} 1, \text{if } \left|L_{eqi} - \hat{L}_{eqi}\right| \leq e \\ 0, \text{otherwise} \end{cases} \quad (4)$$

where L_{eqi}, $\hat{L}_{eqi}$, denote the measured, and estimated traffic noise level values for the i^{th} observation in the dataset, respectively, while $\bar{L}_{eq}$ denote the mean value of the measured noise levels, n is the number of sample data points, and e=±1dB(A) is the acceptable error value.

Table 2 depicts the calculation results of the root mean squared error (RMSE), the coefficient of determination (R^2), and the accuracy (Acc) for each predictive model under consideration. Indeed, it is well known that good model precision is implied by a lower RMSE value and higher R^2 and Acc values. In the present case, the lowest RMSE value and the highest R^2 and Acc values are shown for the NMPB-2008 model. Accordingly, it will be selected to be coupled with the macroscopic first-order traffic model in order to examine the effect of traffic volume variability on road noise levels.

TABLE 2
COMPARISON OF PERFORMANCE MEASURES FOR THE THREE TRAFFIC NOISE PREDICTIVE MODELS

	Traffic Noise Prediction Model		
	NMPB-2008	**CNR**	**RLS90**
RMSE	1.66	2.73	1.90
R^2	0.9264	0.5234	0.8517
Acc [±1 dB(A)]	62.5 %	12.5 %	37.5 %

B. *Modelling Approach*

In this part, a mathematical formulation based on the coupling between the macroscopic first-order traffic model (LWR model) and the French noise prediction model (NMPB-2008) will be constructed. We consider an area of dimensions L×L where each point is represented by its spatial coordinates (x, y) in a Cartesian coordinate system (o, x, y). We consider also a roadway of width Δy passes along the middle of the area under study.

Fig. 2 provides a schematic representation of the spatial grid used to perform the numerical simulation. Hence, the road is split into Nx uniform cells of dimension Δx, and the simulation time into Nt uniform time steps Δt. In this stage, each road cell indexed i is considered as a punctual noise emission source. Besides, the whole domain is subdivided into $N_x \times N_y$ uniform cells of dimensions Δx.Δy. Each cell center is considered as a point receiver R(i, j), located at a distance d_{SR} from the source S(i). The traffic volume at the entrance of the road section is denoted by Q_{in}(veh/h).

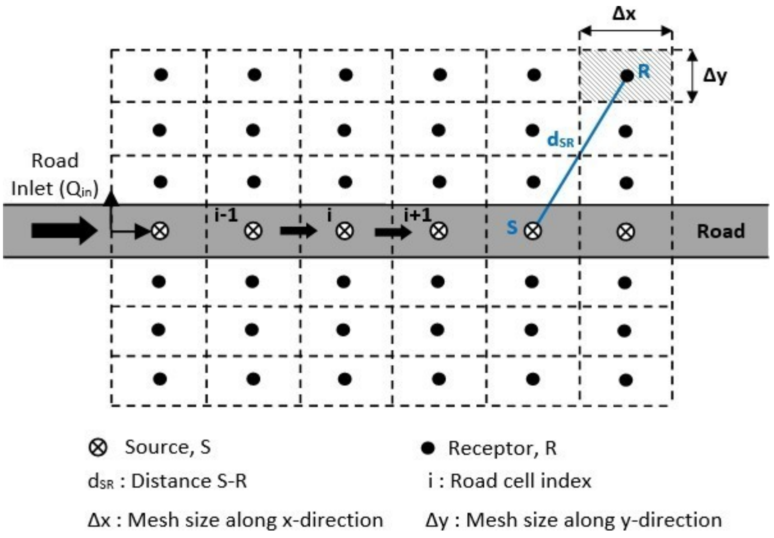

Fig. 2 Schematic representation of the spatial grid used in this study

1) *Road Traffic Modelling:*

On a road section, traffic flow is frequently variable in time and space, so the vehicular density and the mean fleet velocity are also variables from one road cell to another. This variability affects the noise level since it is strongly dependent on these traffic parameters. At this level, the road traffic modelling was introduced to consider these spatial and temporal variations.

In order to model the traffic flow on the road segment, the traffic is assumed to be in an equilibrium state and the lateral dynamics are negligible. Hence, the first-order traffic model proposed by [12] and [13] is expressed as:

$$\begin{cases} \frac{\partial\rho(t,x)}{\partial t} + \frac{\partial Q(t,x)}{\partial x} = 0 \\ Q(t,x) = \rho(t,x)V_f\left(1 - \frac{\rho(t,x)}{\rho_{max}}\right) \end{cases} \quad (5)$$

ρ(veh/km) denotes the vehicular density, and Q(veh/h) the vehicular flow rate. V_f(km/h) and ρ_{max}(veh/km) are the free flow speed and the jam density of the road segment. It is worth noting that, in this case, the equilibrium relationship between Q and ρ is parabolic.

The discrete form of the vehicular density, for each road cell i and each instant t+Δt, is stated as:

$$\rho(t+\Delta t,i) = \rho(t,i) + \frac{\Delta t}{\Delta x}[Q(t,i-1) - Q(t,i)] \quad (6)$$

Q(t, i) is the mean flow rate leaving the cell i to the cell i+1 during the time interval [t, t+Δt]. This flow rate is expressed using the following numerical scheme [44]:

$$Q(t,i) = \mathrm{Min}\{F_d[\rho(t,i)], F_s[\rho(t,i+1)]\} \quad (7)$$

$F_d[\rho(t,i)]$ and $F_s[\rho(t,i+1)]$ denote the local demand function of the cell i and the local supply function of the cell i+1 at time t, respectively. These two functions are expressed as follows:

$$F_d[\rho(t,i)] = \begin{cases} \rho(t,i).V_f\left(1 - \frac{\rho(t,i)}{\rho_{max}}\right) & \text{if } \rho(t,i) < \rho_c \\ Q_{cap} & \text{if } \rho(t,i) \geq \rho_c \end{cases} \quad (8)$$

$$F_s[\rho(t,i+1)] = \begin{cases} Q_{cap} & \text{if } \rho(t,i+1) < \rho_c \\ \rho(t,i+1).V_f\left(1 - \frac{\rho(t,i+1)}{\rho_{max}}\right) & \text{if } \rho(t,i+1) \geq \rho_c \end{cases} \quad (9)$$

where Q_{cap} and ρ_c represent the capacity and the critical density of the road section, respectively.

The initial conditions (i.e., at t=0) are chosen arbitrarily as follows:

- For i=1 (first cell of the road): $\rho(0, 1)=0$
- For i=2 (second cell of the road): $\rho(0, 2)=\rho_{max}/2$
- For i ∈ [3, N_x] (i. e. others cells): $\rho(0, i)=0$

It is interesting to note that the above described numerical approach provides the vehicular density ρ(t, i) and the flow rate Q(t, i) for any road cell i and at any time t if the following stability criterion, called the Courant-Friedrichs-Lewy (CFL) condition, is respected :

$$\frac{\Delta x}{\Delta t} \geq V_{max} \quad (10)$$

2) Road Noise Modelling:

The NMPB-2008 model is based on the breaking down sources into point sources. The calculation procedure is made by third-octave bands ranging from 100 Hz to 5 kHz.

According to the NMPB methodological guide [30], the sound levels in downward-refraction conditions ($L_{i,F}$) and in homogeneous conditions ($L_{i,H}$) for a propagation path and a given third-octave band are written as follows:

$$L_{i,F}(t,i,j,k) = L_{A,w}(t,i,k) - (A_{div}(i,j) + A_{atm}(i,j,k) + A_{sol,F}(i,j,k)) \quad (11)$$

$$L_{i,H}(t,i,j,k) = L_{A,w}(t,i,k) - (A_{div}(i,j) + A_{atm}(i,j,k) + A_{sol,H}(i,j,k)) \quad (12)$$

where $L_{A,w}$ [dB(A)] is the sound power level of the point source i given by [30]:

$$L_{A,w}(t,i,k) = [(L_{W/mLV}(t,i) + 10\log Q_{LV}(t,i)) \oplus (L_{w/mHV}(t,i) + 10\log Q_{HV}(t,i))] + 10\log[l(i)] + R(k) + 10\log(1 - C_a) \quad (13)$$

$L_{W/mLV}$ and $L_{W/mHV}$ are the power levels per unit of length of light and heavy vehicles, respectively [45]. Q_{LV} and Q_{HV} are the vehicular flow rates of light and heavy vehicles, respectively. l(i) is the length of the ith source line, R(k) is the road noise spectrum value standardized at 0 dB and A-weighted [45], and C_a is the sound absorption coefficient ranging from 0 to 1.

Since the traffic is heterogeneous, the flow rates of light and heavy vehicles can be expressed from the total flow rate, Q(veh/h), by using the percentage of heavy vehicles (P_{HV}):

$$Q_{LV}(t,i) = (1 - P_{HV})Q(t,i) \text{ and } Q_{HV}(t,i) = P_{HV}Q(t,i) \quad (14)$$

The attenuation due to the geometric divergence, A_{div} can be expressed as:

$$A_{div}(i,j) = 20\log(d_{ij}) + 11 \quad (15)$$

d_{ij}(m) denotes the distance between source S(i) and receiver R(i, j).

The attenuation due to the atmospheric absorption, A_{atm} is given by:

$$A_{atm}(i,j,k) = \frac{\alpha(k) d_{ij}}{1000} \quad (16)$$

α(k) is the coefficient of atmospheric attenuation at nominal median frequency of each third-octave band.

$A_{sol,H}$ and $A_{sol,F}$ are the attenuations due to the ground effect in homogenous and downward-refraction conditions, respectively. They depend on the ground absorption coefficient, as described in [30]. For the sake of conciseness, we did not provide the mathematical formulas for these two attenuations. Readers may find more in-depth information in the NMPB-2008 technical report [30].

The long-term sound level, $L_{i,LT}$ (dB) due to the source i, is written as [30]:

$$L_{i,LT}(t,i,j,k) = 10\log[p_o 10^{[0.1 L_{i,F}(t,i,j,k)]} + (1 - p_o) 10^{[0.1 L_{i,H}(t,i,j,k)]}] \quad (17)$$

p_o denotes the average occurrence probability of the downward-refraction conditions in a given propagation path.

The total sound level (in dB) at a receiver R(i, j) for a given third-octave band k is obtained by summing the sound contributions from all sources S(i) and their images S(i') by reflection on vertical obstacles [30]:

$$L_{eq,LT}(t,i,j,k) = 10\ \log[\sum_{i=1}^{NX} 10^{0.1\ L_{i,LT}(t,i,j,k)} + \sum_{i'=1}^{NX} 10^{0.1\ L_{iF,LT}(t,i',j,k)}] \quad (18)$$

Finally, the total sound level, in dB(A), is obtained by summing all levels in each third-octave band as follows [30]:

$$L_{Aeq,LT}(t,i,j) = 10\ \log[\sum_{k=1}^{18} 10^{0.1 L_{eq,LT}(t,i,j,k)}] \quad (19)$$

It is worth noting that, in the current study, the background sound level is taken equal to 30 dB(A).

3) Algorithm Implementation:

Table 3, provides the main parameters used in this investigation. Furthermore, the numerical procedure is iterative according to the following algorithm.

```
Begin
Input parameters and variables
  t=0
  Initializing problem variables
  Do while ($t \le t_{sim}$)
  Traffic calculation
    For i=1:$N_x$
    Calculate local demand and supply functions (8-9)
    Calculate mean vehicular flow rate (7)
    Calculate vehicular density (6)
    Calculate flow rates of light and heavy vehicles (14)
    End For
  Noise calculation
    For i=1: $N_x$
      For j=1: $N_y$
        For k=1:18
        Calculate sound power level (13)
        Calculate all attenuations (15-16)
        Calculate sound level in homogenous and downward-refraction conditions (11-12)
        Calculate long-term sound level (17)
        Calculate equivalent long-term sound level (Eq. 18)
        Calculate total sound level (Eq. 19)
        End For
      End For
    End For
  End do while
  t=t+$\Delta$t
Storage of results
End
```

TABLE 3
SIMULATION PARAMETERS

Parameter	**Value**
Free flow velocity	$V_f = 60$ km/h
Jam density	$\rho_{max} = 165$ veh/km
Critical density	$\rho_c = 82{,}5$ veh/km
Road capacity	$Q_{cap} = 2475$ veh/h
Road length	$L = 1000$ m
Source height	$H_S = 0{,}3$ m
Receiver height	$H_R = 2.1$ m
Mesh size	$\Delta x \times \Delta y = 50\ \text{m} \times 10\ \text{m} = 500\ \text{m}^2$
Number of points sources	$N_x = 20$
Number of points receivers	$N_x \times N_y = 20 \times 100 = 2000$
Time step	$\Delta t = 2.4$ s

III. RESULTS AND DISCUSSION

In this section, the simulation results will be presented and discussed. Indeed, we will analyze and discuss the road traffic as well as the noise simulation findings.

A. *Road Traffic Analysis*

Predicting traffic dynamics is the major goal of solving the first-order traffic model. This phase is crucial since it allows to know the spatiotemporal distribution of vehicle densities on the road segment under study. Furthermore, it provides information on the traffic flow's kinematics.

Fig. 3 depicts the time-space evolution of the vehicular density. In this case, at the beginning of the process (i.e., at t = 0), as the vehicular density of the first cell is chosen to be lower than that of the second cell, a shockwave is formed at the interface level between these two cells. The shock path is represented by a dotted line where the characteristic curves intersect to indicate the transition from a fluid traffic state to a denser one. In practice, this situation is observed when a fast-vehicle platoon joins a slow one or when stopping at a red traffic light.

Conversely, as the vehicular density of the third cell is lower than that of the second cell, a fan is formed to indicate the transition from a denser traffic state to a fluid one. At the beginning of the process, the characteristic curves intersect at a single point, and they diverge as time goes on. In practice, this situation is observed, for example, at the startup at a green traffic light.

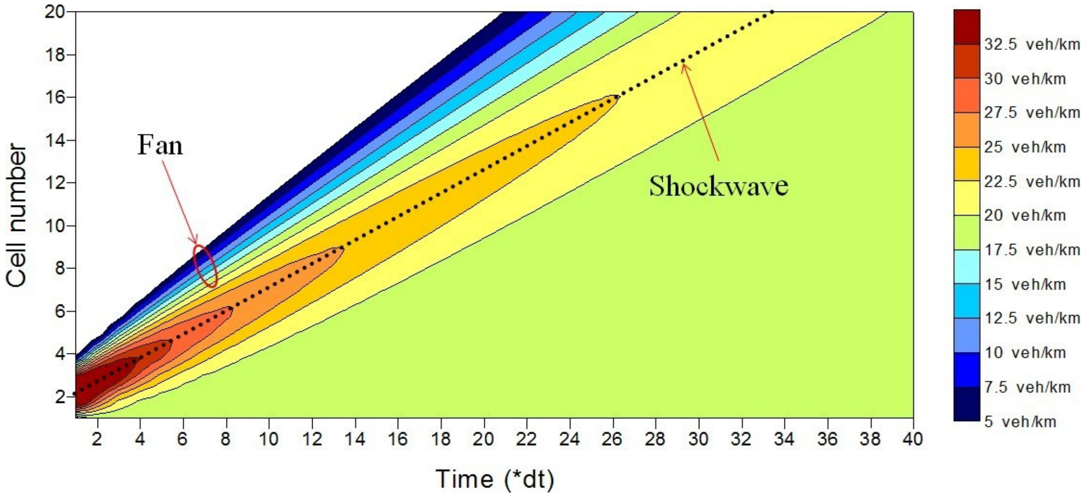

Fig. 3 Time-space evolution of the traffic density

In order to examine the effect of traffic volume variability at the road inlet on the traffic equilibrium state, we have plotted the temporal variations of the cell filling rates under three different traffic volumes: low, medium, and high. Cell filling rate is defined as the ratio of the vehicular density of the i^{th} road cell, $\rho(t, i)$ to the jam density, ρ_{max} at time t. This parameter provides an idea on the occupancy percentage of each cell of the road section. Hence, high values indicate that the cell is congested, while low values indicate fluid circulation.

$$\tau(t,i) = 100\,\frac{\rho(t,i)}{\rho_{max}} \qquad (20)$$

Fig. 4 presents the histograms of road cell filling rates at different simulation times and for three types of traffic volume: low, medium, and high. As shown by this figure, for low road traffic volume, the majority of road cell filling rates have the same value from t=30Δt, the road traffic is fluid, and, therefore, the traffic equilibrium state was rapidly established compared to medium and high road traffic volumes.

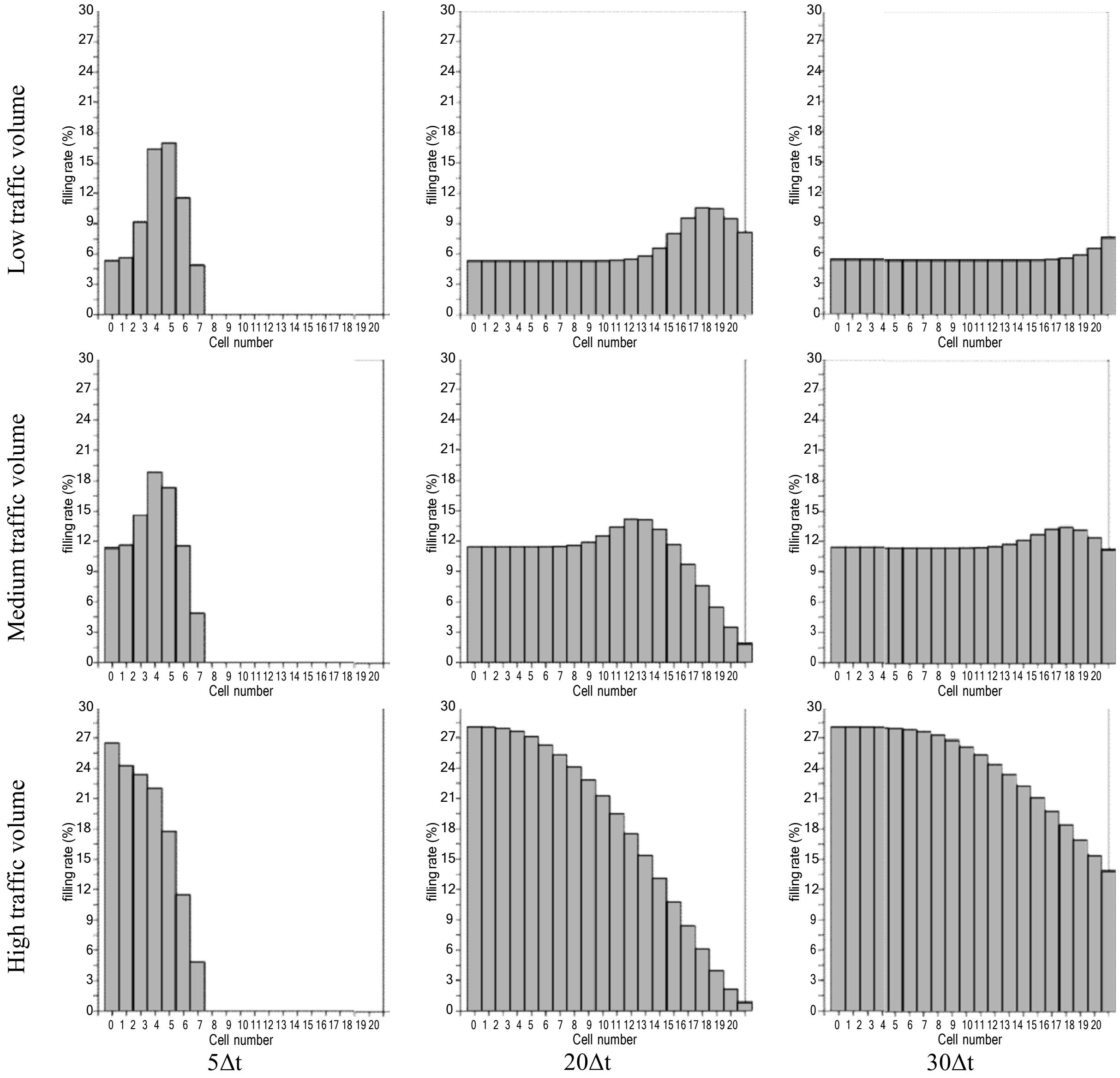

Fig. 4 Histograms of road cells filling rates at different simulation times, for three types of traffic volume: low, medium and high

B. *Road Traffic Noise Analysis*

It is well known that traffic noise levels increase with traffic volumes. According to [46], when doubling the traffic volume, the hourly A-weighted continuous equivalent noise level increases by about 3 dB(A) if the average speed does not change. Despite this trend, the relationship between these two variables is not linear since increasing traffic volume is generally balanced by a drop in average fleet velocity.

Fig. 5 illustrates the traffic noise level variations versus traffic volume at midway (x=L/2) and for different y distances from the road axis. By examining this figure, it can be noticed that the three curves present the same shape. Moreover, when doubling the traffic volume, the noise level rises from about 1.5 to 4 dB(A) depending on the y distance from the road axis. Furthermore, each curve is subdivided into three parts. When traffic volume is below 600 veh/h, the noise level variation shows high growth. For traffic volumes ranging from 600 to 1650 veh/h, the growth is substantially slower. However, from 1650 veh/h, the noise level remains almost stable and practically insensitive to changes in traffic volume. Once traffic volume reaches a threshold value, the increase in vehicular flow rate is counterbalanced by a decrease in average fleet velocity, which explains the noise level stability. In this case, noise level stability appears when the traffic volume reaches approximately 1650 veh/h.

Fig. 6 displays the time variations of (a) traffic noise level, (b) average fleet velocity, and (c) traffic volume for road cells 5, 10, and 15. The noise level reaches maximum values of 39 dB(A), 52 dB(A), and 68 dB(A) at times 6.5Δt, 17.5Δt and 28.5Δt, respectively. Beyond these times, the noise level remains stable. By looking at the average velocity and traffic volume curves, we can perceive that these three times (6.5Δt, 17.5Δt and 28.5Δt) correspond to an average fleet velocity of 47.25 km/h and a traffic volume of 1650 veh/h. Under these conditions, the road traffic density is found to be equal to 1650/47.25≈35 veh/km.

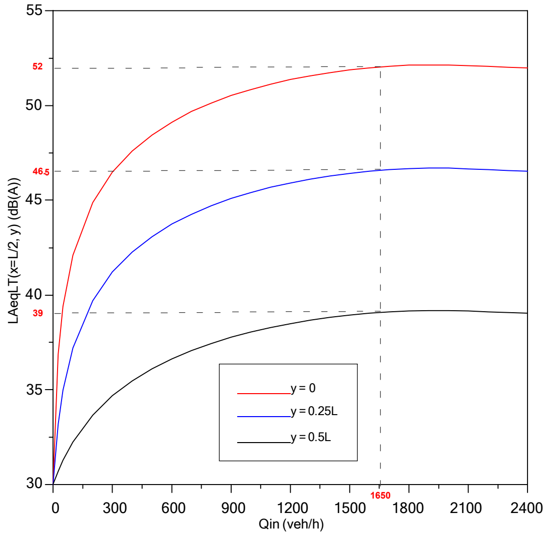

Fig. 5 Traffic noise level versus traffic volume at the road inlet at midway location (x=L/2) and for different transverse coordinates (y)

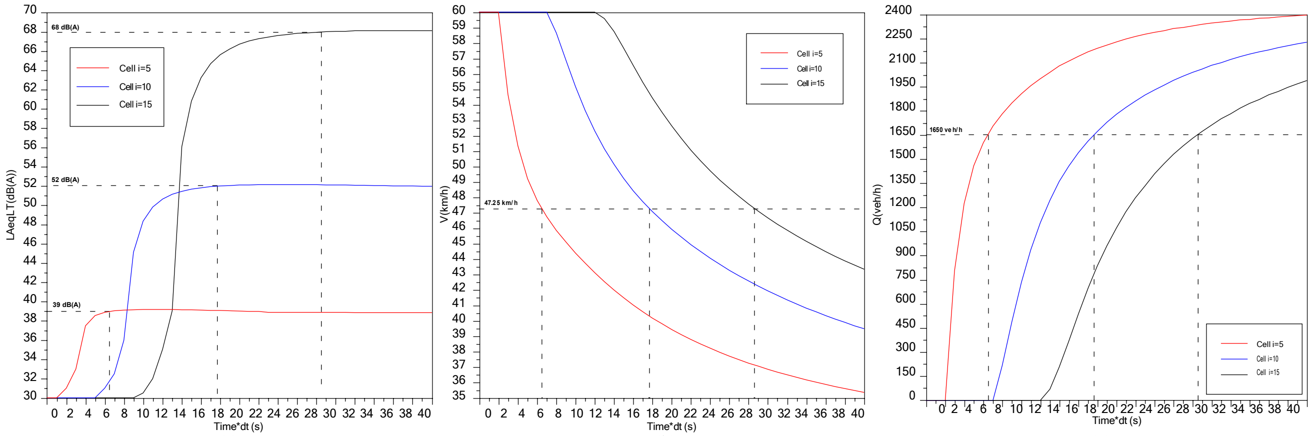

(a)
(b)
(c)

Fig. 6 Variations over time of (a) road noise level, (b) average fleet velocity, and (c) traffic volume in the road cells number 5, 10, and 15

IV. CONCLUSIONS

In this paper, we have investigated the effect of traffic volume variability on road noise levels under continuous and heterogeneous traffic conditions. Firstly, a comparative study has been carried out to select the most satisfactory traffic noise prediction model for our case. Secondly, road traffic simulation has been performed to predict the road traffic variables, including traffic density, average fleet velocity, and traffic volume along the studied road segment. Thirdly, the road traffic simulation results were used, thereafter, by the French road noise prediction model (NMPB-Roads-2008) in order to study the influence of traffic volume variability on road noise levels. Accordingly, the following conclusions were drawn:

i. The comparison between several transportation noise models shows that the French outdoor noise prediction model, NMPB-Roads-2008, is the most suitable one to predict traffic noise level compared to German (RLS-90) and Italian (CNR) methods. Thereby, compared to some field measurements, the NMPB-Roads-2008 model gives the lowest value of the root mean squared error (RMSE) and the highest values of the coefficient of determination (R^2) and the accuracy (Acc).

ii. The traffic noise level increases with the traffic volume until a threshold value (in our case, 1650 veh/h) beyond which the traffic noise level remains almost stable. This threshold value of traffic volume corresponds to an average fleet velocity of 47.25 km/h and a traffic density of 35 veh/km.

ACKNOWLEDGMENT

The authors express their gratitude to everyone who contributed to the elaboration of this study, with special recognition to the staff members of the Department of Transportation Technology of the Higher Institute of Transportation and Logistics of Sousse (ISTLS).

REFERENCES

[1] R. B. Ranpise, and B. N. Tandel, “Urban road traffic noise monitoring, mapping, modelling, and mitigation: A thematic review,”. *Noise Mapping,* vol. 9, pp. 48-66, April 2022. doi: https://doi.org/10.1515/noise-2022-0004

[2] G. Rey-Gozalo, J. M. B. Morillas, and D. M. González, “Analysis and Management of Current Road Traffic Noise,” *Current Pollution Reports,* vol. 8, pp. 315–327, December 2022. doi: https://doi.org/10.1007/s40726-022-00234-7

[3] P. Aumond, A. Can, V. Mallet, B. Gauvreau, and G. Guillaume, “Global sensitivity analysis for road traffic noise modelling,” *Applied Acoustics,* vol. 176, 107899, May 2021. doi: https://doi.org/10.1016/j.apacoust.2020.107899

[4] Y. Lan, H. Roberts, M. Kwan, and M. Helbich, “Transportation noise exposure and anxiety: A systematic review and meta-analysis,” *Environmental Research,* vol. 191, 110118, December 2020 doi: https://doi.org/10.1016/j.envres.2020.110118

[5] H. Wang, Z. Wu, X. Yan, and J. Chen, “Impact Evaluation of Network Structure Differentiation on Traffic Noise during Road Network Design,” *Sustainability,* vol. 15, 6483, April 2023. doi: https://doi.org/10.3390/su15086483

[6] S. S. A. Dehrashid, H. R. Jafari, and A. Amjadi, “Computing a psychological health risk assessment model for road traffic noise,” *Journal of Transport & Health*, vol. 29, 101570, March 2023. doi: https://doi.org/10.1016/j.jth.2023.101570

[7] E. Murphy, and E. A. King, “Scenario analysis and noise action planning: Modeling the impact of mitigation measures on population exposure,” *Applied Acoustics*, vol. 72, pp. 487-494, July 2011. doi: https://doi.org/10.1016/j.apacoust.2010.10.006

[8] P. H. T. Zannin, and D. Q. de Sant’Ana, “Noise mapping at different stages of a freeway redevelopment project. A case studyin Brazil. *Applied Acoustics,* vol. 72, pp. 479-486, July 2011. doi: https://doi.org/10.1016/j.apacoust.2010.09.014

[9] J. R. Gloaguen, A. Can, M. Lagrange, and J. F. Petiot, “Road traffic sound level estimation from realistic urban sound mixtures by Non-negative Matrix Factorization,” *Applied Acoustics*, vol. 143, pp. 229-238, January 2019. doi: https://doi.org/10.1016/j.apacoust.2018.08.018

[10] G. Costeseque, and J. P. Lebacque, “A variational formulation for higher order macroscopic traffic flow models: Numerical investigation,” *Transportation Research Part B: Methodological*, vol. 70, pp. 112-133, December 2014. doi: https://doi.org/10.1016/j.trb.2014.08.012

[11] R. Mohan and G. Ramadurai, “State-of-the art of macroscopic traffic flow modeling,” *International Journal of Advances in Engineering Sciences and Applied Mathematics,* vol. 5, pp. 158–176, August 2013. doi: https://doi.org/10.1007/s12572-013-0087-1

[12] M. J. Lighthill, and G. B. Whitham, “On kinematic waves II. A theory of traffic flow on long crowded roads,” *Proceedings of the Royal Society A, Mathematical, Physical and Engineering Scie*nces, vol. 229, pp. 317-345, May 1955. doi: https://doi.org/10.1098/rspa.1955.0089

[13] P. I. Richards, “Shock waves on the highway,” *Operations Research*, vol. 4, pp. 42-51, February 1956. doi: https://doi.org/10.1287/opre.4.1.42

[14] L. Leclercq, “Dynamic traffic modeling and applications to road noise estimation,” Thesis, National Institute of Applied Sciences of Lyon, France, 2002.

[15] J. Quartieri, G. Iannone, C. Guarnaccia, S. D'Ambrosio, A. Troisi and T. Lenza, “A Review of Traffic Noise Predictive Noise Models,” in *Proc. MECHANICS '09, 2009,* p. 9.

[16] C. Guarnaccia, J. Bandeira, M. C. Coelho, P. Fernandes, J. Teixeira, G. Ioannidis, and J. Quartieri, “Statistical and semi-dynamical road traffic noise models comparison with field measurements,” *AIP Conference Proceedings*, vol. 1982, pp. 1-6, July 2018. doi: https://doi.org/10.1063/1.5045445

[17] M. A. Burgess, “Noise prediction for urban traffic conditions-related to measurements in the Sydney Metropolitan Area,” *Applied Acoustics*, vol. 10), pp. 1-7, January 1977. doi: https://doi.org/10.1016/0003-682X(77)90002-0

[18] I. D. Griffiths and F. J. Langdon, “Subjective Response to road traffic noise,” *Journal of Sound and Vibration,* vol. 8, pp. 16-32, July 1968. doi: https://doi.org/10.1016/0022-460X(68)90191-0

[19] C. Fagotti, and A. Poggi, “Traffic noise abatement strategies. The analysis of real case not really effective,” in *Proc. of the 18th International Congress for Noise Abatement*, 1995, p. 10.

[20] W. K. Lui, K. M. Li, P. L. Ng, and G. H. Frommer, “A comparative study of different numerical models for predicting train noise in high-rise cities,” *Applied Acoustics,* vol. 67, pp. 432-449, May 2006. doi: https://doi.org/10.1016/j.apacoust.2005.08.005

[21] K. Yamamoto, “Road traffic noise prediction model ASJRTN-Model 2008: Report of the Research Committee on Road Traffic Noise,” *Acoustical Science and Technology*, vol. 31, pp. 2-55, January 2010. doi: https://doi.org/10.1250/ast.31.2

[22] B. Li, S. Tao, R.W. Dawson, J. Cao, and K. Lam, “A GIS based road traffic noise prediction model,” *Applied Acoustics,* vol. 63, pp. 679-691, June 2002. doi: https://doi.org/10.1016/S0003-682X(01)00066-4

[23] S. Givargis, and M. Mahmoodi, “Converting the UK calculation of road traffic noise (CORTN) to a model capable of calculating $L_{Aeq,1h}$ for the Tehran's roads,” *Applied Acoustics,* vol. 69, pp. 1108-1113, Novembre 2008. doi: https://doi.org/10.1016/j.apacoust.2007.08.003

[24] G. B. Canelli, K. Gluck, and S. Santoboni, “A mathematical model for evaluation and prediction of the mean energy level of traffic noise in Italian towns,” *Acta Acustica united with Acustica*, vol. 53, pp. 31–36, May 1983.

[25] E. Wetzela, J. Nicolas, P. Andre, and J. Boreux, “Modelling the propagation pathway of street-traffic noise: practical comparison of German guidelines and real-world measurements,” *Applied Acoustics*, vol. 57, pp. 97-107, June 1999. doi: https://doi.org/10.1016/S0003-682X(98)00048-6

[26] S. Y. Lee Cynthia, G. G. Fleming, G. S. Anderson, and C. W. Menge, “FHWA Traffic Noise Model, Version 1.0: User’s Guide,” Federal Highway Administration, United States, Tech. Rep. FHWA-PD-96-009, 1998. Available: https://rosap.ntl.bts.gov/view/dot/8920

[27] H. G. Jonasson, and S. Storeheier, « Nord 2000. New Nordic prediction method for road traffic noise,” Swedish National Testing and Research Institute. Tech. Rep. ISBN: 91-7848-853-2, 2001. Available: http://www.diva-portal.org/smash/record.jsf?pid=diva2%3A1190134&dswid=-5640.

[28] K. Heutschi, “SonRoad: New Swiss road traffic noise model,” *Acta Acustica United with Acustica* vol. 90, pp. 548-554, 2004. Available: https://www.dora.lib4ri.ch/empa/islandora/object/empa:3523

[29] T. Suksaard, P. Sukasem, S. M. Tabucanon, I. Aoi, K. Shirai, and H. Tanaka, “Road traffic noise prediction model in Thailand,” *Applied Acoustics,* vol. 58, pp. 123-130, October 1999. doi: https://doi.org/10.1016/S0003-682X(98)00069-3

[30] SETRA, “Road noise prediction: 2 - Noise propagation computation method including meteorological effects (NMPB 2008),” SETRA edition, Methodologic guide, France, 2009.

[31] S. Erik, V. M. Dirk, D. Jérôme, and R. Foort, “The Harmonoise Sound Propagation Model,” *Acta Acustica united with Acustica* vol. 97, pp. 62-74, February 2011. doi: https://doi.org/10.3813/AAA.918387

[32] S. Kephalopoulos, M. Paviotti, F. Anfosso-Lédée, D. V. Maercke, S. Shilton, and N. Jones, “Advances in the development of common noise assessment methods in Europe: The CNOSSOS-EU framework for strategic environmental noise mapping,” *Science of The Total Environment*, vol. 482–483, pp. 400-410, June 2014. doi: https://doi.org/10.1016/j.scitotenv.2014.02.031

[33] F. Ibili, E. K. Adanu, C. A. Adams, S. A. Andam-Akorful, S. S. Turay, and S. A. Ajayi, “Traffic noise models and noise guidelines: A review,” *Noise & Vibration Worldwide,* vol. 53, pp. 65-79, January 2022. doi: https://doi.org/10.1177/09574565211052693

[34] J. Chebil, J. Ghaeb, M. A. Fekih, and M. H. Habaeb. “Assessment of Road Traffic Noise: A Case Study in Monastir City,” *Jordan Journal of Mechanical and Industrial Engineering*, vol. 13, pp. 149 – 154, October 2019.

[35] H. N. Rajakumara, and R. M. M. Gowda, “Road traffic noise prediction models: A review,” *International Journal of Sustainable Development and Planning*, vol. 3, pp. 257 – 271, 2008. doi: https://doi.org/10.2495/SDP-V3-N3-257-271

[36] N. Garg, and S. Maji, “A critical review of principal traffic noise models: Strategies and implications,” *Environmental Impact Assessment Review,* vol. 46, pp. 68-81, April 2014. doi: https://doi.org/10.1016/j.eiar.2014.02.001

[37] P. R. Nandurkar, M. P. Nawathe, and C. R. Patil, “Study of traffic noise models in the evaluation of traffic noise levels: A review,” *International Journal of Engineering Sciences & Research Technology,* vol. 4, pp. 497-504, February 2015.

[38] S. de Lisle, “Comparison of Road Traffic Noise Prediction Models: CoRTN, TNM, NMPB, ASJ RTN,” *Acoustics Australia* vol. 44, pp. 409–413, June 2016. doi: https://doi.org/10.1007/s40857-016-0061-8

[39] J. Khan, M. Ketzel, K. Kakosimos, M. Sørensen, and S. S. Jensen, “Road traffic air and noise pollution exposure assessment - A review of tools and techniques,” *Science of the Total Environment,* vol. 634. Pp. 661-676, September 2018. doi: https://doi.org/10.1016/j.scitotenv.2018.03.374

[40] T. Subramani, M. Kavitha, and K. P. Sivaraj, “Modelling of Traffic Noise Pollution,” *International Journal of Engineering Research and Applications,* vol. 2, pp. 3175-3182, January 2012.

[41] R. Patel, P. K. Singh, and S. Saw, “Recent advancements in the challenges and strategies of globally used traffic noise prediction models,” *Environmental Science and Pollution Research,* vol. 29, pp. 48168–48184, May 2022. doi: https://doi.org/10.1007/s11356-022-20693-1

[42] A. Petrovici, C. Tomozei, F. Nedeff, O. Irimia, and M. P. Lehadus, “Review on the Road Traffic Noise Assessment,” *Journal of Engineering Studies and Research,* vol. 22, pp. 81-89, 2016.

[43] D. Singh, S. P. Nigam, V. P. Agrawal, and M. Kumar, “Vehicular traffic noise prediction using soft computing approach,” *Journal of Environmental Management,* vol. 183, pp. 59-66, December 2016. doi: https://doi.org/10.1016/j.jenvman.2016.08.053

[44] S. K. Godunov, I. Bohachevsky, “Finite difference method for numerical computation of discontinuous solutions of the equations of fluid dynamics,” *Matematičeskij sbornik*, vol. 47, pp. 271-306? 1959.

[45] SETRA, “Road noise prediction: 1 - Calculating sound emissions from road traffic,” SETRA edition, Methodologic guide, France, 2009.

[46] W. Yanga, J. He, C. He, and M. Cai, “Evaluation of urban traffic noise pollution based on noise maps,” *Transportation Research Part D: Transport and Environment*, vol. 87, 102516, October 2022. doi: https://doi.org/10.1016/j.trd.2020.102516

Conférence Internationale sur les Sciences Appliquées et l'Innovation (CISAI-2023)
Proceedings of Engineering & Technology-PET-Vol 77

Optimizing Worker and Vehicle Allocation for Ground Handling at Airports

Siwar Moumni*[1], Abdelkarim Elloumi *[2]

* *Quantitative Methods Department, Faculty of Economic Sciences and Management of Sfax,*
Sfax, Tunisia

[1] moumni.siwar@hotmail.fr
[2] abdelkarim.elloumi@laposte.net

***Abstract*— One of the currently established extensions of Vehicle Routing Problems is the vehicle routing problem with worker and vehicle synchronizations (VRPWVS) with multiple synchronization constraints. It plays a major role in many industries such as logistics, healthcare or airport ground handling. Synchronization arises when efficiently routing workers to jobs, while meeting each job's time window. In large airports, which cover extensive areas and adhere to strict security regulations, workers rely on vehicles to commute between jobs. This demands the synchronization of movements in both time and space to ensure efficient operations. Furthermore, the vehicles act as a mobile unit, capable of transporting several workers together to various job sites or tasks. This feature promotes effective resource utilization and fosters a sense of teamwork and collaboration among the workers.**

This paper addresses Vehicle Routing Problem with Multiple Synchronization Constraints presented by a mathematical formulation by using spatio-temporal networks as the basis, an efficient modelling approach is used to capture and represent five distinct types of synchronization. These encompass various aspects, such as motion synchronization and load synchronization, allowing a complete and efficient representation of the synchronization dynamics within the system.

***Keywords*— Vehicle Routing Problem, Worker Assignment, Ground Handling, Multiple synchronization constraints, Mixed-integer problem.**

I. INTRODUCTION

Given the rapidly growing volume of air traffic, efficient ground operations are a critical aspect of airport management, encompassing a wide range of activities that are essential for the smooth functioning of an airport. An efficient management of the airport infrastructures is therefore crucial in order to avoid congestions and delays which are causes for high costs and customer dissatisfaction. Poor planning of ground handling is one of the main sources of delays [5]. Ground handling consists of those services which are necessary to prepare the aircraft for its next flight and are performed at the gates or at parking positions [5]. Such services include baggage loading and unloading, interior cleaning of the aircraft and refuelling. Since ground handling tasks, from now on simply denoted as tasks, are interdependent, any delay could propagate to other tasks. Missing the due date of a task might lead to a flight delay, which translates to penalty costs and reduced quality service for the ground handler. The vehicles act as a crucial link that enables seamless coordination between the workers and the various job sites. They serve as a mobile platform, allowing workers to efficiently reach their designated locations, perform tasks, and move between different work areas as needed. This communication and shared mobility provided by the vehicles contribute to the overall efficiency and productivity of the workforce, ensuring that tasks are executed in a timely and coordinated manner. In order to achieve effective planning, it becomes imperative to establish a well-coordinated synchronization between the workers and the vehicles. This

ISSN: 1737-933484

synchronization plays a pivotal role in optimizing operations and achieving desirable outcomes. Moreover, synchronization promotes better communication and collaboration among the workforce and vehicle operators. It facilitates real-time updates and adjustments, enabling the planning team to respond swiftly to unforeseen changes or emergencies. Ultimately, a well-executed synchronization between workers and vehicles enhances productivity, minimizes downtime, reduces operational costs, and contributes to a more efficient and successful planning process. It is a critical element in achieving smooth and optimized operations within any complex system that involves the coordination of human resources and vehicular assets. Despite its importance in the real world, the synchronization of various units is very rare in the vehicle routing problem (VRP) literature [9],[13] especially when it comes to movement and load synchronization.

An increasing number of researchers are studying vehicle routing problems (VRPs) and their variants considering real-life applications and scenarios. The practical relevance and challenging nature of the Vehicle Routing Problem (VRP) have motivated the operations Research community to consider different practical requirements and problem variants throughout the years. No literature contextualises synchronisation among other types of problem aspects of the VRP, increasing ambiguity in the nomenclature used by the community.

In this research, we investigate the Ground handling operations for the outgoing flights on airport, which includes the assignment of the workers to the carousels and deals with routing worker and vehicles in an airport ground handling setting.

II. RELATED WORKS

Scheduling ground handling means have received less attention than other resources, both in industrial solutions and scientific literature. Expensive resources like aircraft or crews. Also, an increasing number of researchers are studying vehicle routing problems (VRPs) and their variants considering real-life applications and scenarios. Furthermore, with the rapid growth in the processing speed and memory capacity of computers, various algorithms can be used to solve increasingly complex instances of VRPs. Vehicle Routing Problems (VRPs) is a family of Combinatorial Optimization Problems generally used to solve different issues in transportation systems. Since the first definition of the VRP by Dantzig and Ramser in [Dantzig and Ramser, 1959] which serve for developing a model to minimize travel distance for homogeneous trucks supplying oil from a central hub to multiple gas stations. Several variants have been proposed throughout the years in order to deal with various practical applications and challenges related to transportation.

This includes the original VRP with additional characteristics used to model customers' preferences and requirements like time windows, pickup and delivery services, as well as constraints imposed on the vehicles like limited travel times, multiple depots, multiple periods, etc. A multitude of precise methodologies have been introduced to address the Vehicle Routing Problem (VRP), predominantly relying on sophisticated techniques such as branch-and-cut and column generation [12]. On the other hand, concerning more approximate approaches, several methods have been put forth. These include Tabu Search (TS) [11] [4], Simulated Annealing (SA) [7], and Ant Colony Optimization (ACO) [1], [6], [3] ,[2]. These approximate methods, while not providing exact optimal solutions, offer efficient and effective means to tackle the complexities of VRP, making them valuable tools for real-world applications where computational efficiency is essential.

A. Vehicle Routing Problems (VRP) and Its Diverse Problem Variants

1) VRP:

Vehicle Routing stands as an intensely studied and demanding field in combinatorial optimization. Particularly in market sectors where transportation costs significantly impact the value added to goods, employing effective optimization tools to minimize these expenses can lead to substantial overall cost reductions, as previously demonstrated. Over the past few decades, numerous surveys and studies have been conducted, delving into this problem and its various forms [10].

The Vehicle Routing Problem (VRP) constitutes a wide-ranging class of combinatorial optimization challenges that involves finding optimal routes for a fleet of vehicles originating from one or multiple depots. The objective is to serve a number of geographically dispersed points, referred to as customers. These vehicles are managed by designated crews, commonly known as drivers, and they traverse the road network to reach the customers efficiently. The ultimate goal of solving the VRP is to determine a set of routes, where each route is exclusively covered by a single vehicle that begins and concludes its journey at its assigned depot. This ensures that all customer requirements are met, operational constraints are adhered to, and the overall transportation cost is minimized. As a fundamental problem in logistics and operations management, the VRP has practical significance in various industries where efficient routing of vehicles is crucial. By devising optimal solutions, businesses can reduce transportation costs, enhance customer service, and streamline their overall operations. Consequently, extensive research has been conducted on VRP and its numerous variants over the years to tackle real-world challenges and devise efficient algorithms to obtain optimal solutions.

2) VRP's Diverse Problem Variants:

Numerous and diverse variants of the VRP have been developed to address this need. A comprehensive overview of these VRP variants can be found in the book [13].

The mentioned literary sources cover various VRP variants extensively. Nonetheless, none of them provide the capability to incorporate both workers and vehicles within specified timeframes simultaneously. Authors Thomas et al [15] generated an extended classification of Vehicle Routing Problem (VRP) variants, building upon the initial hierarchy proposed by Weise et al [8]. This new framework is rooted in a contemporary understanding of the VRP landscape, reflecting the state of the field during the time they conducted their research. By revisiting and augmenting the existing categorization, the authors aimed to capture the evolving nuances and complexities present in the modern VRP literature, thus providing a more comprehensive and up-to-date taxonomy of VRP variations and their interconnections. Expanded hierarchy is shown in Fig.1.

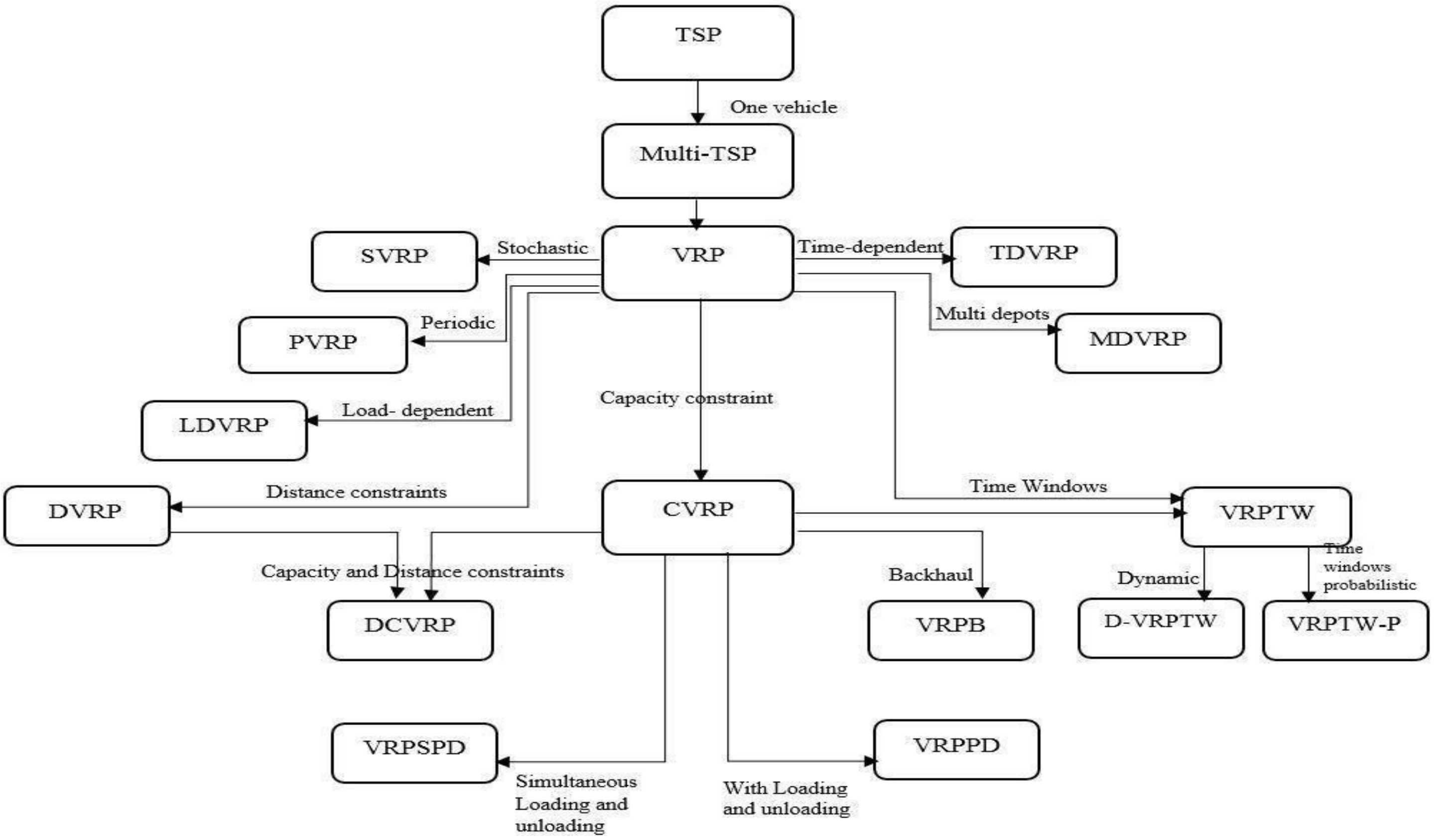

Fig. 1. VRP Variants

The following text in this paper is a summary of common VRP variants, there exists different variants of the VRP, the figure 1 below shows the connections existing between them. The arrows in this graph link between two problems and indicates that there is an extension; for instance, the VRP is an extension of the TSP and Multi-TSP, while CVRP is an extension of the VRP and a lot of extensions like it is showing in the figure: the multi-depot vehicle routing problem (MDVRP) is another variant of the VRP, the periodic vehicle routing problem (PVRP), The distance constrained vehicle routing problem (DVRP),the distance-constrained capacitated vehicle routing problem (DCVRP),The vehicle routing problem with pick-ups and deliveries (VRPPD),The Vehicle routing problem with simultaneous pickups and deliveries (VRPSPD),The vehicle routing problem with backhauls (VRPB),the vehicle routing problem with time windows (VRPTW),the vehicle routing problem within time windows-probabilistic (VRPTW-P),The stochastic vehicle routing problem with soft time windows (SVRPSTW),the dynamic vehicle routing problem with fuzzy time windows (DVRPFTW),the load-dependent vehicle routing problem(LDVRP).

B. Solutions for VRPs

Numerous researchers have explored algorithms to implement various VRP variants, which can be categorized as exact or heuristic algorithms.

Sandhya [17] provided an insightful description of algorithmic solutions for the VRP and its variants. This segment presents a comprehensive depiction of algorithmic solutions tailored to address the Vehicle Routing Problem (VRP) and its diverse variations. It offers an in-depth insight into the methodologies employed to tackle the intricacies of VRP and its multifaceted challenges. Through a detailed exploration of these algorithmic approaches, it provides a profound understanding of how researchers and experts have strived to devise effective strategies for optimizing routes, managing resources, and enhancing overall operational efficiency in the context of the VRP and its various forms, as illustrated in the following Fig.2:

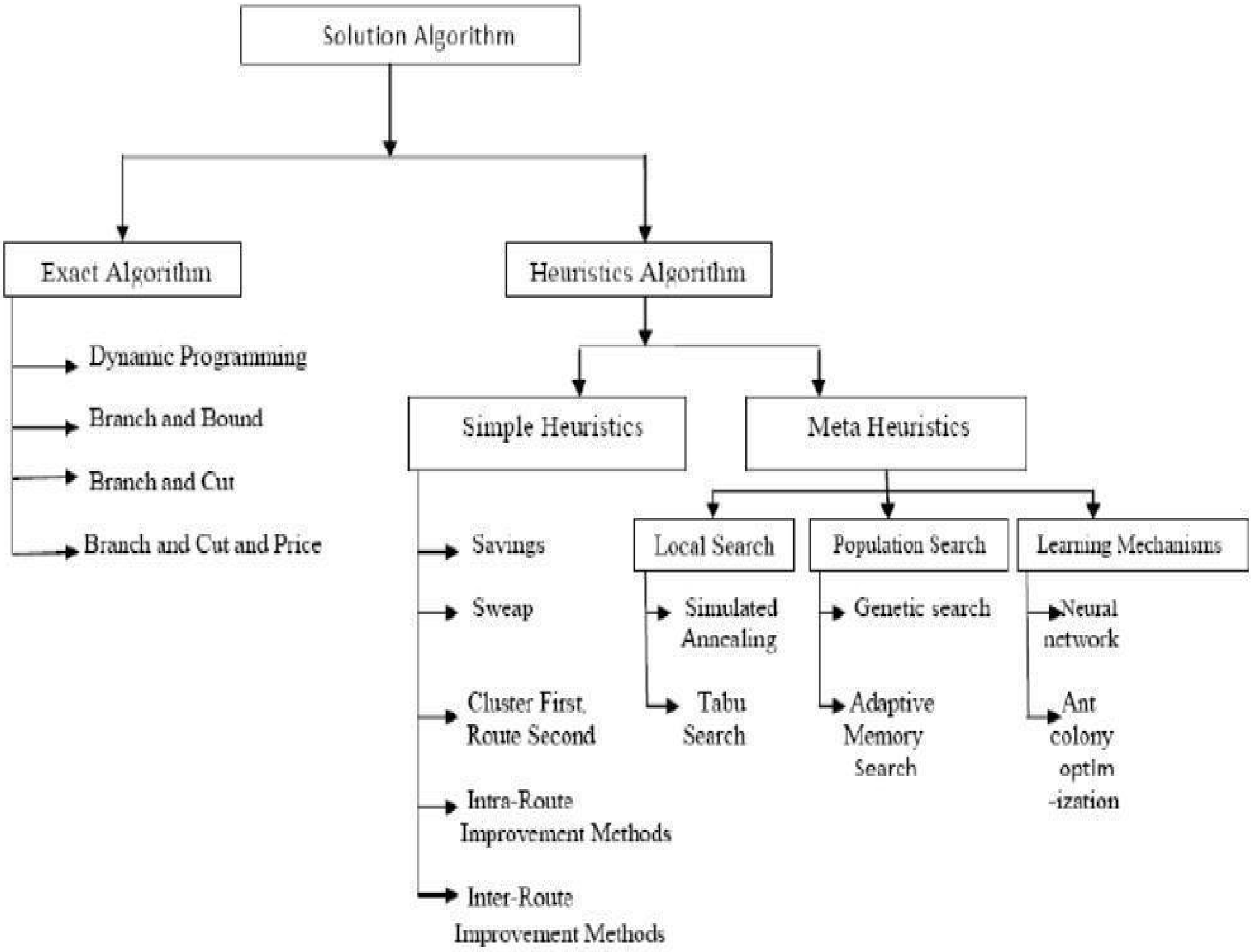

Fig. 2. Solutions VRP

ISSN: 1737-933484

III. STATEMENT OF THE PROBLEM

A. Description

Ground handling planning involves a blend of routing, assignment, and scheduling challenges, this planning is essential for all aircraft. The tasks are performed by teams of workers and grouped into teams making sure they have an adequate qualification to perform the assigned tasks [8]. Since the tasks are located at different parking positions, we have to plan a route for the workers, so that they are present at the locations of the tasks in time to carry them out and for expediting the process. An execution mode defines the number of workers needed to perform the task within a given time frame. Some of the tasks can be performed in more than one execution mode. Modes that demand more workers to complete a task also take less time. Teams may only carry out tasks that involve a mode requiring a number of workers equal to the number of team members [5]. Furthermore, the number and duration of these jobs vary based on factors such as the aircraft type, airline, destination, and passenger count. In compliance with apron security regulations and to maximize worker efficiency, a worker's waiting time before and after a job's execution should be limited to a defined upper threshold, usually around 10 minutes. If a worker remains unassigned to a new job within this maximum waiting time, they are required to return to the depot. The availability of each worker is contingent upon their designated shift, and at the commencement and conclusion of their respective shifts, they are stationed at a depot. This setup guarantees a systematic and well-organized deployment of workers during their working hours. It ensures that workers are efficiently placed and ready to undertake tasks according to their scheduled shifts, facilitating smooth and coordinated operations.

B. Our Model

We propose the model that deals with this problem this formulation based on a time-space network:

$$\text{Minimize} \qquad \alpha.\sum_{\substack{h\in J\\ w\in W}} \sigma_h.\sum_{tgT_h^s}(t - ES_h) \qquad + \beta.\sum C_W^W + \qquad \gamma.\sum_{k\in k} C_k^k$$

The objective function of this model aims to minimize three components: the sum of weighted job delays, the sum of the tours completed by workers, and the sum of the tours' durations for vehicles. To achieve this, the model includes various constraints that can be categorized into different clusters:

Job synchronization constraints where each job is initiated precisely once in a single mode, worker synchronization constraints ensures that every worker departs from and returns to the depot, vehicle synchronization constraints: this condition grants vehicles the flexibility to either depart from the depot or remain stationed there. However, if vehicles leave the depot, they must subsequently return. Besides the movement synchronization constraints for shared travel arcs, the number of workers must be at least equal to the number of vehicles to ensure at least one driver per vehicle. Additionally, the number of workers on the same arc should not exceed the capacity of the vehicles. Movement synchronization is necessary only when the travel time on a travel arc exceeds zero. Additionally, the model comprises variable declarations to represent the necessary parameters and entities involved in the optimization process. load synchronization guarantees the preservation and accurate delivery of all transferred loads between different units. To further enhance load synchronization, the concept is expanded to distinguish between active load (e.g., workers) and passive load, as explained in Fink et al. [12].In Our paper , we covers both types of load synchronization in which we will consider the passive load in our example (the baggage).This constraint ensures that the quantity of baggage demanded for an aircraft must not exceed the capacity of the vehicle responsible for transferring it. In other words, the vehicle designated to handle the baggage should have enough space to accommodate the requested amount without surpassing its own capacity limit. This safeguards against overloading the vehicle and ensures that the baggage transfer process is carried out efficiently and safely.

C. Results

All experiments are run on a Windows 10 platform with a 3.4 gigahertz CPU and 12 gigabyte RAM and on a single thread. The MILP is solved with the off-the-shelf solver IBM CPLEX 12.7.1 and is implemented in the programming language C++ and using the Visual Studio 2019.We use data arbitrarily; we can observe that the solution value of the MILP is not bed, but our objective is to enhance the current approach by implementing more efficient methods such as heuristics and metaheuristics. These advanced techniques are intended to yield results that come close to achieving optimality in our problem-solving process. By leveraging these powerful algorithms, we aim to significantly improve the quality of our solutions and achieve better outcomes in tackling complex optimization challenges.

IV. SUMMARY AND CONCLUSIONS

The practical importance of Vehicle Routing Problems (VRPs) in real-life scenarios has been increasingly recognized, leading to a surge in research interest in recent years. Scholars and researchers have been actively investigating various aspects of VRPs to optimize real-world logistics and transportation operations. Early research efforts predominantly focused on traditional cost-related objectives, notably the minimization of total cost and travel distance. These objectives are crucial in achieving cost-effective and efficient routing solutions, and they have served as the foundation for many VRP studies. However, with evolving complexities in modern logistics and transportation, researchers have started exploring multiple objectives to address diverse real-world challenges. These multiple objectives may include minimizing delivery time, maximizing resource utilization, considering environmental impacts, or satisfying specific customer requirements. As a result, the ongoing research on VRPs is advancing our understanding of complex logistics problems and paving the way for innovative solutions that can significantly enhance the efficiency, sustainability, and overall performance of transportation systems in the real world. To address the VRP with synchronizations at airports, there is a need for researchers to create publicly available datasets and develop effective and efficient methods to tackle these challenges.

REFERENCES

[1] B.Bullnheimer,R. F. Hartl, and C.Strauss," An improved ant system algorithm for the vehicle routing problem". *Annals of operations research*, 89 :319-328, 1999.

[2] B.Oreschko, M.Schultz, and H.Fricke,"Skill analysis of ground handling staff and delay impacts for turnaround modeling*", Air Transp. Oper*, pp. 310-318,2011.

[3] B.Yu, Z.-Z.Yang, and B. Yao," An improved ant colony optimization for vehicle routing problem", *European journal of operational research*, 196(1) :171-176, 2009.

[4] E.Taillard," Parallel iterative search methods for vehicle routing problems", Networks, 23(8) :661-673,1993.

[5] G.Dall'Olio, R.Kolisch," "Scheduling and Routing Workers Teams for Ground Handling at Airports with Column Generation." *Book of Extended Abstracts*: 107.

[6] H.Kawamura,M. Yamamoto, T. Mitamura, K.Suzuki, and A.Ohuchi," Cooperative search based on pheromone communication for vehicle routing problems". *IEICE transactions on fundamentals of electronics, communications and computer sciences,* 81(6) :1089-1096,1998.

[7] I. H. Osman,"Meta strategy simulated annealing and tabu search algorithms for the vehicle routing problem". *Annals of operations research*, 41(4) :421-451,1993.

[8] J.G.Feliu ,"*Models and methods for the City Logistics : The Two-Echelon Capacitated Vehicle Routing Problem*",Thesis · May 2008.

[9] M. Drexl," Synchronization in Vehicle Routing A Survey of VRPs with multiple synchronization constraints". *Transportation Science*, 46(3), 297–316, (2012).

[10] M.Fink ,M. Frey ,F. Kiermaier and R.Kolisch ,"Synchronized worker and vehicle routing for ground handling at airports*," Canadian Operational Research Society/INFORMS 2015 Joint International Meeting. 2015.*

[11] M.Gendreau, A.Hertz, and G. Laporte, "A tabu search heuristic for the vehicle routing problem. *Management science*, 40(10) :1276-1290,1994.

[12] P.Toth, D. Vigo," *Vehicle routing : problems, methods, and applications*",2nd ed. MOS-SIAM series on optimization, SIAM,2014.

[13] R.Lahyani, M. Khemakhem, and F. Semet,"Rich vehicle routing problems:From a taxonomy to a definition" . *European Journal of Operational Research*, 241(1), 1–14,2015.

[14] S.-Y.Tan, ,W.-C.Yeh," The Vehicle Routing Problem: State-of the- Art Classification and Review". *Applied Scien*ces.11, 10295, 2021.

[15] T. Režnar, T., J Martinovič,K. Slaninová,E. Grakova, &V.Vondrák, (2017). Probabilistic time-dependent vehicle routing problem. *Central European Journal of Operations Research*, 25, 545-560.

[16] T.Weise ,A. Podlich and C. Gorldti," Solving real-world vehicle routing problems with evolutionary algorithms. *In Natural intelligence for scheduling, planning and packing problems* (pp. 29-53). Berlin, Heidelberg: Springer Berlin Heidelberg.2009

[17] V.K.Sandhya, "Issues in Solving Vehicle Routing Problem with Time Window and its Variants using Meta heuristics-A Survey". International Journal of Engineering and Technology, 3(6), 668-672, (2013).

Optimizing the Maintenance Planning for Water Distribution Networks: new model extensions

Afef Jalleb*[1], Abdelkarim Elloumi *[2], Racem Mellouli *[3]

* *Quantitative methods department, Faculty of Economic Sciences and Management of Sfax, Tunisia*

[1] afef.jalleb@gmail.com
[2] abdelkarim.elloumi@fsegs.usf.tn
[3]racem.mellouli@fsegs.usf.tn

***Abstract*— A water transmission system moves water from water supply points to various areas where there is a fluctuating need for water for household, business, and industrial purposes. A system comprises of pipelines that connect water supply sources, pumping stations, and water demand points. One of the biggest issues facing human society is the management of water resources. The nonlinearities in physics and frequently binary character of decisions make it difficult to solve the optimization challenges that arise in water networks. Water distribution systems, including all water utility components for the distribution of finished or potable water using gravity storage feed or pumps through distribution equalizing storage, must be managed well in order to ensure good management of water resources. Additionally, good management of all construction (structures, pipe, equipment) necessary for the collection, transportation, pumping, treatment, and storage must be ensured. C1hoosing which leaky pipes to replace in order to reduce pressure-driven leakage while staying within a certain budget is a design problem that is discussed in this paper, along with the problem of fixing a pipe break. It is suggested that new strategies based on simulation optimization be used to solve these issues. A network from the literature is used to offer extensive test results for the suggested solution algorithms**.

***Keywords*— water resources management, water distribution system, Pipe replacement, pipe repairing, water shortages.**

I. INTRODUCTION

The water distribution system [1] is an important infrastructure network that is crucial to providing communities, homes, and businesses with clean, safe water. It includes a sophisticated system of reservoirs, pumps, valves, pipes, and treatment facilities that work together to deliver water reliably and effectively from the source to the end users. An adequate and consistent supply of potable water for uses like drinking, cooking, sanitation, irrigation, and industrial processes is the main goal of a water distribution system. Water

ISSN: 1737-933484

extraction from a natural source, such as rivers, lakes, or groundwater aquifers, usually marks the start of the system. Then, this water is purified to ensure that it satisfies the required quality standards. A city or region’s network of pipes, connecting different distribution points like water mains, pumping stations, and storage reservoirs, distributes the water after it has been treated. Considerations like population density, geographic topography, and water demand are taken into account during the network’s careful design to ensure equitable and effective distribution. Water pressure and flow are controlled by valves and pumps strategically positioned throughout the distribution system to make sure it reaches every consumer with enough force.

During times of low demand, excess water is kept in storage reservoirs or water towers to ensure a steady supply during times of high demand or emergencies. Modern water distribution systems include monitoring and control systems that enable operators to keep an eye on water quality, pressure levels, and quickly spot and fix any leaks or system failures. Advanced technologies are increasingly being used to enhance system performance, find anomalies, and boost overall effectiveness. Examples include remote sensors, telemetry, and data analytics. The longevity and dependability of the system depend on effective maintenance and routine upgrades to the water distribution infrastructure. This includes the installation of smart technologies for real-time monitoring and management, pipe replacement, valve upkeep, pump upgrades, and smart technology implementation. Overall, maintaining public health, fostering economic growth, and supporting different facets of daily life all depend on the water distribution system. To guarantee a sustainable and resilient water supply for communities now and in the future, careful planning, engineering, and ongoing management are required. This study presents a new way for selecting and organizing maintenance tasks for a water distribution system. It considers various low-cost maintenance options, such as pipe replacement [3] , pipe repairing [2], and temporary shut-down of pipeline pumps. Due to shifting demand, there are additional expenditures associated with the water shortages. The inclusion of dynamic sets in the issue parameters, particularly the sub-sets of the pipes between (1) inserted in the network, (2) removed or (3) in spare parts, presents a challenge in terms of mathematical formulation. This is different from traditional optimization problems, where the data sets representing the resources, procedures, or actions that must be managed have rather static cardinalities. To get around this problem, state variables that must be updated from one period to the next in a rolling planning horizon and in accordance with the set of combinatorial decisions to be made are included. The complexity of the problem is increased when there are several factors that decide whether to perform maintenance. Due to the latter, it is now possible to use sophisticated Mixed Integer Programming (MIP) [4] modelling techniques. The maintenance options can be more closely linked using an expanded version of our core mathematical approach. It should be noted that the model has assignment variables that link certain pipelines to recurrently updated edges. It is also looked at whether or not new pipelines of various sizes could be installed. In a real-world scenario that is based National Water Exploitation and Distribution Company, the suggested method is employed to produce promising results.

II. THE WATER DISTRIBUTION NETWORK

Delivering water to consumers with the proper quality, quantity, and pressure is the goal of the water distribution system. The infrastructure that transport water from its source to its destination are referred to as the water distribution system together. Figure 1 shows the water flow from the source to the consumer:

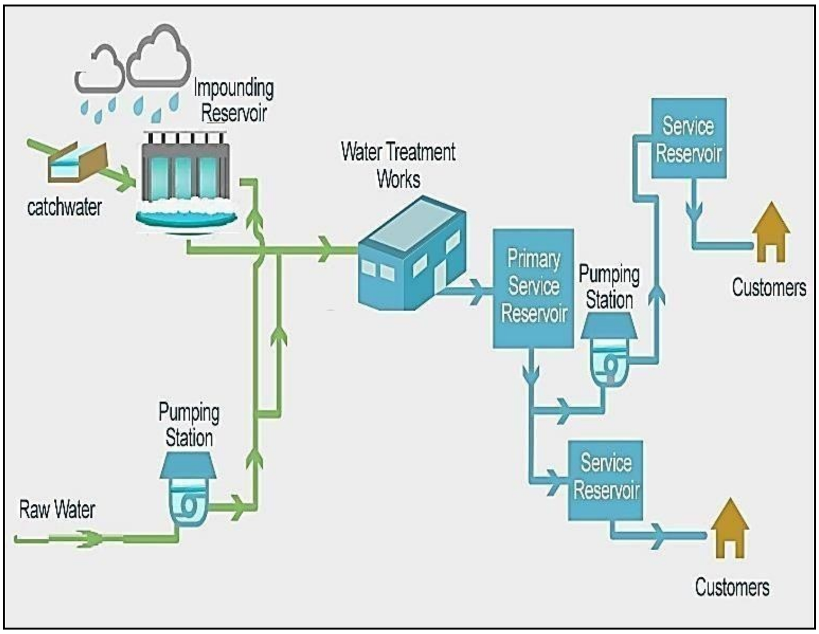

Fig.1 water network

The three main steps in the supply of fresh water are raw water collection, water purification, and distribution. Large transfer mains and tunnels transport untreated water from impounding reservoirs and raw water to water treatment facilities. Treated water is then pumped through substantial trunk mains or tunnels to fill reservoirs, and it then travels by gravity through the distribution system to a variety of structures, including residential and commercial buildings, hotels and restaurants, factories and warehouses, among others, before reaching the location where it was intended to be delivered.

A. *literature review and problem formulation*

Today, operations research is a technique for applying scientific approaches to decision-making. It can also be considered science in the sense that it describes, comprehends, and predicts the behavior of systems, particularly man-machine systems. Among the several strategies suggested by researchers thus far:

A water distribution system is described by the American Water Works Association as" including all water utility components for the distribution of finished or potable water using gravity storage feed or pumps through distribution equalizing storage." Both the initial capital expenditures and ongoing operating, maintenance, and repair costs for the water distribution network service to end customers are high; designers aim to lower the system's overall cost. However, because there are so many factors that can affect cost, it is quite challenging to find a water distribution system solution that is minimally expensive. Optimization of water distribution system design is a well-established research field, which has been extremely productive since the end of the 1980s. Its primary focus is to minimize the cost of a proposed pipe network infrastructure.[3],[5] More details about the use of water lines from storage to its end (stand post/ household tap etc.) are called distribution lines.[6] A water transmission system transports water from sources of supply to various locations where there is a varying water demand types (residential, commercial, and industrial uses) [7].

A system consists of sources of water supply, pumping stations and demands for water, all connected by pipelines. Shamir [8] created a methodology for the most effective design and/or operation of a water distribution system that will work under one or more loading circumstances. The decision factors may be design variables, like pipe diameters, or control variables, like heads and flows. The initial design cost, operating costs, performance measurements in terms of physical attributes, and sanctions for breaking limitations are all examples of objective functions. A modified Newton-Raphson method utilizing sparse matrix techniques is used to derive the flow solutions. Combining the generalized reduced gradient and penalty approaches produces optimization. Many different techniques are used in the field of research to analyze and examine a wide range of subjects. Karpouzos [9] develops and presents a genetic optimization strategy to reduce the overall cost of a pumping irrigation network, which includes the cost of electricity and pipeline investments. The hydraulic limitations (pressure and velocity requirements) are handled by specially customized elements of evolutionary algorithms, and the commercial pipe widths are represented by discrete value coding of variables.

In order to improve the efficiency of drinking water networks, Gratien et all [10] develop a model for branched configurations of pipes, which optimizes pumping schedules by taking into account electricity tariffs, pumps characteristics and network constraints on a daily basis Joe et all [3] consider an operational problem of pump scheduling and the design problem of leaky pipe replacement. New approaches for these problems based on simulation optimization are proposed as solution methodologies. For the pump scheduling problem, a novel decomposition technique uses solutions from a simulation based sub-problem to guide the search. For the leaky pipe replacement problem, a knapsack-based heuristic is applied. A new strategy developed by Dridi et all [11] for pipe renewal based on a cost function is presented. The strategy allows the minimization of a cost function while also considering hydraulic criterion and it was tested on a short planning horizon of five years. The pipe number to be replaced and the optimal moment for renewal are identified using three different optimization techniques such as Island Genetic Algorithm, Niched Pareto Genetic Algorithm 2, and Non-dominated Sorting Genetic Algorithm-II.

B. *the costs of repairing*

Shamir [5] described a method that forecasts the failure rate of newly installed pipes using a separate study and the history of previous main breaks to determine how the frequency of breaks will evolve over time if the pipe were left alone. The ideal replacement date is calculated using these projections, cost information, and a discount rate that takes inflation into account. Dandy and Engelhardt [6] represent the use of the genetic algorithm technique to determine a near-optimal plan for replacing water supply pipes, with the goal of minimizing the present value of capital, repair, and damage expenses. The examined water distribution system, which is being optimized for maintenance, has two types of retained vertices: water source nodes $s \in S$ (a small number) with given suppliable water flow rate capacities, and numerous aggregated demand nodes used to satisfy detailed requests. The latter are aggregated demand nodes known as distribution junction nodes. Each junction node has a time indexed demand, and each edge (pipeline) has a changing maximum flow rate capacity based on the installed pipe size, the evolving needs and the time-indexed consequences of maintenance on the network. A set of expected times for high pipeline failure probability is calculated and known ahead of time for each network edge. A maintenance action must be decided at these dates and/or after a temporary decision with restricted allowed flexibility is made. A maximum number of repairments must finish with replacement, and a maximum number of consecutive periods of pipeline close-up must terminate with a repairing or replacement operation. Let Crp_i, W_{ipt} and C^{w}_{t}be respectively the repairing costs of pipeline $i\ (for\ i \in E)$, the replacement costs in pipeline i with spare pipe $p\ (for\ p \in P)$ during period t, and the unitary water shortage cost during period t. The water demand of vertex $k \in V$ at period t is noted d_{kt}. This is a data sample used to describe the problem, which has the characteristics of a dynamic multi-flow problem with maintenance decisions and a retreated cost criteria under a cumulative budget, spare pipe, and other technical constraints.

III. THE NEW PROPOSED MIXED INTEGER PROGRAMMING MODEL

The decision variables include x_{it} that represents the repairing decision on pipe i in period t, y_{ipt} as the replacement decision of the pipe of edge i with a new pipe p at period t, C_{it} as the close-up state decision. Last but not least, L_{kt} stands for the unmet demand, which is the water loss volume or water shortage for vertex k at period t. Other technical variables are involved such that those related to the deliverable flow rate through the network edges and their related flow rate capacities. Through the objective function, our method reduces the total cost of maintaining and replacing pipelines as well as those of water shortages.

$$\sum_{i}^{E} \sum_{t}^{T} \left(Crp_i + \sum_{p}^{P} W_{ipt}\, y_{ipt} \right) + \sum_{k}^{V} \sum_{t}^{T} C^{w}_{t}\, L_{kt}$$

Failure events, pipe status, edge and vertices status, assignment uniqueness, pipeline closure states, maintenance options, network flows (deliverable flows, flow capacity), water availability, water loss, and budgetaryconstraints are all subject to our enforcement throughout the model. It would be feasible to provide appropriate maintenance planning while taking into consideration all of these complexity-increasing factors. The proposed method was tested on many numerical instances of data drawn from real-world contexts (certain parameters were provided by the Tunisian water business SONEDE). The computation Time increases in proportion to the size of the problem, reaching 1464 seconds (for 3 sources, 50 junction nodes, 70 pipelines, and 210 pipes in the system). From the first 50 to 600 seconds, the ideal solution appears throughout the solver rum with $n \leq 70$ edges. For all solutions (" optimum found"), the relative GAP was equal to 0. Furthermore, despite the inclusion of numerous binary variables (principle and dummy), the linear bound is around 0.2% to the optimum. These positive signs demonstrate the effectiveness of the proposed mathematical model.

IV. CONCLUSIONS

Reduced pipeline repair and replacement costs are critical for effective resource allocation and budget use. Water scarcity must be minimized in order to ensure a stable water supply and meet consumer needs. This reduces service interruptions, consumer dissatisfaction, and significant health and safety issues. In this study, a new conception of water distribution network maintenance planning is prompted by a real-life circumstance and used to construct an efficient mixed integer programming model. Using the provided approach, small and medium-sized problems can be solved effectively and in a reasonable amount of time. The latter is a preliminary step in developing a meta-heuristic for large-scale instances of the problem.

REFERENCES

[1] D. B. Paneria and B. V. Bhatt, “Modernization in water distribution system,” 2017.

[2] Q. Xu, Q. Chen, J. Ma, and K. Blanckaert, “Optimal pipe replacement strategy based on break rate prediction through genetic programming for water distribution network,” *Journal of Hydro-Environment Research*, vol. 7, no. 2, pp. 134–140, 2013.

[3] J. Naoum-Sawaya, B. Ghaddar, E. Arandia, and B. Eck, “Simulationoptimization approaches for water pump scheduling and pipe replacement problems,” *European Journal of Operational Research*, vol. 246, no. 1, pp. 293–306, 2015.

[4] A. Kaufmann and H. LABORDERE, “Integer and mixed programming. theory and applications.” 1977.

[5] U. Shamir and C. D. Howard, “An analytic approach to scheduling pipe replacement,” *Journal-American Water Works Association*, vol. 71, no. 5, pp. 248–258, 1979.

[6] G. C. Dandy and M. Engelhardt, “Optimal scheduling of water pipe replacement using genetic algorithms,” *Journal of water resources planning and management*, vol. 127, no. 4, pp. 214–223, 2001.

[7] I. Gupta, “Linear programming analysis of a water supply system,” *AIIE Transactions*, vol. 1, no. 1, pp. 56–61, 1969.

[8] U. Shamir, “Optimal design and operation of water distribution systems,” *Water resources research*, vol. 10, no. 1, pp. 27–36, 1974.

[9] K. Katsifarakis and D. Karpouzos, “Genetic algorithms and water resources management: an established, yet evolving, relationship,” *WIT Transactions on State-of-the-art in Science and Engineering*, vol. 56, 2012.

[10] G. Bonvin, A. Samperio, C. Le Pape, V. Mazauric, S. Demassey, and N. Ma¨ızi, “A heuristic approach to the water networks pumping scheduling issue,” *Energy Procedia*, vol. 75, pp. 2846–2851, 2015.

[11] L. Dridi, M. Parizeau, A. Mailhot, and J.-P. Villeneuve, “Using evolutionary optimization techniques for scheduling water pipe renewal considering a short planning horizon,” *Computer-Aided Civil and Infrastructure Engineering*, vol. 23, no. 8, pp. 625–635, 2008.

Study of air pollution from the road transport sector in Tunisia Sahel

N. Kechiche[#1], *A. Jbara*[#1], *I. Daouas*[#1], *K.Kammoun*[#1], *A.Souiden*[#2].

[#1] *Higher Institute of Transport and Logistics*
University of Sousse ; Tunisia

[#2] *Head of the air quality monitoring program atthe National*
Agency for Environment Protection (ANPE)
kechiche2000@gmail.com

Abstract— **Air pollution caused by road traffic is a global problem that requires a global approach and concrete actions. Continued research in this area is crucial to developing effective policies and solutions to reduce vehicle emissions and improve the quality of the air we breathe. This will protect people's health and preserve our planet for future generations.**

The aim of this research was to analyze vehicle emissions on road networksof the Sahel region in Tunisia. We calculated the emissions of pollutants: CO, NOx, VOC, PM10, PM2.5 and heavy metals using COPERT software. The results showed that the emissions values depend on vehicle types, fuel and roads for the Sahel cities. In addition, the city of Sousse has high pollution rates compared to those of the cities of Monastir and Mahdia.

Keywords— **Air pollution, Road traffic, vehicle emissions, COPERT.**

I. INTRODUCTION

Air pollution is a major concern for researchers and public authorities because of its impact on the environment and on the health[1, 2].

According to the World Health Organization (WHO), outdoor air pollution is responsible for millions of deaths around the world in both urban and rural areas [3].

The growth of the vehicular fleet and the related fuel consumption can lead to an increase in the emission of air pollutants. Therefore, the development of a robust vehicle emissions inventory (VEI) is required for a given study area, which may support the researchers and states to develop strategies in urban centers to reduce pollutant emissions [4]. In addition, certain actions must be carried out, such as actions on urban development and the choice of the location of buildings and road development.

The study conducted by Peng Wang et al.focused on vehicle emissions as a major cause of air pollution and adverse health effects, particularly in urban areas. Traffic jams are identified as an aggravating factor in pollutant emissions, which deteriorate air quality. The study proposes a new approach to analyze the impact of congestion on air quality and health[5].

Siti Haslina Mohd Shafie, Mastura Mahmud et al. examined particulate matter (PM_{10}) emissions from exhaust and non-exhaust sources, as well as gaseous pollutants such as carbon monoxide (CO) and nitrogen oxide (NOx) emitted by different classes of motor vehicles in the tropical city of Kuala Lumpur. The results showed that newly registered passenger cars were the biggest contributors to PM_{10} emissions. In terms of gaseous pollutants, passenger cars emitted more CO and NOx in 2014 compared to emissions in 2010 [6].

Ruipeng Tong et al. conducted a study in an urban area of Beijing to assess the impact of air pollution due to emissions from mobile sources. The researchers used the Motor Vehicle Emissions Simulation Model (MOVES). Then, two $PM_{2.5}$ exposure scenarios were simulated using an atmospheric dispersion model. The results showed that vehicle $PM_{2.5}$ emission levels were generally higher on weekdays, especially during peak hours, than on weekends [7].

ISSN: 1737-933484

Pul yu et al. conducted a study that examines different methods of measuring vehicle emissions, including laboratory measurements, on-road measurements and tunnel measurements. They also reviewed the factors that influence the assessment of vehicle emissions in operation, taking into account vehicle operating characteristics and the road environment [8].

Achmad Rizki Pratama, Joni Arliansyah et al. conducted a study to analyze road network performance and vehicle exhaust emissions in the Beringin Janggut area of Palembang. They used Vissim software to simulate traffic andEnViver software to calculate vehicle exhaust emissions. The researchers proposed alternative solutions: Alternative 1, which consists of rearranging the parking lot and which proved to be more effective than Alternative 2, involving the separation of lanes between public and private vehicles, to improve the performance of the road network and reduce total vehicle exhaust emissions [9].

The study by Xiaowei Song et al. has proven that vehicle emissions are a major source of air pollution, requiring effective action to preserve the environment. The study was carried out in the Chengdu-Chongqing Urban Agglomeration (CCUA), a less developed region in southwest China characterized by high vehicle density. The objective of this research was to establish emission inventories of ten air pollutants from vehicles over a period of several years, and to analyze this data to develop eight emission control policy scenarios. Among the scenarios studied, the elimination of non-compliant vehicles proved to be the most effective policy for reducing pollutant emissions (NOx, $PM_{2.5}$, PM_{10}, etc.) [10].

Piotr Holnicki's research work was concerned with the analysis of the impact of the modernization of road traffic on air pollution in the agglomeration of Warsaw, Poland. The researcher used the Calpuff model to simulate the average annual concentrations of NOx, CO, PM_{10} and $PM_{2.5}$, as well as to assess the exposure of the population to these pollutants. The results showed that road traffic was the main source of NOx and CO in the air of the city. Using Euro emissions standards, a vehicle emissions reduction scenario was formulated, based on the assumed modernization of the vehicle fleet and the switch to Euro 6 emission standards. The simulations indicated a reduction in concentrations of NOx attributed to mitigating emissions from passenger cars, trucks, vans and transit buses. However, the improvement of air quality in terms of CO concentrations depended mainly on the modernization of gasoline-powered vehicles. The implementation of the proposed scenario resulted in a significant reduction in the exposure of the population to air pollution [11].

Zelalem Birhanu Biramo et al. carried out a study on the impact of the deployment of automated vehicles on emissions and fuel consumption in the road transport sector. Their results reveal that drivers' driving behaviors have a significant impact on emissions and fuel consumption, mainly due to differences in the use of acceleration and speed. Researchers explored the use of programmable automated vehicles as a potential solution to reducing fuel consumption, especially in urban areas. In their most optimistic scenario, where all vehicles are replaced by maximum level automated vehicles, significant emission reductions were observed at the grid level for carbon monoxide (CO), carbon dioxide (CO2), hydrocarbons (HC), for particles (PM_x) and for nitrogen oxides (NOx)[12].

In recent decades, significant reductions have been observed in emissions of particulate matter (PM), nitrogen oxides (NOx), carbon monoxide (CO), hydrocarbons (HC), carbon dioxide sulfur (SO_2) and lead (Pb) from vehicles. These advances have been made possible through the development of advanced emissions after-treatment technologies for gasoline and diesel vehicles, enabling compliance with increasingly stringent regulations. Despite the increase in the number of miles traveled by vehicles, these efforts have resulted in an absolute reduction in the emissions of the fleet in circulation. These measures have had a significant impact on air quality in cities across the United States and Europe [13].

II. METHOD AND MATERIALS

In our study we have used COPERT (Computer Program to Calculate Emissions from Road Transport) to calculate the emissions from road transport, which was developed by the European Commission (EC).

COPERTestimates the emissions of air pollutants produced by different vehicle categories (passenger cars, light commercial vehicles, HDV, buses, motorcycles, and mopeds). In COPERT, all major air pollutants and greenhouse gas emissions, including CO, NOx, VOC, PM, NH_3, SO_2, CO_2, N_2O and CH_4, emitted from vehicles can be estimated. This model employs a significant amount of reliable experimental data, which are compatible with the statistical calibrations and parameter variables of different countries.

COPERT uses the statistical data of fuel sales within a region as its basic data, which has better applicability in regions lacking basic traffic data. The COPERT model classifies vehicle types in detail andevaluates many kinds of pollutants.

The calculation carried out by COPERT makes it possible to estimate the global emissions of the various pollutants of the road traffic and a list of heavy metals such as lead, cadmium, and copper[14].

In what follows, we will focus our work on five pollutants resulting from road traffic such as CO, NOx, VOC,$PM_{10}$and $PM_{2.5}$ for the Sahel region in Tunisia.

III. RESULTS

Emissions in the Sahel region

According to Fig.1, we notice that the most polluted city is Sousse with the value of 43% for all pollutants followed by Monastir city with 37% while the city of Mahdia is the least polluted in the area of Sahel with a percentage of 21%.This result is explained by the economic, educational and tourist activities in the two cities Sousse and Monastir compared to Mahdia city.

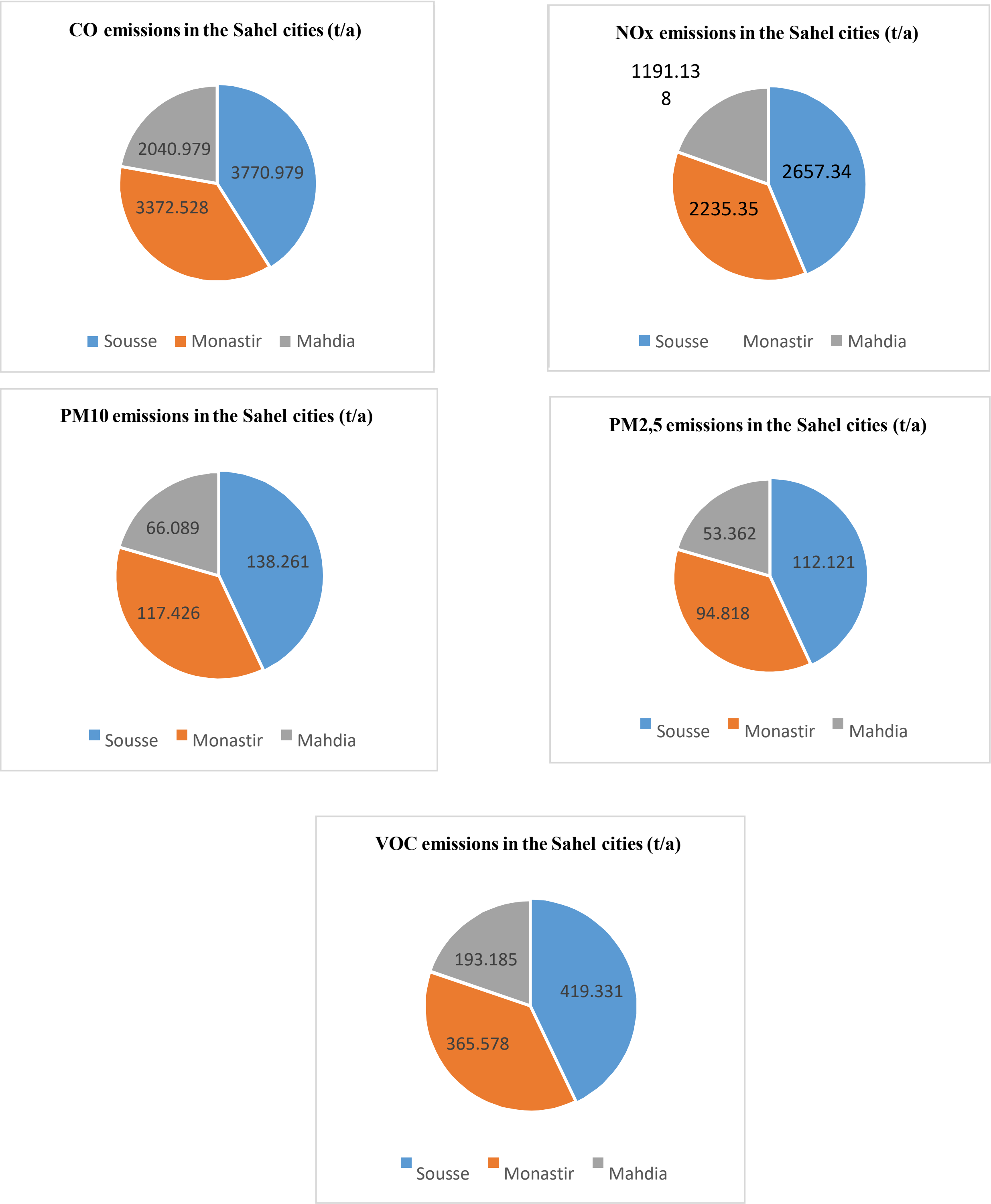

CO emissions in the Sahel cities (t/a)

NOx emissions in the Sahel cities (t/a)

PM10 emissions in the Sahel cities (t/a)

PM2,5 emissions in the Sahel cities (t/a)

VOC emissions in the Sahel cities (t/a)

Fig.1 Pollutants emissions in the Sahel region.

CO emissions

In fig.2, it can be seen that CO emissions from vans are higher than emissions from private vehicles, while low emissions are observed from other transport means. It is also indicated that gasoline vehicles emit more CO than diesel vehicles, and the road most exposed to pollution and emissions is the urban area followed by the rural area while emissions in the highway are low, and this is due to the road congestion existing especially in the urban area.

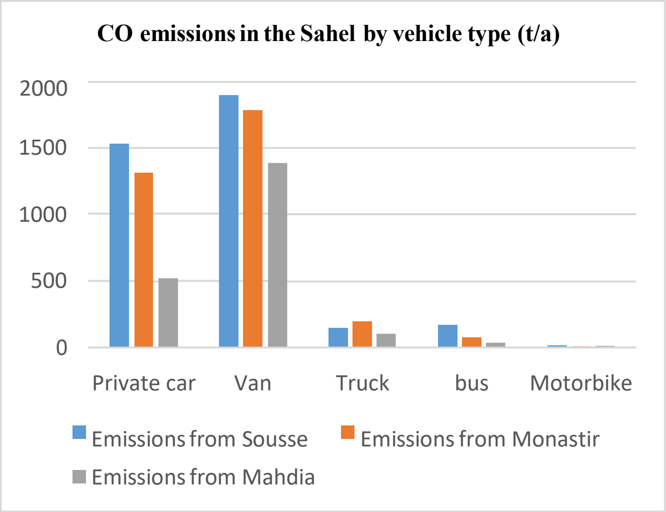

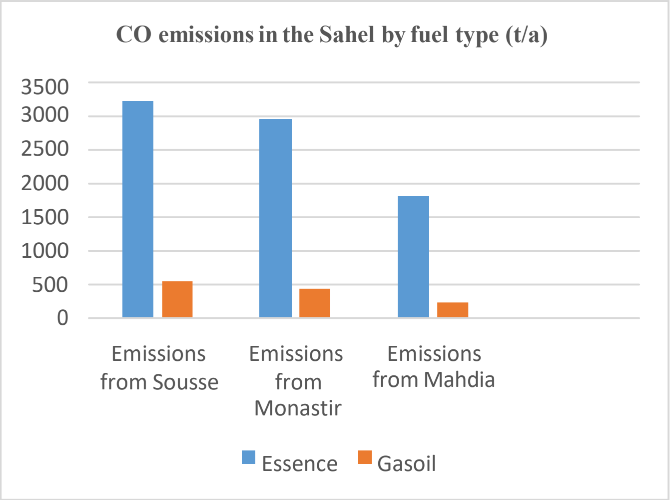

Fig.2 CO emissions by type of vehicle, fuel and road.

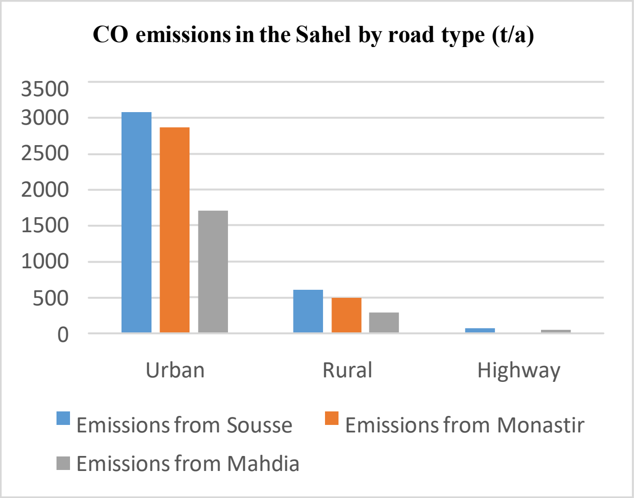

NOx emissions

According to fig.3, we notice that the NOx emissions caused by trucks are more important than the emissions of private cars and vans with high values of emissions by buses especially in Sousse and very low values of emissions caused by motorcycles.

NOx emissions from diesel vehicles are higher than emissions from gasoline vehicles for all the cities.

There is a significant NOx emission in the urban area compared to the rural area and a low quantity emission in the highway.

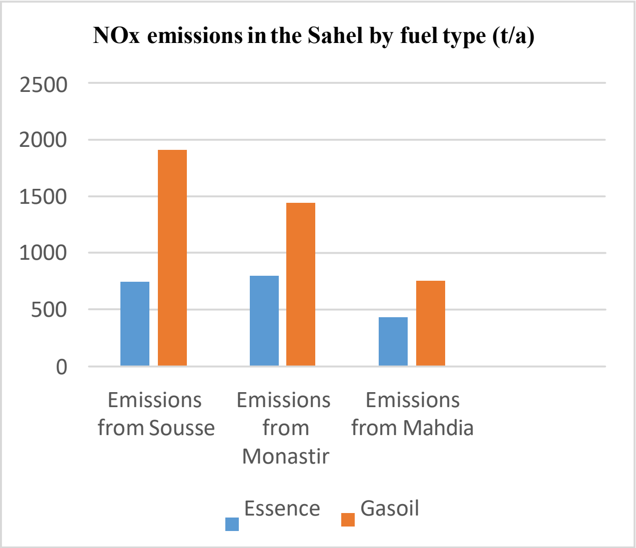

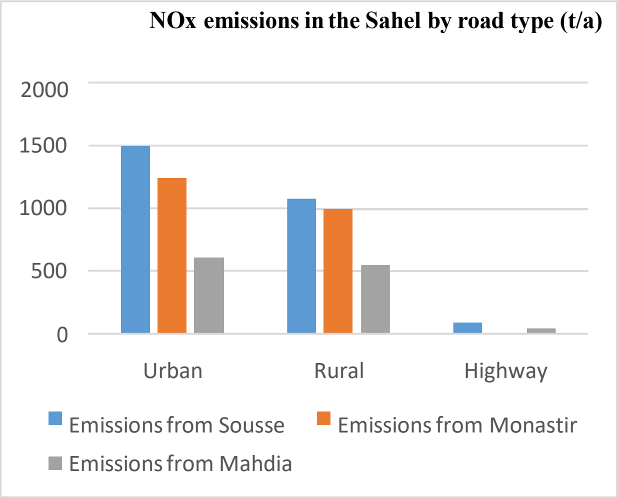

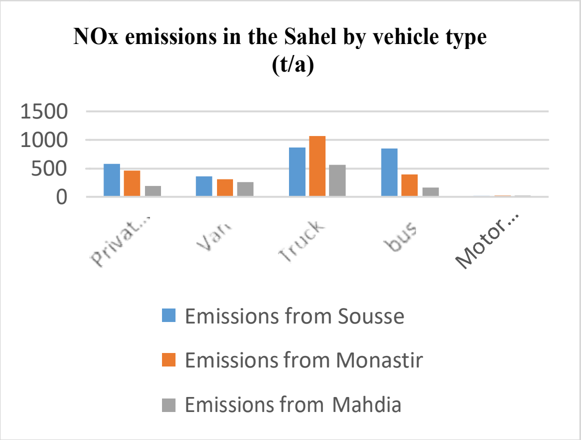

Fig.3 NOx emissions by type of vehicle, fuel and road.

VOC emissions

According to fig.4, it is noted that VOC emissions from private vehicles are higher than vans while emissions from trucks and buses present lower quantities with negligible values for motorcycles.

Gasoline vehicles have higher VOC emissions than diesel vehicles. The urban area is the most polluted area compared to the rural roads and highway.

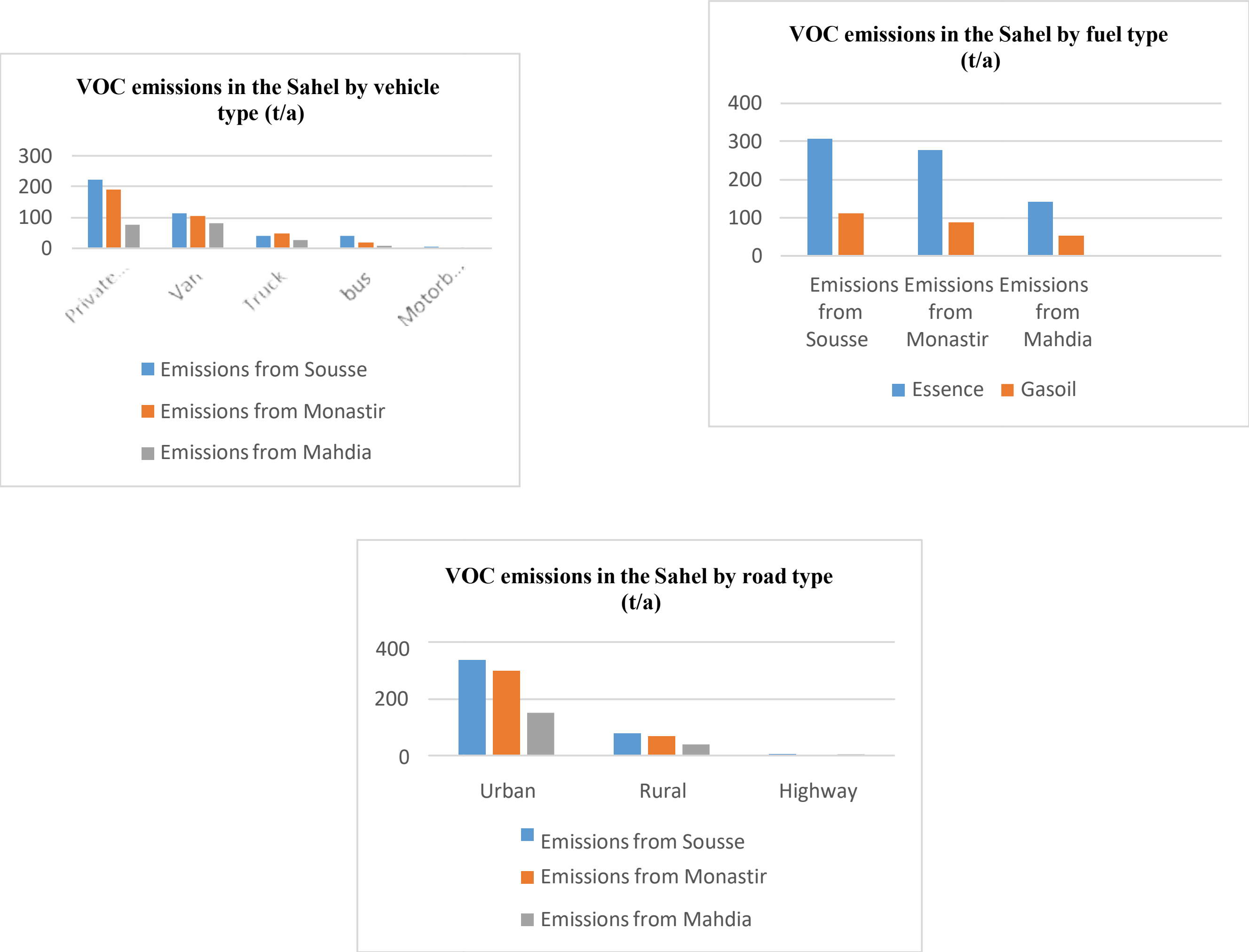

Fig.4 VOC emissions by type of vehicle, fuel and road.

ISSN: 1737-933484

PM_{10} emissions

From fig.5 we noted that the emission of PM_{10} caused by private cars is higher than the emissions from vans and trucks, with a low quantity emission by buses and a negligible quantity by motorcycles.
Diesel vehicles emit more PM_{10} than gasoline vehicles, and we note the presence of pollution in the urban area than the rural area and highway.

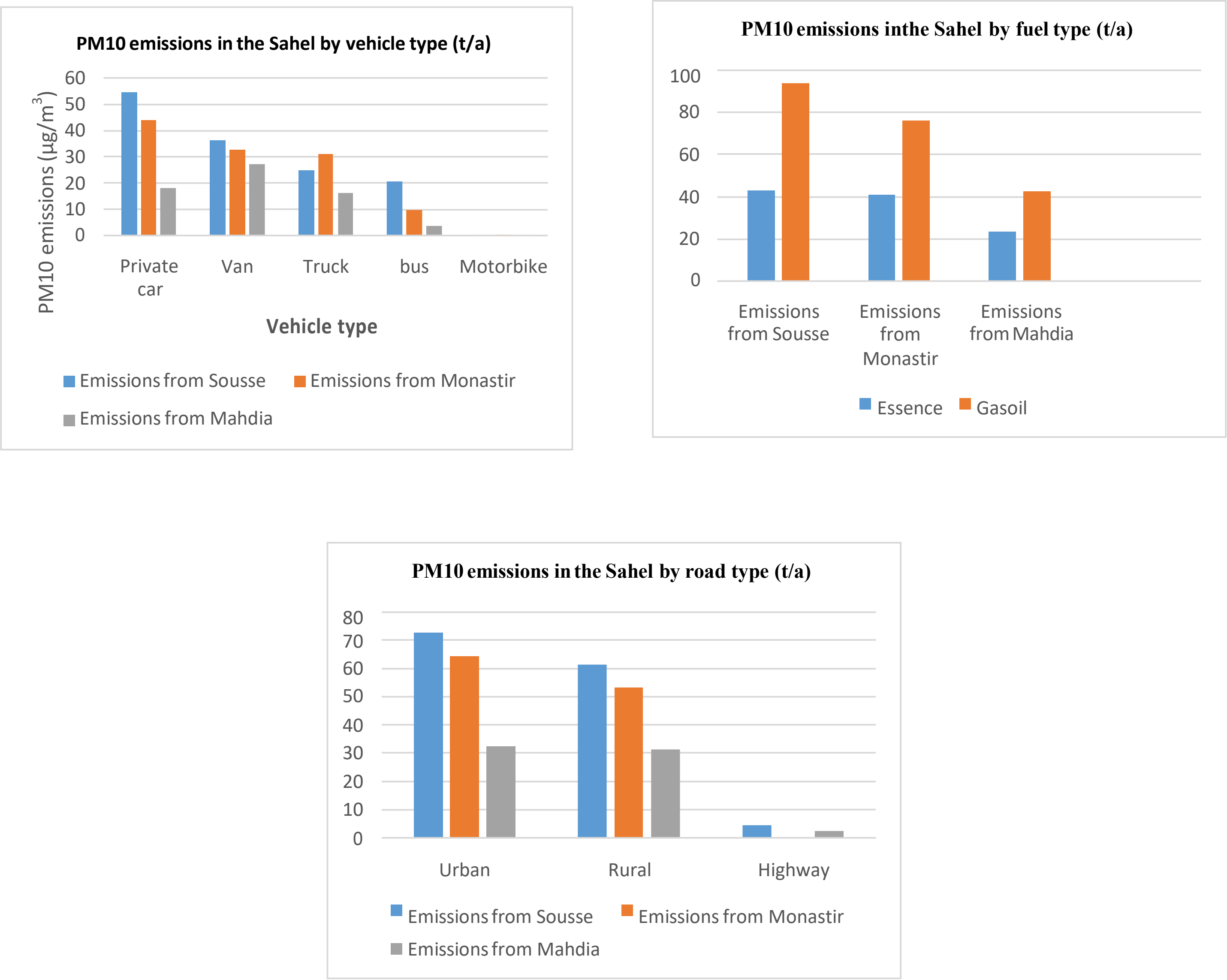

Fig.5 PM_{10} emissions by type of vehicle, fuel and road.

$PM_{2.5}$ emissions

In fig.6, it can be seen that passenger cars emit more $PM_{2.5}$ than vans, trucks and buses, with a negligible amount emitted by motorcycles.
The emission of $PM_{2.5}$ is caused by diesel vehicles than gasoline vehicles.
The urban area is the area most exposed to $PM_{2.5}$ emissions than the rural area and the highway.

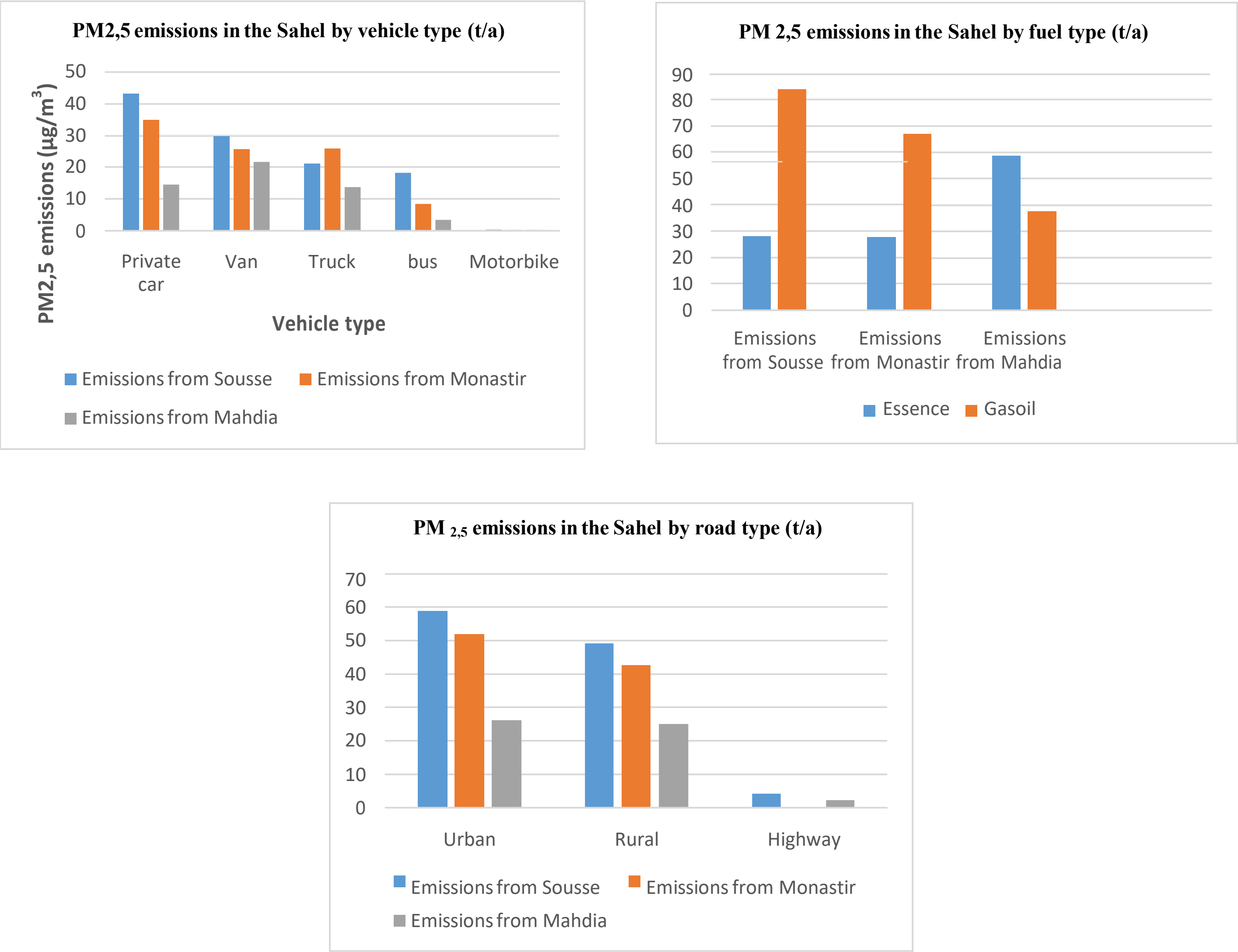

Fig.6 PM$_{2.5}$ emissions by type of vehicle, fuel and road.

Heavy metal emissions

TABLE 1 shows that the emissions of heavy metals in the city of Sousse are higher than those of Monastir and Mahdia cities and the lowest emissions are recorded inMahdiacity.

TABLE 1. The emission of heavy metals in the Sahel region.

	Plomb	Cadmium	Chrome	Nickel		Zinc	Total
Sousse	33,48	0,156	12,399	1,967		105,16	153,162
Monastir	27,067	0,125	10,029	1,587	84,009	122,817	
Mahdia	11,249	0,133	4,166	0,661	35,33	51,539	

The fig.7 shows that for each city, we note that zinc emissions are higher than the other metals, followed by lead and chromium emissions, while low values are noted for nickel and cadmium emissions.

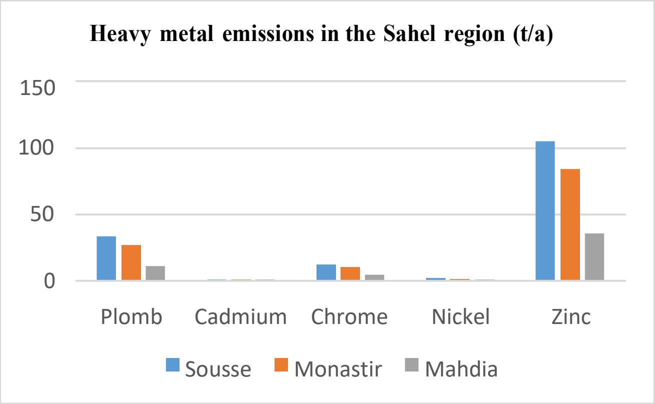

Fig.7Heavy metal emissions in the Sahel region.

IV. CONCLUSION

In this work, we have calculated the vehicular emissions of five pollutants (CO, NOx, VOC, PM_{10} and $PM_{2.5}$) and heavy metals at theTunisia Sahel region.

Based on the results obtained from data analysesof the road network in the Sahel region of Tunisia, it can be concluded as follows:

- The passengers cars have the largest share of emissions of the two pollutants, PM_{10} and $PM_{2.5}$ than the others vehicles types.

-The Diesel vehicles emit much more NOx and PM than gasoline vehicles, which in turn emit more CO and VOC pollutants.

-The area most exposed to pollution and emissions is the urban area followed by the rural area while emissions in the highway are low.

- Emissions of atmospheric pollutants as well as heavy metals are more important in the city of Sousse than those of Monastir and Mahdia cities.

- The most polluted city is Sousse followed by Monastir city while Mahdia city is the least polluted in the Tunisia Sahel region.

ACKNOWLEDGMENT

The authors express their gratitude to everyone who contributed to the elaboration of this study, with special recognition to Mrs Amina Souiden head of the air quality monitoringprogram at the National Agency for Environment Protection (ANPE).

REFERENCES

[1] S. Host et al. Health risk assessment of traffic-related air pollution near busy roads, Revue d'Épidémiologie et de Santé Publique, Volume 60, Issue 4, August 2012, Pages 321-330.

[2] Kumar, P., Patton, A.P., Durant, J.L., Frey, H.C. (2018). A review of factors impacting exposure to PM2.5, ultrafine particles and black carbon in Asian transport microenvironments. Atmospheric Environment.

[3] World Health Organization (WHO): Ambient (outdoor) air quality and health, Genebra 2018.

[4] Janaina Antonino Pinto et al. Traffic data in air quality modeling: a review of key variables, improvements in results, open problems and challenges in current research November 2019Atmospheric Pollution Research 11(3) DOI: 10.1016/j.apr.2019.11.018.

[5] Peng Wang, Ruhan Zhang, Shida Sun, Meng Gao, Bo Zheng, Dan Zhang, Yanli Zhang,Gregory R. Carmichael, and Hongliang Zhang, Aggravated Air Pollution and Health Burden due to Traffic Congestion in Urban China, Atmospheric chemistry and physics, https://doi.org/10.5194/acp-2022-577.

[6] Siti Haslina Mohd Shafie, Mastura Mahmud, Urban Air Pollutant from Motor Vehicle Emissions in Kuala Lumpur, Malaysia, Aerosol and Air Quality Research, 20: 2793–2804, 2020 ISSN: 1680-8584 print / 2071-1409 online Publisher: Taiwan Association for Aerosol Research https://doi.org/10.4209/aaqr.2020.02.0074.

[7] Ruipeng Tong, Jiefeng Liu, Wei Wang, Yingqian Fang, Health effects of PM2.5 emissions from on-road vehicles during weekdays and weekends in Beijing, China, Atmospheric Environment 223 (2020) 117258.

[8] Pu Lyu, Peirong (Slade) Wang, Yuanyuan Liu, Yuanqing Wang, Review of the studies on emission evaluation approaches for operating vehicles, journal of traffic and transportation engineering (english edition) 2021 ; 8 (4) : 493 e 509.

[9] Achmad Rizki Pratama, Joni Arliansyah, and Melawaty Agustien, Analysis of Air Pollution due to Vehicle Exhaust Emissions on The Road Networks of Beringin Janggut Area, IOP Conf. Series: Journal of Physics: Conf. Series 1198 (2019) 082030, doi:10.1088/1742-6596/1198/8/082030.

[10] Xiaowei Song, Yongpei Hao and Xiaodong Zhu, Aggravated Air Pollution and Health Burden due to Traffic Congestion in Urban China, Sustainability 2019, 11, 6503; doi:10.3390/su11226503.

[11] Piotr Holnicki, Zbigniew Nahorski and Andrzej Kałuszko, Impact of Vehicle Fleet Modernization on the Traffic-Originated Air Pollution in an Urban Area—A Case Study, Atmosphere 2021, 12, 1581. https://doi.org/10.3390/atmos12121581.

[12] Zelalem Birhanu Biramo1 and Anteneh Afework Mekonnen, Modeling the potential impacts of automated vehicles on pollutant emissions under different scenarios of a test track, Environmental Systems Research (2022) 11:28, https://doi.org/10.1186/s40068-022-00276-2.

[13] Timothy J.Wallington, James E. Anderson, Rachael H. Dolan and Sandra L. Winkler, Vehicle Emissions and Urban Air Quality: 60 Years of Progress, Atmosphere 2022, 13, 650. https://doi.org/10.3390/atmos13050650.

[14] Saharidis, G.K.D., Konstantzos, G.E., 2018. Critical overview of emission calculation models in order to evaluate their potential use in estimation of greenhouse gas emissions from in port truck operations. Journal of Cleaner Production 185, 1024e1031.

Spiral porous fin with simultaneous heat and mass transfer

DARADJI Nadia[#1], BOUAZIZ Mohamed Nadjib [*2]

[#1] Biomaterials and Transport Phenomena Laboratory, University Medea 26000, Algeria
daradji.n@gmail.com

[*2] Biomaterials and Transport Phenomena Laboratory, University Medea 26000, Algeria
mn_bouaziz@email.com

Abstract— **The combined heat and mass transfer mechanisms owing to the temperature and humidity ratio differences and their influence on the efficiency of a spiral porous fin are analyzed in this paper. The mathematical representation resulting from an analysis is a highly non-linear 2nd order differential equation. Complemented by the boundary conditions, the nonlinear system was solved numerically using MATLAB software.**

For the mathematical analysis of a wet fin equation, a relationship between humidity ratio and temperature of the saturation air is needed. The driving forces for the heat and mass transfer are the temperature and humidity ratio differences, respectively. The interaction between the porous medium and the fluid is simulated by Darcy's formulation. The effects of relative humidity, the fin parameter, air temperature and Rayleigh number on the efficiency of the fin were investigated. We have found that if the humidity percent is increased , the difference temperature between fin and air is decreased and fin temperature is increased, and higher air temperature , makes higher surface temperature due to release of latent heat of condensation.

Keywords— **Spiral Porous fin, relative humidity, mass transfer, heat transfer, dew point temperature fully wet fin, Rayleigh number.**

I. INTRODUCTION

Extended surfaces that are well known as fins are commonly used to enhance heat transfer in many industries. Applications for finned surfaces are widely seen in air-conditioning, refrigeration, cryogenics, and electronic devices as well as in heat exchangers and power generators working with high temperature. On the other hand, heat transfer takes place in porous materials of various types. A primary aim is common to maximize either the thermal resistance or the rate of thermal equilibration between the material and a fluid passing through it - i.e. to facilitate heat exchange, and less material is consumed in the case of a solid fin is replaced by a porous fin, knowing that to reduce the size and price of fins are the first fins industry goals. There is lot of practical applications in which the base temperature is kept at a lower value than the surrounding temperature. In these components, the heat is transferred from the surrounding to the fin surface. In refrigeration and air conditioning systems, the air being cooled when it passes over the fin surface maintained at a lower temperature. If the fin surface temperature is below the dew-point temperature of the surrounding air, the simultaneous heat and mass transfer mechanism takes place on the fin surface. The humid air strikes on a surface which is below the dew-point temperature, condensation of moisture occurs on the fin surface by evolving the latent heat of condensation. The motive force, temperature difference between surrounding and fin surface, is responsible for sensible heat transfer and difference of humidity ratio between the surrounding and that on the fin surface is the motive force for the mass transfer. Many researchers are applied on simultaneous heat and mass transfer in fins Mc Quiston [1] studied analytically the overall efficiency of a fully wet straight fin. He assumed that the driving force for the mass transfer, as given by the difference in the humidity ratio between the incoming air and the existing one on the fin surface, is linearly related to the corresponding temperature difference. The following work of Elmahdy and Briggs [2] indicated that the fin efficiency strongly depends on the relative humidity. Wu and Bong [3] provided an analytical solution for the efficiency of a straight fin under both fully wet and partially wet conditions by using the temperature and humidity ratio differences as the driving forces for heat and mass transfer. He assumed the same linear relationship between the humidity ratio of the saturated air on the fin surface and its temperature as that of Elmahdy and Briggs, their

ISSN: 1737-933484

result shows that there is not much change in the fin efficiency with the relative humidity. Sharqawy and Zubair [4] considered the efficiency of an annular fin in simultaneous mass and heat transfer situations. They obtained an analytical solution for efficiency and rate of heat transfer for an annular fin when exposed to fully wet condition. Sharqawy and Zubair [5] provided an analytical solution for the efficiency of a straight fin under fully wet conditions by using the temperature and humidity ratio differences as the driving forces for heat and mass transfer mechanisms, respectively.

The spiral porous fin in simultaneous mass and heat transfer has not been studied until now, and we can found this shape of fins in refrigeration and air conditioning where the fin surface temperature is below the dew point temperature.

This shape favors the rotational vortices acting downstream; the spiral fin has a greater disposition to increased heat exchange. Also a heat exchanger with spiral fins is more compact than any other heat exchanger. The flow in this heat exchanger is counter-current, co-current, or cross-flow. Introducing porosity to the fin is an effective strategy for enhancing its performance.

In the present paper, numerical solution of fin temperature distribution has been studied for spiral porous fin. The main purpose of current study is to see how our fin acts in an air conditioning or refrigeration system with different air temperatures and with different relative humidity.

II. MATHEMATICAL FORMULATION

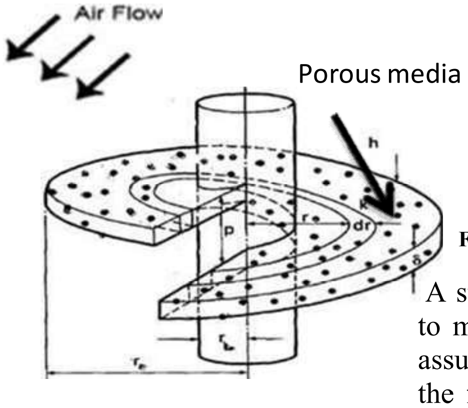

Fig 1. Schematics of a fully wet spiral porous fin.

A steady state analysis is carried out on an porous spiral fin when exposed to moving moist air stream, as shown in Fig. 1. In this regard, the following assumptions are made to simplify the analysis. (1) The thermal conductivity of the fin, heat transfer coefficient and latent heat of condensation of the water vapor are constant;
(2) The thermal resistance associated with the presence of thin water film due to condensation is small and may be neglected; (3) The effect of air pressure drop due to air flow is neglected. These are essentially the classical assumptions that are typically used. Applying an energy balance on an infinitesimal area,
Which is shown in Fig. 1.

$$q_r - q_{r+dr} = hA(1-\varepsilon)\,(T(r)-T_a) + \dot{m}c_p(T(r)-T_a) + Ah_D i_{fg}\,(1-\varepsilon)(w(r)-w_a) \qquad (1)$$

Where ε is porosity and (1- ε) denotes to the fraction of fin area which is solid or subtracted the pores area which is necessary for convection surface. Cp is the specific heat at a constant pressure of the fluid; A is the section area of fin, Ta the air temperature for convection, while q denotes the heat flux. The mass flow rate of the fluid passing through the porous material is

$$m = \rho v_w S \qquad (2)$$

i_{fg} : latente heat of evaporation of water (water vapor from the air will also condense on the fin surface by releasing the latent heat)
h_D: Mass Transfer convective coefficient
w :Humidity ratio
Where S = 2π r’dr and r is the radial direction. The Length of a whorl of one circular helix r’ linked to the pitch of the spiral fin P is

$$r' = 2\pi\sqrt{\left(\frac{P}{2\pi}\right)^2 + r^2} \qquad (3)$$

The heat transfer and mass transfer coefficients are related by the Chiltone-Colburn analogy

$$\frac{h}{h_D} = C_p Le^{2/3} \qquad (4)$$

ISSN: 1737-933484

$$\theta = \frac{T(r) - T_a}{T_b - T_a} \qquad (5)$$

$$R = \frac{r}{r_b}, Pe = \frac{P}{2\pi r_b}, Da = \frac{K}{r_b^2}, \psi = \frac{\delta}{r_b} \qquad (6)$$

.

Therefore the energy balance on the elemental volume yields the following differential equation:

$$\frac{d^2\theta}{dR^2} = \frac{-R}{Pe^2 + R^2}\theta' + R\,Pe\,Da\,\theta^2 + m^2(1-\varepsilon)\theta + N^2 B(1-\varepsilon)C \qquad (7)$$

with boundary condition:

$$\theta(1) = 1, \left(\frac{d\theta}{dR}\right)_{R=Re} = 0 \qquad (8)$$

$$B = \frac{i_{fg}}{C_p Le^{2/3}}, a_2 = w_b - \frac{w_{dp} - w_b}{T_{dp} - T_b} T_b, b_2 = \frac{w_{dp} - w_b}{T_{dp} - T_b}, N^2 = \frac{h\, r_i^2}{\delta\, k_{eff}}$$
$$C = \frac{a_2 + b_2 T_a - w_a}{T_b - T_a}, m^2 = N^2(1 + B b_2) \qquad (9)$$

A linear relationship between w and T over the temperature range ($T_b < T(r) < T_{dp}$) as Sharqawy and Zubair [4].

$$w(r) = a_2 + b_2 T \qquad (10)$$

TABLE I
THE NECESSARY DATA FOR CALCULATING A2 AND B2 CONSTANTS.H_R=100 %, 80%, 60%, AND 40%, T_B=15°C

T_a (°C)	H_r (%)	W_a (kg_w/kg_a)	T_{dp} (°C)	w_{dp}(kg_w/kg_a)	$W_{s,b}$(kg_w/kg_a)	a_2	b_2	c
10	100	0.00767	10	0.00767	0.01066	0,00169	0,000598	0
20	100	0.01466	20	0.01466	0.01066	-0,00134	0,0008	0
30	100	0.02680	30	0.02680	0.01066	-0,00548	0,001076	0
40	100	0.04716	40	0.04716	0.01066	-0,01124	0,00146	0
10	80	0.00613	6.7	0.00490	0.00852	0,00197783	0,0004361	4,18554E-05
20	80	0.01171	16.4	0.00933	0.00852	-0,0001585	0,0005785	5,94286E-05
30	80	0.02137	26.2	0.01709	0.00852	-0,0029576	0,0007651	9,14881E-05
40	80	0.03751	35.9	0.02992	0.00852	-0,0068388	0,0010239	0,000135677
10	60	0.00459348	2.6	0.002757	0.006384	0,0019965	0,0002925	6,5604E-05
20	60	0.00876773	12	0.005246	0.006384	0,000694	0,0003793	9,74127E-05
30	60	0.01598114	21.4	0.009565	0.006384	-0,0010714	0,0004970	0,000142778
40	60	0.02797858	30,7	0.016644	0.006384	-0,0034185	0,0006535	0,00021028
10	40	0.00305	-3.1	0.00121	0.00425	0,00173066	0,0001679	7,20442E-05
20	40	0.00583	6.0	0.00232	0.00425	0,00103333	0,0002144	0,000101556
30	40	0.01061	14.9	0.00422	0.00425	-0,00025	0,0003	0,000124
40	40	0.01854	23.8	0.00736	0.00425	-0,0010511	0,0003534	0,000218191

ISSN: 1737-933484

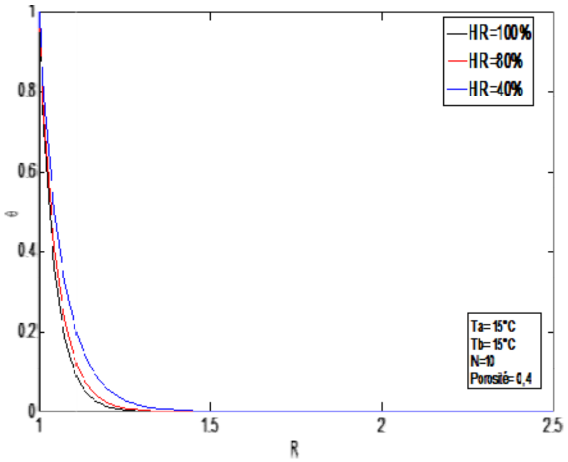

Fig 2. Effect of relative humidity H_R for porous spiral fin.

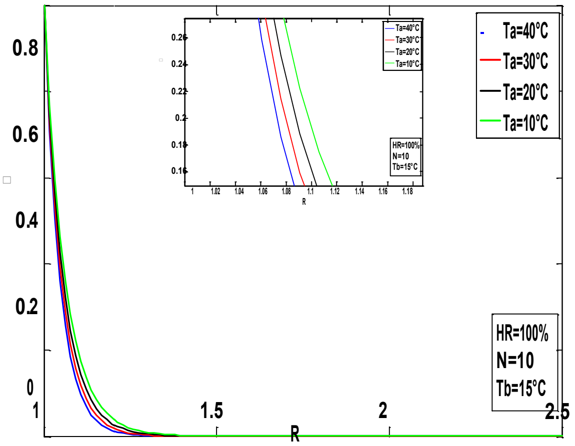

Fig 3. Effect of air temperature on the distribution of temperature for R_H=100%

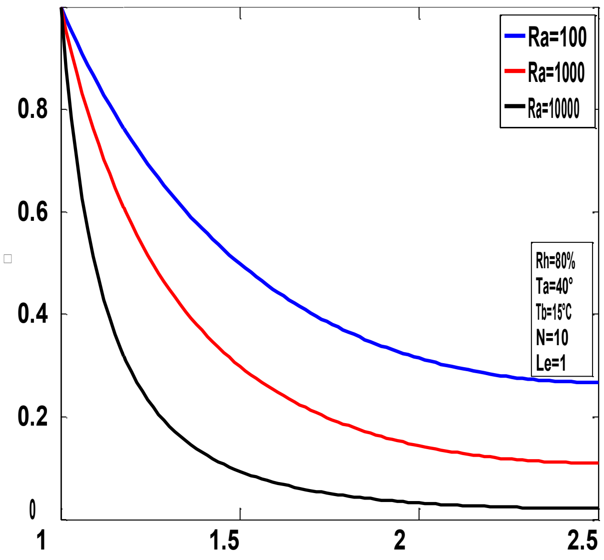

Fig 4. Effect of Rayleigh number on temperature distribution

ISSN: 1737-933484

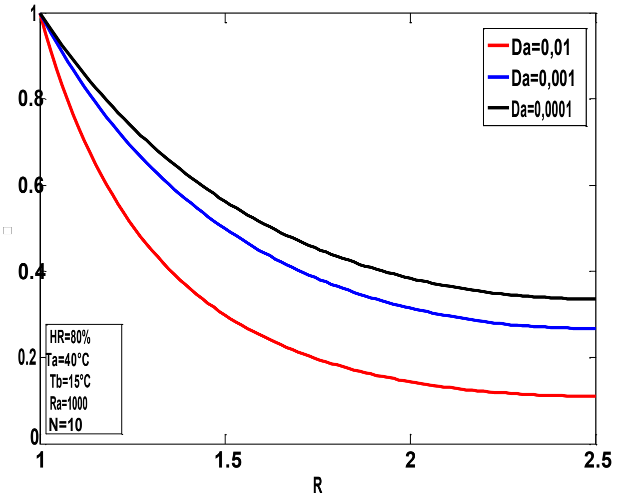

Fig 5. Effect of Darcy number on temperature distribution

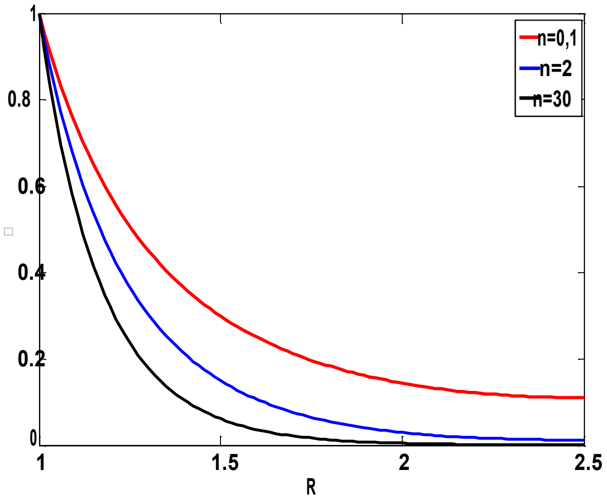

Fig 6. Effect of dry fin parameter on temperature distribution.

III. RESULTS AND DISCUSSION

Temperature distribution on fin surface versus distance from fin basis is plotted for 40, 70, 80 humidity percent. For these humidity percentages, temperature of fin tip is under dew point therefore fin will be fully wet.

According to Fig. 2, if the humidity percent is increased, the difference temperature between fin and air is decreased. Thus, whatever we come closer to fully wet condition, this difference is decreased and fin temperature is increased.

Fig. 3 is illustrating the Effect of air temperature on the distribution of temperature for 100% of relative humidity, it is illustrated that air temperature has a major influence on the temperature distribution of the fin, so by increasing the air temperature, fin temperature increases, so higher air temperature, makes higher surface temperature due to release of latent heat of condensation.

Fig.4 explains that decreasing the Ra number increases the fin efficiency. The main purpose of the wet fin applications is refrigerating due to lower temperature than ambient, when fin temperature reduces due to reducing Ra, it makes more refrigeration, so fin efficiency increases.

The effect of Darcy number on the temperature distribution is illustrated in fig 5, this number is proportional to the permeability, which increases as the permeability increases and therefore increases the ability of the working fluid to penetrate through the fin pores and thus convects more heat.

Fig.6 illustrates the effect of the fin parameter on the temperature distribution, while the other parameters are constant. As seen, when this parameter increases the convective transfer is dominant over the conductive transfer within the fin. It is evident that a weak fin parameter is desired in these circumstances. This result is well known and becomes as a classical condition to use the fins

IV . CONCLUSIONS

In this paper heat transfer equations for a spiral porous fin with simultaneous heat and mass transfer are presented and a numerical method has been applied to access to the temperature distribution. The following main points can be drawn from the present study.

The results show that the overall fin efficiency depends on the condition of the fin surface and on the air temperature .In addition, by closing to the fully wet conditions the fin temperature increases,

- If the humidity percent is increased, fin temperature is increased.

- increasing the air temperature, fin temperature increases, so higher air temperature, makes higher surface temperature due to release of latent heat of condensation.

- Increasing the Rayleigh number decreases in fin efficiency.

. Increasing the Darcy number decreases in fin efficiency

- A decrease in the fin parameter N implies an improvement of the fin heat transfer.

REFERENCES

[1] F.C. McQuiston Fin efficiency with combined heat and mass transfer ASHRAE Trans., 81 (Part 1) (1975), pp. 350-355.

[2] A.H. Elmahdy, R.C. Briggs ,Efficiency of extended surfaces with simultaneous heat and mass transfer .ASHRAE Trans., 89 (Part 1A) (1983), pp. 135-143 .

[3] G. Wu, T.Y. Bong, Overall efficiency of a straight fin with combined heat and mass transfer, ASHRAE Transactions 100 (Part 1) (1994) 367e374.

[4] Sharqawy, M.H., Zubair, S.M., 2007. Efficiency and optimization of an annular fin with combined heat and mass transfer e an analytical solution. Int. J. Refrigeration 30, 751e757.

[5] Sharqawy, M.H., Zubair, S.M., 2008. Efficiency and optimization of straight fins with combined heat and mass transfer e an analytical solution. Appl. Therm. Eng. 28, 2279e2288.S. M. Metev and V. P. Veiko, *Laser Assisted Microtechnology*, 2nd ed., R. M. Osgood, Jr., Ed. Berlin, Germany: Springer-Verlag, 1998.

Conférence Internationale sur les Sciences Appliquées et l'Innovation (CISAI-2023)
Proceedings of Engineering & Technology-PET-Vol 77

Impact of Wind Energy Production on Nord Pool Electricity Market Prices pre- and during Covid-19

Seifeddine Gurdally ^{*1}, Emna Trabelsi $^{\#*2}$

$^{\#}$*University of Tunis, Higher Institute of Management, Social and Economic Policy Analysis Laboratory, 2000, Tunisia*

**University of Sousse, Department of Quantitative Methods, Faculty of Economic and Management Sciences of Sousse, 4023, Tunisia*

[1]seif.guerdally@gmail.com
[2]emna.trabelsi2007@yahoo.fr

Abstract— **The aim of this study is to investigate the relationship between wind energy production and Local electricity price in Nord Pool countries (Sweden, Norway, Finland, Denmark, Latvia, Estonia, and Lithuania) for the period 2013-2020 before and during covid19. We believe that this is the first attempt using controlled variables as environmental stringency Index, containment Health Index, economics policy index, total death by covid19, and total confirmed cases by covid19 to test the impact of wind energy production on local electricity price in Nord Pool countries during COVID-19. Applying the Panel Pooled Mean Group Autoregressive Distributive Lag (PMG-ARDL) estimator, we found a significant relationship between wind energy production and local electricity price. This suggest that wind energy production has a negative and significant long-run effect on local electricity prices in all models estimated pre and during COVID-19, indicating that over time, higher wind energy production may lead to lower prices. However, the short-run results confirm the existence of granger causality paired relationship between wind energy production (WEP) and local electricity price (LEP) and that effects from the same PMG-ARDL estimator do not vary across models indicating that one day lagged wind energy production has a positive impact on local electricity prices starting from one day of lagged period of wind energy production with reduced impact on the following days. The findings suggest that government policies and restrictions do not have a significant impact on local electricity prices in the short run during COVID-19, as with better containment of the virus, higher wind energy production not leading to lower prices in the short run, this could be explained by the fast increase in demand compared to supply due to the pandemic offset in addition of the government policies and restrictions that take time to have an impact on local electricity prices because they involve complex processes and reactions that may take some time to unfold in the electricity market.**

Keywords— **Wind energy production; Electricity price; Renewable energy; Nord Pool electricity market; Panel ARDL PMG**

I. INTRODUCTION

The use of renewable energy sources, such as wind energy, has become increasingly important in recent years due to concerns about climate change and the need to reduce greenhouse gas emissions. Wind energy is a particularly attractive option because it is abundant, widely available, and does not produce harmful emissions. However, there are still many questions about how wind energy production affects electricity

ISSN: 1737-933484

prices in different regions. The Nord Pool region is one area where wind energy production has been growing rapidly in recent years. This region includes several countries in Northern Europe, including Norway, Sweden, Finland, Denmark, Estonia, Latvia, and Lithuania. The impact of wind energy production on electricity prices in this region is an important topic for policymakers and industry stakeholders alike.

The main objective of this study is to investigate the impact of wind energy production on electricity prices in the Nord Pool region, both before and during the COVID-19 pandemic.

Specifically, the study aims to answer the following research questions:

- What is the impact of wind energy production on Nord Pool electricity markets prices pre- and during COVID-19?
- How does the change in wind energy production influence the local electricity price?

in the short run and the long run?

- Do government containment policies during the COVID-19 pandemic affect the relationship between wind energy production and electricity prices in Nord Pool markets?

This study provides a comprehensive analysis of the impact of wind energy production on local electricity prices before and during COVID-19, structured into four main outlines: literature review, data presentation, and methodology, Panel ARDL PMG steps and analysis, and finally empirical results and their discussion. In the literature review section, we provide a comprehensive analysis of the existing empirical literature on wind energy production and its impact on electricity prices within the Nord Pool countries. We examine the various methodologies used in previous studies and highlight their strengths and limitations. This section also discusses the theoretical framework that underpins our study and provides a rationale for our research questions. The data presentation and methodology section outline how we collected our data and describes the models we used to estimate the relationship between wind energy production and local electricity prices. We provide a detailed description of our dataset, including its sources, variables, and time period. We also discuss the econometric models we used to estimate this relationship, including the Panel ARDL PMG model. The Panel ARDL PMG analysis section provides a step-by-step guide on how we estimated our models during COVID-19 as well as pre-COVID-19 conditions. We describe how we selected our variables, determined appropriate lags, tested for unit roots, cointegration, and cross-sectional dependence. This section also explains how we conducted model diagnostics to ensure that our models were well-specified. Finally, in the empirical analysis and results section, we expose our findings on the impact of wind energy production on local electricity prices before and during COVID-19. We discuss the statistical significance of our results, their economic implications, and their policy relevance. This section also includes sensitivity analyses to test the robustness of our findings to alternative model specifications. To the best of the authors' knowledge, no attempt has been made so far to investigate the long-run relationship between Wind energy production and local electricity price in case of Covid19 pandemic. Hence, the present study is an attempt to fill the gap in the existing literature.

II. REVIEW OF PAST STUDY

Empirical literature, in general, has shown that wind energy production exhibits a negative effect on the electricity price within the Nord Pool.

There is a vast literature examining the relationship between electricity price and wind energy production as a result. Only a selective literature review will be presented here.

Regarding Germany, (Sensfuß et al., 2008b) have shown that wind energy production lowers electricity prices. Despite having a high capital intensity, the installation of renewable energies always has a zero marginal cost. The most expensive conventional power plants are used, and electricity prices subsequently decrease. (Jónsson et al., 2010) analyzed hourly data using non-parametric estimation techniques. They tested the effect of future values of wind generation on the average Danish electricity price in the Elspot Nord Pool market. The results converge towards the idea that wind energy sources exhibit statistically significant effects on the price level as well as its volatility. (Green et al., 2011) showed that the future values of electricity prices, for the case of Great Britain, are affected in a statistically significant way by the increase in wind production. (Würzburg et al., 2013a) conducted a comparative analysis related to the effect of wind generation on electricity prices. The results show that the effect remains less significant for large markets, such as the German and Nordic markets. Research by (Gürtler & Paulsen, 2018) showed the effects of wind and solar power generation forecasts on electricity prices. Using a dataset comprising twenty-four daily observations of day-ahead and intra-day prices from 2010 to 2016 and applying a regression model, the authors showed a negative effect of production on price. (Brown et al., 2012) identified the impact of wind generation on the local economy of a set of countries from 2000-2008. By using a panel data model combined with the method of instrumental variables, the results converged on the idea that an increase of one megawatt (MW hereafter) makes it possible to increase GDP per capita by 11.50 dollars. Moreover, (Brown et al., 2012) showed that the same increase created 0.48 jobs. (Jensen et al., 2014) examined the impact of wind generation on Danish property prices. The results revealed a drop in housing prices between 3 and 7% following the combined visual and noise impacts. A paper published by (J. C. Ketterer, 2014) provided an overview of the relationship between intermittent wind power generation and electricity price behavior in Germany using a GARCH model. According to the findings, wind power leads to a decrease in price levels, but it increases their volatility. (Klementavicius et al., 2014) presented a new method that provides a statistical evaluation of the variation of the wind power generation process based on a new concept of homogeneous generation periods (HGP). This method is validated using a numerical configuration representing the Lithuanian wind group over a 13-day windy period. The results of the validation underline the effectiveness of the suggested method for the ex-post quantification of the variation of wind production in the short term. According to a study by (Buttler et al., 2016) which is used to quantify the variations and characteristics of wind energy production from the time series measured for the year 2014, collected from transmission system operators in the European Union (EU), the production of wind energy is the greatest during the winter season. Regarding Germany and considering the uncertainty associated with forecasting wind energy production, (Shen & Ritter, 2016) examined the volatility forecasting capabilities of different GARCH-type models for wind power generation. In addition, due to characteristics of the wind process, such as heteroscedasticity and non-linearity, they also investigated the use of a commutative GARCH model. Markov regime action (MRS-GARCH) to predict wind energy volatility. They found that the MRS-GARCH model significantly outperforms traditional GARCH models in predicting wind energy volatility, whereas the exponential GARCH model is superior to traditional GARCH models. (Katinas et al., 2014) established a simulation model to describe the wind energy resources of places with different climatic conditions in Lithuania. For the Weibull calculation parameters, 8760 hourly wind speed data were used in 2014. They found that the proposed model could be successfully used to find suitable locations for wind power development in regions having the same surrounding parameters. (Vincent & Trombe, 2017) emphasize fluctuations in wind power generation that are caused by fluctuations in wind speed. Forecasting wind variability requires statistical and physical modeling. Predictors of wind and energy variability include large-scale weather patterns, wind speed time series, and information about upcoming weather patterns. Numerical weather prediction models have been proven to be a useful tool for predicting wind generation variability. Renewable energy sources are highly dependent on weather and climate variability. Indeed, (Weber et al., 2018) studied the relationship between wind generation and climate change in many parts of Europe. They found that the occurrence of wind speeds below the trigger speed becomes more likely to happen and results in lower wind power generation. They also observed an increasing seasonal variability of winds over most of central and northwestern Europe. This could increase the education in winter and standby power requirements in summer. (Maniatis & Milonas, 2022) observed that the rise in the spot price of the wholesale electricity market in Greece is correlated with a decrease in the instability of the prices for wholesale electricity.

III. DATA PRESENTATION AND METHODOLOGY

A. DATA AND VARIABLES

Data of the study was obtained from Nord Pool power market (Nord Pool) database and Our World in Data (Mathieu et al., 2020), covering the period of mid-2013 to 2020, and includes 7 countries with 15 areas/regions divided in two periods, Pre-COVID-19 (1/6/2013 - 31/12/2019) and a restricted period during-COVID-19, (1/1/2020 to 31/12/2020). Data include electricity price associated for each area

(LOCAL_PRICE2) in Euro, wind energy production (PRODUCTION) in MWh, Stringency Index, Containment Health Index, Economics Policy Index, Total Deaths by COVID-19 and Total Confirmed Cases by COVID-19 in numbers (see Table 1)

Table 1: Variables, symbols, and Measurement

Variables	Symbols	Measurements
Local Price	LOCAL_PRICE2	Local Electricity Price in Euro (€)
Production	PRODUCTION	Wind energy production in MWh
Stringency Index	STRINGENCY_INDEX	Ranges from 0 to 100, where higher values indicate stricter government policies and restrictions in response to the COVID-19 pandemic.
Containment Health Index	CONTAINMENT_HEALTH_INDEX	The index typically ranges from 0 to 100, where higher values indicate better containment of the virus.
Economics policy index	ECONOMICPOLICY_INDEX	The index typically ranges from 0 to 100, where higher values indicate a more accommodative economic policy stance and lower values indicate a more restrictive stance
Total Death by COVID-19	DETH_COV	Total number of deaths attributed to COVID-19
Total Confirmed Cases by COVID-19	C_CASES	Total number of total confirmed cases of COVID-19

Source: Authors

B. DESCRIPTIVE STATISTICS

- First period: Pre-COVID19 (01/06/2013-31/12/2019)

Table 2 indicate that the mean value of the electricity price was 34.75 Euro per region, with a standard deviation of 11.73. This suggests that the majority of the observed electricity prices during the period were within a range of approximately +/- 12 Euro from the mean value. The median value of the electricity price was lower than the mean, indicating that the distribution of electricity prices may be positively skewed, which is further supported by the positive skewness value of 1.74. Additionally, the very high kurtosis value of 42.78 suggests that the distribution of electricity prices was very peaked, with a heavy tail on both sides.

In contrast, the wind energy production during the same period had a mean value of 74,397.26 MWh, with a standard deviation of 65,781.17. This suggests a greater variability in wind energy production compared to electricity prices. The median value of wind energy production was 54,172.00 MWh, which is also lower than the mean, indicating a possible positive skewness in the distribution. The skewness value of 1.34 further supports this interpretation. The kurtosis value of 4.19 indicates that the distribution of wind energy production was moderately peaked, with a narrower spread than the electricity price distribution.

The Jarque-Bera test for normality showed that neither the electricity price nor wind energy production was normally distributed. The probability values associated with both variables were 0.000, which indicates that the distribution of both variables was significantly different from a normal distribution. This suggests that a different type of distribution may be more appropriate for modeling these variables.

Table 2: Descriptive statistics of pre-COVID-19

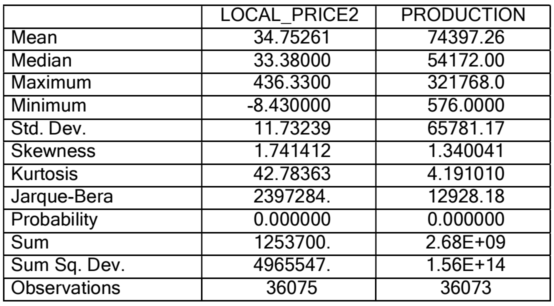

	LOCAL_PRICE2	PRODUCTION
Mean	34.75261	74397.26
Median	33.38000	54172.00
Maximum	436.3300	321768.0
Minimum	-8.430000	576.0000
Std. Dev.	11.73239	65781.17
Skewness	1.741412	1.340041
Kurtosis	42.78363	4.191010
Jarque-Bera	2397284.	12928.18
Probability	0.000000	0.000000
Sum	1253700.	2.68E+09
Sum Sq. Dev.	4965547.	1.56E+14
Observations	36075	36073

Source: Authors using Eviews

- Second period: During COVID-19 - Restricted (01/06/2013-31/12/2019)

The analysis of the statistical output of the restricted period of the COVID-19 pandemic, spanning from January 1, 2020, to December 31, 2020, reveals several significant insights. The study focused on seven variables, including local electricity price in Euro (€), wind energy production in MWh, the stringency index, containment health index, economic policy index, total confirmed cases of COVID-19, and the number of total deaths attributed to COVID-19.

The mean local electricity price during the period was €20.34, with a standard deviation of €15.20. The median was €17.74, indicating that the distribution of prices was skewed, with a positive skewness value of 0.95. The highest and lowest prices observed during the period were €107.42 and €-14.37, respectively, indicating the presence of negative prices and suggesting significant price fluctuations in response to the pandemic.

The mean wind energy production during the period was 75,944.61 MWh, with a standard deviation of 63,686.25 MWh. The median value was 61,512 MWh, indicating a skewed distribution of production. The highest and lowest production levels observed during the period were 307,951 MWh and 2,431 MWh, respectively, indicating that wind energy production was impacted by the pandemic.

The government policy indices which range from 0 to almost 100 indicate that the stringency index measures the severity of government policies and restrictions in response to the pandemic, had a mean value of 43.50 and a standard deviation of 23.19. The containment health index, which measures the effectiveness of measures to contain the virus, had a mean value of 40.01 and a standard deviation of 18.86. The economic policy index, measures the accommodative or restrictive nature of economic policies, had a mean value of 43.26 and a standard deviation of 27.83. These statistics suggest that governments around the world implemented a variety of policies with varying degrees of success in response to the pandemic revealing that the COVID-19 pandemic had a significant impact on health outcomes, with a total of 6,664,127 confirmed cases and 1,213.866 deaths attributed to the virus during the period. The median number of confirmed cases was 8,912.5, indicating a skewed distribution of the confirmed cases. The median number of deaths was 255, indicating that some regions experienced significant mortality impacts due to the pandemic (see Table 3).

Table 3: Descriptive statistics during COVID-19 (Restricted period)

	LOCAL_PRICE2	PRODUCTION	STRINGENCY_INDEX	CONTAINMENT_HEALTH_INDEX	ECONOMICPOLICY_INDEX	C_CASES	DETH_COV
Mean	20.33955	75944.61	43.50066	40.00940	43.26275	31203.96	1213.866
Median	17.73500	61512.00	50.00000	47.62000	37.50000	8912.500	255.0000
Maximum	107.4200	307951.0	87.04000	76.67000	100.0000	437379.0	8727.000
Minimum	-14.37000	2431.000	0.000000	0.000000	0.000000	0.000000	0.000000
Std. Dev.	15.20087	63686.25	23.19269	18.86467	27.83101	61426.05	2165.384
Skewness	0.952031	1.036769	-0.684225	-1.063694	-0.014762	3.757571	1.801314
Kurtosis	4.155320	3.399146	2.443343	2.910775	2.348256	19.45588	4.638427
Jarque-Bera	1134.650	1019.967	499.2516	1037.094	97.36563	74863.76	3582.996
Probability	0.000000	0.000000	0.000000	0.000000	0.000000	0.000000	0.000000
Sum	111664.1	4.17E+08	238818.6	219651.6	237512.5	1.71E+08	6664127.
Sum Sq. Dev.	1268323.	2.23E+13	2952538.	1953403.	4251587.	2.07E+13	2.57E+10
Observations	5490	5490	5490	5490	5490	5490	5490

Source: Authors using Eviews

- Comparative results and preliminary conclusions:

Results between both period reveals some interesting differences. Firstly, in terms of wind energy production, the mean production during the pre-COVID-19 period was 74,397.26 MWh, while during the COVID-19 period it was slightly higher at 75,944.61 MWh. However, the standard deviation of production during the COVID-19 period was much lower (63,686.25 MWh) compared to the pre-COVID-19 period (65,781.17 MWh). This indicates that wind energy production during the COVID-19 period was more consistent than before, mean that the values of the data points are clustered closely around the mean. In other words, the variability or dispersion of the data around the mean is relatively small shows that wind energy production during COVID-19 is more stable and less prone to large fluctuations or outliers which is desirable in many situations as it implies that the data is reliable and trustworthy with less volatility in the data leading to a more consistent mean.

The consistency in wind energy production during the COVID-19 period can be attributed to the fact that wind energy is generated from a renewable resource, which is not affected by the pandemic in the same way that non-renewable resources are. Wind turbines continue to generate energy as long as the wind blows, regardless of whether there is a pandemic or not. Therefore, the wind energy production remains consistent even during times of crisis, providing a stable and reliable source of electricity for consumers.

Additionally, the economic policies implemented by governments during the COVID-19 period, such as economic stimulus packages and accommodative monetary policies, may have also played a role in maintaining the consistency of wind energy production. These policies aimed to support economic activity and prevent a severe recession, which would have negatively impacted energy demand and production. The containment measures implemented by governments also led to a shift towards remote work and reduced industrial activity, resulting in a lower overall energy demand (Juergensen et al., 2020). However, the demand for renewable energy remained stable due to the long-term contracts and incentives provided by governments, ensuring that the production of wind energy remained consistent.

Secondly, the mean local electricity price during the pre-COVID-19 period was €34.78, which is higher than the mean price during the COVID-19 period (€20.34). The standard deviation of the local price was also higher during the pre-COVID-19 period (€11.75) compared to the COVID-19 period (€15.20), indicating that electricity prices were more volatile during the pre-COVID-19 period.

Thirdly, the statistics related to the COVID-19 pandemic (i.e., stringency index, containment health index, total confirmed cases, and total deaths) show a significant difference between the two periods suggesting that governments adopted more accommodative economic policies during the COVID-19 period to support the economy.

The comparative analysis shows that the COVID-19 period had a significant impact on the wind energy market, local electricity prices, and the economy. However, wind energy production during the COVID-19 period was more consistent, and the efforts to contain the virus had some impact as indicated by the higher containment health index.

C. POOLED OLS MODEL ESTIMATION: PRELIMINARY ESTIMATION

Pooled Ordinary Least Squares (Pooled OLS) estimation involves fitting a linear regression model to the panel data, where the regression coefficients are estimated using ordinary least squares (OLS) separately for each individual or entity in the panel. This approach allows for individual-specific intercepts and slopes, as well as common trends over time, it accounts for both within-individual and between-individual variation, which can improve the precision and accuracy of parameter estimates. It is also flexible enough to handle different types of panel data structures, such as balanced or unbalanced panels, and can be extended to handle more complex models, such as dynamic panel data models.

According to (Okui & Wang, 2021), Pooled OLS is a widely used method for estimating panel data models. The method involves estimating separate regressions for each individual and then combining the results to obtain panel estimates. Pooled OLS is particularly useful when dealing with unbalanced panels and is robust to heteroskedasticity and autocorrelation. On the other hand, (Baltagi & Baltagi, 2009) notes that Pooled OLS assumes that the individual-specific effects are uncorrelated with the regressors, which may not always be the case. Additionally, Pooled OLS assumes that the errors are independently and identically distributed, which may not hold in certain applications.

PRE-COVID19 POOLED OLS MODEL ESTIMATION

Table 4 shows that PRODUCTION has a negative coefficient of -1.98E-05 with a t-statistic of -22.09552, which indicates that as the value of PRODUCTION increases by one unit, LOCAL_PRICE2 decreases by -1.98E-05 units, holding other factors constant. The coefficient is statistically significant at the 1% level, as the associated probability value is 0.00. This implies that PRODUCTION is a significant predictor of LOCAL_PRICE2.

The constant, C, has a coefficient of 29.99326, which means that when the value of all independent variables is zero, the expected value of LOCAL_PRICE2 is 29.99326. The coefficient of the trend variable, @TREND, is positive at 0.004608, implying that LOCAL_PRICE2 increases by 0.004608 units for each one-unit increase in the time trend. The t-statistic is significant at the 1% level, indicating that the effect of time on LOCAL_PRICE2 is statistically significant.

The R-squared value of 0.085964 indicates that the independent variables explain only a small proportion of the variance in the dependent variable. The adjusted R-squared is also very low at 0.085913, which suggests that the model is not a good fit. The root mean squared error (RMSE) indicates that the average difference between the actual and predicted values of LOCAL_PRICE2 is 11.21690. The standard deviation of the dependent variable, LOCAL_PRICE2, is 11.73268. The Akaike information criterion (AIC) value is 7.672886, and the Schwarz criterion (SC) is 7.673592. Both criteria suggest that the model may not be the best fit.

The sum of squared residuals is 4,538,661, which indicates that the model has some unexplained variance. The F-statistic value is 1696.174, and the associated probability value is 0.0000, indicating that the overall regression model is significant. The Durbin-Watson statistic is 0.365582, which is less than two, suggesting that there might be autocorrelation in the error term.

Overall, the results suggest that PRODUCTION and @TREND have a significant effect on LOCAL_PRICE2. However, the low R-squared and adjusted R-squared values indicate that the model does not explain a large amount of the variation in the dependent variable. The low values of AIC and SC criteria also suggest that the model may not be the best fit. Additionally, the presence of autocorrelation in the error term may indicate that the model has some shortcomings that need to be addressed.

Table 4: Pre-COVID19 Pooled OLS model estimation

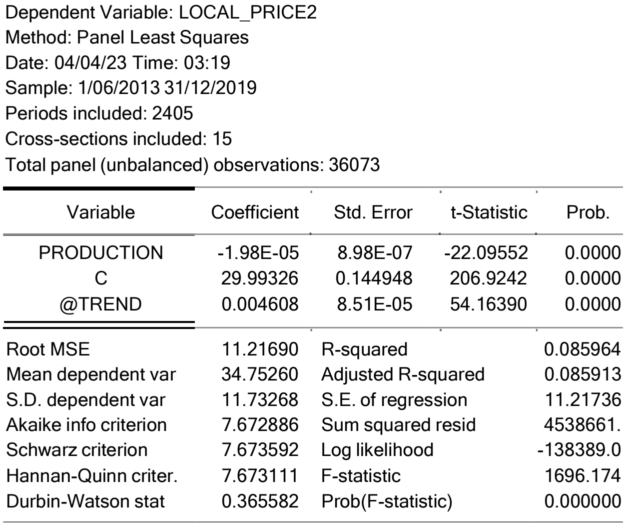

```
Dependent Variable: LOCAL_PRICE2
Method: Panel Least Squares
Date: 04/04/23 Time: 03:19
Sample: 1/06/2013 31/12/2019
Periods included: 2405
Cross-sections included: 15
Total panel (unbalanced) observations: 36073

        Variable         Coefficient   Std. Error   t-Statistic    Prob.

      PRODUCTION          -1.98E-05     8.98E-07    -22.09552     0.0000
           C               29.99326     0.144948     206.9242     0.0000
        @TREND             0.004608     8.51E-05     54.16390     0.0000

Root MSE                   11.21690   R-squared                 0.085964
Mean dependent var         34.75260   Adjusted R-squared        0.085913
S.D. dependent var         11.73268   S.E. of regression        11.21736
Akaike info criterion      7.672886   Sum squared resid         4538661.
Schwarz criterion          7.673592   Log likelihood           -138389.0
Hannan-Quinn criter.       7.673111   F-statistic               1696.174
Durbin-Watson stat         0.365582   Prob(F-statistic)         0.000000
```

Source: Authors using Eviews

DURING COVID19 POOLED OLS MODEL ESTIMATION

The results of Table 5 show that the production rate has a negative and statistically significant effect on local prices. A one-unit increase in production decreases local prices by 3.82E-05. Also, an increase in the number of COVID19 confirmed cases results in a positive and significant effect on local prices, implying that local prices increase with an increase in COVID19 cases. The Stringency Index, which measures the strictness of government policies, has a negative and significant effect on local prices, indicating that more stringent government policies decrease local prices. The Containment Health Index has a positive and significant impact on local prices, implying that countries' efforts to contain the spread of the virus by investing in healthcare increase local prices. Similarly, the Economic Support Index has a positive and significant effect on local prices, indicating that providing economic support increases local prices.

The coefficient of the variable DETH_COV is statistically insignificant, indicating that they have no significant impact on local prices. The root mean square error (RMSE) is 13.04712, indicating that the model has a good fit. The R-squared value is 0.263162, indicating that the model can explain 26.32% of the variation in local prices. The Adjusted R-squared value is 0.262221, indicating that the independent variables explain 26.22% of the variation in local prices. The standard deviation (SD) of the dependent variable is 15.20087, and the standard error (SE) of regression is 13.05664 this result could be explained by the fact that DETH_COV, which represents the number of COVID19 deaths per capita in a given area, may not be a major driver of local prices. Other factors, such as the level of economic support provided by the government, the production of goods and services in the area, and the stringency of the containment measures, could have a stronger influence on local prices than the number of COVID19 deaths. Moreover, the insignificant coefficient of DETH_COV could also be attributed to the fact that the variable may not have captured the full extent of the impact of the pandemic on local prices. The number of COVID19 deaths may not fully reflect the overall health and economic impacts of the pandemic on the area, as there could be other factors, such as job losses, business closures, and changes in consumer behavior, that could have influenced local prices. Another possible explanation for the insignificance of DETH_COV is that the variable may not have been measured accurately or effectively. For example, the data used to calculate DETH_COV may have been incomplete or unreliable, these assumptions could have led to a less precise estimate of the variable’s impact on local prices.

The Akaike Information Criterion (AIC) value is 7.977927, while the Schwarz criterion (’C) is 7.987560. Both values are relatively close to each other, suggesting that the model’s accuracy is not significantly affected by the inclusion or exclusion of variables. The Hannan-Quinn Criterion (HQC) value is 7.981287, indicating that the model has a good fit. The F-statistic value is 279.6999, with a p-value of 0.0000, indicating that the overall model is statistically significant. Finally, the Durbin-Watson (DW) statistic is 0.475688, which is below 2.0, indicating that the model has a positive autocorrelation.

Regarding the significance of @TREND in the restricted period, it still appears to be statistically significant with a t-statistic of -4.659805 and a p-value of 0.0000. This suggests that there is a significant linear trend in the dependent variable over time, even when restricting the analysis to the period between 1/01/2020 and 31/12/2020.

It is worth noting that the coefficient for @TREND is negative, which means that the dependent variable is decreasing over time during this period. This is also supported by the negative slope of the trend line in the scatter plot of the dependent variable over time.

In addition to @TREND, the coefficients for PRODUCTION, C_CASES, STRINGENCY_INDEX, CONTAINMENT_HELTH_INDEX, and ECONOMIC_SUPPORT_INDEX are also statistically significant with p-values of 0.00. These variables are all important predictors of LOCAL_PRICE2 during the restricted period, and their coefficients indicate the direction and strength of their effects on the dependent variable.

Table 5: During COVID-19 Pooled OLS model estimation (Restricted)

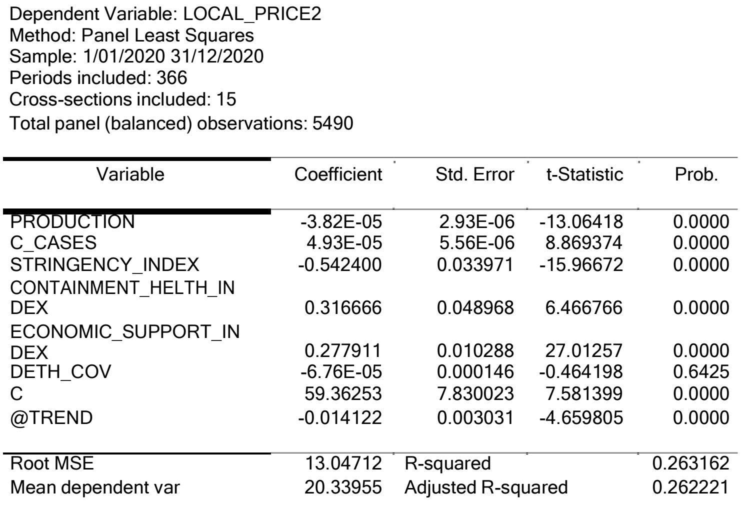

```
Dependent Variable: LOCAL_PRICE2
Method: Panel Least Squares
Sample: 1/01/2020 31/12/2020
Periods included: 366
Cross-sections included: 15
Total panel (balanced) observations: 5490

Variable                 Coefficient   Std. Error   t-Statistic   Prob.

PRODUCTION                -3.82E-05     2.93E-06    -13.06418    0.0000
C_CASES                    4.93E-05     5.56E-06     8.869374    0.0000
STRINGENCY_INDEX          -0.542400     0.033971    -15.96672    0.0000
CONTAINMENT_HELTH_IN
DEX                        0.316666     0.048968     6.466766    0.0000
ECONOMIC_SUPPORT_IN
DEX                        0.277911     0.010288     27.01257    0.0000
DETH_COV                  -6.76E-05     0.000146    -0.464198    0.6425
C                          59.36253     7.830023     7.581399    0.0000
@TREND                    -0.014122     0.003031    -4.659805    0.0000

Root MSE                   13.04712   R-squared                  0.263162
Mean dependent var         20.33955   Adjusted R-squared         0.262221
```

S.D. dependent var	15.20087	S.E. of regression	13.05664
Akaike info criterion	7.977927	Sum squared resid	934548.8
Schwarz criterion	7.987560	Log likelihood	-21891.41
Hannan-Quinn criter.	7.981287	F-statistic	279.6999
Durbin-Watson stat	0.475688	Prob(F-statistic)	0.000000

Source: Authors using Eviews

- Pre-COVID19 correlation matrix

Table 6 shows that the correlation coefficient between LOCAL_PRICE2 and PRODUCTION is -0.107804, which indicates a weak negative relationship between the two variables. This suggests that as wind energy production increases, the local electricity price decreases slightly.

The p-value for the correlation coefficient is 0.0000, which indicates that this correlation is statistically significant, meaning that it is unlikely to have occurred by chance alone.

Table 6: Correlation matrix of pre-COVID19

Covariance Analysis: Ordinary
Sample: 1/06/2013 31/12/2019
Included observations: 36073
Balanced sample (listwise missing value deletion)

Correlation Probability	LOCAL_PRICE2	PRODUCTION
LOCAL_PRICE2	1.000000	
PRODUCTION	-0.107804	1.000000

Source: Authors using Eviews

- Correlation matrix during COVID-19:

Table 7 output shows that the correlation coefficients between the variables are as follows:

There is a moderate negative relationship between LOCAL_PRICE2 and PRODUCTION (r = -0.231703), indicating that as wind energy production increases, the local electricity price decreases moderately.

There is a weak positive relationship between C_CASES and PRODUCTION (r = 0.146751), suggesting that there may be a small positive association between the two variables.

There is a weak negative relationship between STRINGENCY_INDEX and LOCAL_PRICE2 (r = -0.102315), suggesting that as government policies and restrictions in response to the COVID-19 pandemic become stricter, local electricity prices decrease slightly.

There is a weak negative relationship between CONTAINMENT_HELTH_INDEX and LOCAL_PRICE2 (r = -0.008198), indicating that the containment of the virus has little to no impact on local electricity prices.

There is a moderate positive relationship between ECONOMIC_SUPPORT_INDEX and LOCAL_PRICE2 (r = 0.284449), suggesting that as the economic policy stance becomes more accommodative, local electricity prices increase moderately.

The statistical output indicates that the COVID-19 pandemic had a varied impact on the relationships between these variables, with some showing stronger associations than others.

Table 7: Correlation matrix during COVID-19 (Restricted)

Covariance Analysis: Ordinary
Sample: 1/01/2020 31/12/2020
Included observations: 5490

Correlation Probability	LOCAL_PRICE2	PRODUCTION	C_CASES	STRINGENCY_INDEX	CONTAINMENT_HELTH_INDEX	ECONOMIC_SUPPORT_INDEX
LOCAL_PRICE2	1.000000					
PRODUCTION	-0.231703	1.000000				
C_CASES	0.087915	0.146751	1.000000			
	0.0000	0.0000	-----			
STRINGENCY_INDEX	-0.102315	-0.047411	0.337575	1.000000		
	0.0000	0.0004	0.0000	-----		
CONTAINMENT_HELTH_INDEX	-0.008198	-0.085018	0.360282	0.958722	1.000000	
	0.5436	0.0000	0.0000	0.0000	-----	
ECONOMIC_SUPPORT_INDEX	0.284449	-0.213782	0.212505	0.634595	0.729088	1.000000

Source: Authors using Eviews

IV. PANEL ARDL PMG STEPS AND ANALYSIS

A. PANEL UNIT ROOT TEST

Panel unit root tests are statistical methods commonly used in econometrics to assess the stationarity or non-stationarity of panel datasets, which consist of data collected over time for multiple cross-sectional units (Pedroni et al., 2004). Stationarity refers to the property of a time series where the statistical properties, such as mean and variance, remain constant over time. Non-stationarity, on the other hand, means that the statistical properties change over time, which can lead to spurious regression results and unreliable inference.

One important consideration in panel unit root testing is the presence of cross-sectional dependence or common factors among the units in the panel dataset (Bai, 2009). Cross-sectional dependence refers to the potential correlation or interdependency among the cross-sectional units, which can violate the assumption of independence among observations. Therefore, it is crucial to account for cross-sectional dependence in panel unit root tests to obtain accurate results.

The second generation of panel unit root tests refers to a more advanced and refined set of tests that have been developed to address the limitations of the first generation of panel unit root tests (Moon et al., 2004). The second-generation tests incorporate more sophisticated methodologies, such as panel cointegration and factor augmented panel regressions, to account for cross-sectional dependence and improve the accuracy of panel unit root testing (Pesaran, 2007).

PANEL CROSS-SECTIONAL DEPENDENCE TEST

The cross-section dependence test used to determine if there is a correlation between the regions included in the dataset. In this case, the regions refer to the different locations where the local electricity price (LOCAL_PRICE2) and wind energy production (PRODUCTION) were measured.

Pre-COVID19 output (see Table 8) shows the results of three different tests: the Breusch-Pagan LM test, the Pesaran scaled LM test, and the bias-corrected scaled LM test. The null hypothesis for each test is that there is no cross-section dependence (correlation)
between the regions. The first column shows the test being performed (Breusch-Pagan LM, Pesaran scaled LM, or bias-corrected scaled LM). The second and fourth columns show the test statistic for LOCAL_PRICE2 and PRODUCTION, respectively. The third and fifth columns show the probability (p-value) associated with the test statistic. In all the three tests, the p-values for both LOCAL_PRICE2 and PRODUCTION are less than 0.05, indicating that the null hypothesis of no cross-section dependence is rejected. Therefore, there is evidence of cross-sectional dependence (correlation) between the regions for both variables.

In the same vein for COVID19 restricted period (see Table 9)
for each variable, the output shows the test statistics and probabilities associated with each test. The probabilities (p-values) are all less than 0.05, indicating strong evidence against the null hypothesis of no cross-sectional dependence. Therefore, the results suggest that there is a significant correlation between the observations from different regions in the dataset, which should be considered in any subsequent analyses.

Consequently, cross-section dependence is present in all series because all probabilities are lower than the 5% level as a result, we have to conduct the second generation of panel unit root tests.

Table 8: Pre-COVID19 cross-sectional dependence test

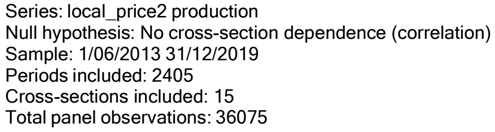

```
Cross-Section Dependence Test
Series: local_price2 production
Null hypothesis: No cross-section dependence (correlation)
Sample: 1/06/2013 31/12/2019
Periods included: 2405
Cross-sections included: 15
Total panel observations: 36075
```

Note: non-zero cross-section means detected in data
Cross-section means were removed during computation of correlations.

pre_covid	local_price2		production	
Test	Statistic	Prob.	Statistic	Prob.
Breusch-Pagan LM	135210.2	0.0000	42617.25	0.0000
Pesaran scaled LM	9323.142	0.0000	2933.624	0.0000
Bias-corrected scaled LM	9323.139	0.0000	2933.621	0.0000
Pesaran CD	353.6795	0.0000	167.1600	0.0000

Source: Authors using Eviews

Table 9: During COVID19 cross-sectional dependence test

Cross-Section Dependence Test
Series: local_price2 production stringency index c_cases deth_cov containment_index economic_index
Null hypothesis: No cross-section dependence (correlation)
Sample: 1/01/2020 31/12/2020
Periods included: 366
Cross-sections included: 15
Total panel observations: 5490
Note: non-zero cross-section means detected in data
Cross-section means were removed during computation of correlations

Restricted	local_price2		production			
Test	Statistic	Prob.	Statistic	Prob.		
Breusch-Pagan LM	14005.79	0.0000	5312.917	0.0000		
Pesaran scaled LM	959.2455	0.0000	359.3804	0.0000		
Bias-corrected scaled LM	959.2249	0.0000	359.3599	0.0000		
Pesaran CD	102.7843	0.0000	53.56542	0.0000		
Restricted	**stringency_index**		**c_cases**			
Test	Statistic	Prob.	Statistic	Prob.		
Breusch-Pagan LM	31684.81	0.0000	36387.38	0.0000		
Pesaran scaled LM	2179.214	0.0000	2503.722	0.0000		
Bias-corrected scaled LM	2179.193	0.0000	2503.701	0.0000		
Pesaran CD	177.5544	0.0000	190.6909	0.0000		
Restricted	**deth_cov**		**containment_index**		**economic_index**	
Test	Statistic	Prob.	Statistic	Prob.	Statistic	Prob.
Breusch-Pagan LM	31350.07	0.0000	34072.50	0.0000	28041.83	0.0000
Pesaran scaled LM	2156.115	0.0000	2343.980	0.0000	1927.824	0.0000
Bias-corrected scaled LM	2156.094	0.0000	2343.959	0.0000	1927.804	0.0000
Pesaran CD	174.3654	0.0000	184.4641	0.0000	165.9556	0.0000

Source: Authors using Eviews

SECOND GENERATION OF PANEL UNIT ROOT TESTS

The second generation of panel unit root tests should be used when cross-sectional units in the data are not cross-sectionally independent, and there is a possibility of cross-sectional dependence. The first generation of panel unit root tests assumes that cross-sectional units are independent, while the second generation relaxes this assumption and allows for cross-sectional dependence. The second-generation tests are useful in situations where the data has a unit root, and the panels are heterogeneous, meaning there is no common autoregressive (AR) structure in the series. The first-generation tests can be used for unbalanced panels except for the (Hadri, 2000) test, which tests for non-stationarity instead of stationarity.

In Table 10 results suggest that in level, some variables have a unit root for both pre-COVID-19 and during COVID-19 periods. However, in first difference and with imposing restrictions, such as a constant or a constant and trend in first difference, the unit root is rejected for all the variables. The rejected null hypothesis of a unit root indicates that the variables are stationary at first difference (see Table 11), and therefore, the time series data of the variables are less likely to produce spurious regression results.

The CIPS test takes into account the cross-sectional dependence that may exist among the units in the panel, which can lead to a loss of power if not properly addressed. It does this by augmenting the IPS test with additional regressors that capture the cross-sectional dependence in the data. Truncated CIPS (or TCIPS) is a modification of the CIPS test that addresses the issue of size distortion, which can occur when testing for the stationarity of panels with a large number of cross-sectional units. The test statistic is truncated to a maximum value, which helps to control for size distortions in such panels. IPS stands for "Im, Pesaran, and Shin," which is a first-generation panel unit root test used to test the stationarity of a panel dataset. It was developed by Im, Pesaran, and Shin (Im et al., 2003) and is based on the Augmented Dickey-Fuller (ADF) test, which is commonly used for testing the unit root in individual time series data.

Summarizing, local_price2, production, stringency_index, containment_health_index, and economicpolicy_index are I(0) and I(1). The variable c_cases is I(1) according to CIPS and Truncated CIPS (none). The variable deth_cov is I(0) and I(1) according to truncated CIPS with constant and trend. We can use CADF for the second generation of the panel unit root test. It gives, however, results per cross-section. Thus, we conclude that the results of the panel unit root tests suggest that most of the variables in the dataset become stationary in first difference. This suggests that the probability of obtaining false regression results from the time series data of these variables is lower.

Table 10: Unit root test in level

Pre_covid	None			
	CIPS T-stat	p-value	Truncated CIPS T-stat	p-value
local_price2	-7,62985	<0,01	-5,74343	<0,01
production	-6,79015	<0,01	-5,65831	<0,01
Restricted	None			
	CIPS T-stat	p-value	Truncated CIPS T-stat	p-value
local_price2	-3,88014	<0,01	-3,88014	<0,01
production	-3,51233	<0,01	-3,51233	<0,01
stringency_index	-2,21927	<0,01	-2,21927	<0,01
c_cases	-1,07349	>=0,1	-1,78589	<0,05
deth_cov	-0,35708	>=0,1	-0,67443	>=0,1
containment_index	-1,86017	<0,01	-1,86017	<0,01
economic_index	-3,27169	<0,01	-3,27169	<0,01
Pre_covid	With constant			
	CIPS T-stat	p-value	Truncated CIPS T-stat	p-value
local_price2	-8,62593	<0,01	-5,88523	<0,01
production	-7,42553	<0,01	-5,86657	<0,01
Restricted	With constant			
	CIPS T-stat	p-value	Truncated CIPS T-stat	p-value
local_price2	-4,10308	<0,01	-4,10308	<0,01
production	-4,08823	<0,01	-4,07992	<0,01
stringency_index	-2,55766	<0,01	-2,55766	<0,01
c_cases	-1,35202	>=0,1	-2,04964	>=0,1
deth_cov	-0,47934	>=0,1	-0,89795	>=0,1
containment_index	-2,12315	<0,01	-2,121315	<0,01
economic_index	-3,29349	<0,01	-3,29349	<0,01
Pre_covid	With constant & trend			
	CIPS T-stat	p-value	Truncated CIPS T-stat	p-value
local_price2	-8,58781	<0,01	-6,18446	<0,01
production	-7,73168	<0,01	-6,1862	<0,01
Restricted	With constant & trend			
	CIPS T-stat	p-value	Truncated CIPS T-stat	p-value
local_price2	-4,24799	<0,01	-4,29799	<0,01
production	-4,38077	<0,01	-4,31591	<0,01
stringency_index	-2,40792	>=0,1	-2,40792	>=0,1
c_cases	-2,32947	>=0,1	-2,32947	>=0,1
deth_cov	0,03405	>=0,1	-3,41875	<0,01
containment_index	-2,04407	<0,01	-2,04407	<0,01
economic_index	-3,72087	<0,01	-3,72087	<0,01

Source: Authors using Eviews

Table 11: Unit root test in first difference

Pre_covid	None			
	CIPS T-stat	p-value	Truncated CIPS T-stat	p-value
local_price2	-25,93878	<0,01	-6,12	<0,01
production	-24,0152	<0,01	-6,12	<0,01
Restricted	None			
	CIPS T-stat	p-value	Truncated CIPS T-stat	p-value
local_price2	-10,97256	<0,1	-5,99797	<0,1
production	-12,44047	<0,1	-6,12	<0,1
stringency_index	-9,34911	<0,1	-6,12	<0,1
c_cases	-1,7889	<0,1	-0,13482	<0,1
deth_cov	0,65766	>=0,1	-0,13482	>=0,1
containment_index	-11,48152	<0,1	-6,12	<0,1
economic_index	-10,63739	<0,1	-6,12	<0,1
Pre_covid	With constant			
	CIPS T-stat	p-value	Truncated CIPS T-stat	p-value
local_price2	-25,92348	<0,01	-6,19	<0,01
production	-24,0472	<0,01	-6,19	<0,01
Restricted	With constant			
	CIPS T-stat	p-value	Truncated CIPS T-stat	p-value
local_price2	-10,96015	<0,1	-6,0566	<0,1

production	-12,42641	<0,1	-6,19	<0,1
stringency_index	-9,38225	<0,1	-6,19	<0,1
c_cases	-2,06773	>=0,1	-2,06773	>=0,1
deth_cov	0,74254	>=0,1	-0,71244	>=0,1
containment_index	-11,49814	<0,1	-6,19	<0,1
economic_index	-10,63144	<0,1	-6,19	<0,1
Pre_covid	With constant & trend			
	CIPS T-stat	p-value	Truncated CIPS T-stat	p-value
local_price2	-25,91918	<0,01	-6,42	<0,01
production	-24,04283	<0,01	-6,42	<0,01
Restricted	With constant & trend			
	CIPS T-stat	p-value	Truncated CIPS T-stat	p-value
local_price2	-11,10454	<0,1	-6,2913	<0,1
production	-12,42848	<0,1	-6,42	<0,1
stringency_index	-9,44568	<0,1	-6,42	<0,1
c_cases	-2,23269	>=0,1	-2,23269	>=0,1
deth_cov	0,28484	>=0,1	-3,20967	<0,1
containment_index	-11,58176	<0,1	-6,42	<0,1
economic_index	-10,63195	<0,1	-6,42	<0,1

Source: Authors using Eviews

B. PANEL ARDL COINTEGRATION TEST OF SECOND GENERATION (WESTERLUND)

The second-generation panel cointegration tests, such as the (Westerlund, 2007) test, are used to test the cointegration relationship among variables in a panel dataset while accounting for cross-sectional dependence. When analyzing a panel dataset, it is important to consider the potential for cross-sectional dependence. If cross-sectional dependence exists, the standard panel unit root and panel cointegration tests may produce invalid results. The second-generation panel cointegration tests, such as the (Westerlund, 2007) test, are specifically designed to address this issue by accounting for cross-sectional dependence.

The (Westerlund, 2007) test is one of the most popular second-generation panels cointegration tests. It extends the first-generation panel cointegration tests, such as the (Pedroni, 1999) and (Kao, 1999) tests, by allowing for cross-sectional dependence. The test is based on the residual augmented least squares (RALS) estimator and is robust to a variety of different forms of cross-sectional dependence, such as common factors and spatial correlation.

Based on the above findings (Panel unit test for the second generation and dependance test), we proceeded to investigate the potential cointegration relationship among all the selected factors, aiming to determine if there is a long-run equilibrium process among the series. To achieve this, we utilized the Durbin Hausman group mean cointegration test proposed by (Westerlund & Edgerton, 2008), which offers several advantages. Firstly, this test does not heavily rely on prior knowledge about the order of integration, and it accounts for cross-sectional dependency, allowing for differentiation of stability ranks among the explanatory variables. Secondly, the Panel tests (Pt and Pa) examine the overall cointegration of the panel, while as per (Persyn et al., 2008), the Group-mean tests (Gt and Ga) assess the cointegration for at least one unit.

The results presented in Table 12 indicate that the Gt and Pa tests provide support for the existence of a long-run relationship among renewable energy production and the explanatory variables across the entire panel and the fifty subpanel regions during the period of 2013-2020. This supports the hypothesis that a long-run equilibrium exists among these variables (Belaid & Elsayed, 2019).

- Pre-COVID-19 Westerlund Panel cointegration test and results:

Table 12 shows the results of the Westerlund Panel cointegration test of second generation for the pre-COVID19 period. The test was conducted under three different specifications: without a constant, with a constant, and with both a constant and trend. The statistics and p-values are reported for four tests: among group Gt and between group Ga for the existing of cointegration individual panels, among panel Pt and between panel Pa for the existing of cointegration in the whole panel.

The statistics for the four tests are negative and highly significant at the 1% level, with p-values of 0.000. This indicates that there is strong evidence of cointegration among the variables,

implying a long-run relationship between them. The magnitude of the statistics is larger for the specifications that include a constant and trend, suggesting that the inclusion of these terms improves the fit of the model. Results conclude a stable long-run relationship in the pre-COVID19 period.

Table 12: Westerlund (2007) Panel Cointegration Test (pre-COVID-19)

	None Statistic	P-value	With constant Statistic	P-value	With constant & trend Statistic	P-value
Gt	-5.671	0.000	-7.911	0.000	-8.023	0.000
Ga	-108.077	0.000	-211.709	0.000	-216.935	0.000
Pt	-22.730	0.000	-32.081	0.000	-32.471	0.000
Pa	-101.662	0.000	-189.474	0.000	-194.020	0.000

Source: Authors using Stata

- During COVID-19 Westerlund Panel cointegration test and results:

Table 13 shows the results of the Westerlund Panel cointegration test of second generation for different variables during the COVID-19 period. The test was conducted with different specifications, including without constant, with constant, and with constant and trend, all models have statistically significant results (p-value < 0.01) for all variables. This suggests that there is a long-term relationship among the variables, and they move together in the long run and the strength of the cointegration relationship differs across the models and variables. For instance, the model with "Production, stringency index" has the highest statistic values in all specifications, indicating the strongest cointegration relationship. On the other hand, the model with "Production, economic policy index" has relatively weaker cointegration relationships than other models.

The results suggest that there is a long-term relationship among the variables during the COVID-19 period, and the strength of the relationship varies among different variables and models and that all variables are cointegrated in the long run in all models.

Table 13: Westerlund (2007) Panel Cointegration Test (During COVID-19/restricted)

Model		None Statistic	P-value	With constant Statistic	P-value	With constant & trend Statistic	P-value
Production, stringency index	Gt	-4.580	0.000	-5.302	0.000	-6.167	0.000
	Ga	-48.293	0.000	-61.511	0.000	-83.872	0.000
	Pt	-19.123	0.000	-22.113	0.000	-25.773	0.000
	Pa	-54.719	0.000	-71.842	0.000	-96.157	0.000
Production, containment_health_index	Gt	-4.643	0.000	-5.165	0.000	-6.304	0.000
	Ga	-50.856	0.000	-60.805	0.000	-85.142	0.000
	Pt	-19.674	0.000	-21.994	0.000	-31.948	0.000
	Pa	-57.933	0.000	-71.502	0.000	-111.278	0.000
Production, eocnomicpolicy_index	Gt	-4.643	0.000	-5.135	0.000	-5.912	0.000
	Ga	-50.856	0.000	-60.107	0.000	-76.765	0.000
	Pt	-19.674	0.000	-22.041	0.000	-30.493	0.000
	Pa	-57.933	0.000	-70.971	0.000	-102.307	0.000
Production, c_cases	Gt	-4.778	0.000	-5.674	0.000	-5.805	0.000
	Ga	-41.373	0.000	-59.242	0.000	-65.488	0.000
	Pt	-19.023	0.000	-22.802	0.000	-23.687	0.000
	Pa	-43.927	0.000	-67.149	0.000	-74.475	0.000
Production, deth_cov	Gt	-5.064	0.000	-5.338	0.000	-5.645	0.000
	Ga	-59.064	0.000	-65.803	0.000	-71.414	0.000
	Pt	-20.905	0.000	-21.933	0.000	-22.590	0.000
	Pa	-63.451	0.000	-71.784	0.000	-76.379	0.000

Source: Authors using Stata

V. PANEL ARDL PMG MODEL ESTIMATION

Since the study focuses on identifying the long and short run association between wind energy production and electricity price as well as the speed of adjustment equilibrium, the appropriate technique to be used to the analysis of dynamic panels is autoregressive distributed lag ARDL (p, q) model in the error correction form. Then, we estimate the model based on the pooled mean group (PMG) developed by (Pesaran et al., 1999). Following Wolde-Rufael and Weldemeskel (2020), the panel ARDL PMG is selected over panel ARDL (Mean Group) MG because short-term heterogeneity is allowed as stated by

Osman et al. (2016). Moreover, our analysis focuses on average elasticities across countries once the homogeneity restriction in the long run is valid. It's worth noting that (Pesaran et al., 1999) mentioned that the Dynamic Fixed Effects (DFE) estimator can produce inconsistent and potentially misleading estimates in dynamic panel data models unless the slope coefficients are exactly identical.

A. ERROR CORRECTION BASED AUTOREGRESSIVE DISTRIBUTED LAG (P, Q) ARDL MODEL

(Pesaran et al., 1999) used the maximum likelihood estimation (MLE) approach to measure both the heterogeneous short-run impact and the homogenous long-run impact of the variables on the dependent variable. They assumed that the disturbances εit are normally distributed. The estimation of the PMG model proposed by (Pesaran et al., 1999) follows the format of (Sohag et al., 2015).

$$\boldsymbol{LOCAL\_PRICE2}_{it} = \boldsymbol{u}_i + \sum_{j=1}^{p} \boldsymbol{\lambda}_{ij}\boldsymbol{LOCAL\_PRICE2}_{it-j} + \sum_{j=0}^{q} \boldsymbol{\delta'}_{it}\boldsymbol{X}_{it-j} + \varepsilon_{it} \quad (1)$$

$$\Delta\boldsymbol{LOCAL\_PRICE2}_{it} = \boldsymbol{u}_i + \boldsymbol{\varphi}_i\boldsymbol{LOCAL\_PRICE2}_{it-j} + Q'_i\boldsymbol{X}_{it} + \sum_{j=1}^{p-1} \boldsymbol{\lambda}_{ij*}\Delta\boldsymbol{LOCAL\_PRICE2}_{it-j} + \sum_{j=0}^{q-1} \boldsymbol{\delta'}^{*}_{ij}\,\Delta\boldsymbol{X}_{it-j} + \varepsilon_{it} \quad (2)$$

$$\mathbf{LOCAL\_PRICE2}_{it} = \mathbf{u}_i + \varphi_i(\mathbf{LOCAL\_PRICE2}_{it-1} + \theta'_i\mathbf{X}_{it}) + \sum_{j=1}^{p-1} \lambda_{ij*}\Delta\mathbf{LOCAL\_PRICE2}_{it-j} + \sum_{j=0}^{q-1} \delta'^{*}_{ij}\,\Delta\mathbf{X}_{it-j} + \varepsilon_{it} \quad (3)$$

where i = 1, 2,….., N represents cross sectional unit (regions), t = 1, 2, 3, ….., T represents time (daily), j is the number of time lag. X_{it} is the vector of independent variables, e.g., and finally u_i is the fixed effect. By re-parameterization, the above equation can be written as:

Where:

$$\varphi_i = -1\left(1 - \sum_{j=1}^{p}\lambda_{ij}\right), \beta_i = \sum_{j=0}^{p}\delta_{ij}\ ;\ \lambda_{ij*} = -\sum_{m=j+1}^{p}\lambda_{im}, j = 1,2,\ldots\ldots,p-1, and\ \delta^{*}_{it} = -\sum_{m=j+1}^{p}\delta^{*}_{im}, j = 1,2,\ldots\ldots,q-1.$$

After grouping the variables at different levels, Equation (2) is reformulated as an error correction equation:

where $\theta'_i = -(\beta' i / \varphi i)$ defines the long-run or equilibrium relationship among $\boldsymbol{LOCAL\_PRICE2}_{it}$ and $\boldsymbol{X}_{it}$. In contrast $\boldsymbol{\lambda}_{ij*}$ and $\boldsymbol{\delta'}^{*}_{ij}$ are short run coefficients relating price to its past values and other determinants like $\boldsymbol{X}_{it}$. Finally, the error-correction coefficient $\boldsymbol{\varphi}_i$ measures the speed of adjustment of $\boldsymbol{LOCAL\_PRICE2}_{it}$ toward its long-run equilibrium following a change in $\boldsymbol{X}_{it}$. The condition $\boldsymbol{\varphi}_i < 0$ ensures that a long-run relationship exists. Therefore, a significant and negative value of $\boldsymbol{\varphi}_i$ is treated as evidence of cointegration between $\boldsymbol{LOCAL\_PRICE2}_{it}$ and $\boldsymbol{X}_{it}$. Thus, finally the estimates are measured by:

$$\hat{\theta}_{PMG} = \frac{\sum_{i=1}^{N}\tilde{\theta}_i}{N}, \beta_{PMG} = \frac{\sum_{i=1}^{N}\tilde{\beta}_i}{N}, {}_{jPMG} = \frac{\sum_{i=1}^{N}\lambda_i}{N}, \hat{\gamma}_{jPMG} = \frac{\sum_{i=1}^{N}\gamma_i}{N}$$

Where $, j = 0,1,2,\ldots\ldots,q-1, \hat{\theta}_{PMG} = \tilde{\theta}$

As per the methodology outlined in Equation (3), five different models have been developed. Although the coefficients in these models have the same numeration, they may differ in value for each model. Therefore, the models to be estimated with different lag specifications are:

- Pre-COVID-19:

$$\Delta\mathbf{LOCAL\_PRICE2}_{it} = -\mathbf{u}_{i} + \varphi_{i}(\mathbf{LOCAPRICE2}_{it-1} - \theta_{1}\mathbf{PRODUCTION}_{it-1}) + \sum_{j=1}^{p-1}\lambda_{ij*}\Delta\mathbf{LOCAL\_PRICE2}_{it-j} + \sum_{j=0}^{q-1}\text{✿}_{ij}\,\Delta\mathbf{PRODUCTION}_{it-j} + \varepsilon_{it} \tag{4}$$

- During COVID-19:

$$\Delta\mathbf{LOCAL\_PRICE2}_{it} = \mathbf{u}_{i} + \varphi_{i}(\mathbf{LOCAPRICE2}_{it-1} - \boldsymbol{\theta}_{1}\mathbf{PRODUCTION}_{it-1} - \boldsymbol{\theta}_{2}\mathbf{STRINGENCY\_INDEX}_{it-1}) + \sum_{j=1}^{p-1}\lambda_{ij*}\Delta\mathbf{LOCAL\_PRICE2}_{it-j} + \sum_{j=0}^{q-1}\text{✿}_{1ij}\,\Delta\mathbf{PRODUCTION}_{it-j} + \sum_{j=0}\text{✿}_{2}\,\Delta\mathbf{STRINGENCY\_INDEX}_{it-j} + \varepsilon \tag{5}$$

$$\Delta\mathbf{LOCAL\_PRICE2}_{it} = \mathbf{u}_{i} + \varphi_{i}(\mathbf{LOCAPRICE2}_{it-1} - \theta_{1}\mathbf{PRODUCTION}_{it-1} - \theta_{2}\mathbf{C\_CASES}_{it-1}) + \sum_{j=1}^{p-1}\lambda_{ij*}\Delta\mathbf{LOCAL\_PRICE2}_{it-j} + \sum_{j=0}^{q-1}\text{✿}_{ij}\,\Delta\mathbf{PRODUCTION}_{it-j} + \sum_{j=0}^{q-1}\text{✿}_{ij}\,\Delta\mathbf{C\_CASES}_{it-j} + \varepsilon_{it} \tag{6}$$

$$\Delta\mathbf{LOCAL\_PRICE2}_{it} = \mathbf{u}_{i} + \varphi_{i}(\mathbf{LOCAPRICE2}_{it-1} - \theta_{1}\mathbf{PRODUCTION}_{it-1} - \theta_{2}\mathbf{DETH\_COV}_{it-1}) + \sum_{j=1}\lambda_{ij} * \Delta\mathbf{LOCAL\_PRICE2}_{it-j} + \sum_{j=0}^{q-1}\text{✿}_{1ij}\,\Delta\mathbf{PRODUCTION}_{it-j} + \sum_{j=0}\text{✿}_{2ij}\,\Delta\mathbf{DETH\_COV}_{it-j} + \varepsilon_{it} \tag{7}$$

$$\Delta\mathbf{LOCAL\_PRICE2}_{it} = \mathbf{u}_{i} + \varphi_{i}(\mathbf{LOCAPRICE2}_{it-1} - \theta_{1}\mathbf{PRODUCTION}_{it-1} - \theta_{2}\mathbf{CONTAINMMENT\_HEALTH\_INDEX}_{it-1}) + \sum_{j=1}^{p-1}\lambda_{ij} * \Delta\mathbf{LOCAL\_PRICE2}_{it-j} + \sum_{j=0}^{q-1}\text{✿}_{ij}\,\Delta\mathbf{PRODUCTION}_{it-j} + \sum_{j=0}^{q-1}\text{✿}_{ij}\,\Delta\mathbf{CONTAINMMENT\_HEALTH\_INDEX}_{it-j} + \varepsilon_{it} \tag{8}$$

$$\Delta\mathbf{LOCAL\_PRICE2}_{it} = -\mathbf{u}_{i} + \varphi_{i}(\mathbf{LOCAPRICE2}_{it-1} - \boldsymbol{\theta}_{1}\mathbf{PRODUCTION}_{it-1} - \theta_{2}\mathbf{ECONOMICPOLICY\_INDEX}_{it-1}) + \sum_{j=1}\lambda_{ij*}\Delta\mathbf{LOCAL\_PRICE2}_{it-j} + \sum_{j=0}^{q-1}\text{✿}_{1ij}\,\Delta\mathbf{PRODUCTION}_{it-j} + \sum_{j=0}\text{✿}_{2ij}\,\Delta\mathbf{ECONOMICPOLICY\_INDEX}_{it-j} + \varepsilon_{it} \tag{9}$$

In Equations (4)-(9), θ1, θ2 represent parameters to be estimated and Δ indicates the differenced operator. If the variables are integrated of order I (1), the error term becomes an I (0) process. Cointegration is characterized by short-run disequilibrium converging towards long-run equilibrium at a rate of φi, which represents the error-correcting speed of adjustment term. A φi value of 0 would indicate no evidence of a long-run relationship. Negative and significant φi is expected, assuming variables return to a long-run equilibrium. The validity of the approach depends on conditions such as a negative error-correction term and serially uncorrelated residuals. Incorporating lags into an ARDL model may fulfil these conditions. The approach is useful for comparing long-run equilibrium relationships across countries with similar local electricity prices, as it allows for heterogeneity in coefficients in the short run and homogeneity in the long run. The validity of estimators depends on the large time series dimension of the data.

- Pre-COVID19 model estimation: Model 1 – ARDL (2,2)

The output suggests that the ARDL (2,2) model from 2013 to 2019 is appropriate for analyzing the relationship between the local electricity price dependent variable D(LOCAL_PRICE2) and the WEP (PRODUCTION) independent variable (see

Table 14). The model selection method used is the Akaike information criterion (AIC), which includes 2 lags for both the dependent variable LOCAL_PRICE2 and the dynamic regressor PRODUCTION. The fixed regressors are a constant term C and a trend term @TREND.

The long-run equation indicates that wind energy production (PRODUCTION) has a negative coefficient (-1.99E-05) that is marginally significant at a 10% level of significance. This suggests that in the long run, wind energy production before COVID-19 period has a small negative effect on the local electricity price, an increase in PRODUCTION leads to a decrease in LOCAL_PRICE2. Specifically, a 1% increase in PRODUCTION results in a 0.0199% decrease in LOCAL_PRICE2 in the long run. This can be explained by the basic principles of supply and demand. An increase in wind energy production represents an increase in the supply of electricity, wind energy is harnessed through wind turbines that convert the kinetic energy of wind into electrical energy, which can then be fed into the power grid and used to meet electricity demand, all other factors held constant. Wind power can be expected to have a downward pressure on electricity prices in the long run. This is because wind power is a low-cost source of generation, and as its penetration increases, it can displace more expensive sources of generation, such as coal and natural gas. As a result, the supply curve shifts to the right, leading to a lower equilibrium price. Conversely, a decrease in wind energy production would decrease the supply of electricity, leading to a higher equilibrium price. It is important to note that this analysis assumes that wind energy production is the only factor affecting the local electricity price in the long run.

In the short run, the coefficient of D(LOCAL_PRICE2(-1)) suggests that a 1% increase in the lagged value of LOCAL_PRICE2 results in a 0.1283% decrease in the current value of LOCAL_PRICE2, while the coefficients of D(PRODUCTION) and D(PRODUCTION(-1)) indicate that a 1% increase in PRODUCTION leads to a 0.000206% increase in LOCAL_PRICE2 in the current period and a 0.0000984% increase in LOCAL_PRICE2 in the previous period. This result can be explained by the laws of supply and demand in the short run. When wind energy production increases, there is an increase in the supply of electricity, which can put downward pressure on prices. However, if the demand for electricity remains constant or increases, the increase in supply can be met with an increase in demand, leading to higher prices. Although the negative effect of the lagged value of the local electricity price (LOCAL_PRICE2(-1)) on the current value of the local electricity price in the short run can be explained by the supply and demand dynamics in the market. When the local electricity price increases in the previous period, producers may increase their production in response to the higher profitability, which would lead to an increase in supply. At the same time, consumers may reduce or stabilize their demand for electricity due to the higher price, which would lead to a decrease in demand. As a result, in the short run, the market may experience a surplus of electricity, leading to a decrease in the current value of the local electricity price to reach equilibrium. Therefore, the negative coefficient of the lagged value of LOCAL_PRICE2 suggests that the local electricity market may be efficient in the short run, with prices adjusting to balance supply and demand.

Furthermore, the intercept C indicates that when all the independent variables are zero, LOCAL_PRICE2 is 4.570122. The trend variable @TREND suggests that there is a positive relationship between time and LOCAL_PRICE2, which means that LOCAL_PRICE2 is increasing over time, meaning that as time progresses, the local electricity price tends to increase. This may be due to factors such as increased demand, changes in production costs, or other economic factors that influence the price of electricity.

The speed of adjustment, as indicated by the coefficient of COINTEQ01, is -0.141395 a negative coefficient value implies that there is a tendency for LOCAL_PRICE2 to revert back towards its equilibrium level following any short-term fluctuations. Specifically, a coefficient value of -0.141395 suggests that approximately 14.14% of the deviation from the long-run equilibrium is corrected each period, this means that the market for LOCAL_PRICE2 is relatively efficient in responding to changes in supply and demand conditions. If the price deviates from its long-run equilibrium level due to a temporary shock or imbalance, the market will gradually adjust to eliminate the deviation and bring the price back to its equilibrium level over time. This is an important feature of a well-functioning market, these results are in line with (Nicolosi & Fürsch, 2009) research shown that in the short term, wind power feed-in can cause a decrease in electricity prices, while in the long term, wind power can affect the conventional energy supply, which may eventually be replaced by renewable sources such as wind power.

The low p-values for all the coefficients indicate that the coefficients are statistically significant. Overall, the model suggests that PRODUCTION is an important determinant of LOCAL_PRICE2, and the speed of adjustment suggests that the market for LOCAL_PRICE2 is relatively efficient in responding to deviations from long-run equilibrium. The concept of equilibrium is a key economic principle that suggests that markets tend to naturally adjust towards a state of balance or stability. In this context, the long-run equilibrium value of LOCAL_PRICE2 refers to the price level that corresponds to the intersection of supply and demand in the electricity market.

The model has a relatively low Akaike information criterion (AIC) of 5.92, which suggests that it is a good fit for the data. The standard error of the regression is 6.65, which implies that the model's predictions may deviate from the actual values by an average of 6.65 units.

Table 14: Model 1 - ARDL (2,2) pre-covid

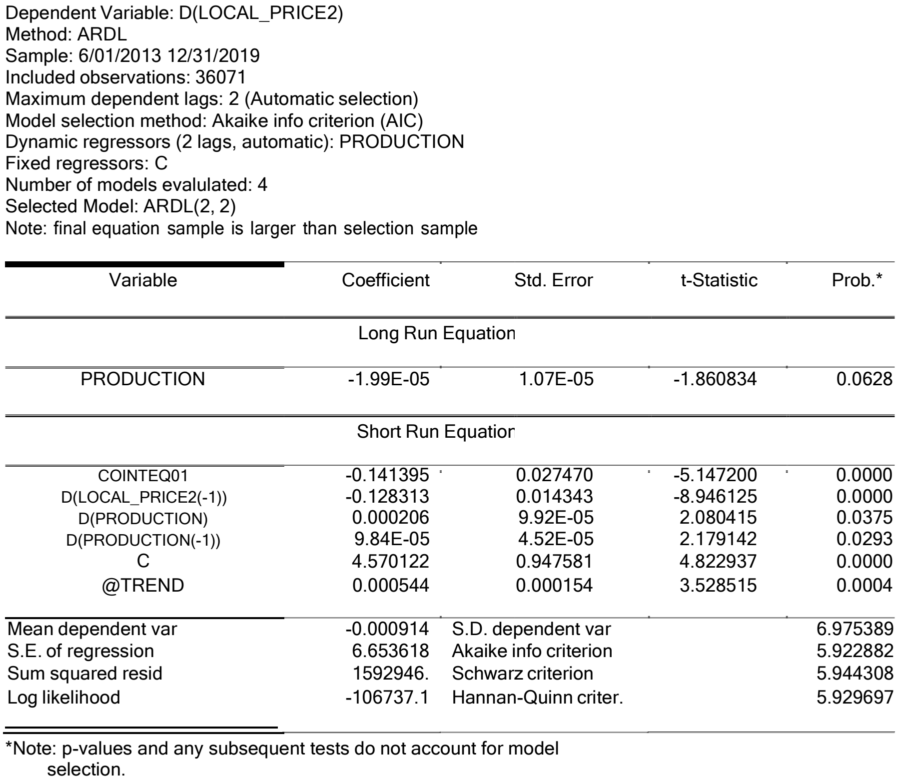

Dependent Variable: D(LOCAL_PRICE2)
Method: ARDL
Sample: 6/01/2013 12/31/2019
Included observations: 36071
Maximum dependent lags: 2 (Automatic selection)
Model selection method: Akaike info criterion (AIC)
Dynamic regressors (2 lags, automatic): PRODUCTION
Fixed regressors: C
Number of models evalulated: 4
Selected Model: ARDL(2, 2)
Note: final equation sample is larger than selection sample

Variable	Coefficient	Std. Error	t-Statistic	Prob.*
	Long Run Equation			
PRODUCTION	-1.99E-05	1.07E-05	-1.860834	0.0628
	Short Run Equatior			
COINTEQ01	-0.141395	0.027470	-5.147200	0.0000
D(LOCAL_PRICE2(-1))	-0.128313	0.014343	-8.946125	0.0000
D(PRODUCTION)	0.000206	9.92E-05	2.080415	0.0375
D(PRODUCTION(-1))	9.84E-05	4.52E-05	2.179142	0.0293
C	4.570122	0.947581	4.822937	0.0000
@TREND	0.000544	0.000154	3.528515	0.0004

Mean dependent var	-0.000914	S.D. dependent var	6.975389
S.E. of regression	6.653618	Akaike info criterion	5.922882
Sum squared resid	1592946.	Schwarz criterion	5.944308
Log likelihood	-106737.1	Hannan-Quinn criter.	5.929697

*Note: p-values and any subsequent tests do not account for model selection.

Source: Authors using Eviews

V.A.1 DURING COVID-19 MODELS ESTIMATION

- Model 2 - ARDL (2,2,2)

Model (2) indicate that wind energy production (PRODUCTION) has a negative and significant long-run effect on the local electricity price, meaning that an increase in wind energy production decreases the local electricity price (see Table 15).

Moreover, the study also finds that a stricter government response to the COVID-19 pandemic (STRINGENCY_INDEX) has a negative and significant long-run effect on the local price of electricity, higher stringency measures lead to a lower electricity price. This may be due to the fact that stricter measures, such as lockdowns and business closures, can lead to a decrease in electricity demand, which in turn can put downward pressure on prices. The closure of businesses, schools, and public spaces, as well as restrictions on travel and gatherings. This reduction in demand, combined with increased share of renewable energy due to disruptions to supply of conventional resources as coal, natural gas, or oil which can put downward pressure on prices. In other words, the decrease in demand due to the pandemic measures may shift the demand curve for electricity to the left, leading to a lower equilibrium price. Therefore, the negative long-run effect of the government's COVID-19 response on the local price of electricity is likely due to the interaction between changes in electricity supply and demand.

In the short run, the study finds that an increase in wind energy production in the previous period (PRODUCTION(-1)) has a positive and significant effect on the current value of the dependent variable. However, an increase in the current period of wind energy production (D(PRODUCTION)) does not have a significant effect on the local electricity price. In the short run, the study finds that lagged values of the dependent variable (LOCAL_PRICE2) have a negative but not significant effect on the current value of the dependent variable. This means that the price of electricity in the current period is not influenced by the price of electricity in the previous period.

Additionally, an increase in wind energy production in the previous period (PRODUCTION(-1)) has a positive and significant effect on the current value of the dependent variable. This implies that the level of wind energy production in the previous period is positively related to the current level of electricity prices. One possible explanation for this relationship is that wind energy production in the previous period may have affected the availability of electricity supply in the current period. If wind energy production was high in the previous period, it could have led to an increase in the overall supply of electricity, which could have put downward pressure on local electricity prices as a consequence this lead to increase current demand for electricity which could have put upward pressure on current prices result in positive relationship with previous wind energy production. In other word, if wind energy production was low in the previous period, it could have led to a decrease in the overall supply of electricity, which could have put upward pressure on lagged prices but could have put downward pressure on the current prices due to a lower electricity demand for the current period as the simulated example in Figure 1. This suggests that wind energy production in the previous period may have a significant impact on the current level of electricity prices and the increase in the current period wind energy production (D(PRODUCTION)) does not have a significant effect on the local price of electricity. This suggests that any increase in wind energy production in the current period is not sufficient to cause a significant change in electricity prices in the short run.

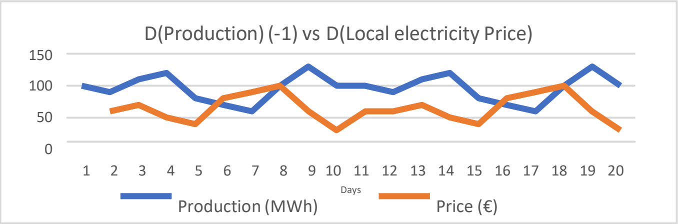

Figure 1: Fictional simulation of D(Production) (-1) vs D(Local electricity Price)

Source: Authors using Excel

Table 15: Model 2 - ARDL (2,2,2) restricted.

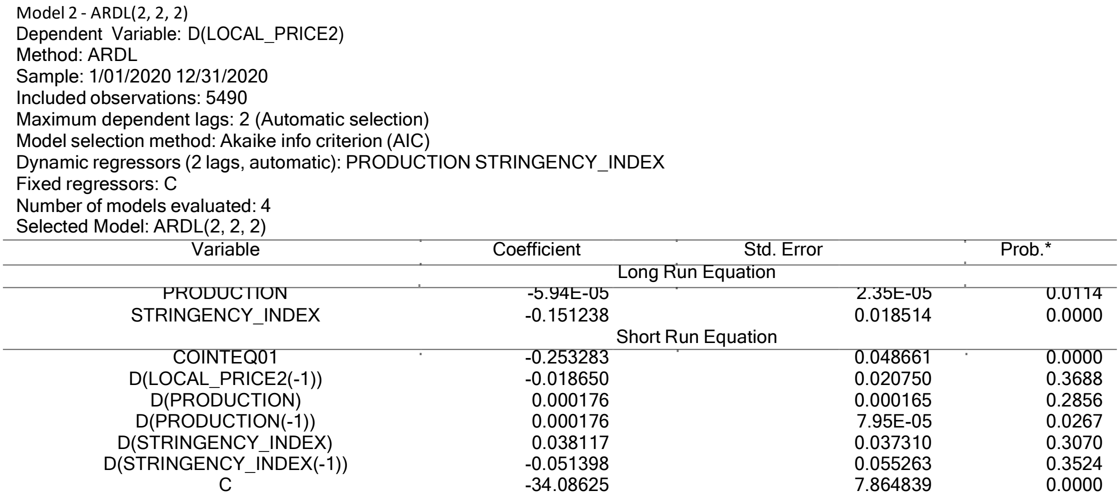

Model 2 - ARDL(2, 2, 2)
Dependent Variable: D(LOCAL_PRICE2)
Method: ARDL
Sample: 1/01/2020 12/31/2020
Included observations: 5490
Maximum dependent lags: 2 (Automatic selection)
Model selection method: Akaike info criterion (AIC)
Dynamic regressors (2 lags, automatic): PRODUCTION STRINGENCY_INDEX
Fixed regressors: C
Number of models evaluated: 4
Selected Model: ARDL(2, 2, 2)

Variable	Coefficient	Std. Error	Prob.*
	Long Run Equation		
PRODUCTION	-5.94E-05	2.35E-05	0.0114
STRINGENCY_INDEX	-0.151238	0.018514	0.0000
	Short Run Equation		
COINTEQ01	-0.253283	0.048661	0.0000
D(LOCAL_PRICE2(-1))	-0.018650	0.020750	0.3688
D(PRODUCTION)	0.000176	0.000165	0.2856
D(PRODUCTION(-1))	0.000176	7.95E-05	0.0267
D(STRINGENCY_INDEX)	0.038117	0.037310	0.3070
D(STRINGENCY_INDEX(-1))	-0.051398	0.055263	0.3524
C	-34.08625	7.864839	0.0000

ISSN: 1737-933484

@TREND	0.015924	0.003569	0.0000
Mean dependent var	-0.001198	S.D. dependent var	6.973186
S.E. of regression	93.19204	Akaike info criterion	6.010961
Sum squared resid	46619773	Schwarz criterion	6.157865
Log likelihood	-16378.09	Hannan-Quinn criter.	6.062205

*Note: p-values and any subsequent tests do not account for model selection.

Source: Authors using Eviews

- Model 3 - ARDL (7,2,2)

Model 3 in Table 16 indicate that in the long-run equation, the variables PRODUCTION and C_CASES are included as independent variables. The model selection method used is the Akaike information criterion (AIC), which select the model with the lowest AIC value. The selected model is an ARDL(7, 2, 2), which means that the maximum number of lags for the dependent variable is 7, and the maximum number of lags for the dynamic regressors (PRODUCTION and C_CASES) is 2.

In the long-run equation, the coefficient of C_CASES is 7.09E-05, which means that a 1% increase in confirmed COVID-19 cases is associated with a 0.007% increase in the local price of electricity in the long run, holding other factors constant. In the short-run equation, the coefficient of D(C_CASES) is 0.002029, which means that a 1% increase in confirmed COVID-19 cases is associated with a 0.203% increase in the local price of electricity in the short run, holding other factors constant. Therefore, we can conclude that the effect of confirmed COVID-19 cases on electricity prices is stronger in the short run than in the long run. This could be explained by the fact that in the short run, the electricity market may not have enough time to adjust to the changes in demand and supply caused by confirmed COVID-19 cases. As a result, the effect of COVID-19 cases on electricity prices may be more immediate and pronounced. However, in the long run, market forces and adjustments in supply and demand may help to mitigate the impact of COVID-19 cases on electricity prices, resulting in a weaker effect. Additionally, changes in consumer behavior and preferences, such as a shift towards renewable energy sources or energy efficiency, may also play a role in shaping the long-run dynamics of the electricity market.

The absence of "@Trend" means that the model does not include a time trend variable such as seasonality or other time-related trends. Therefore, any long-term changes in the dependent variable that are not captured by the other variables in the model are not accounted for.

In the short-run equation, lagged values of the dependent variable and several other independent variables, including PRODUCTION and C_CASES, are included. The coefficients of lagged dependent variables LOCAL_PRICE2 are all negative and significant, which suggests that the local price of electricity tends to revert to its long-run equilibrium in the short run. The coefficient of PRODUCTION in the short run is positive but not significant, which suggests that the current level of wind energy production does not have a significant effect on the local price of electricity in the short run. The short-run equation captures the dynamics of the adjustment process towards the long-run equilibrium. In this equation, lagged values of the dependent variable and other variables are included as independent variables. The negative and significant coefficients of the lagged dependent variables LOCAL_PRICE2 suggest that there is a tendency for the local price of electricity to revert to its long-run equilibrium in the short run. This means that any short-term deviations from the long-run equilibrium will be corrected over time, and the local price of electricity will eventually return to its long-run equilibrium level. This indicates that if the current local price of electricity is above its long-run equilibrium level, it will tend to decrease in the short run to reach its equilibrium level. Conversely, if the current local price of electricity is below its long-run equilibrium level, it will tend to increase in the short run to reach its equilibrium level. This phenomenon is known as mean reversion and suggests that the local price of electricity in the short run is influenced by its previous values. The negative coefficients indicate that the local price of electricity tends to move back towards its long-run equilibrium level after a period of deviation.

This model indicates that the coefficient of current C_CASES is positive and significant in both the short-run at 10% level and long-run equations at 1% level. This suggests that an increase in the number of confirmed COVID-19 cases has a positive effect on the local price of electricity in both the short and long term, however the impact is more important in the short run by 0.2%.

The positive coefficient of PRODUCTION in the short-run equation implies that an increase in wind energy production tends to increase the local price of electricity in the short run. However, this coefficient is not statistically significant, which suggests that the effect of wind energy production on the local price of electricity is not robust in the short run. In other words, the short-run impact of wind energy production on the local price of electricity may be influenced by other factors that are not captured in the model. As a result, the short-run equation suggests that any deviations from the long-run equilibrium in the local price of electricity will be corrected in the short run, but the short-run impact of wind energy production on the local price of electricity is not significant.

Additionally, the magnitude of the COINTEQ01 coefficient indicates the speed of adjustment, with larger absolute values representing faster adjustment. In this case, the magnitude of the coefficient is 0.124524, which suggests that the dependent variable adjusts by approximately 12.45% towards its long-run equilibrium value each day in response to changes in the independent variables. Therefore, it would take approximately 8 days towards its long-run equilibrium after a shock.

Table 16: Model 3 - ARDL (7,2,2) restricted.

Model 3 - ARDL (7, 2, 2)
Dependent Variable: D(LOCAL_PRICE2)
Method: ARDL
Sample: 1/01/2020 31/12/2020
Included observations: 5490
Maximum dependent lags: 7 (Automatic selection)
Model selection method: Akaike info criterion (AIC)
Dynamic regressors (2 lags, automatic): PRODUCTION C_CASES
Fixed regressors: C
Number of models evalulated: 14
Selected Model: ARDL (7, 2, 2)

Variable	Coefficient	Std. Error	Prob.*
	Long Run Equation		
PRODUCTION	-9.11E-05	3.92E-05	0.0201
C_CASES	7.09E-05	2.07E-05	0.0006
	Short Run Equation		
COINTEQ01	-0.124524	0.020824	0.0000
D(LOCAL_PRICE2(-1))	-0.148417	0.028717	0.0000
D(LOCAL_PRICE2(-2))	-0.150052	0.028309	0.0000
D(LOCAL_PRICE2(-3))	-0.100086	0.030750	0.0011
D(LOCAL_PRICE2(-4))	-0.100868	0.024372	0.0000
D(LOCAL_PRICE2(-5))	-0.104590	0.044111	0.0178
D(LOCAL_PRICE2(-6))	-0.067360	0.013026	0.0000
D(PRODUCTION)	0.000143	0.000160	0.3722
D(PRODUCTION(-1))	0.000153	7.51E-05	0.0412
D(C_CASES)	0.002029	0.001113	0.0685
D(C_CASES(-1))	-0.001071	0.000954	0.2620
C	3.705778	0.823669	0.0000

Root MSE	17.78465	Mean dependent var	-0.002598
S.D. dependent var	6.977226	S.E. of regression	18.08697
Akaike info criterion	5.990375	Sum squared resid	1736452.
Schwarz criterion	6.209527	Log likelihood	-16261.58
Hannan-Quinn criter.	6.066822		

*Note: p-values and any subsequent tests do not account for model selection

- Model 4 - ARDL (7,3,3)

Looking at the short-run equation, we can see that the coefficient of the lagged dependent variable (D(LOCAL_PRICE2(-1)) is negative and significant at the 1% level, indicating that there is a negative feedback effect in the short-run, which means that when local prices increase in one period, they tend to decrease in the next period. This could be due to the adjustment of supply and demand forces in the market (see Table 17). In addition, the coefficients of the other lagged dependent variables (D(LOCAL_PRICE2(-2)) to D(LOCAL_PRICE2(-6)) are also negative and significant, indicating that local electricity prices tend to be affected in the short run by their own past values in the presence of daily controlled variables as the number total death by COVID-19.

The coefficient of COINTEQ01 is negative and significant at the 1% level, which means that there is a speed of adjustment in the short-run equivalent of -0.114209 that take around 9 days towards their long-run equilibrium value. In other words, if there is a positive shock to local prices in one period, prices will

ISSN: 1737-933484

decrease in the following periods until they reach their long-run equilibrium value. Therefore, it would take approximately 9 days towards its long-run equilibrium after a shock.

On the other hand, in the long-run equation, we can see that the coefficient of PRODUCTION is negative but not significant, and the coefficient of DETH_COV is positive and significant at the 1% level. This indicates that in the long-run, local prices of electricity tend to be affected by the number of deaths due to COVID-19. The positive coefficient of DETH_COV suggests that higher COVID-19 mortality rates could be associated with higher local prices, possibly due changes in consumer behavior or to supply chain disruptions. It's possible that the effect of wind energy production on local prices is being dominated by the effect of COVID-19 deaths. In other words, the impact of COVID-19 deaths on local prices is stronger than the impact of wind energy production. This is supported by the fact that the coefficient of DETH_COV is significant at the 1% level, while the coefficient of PRODUCTION is not significant. It's also possible that there are other factors not included in the model that are affecting local prices, which could be contributing to the insignificant coefficient of PRODUCTION.

Table 17: Model 4 - ARDL (7,3,3) restricted.

Model 4 - ARDL(7, 3, 3)
Dependent Variable: D(LOCAL_PRICE2)
Method: ARDL
Sample: 1/01/2020 31/12/2020
Included observations: 5490
Maximum dependent lags: 7 (Automatic selection)
Model selection method: Akaike info criterion (AIC)
Dynamic regressors (3 lags, automatic): PRODUCTION DETH_COV
Fixed regressors: C
Number of models evalulated: 21
Selected Model: ARDL(7, 3, 3)

Variable	Coefficient	Std. Error	Prob.*
	Long Run Equation		
PRODUCTION	-6.33E-08	4.17E-05	0.9988
DETH_COV	0.002435	0.000617	0.0001
	Short Run Equation		
COINTEQ01	-0.114209	0.017905	0.0000
D(LOCAL_PRICE2(-1))	-0.158345	0.032926	0.0000
D(LOCAL_PRICE2(-2))	-0.190569	0.029613	0.0000
D(LOCAL_PRICE2(-3))	-0.100800	0.032604	0.0020
D(LOCAL_PRICE2(-4))	-0.099988	0.023547	0.0000
D(LOCAL_PRICE2(-5))	-0.107992	0.044871	0.0161
D(LOCAL_PRICE2(-6))	-0.069974	0.013853	0.0000
D(PRODUCTION)	0.000135	0.000168	0.4218
D(PRODUCTION(-1))	0.000145	8.07E-05	0.0725
D(PRODUCTION(-2))	2.32E-06	4.73E-05	0.9609
D(DETH_COV)	0.064540	0.050294	0.1995
D(DETH_COV(-1))	-0.069117	0.056227	0.2190
D(DETH_COV(-2))	0.081761	0.060282	0.1751
C	2.543353	0.636668	0.0001

Root MSE	17.73943	Mean dependent var	-0.002612
S.D. dependent var	6.977306	S.E. of regression	18.09219
Akaike info criterion	5.975613	Sum squared resid	1727634.
Schwarz criterion	6.230889	Log likelihood	-16191.06
Hannan-Quinn criter.	6.064661		

*Note: p-values and any subsequent tests do not account for model

Source: Authors using Eviews

- Model 5 - ARDL (2,2,2)

Table 18 indicates that wind energy production has a negative long-run relationship with local electricity price, with a coefficient of -6.72E-05 and a standard error of 2.34E-05 shows that an increase in wind energy production leads to a decrease in local electricity prices and that better containment of the virus (as measured by the (CONTAINMENT_HEALTH_INDEX) has a negative impact on local electricity prices in the long-run, with a coefficient of -0.208142 and a standard error of 0.025495. This suggests that stricter government policies and restrictions in response to the COVID-19 pandemic led to lower local electricity prices in the long-run.

In the short run, lagged variables as D(LOCAL_PRICE2) and (CONTAINMENT_HEALTH_INDEX) with mixed signs but not significant at 5% level however lagged values of wind energy production (PRODUCTION(-1)) have a positive and significant impact on local electricity prices, with coefficients of 0.000177 and a significant speed of adjustment of -0.252424 mean that long-run toward local electricity price equilibrium could be attained in approximately 4 days . In addition, the constant value (C) has a negative impact on local electricity prices in the short run, with a coefficient of -38.05059. The trend variable (@TREND) has a positive impact on local electricity prices in the short run, with a coefficient of 0.017584.

Table 18: Model 5 - ARDL (2,2,2) restricted.

Model 5 - ARDL(2, 2, 2)
Dependent Variable: D(LOCAL_PRICE2)
Method: ARDL
Sample: 1/01/2020 12/31/2020
Included observations: 5490
Maximum dependent lags: 2 (Automatic selection)
Model selection method: Akaike info criterion (AIC)
Dynamic regressors (2 lags, automatic): PRODUCTION CONTAINMENT_HEALTH_INDEX
Fixed regressors: C
Number of models evaluated: 4
Selected Model: ARDL(2, 2, 2)

Variable	Coefficient	Std. Error	Prob.*
	Long Run Equation		
PRODUCTION	-6.72E-05	2.34E-05	0.0041
CONTAINMMENT_HEALTH_INDEX	-0.208142	0.025495	0.0000
	Short Run Equation		
COINTEQ01	-0.252424	0.048312	0.0000
D(LOCAL_PRICE2(-1))	-0.019212	0.021217	0.3653
D(PRODUCTION)	0.000178	0.000165	0.2830
D(PRODUCTION(-1))	0.000177	7.95E-05	0.0261
D(CONTAINMMENT_HEALTH_INDEX)	0.003150	0.019276	0.8702
D(CONTAINMMENT_HEALTH_INDEX(-1))	-0.035815	0.062044	0.5638
C	-38.05059	8.812023	0.0000
@TREND	0.017584	0.003949	0.0000
Mean dependent var	-0.001198	S.D. dependent var	6.973186
S.E. of regression	101.0834	Akaike info criterion	6.012165
Sum squared resid	54849417	Schwarz criterion	6.159069
Log likelihood	-16381.39	Hannan-Quinn criter.	6.063410

*Note: p-values and any subsequent tests do not account for model selection.

Source: Authors using Eviews

- Model 6 - ARDL (2,2,2)

The model ARDL (2, 2, 2) in Table 19 includes both long-run and short-run equations. In the long-run equation, the dependent variable is regressed on PRODUCTION and ECONOMICPOLICY_INDEX. The coefficient on PRODUCTION is negative and statistically significant at the 5% level, indicating that there is a negative long-run relationship between the dependent variable and production. The coefficient on ECONOMICPOLICY_INDEX is also negative and statistically significant at the 1% level, indicating that there is a negative long-run relationship between the dependent variable and the economic policy index.

In the short-run equation, the dependent variable is regressed on its first lag (D(LOCAL_PRICE2(-1)) and several other variables, including COINTEQ01, D(PRODUCTION), D(PRODUCTION(-1)), D(ECONOMICPOLICY_INDEX), D(ECONOMICPOLICY_INDEX(-1)), and a constant term. The coefficient on D(LOCAL_PRICE2(-1)) is negative but not statistically significant at the 5% level, indicating that there is no significant short-run relationship between the dependent variable and its lagged value. The coefficient on D(PRODUCTION) is positive but not statistically significant at the 5% level, indicating that there is no significant short-run relationship between the dependent variable and production. The coefficient on D(PRODUCTION(-1)) is positive and statistically significant at the 5% level, indicating that there is a positive short-run relationship between the dependent variable and lagged wind energy production. The coefficient on D(ECONOMICPOLICY_INDEX) is positive but not statistically significant at the 5% level, indicating that there is no significant short-run relationship between the dependent variable and the economic policy index. The coefficient on D(ECONOMICPOLICY_INDEX(-1)) is negative but not statistically significant at the 5% level, indicating that there is no significant short-run relationship between the dependent variable and lagged economic policy index. The constant term and the trend variable (@TREND) are both statistically significant at the 1% level. The AIC value for this model is 6.017486, which is lower than the AIC values of the other models evaluated, indicating that this is the best model among the five models.

Table 19: Model 6 - ARDL (2,2,2) restricted.

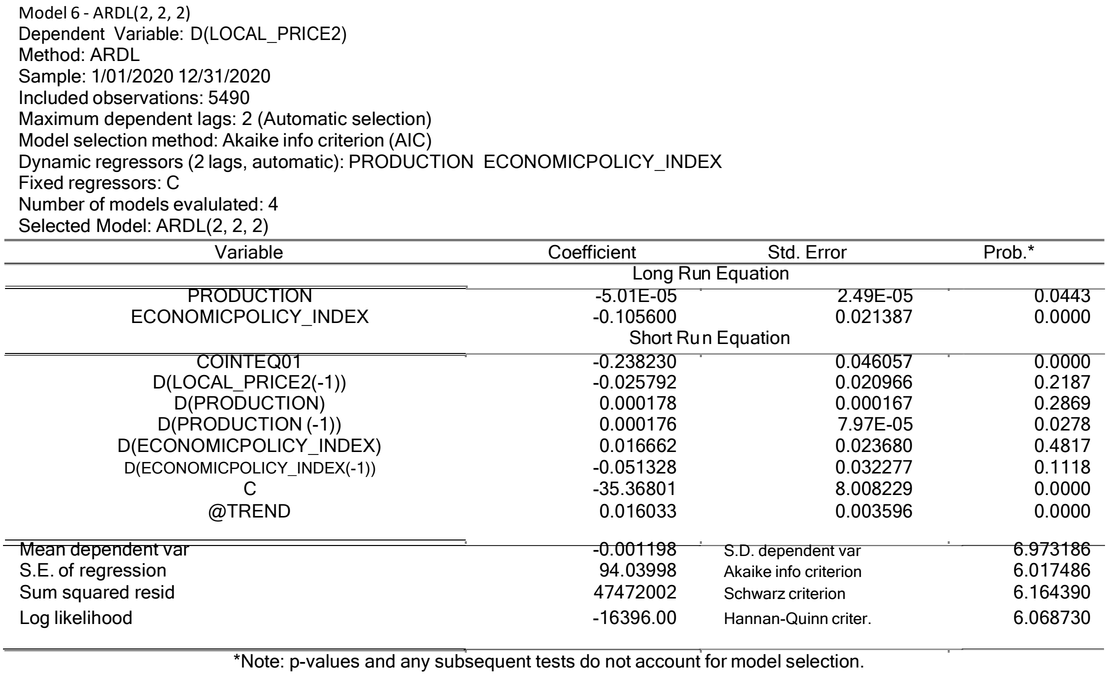

Model 6 - ARDL(2, 2, 2)
Dependent Variable: D(LOCAL_PRICE2)
Method: ARDL
Sample: 1/01/2020 12/31/2020
Included observations: 5490
Maximum dependent lags: 2 (Automatic selection)
Model selection method: Akaike info criterion (AIC)
Dynamic regressors (2 lags, automatic): PRODUCTION ECONOMICPOLICY_INDEX
Fixed regressors: C
Number of models evalulated: 4
Selected Model: ARDL(2, 2, 2)

Variable	Coefficient	Std. Error	Prob.*
Long Run Equation			
PRODUCTION	-5.01E-05	2.49E-05	0.0443
ECONOMICPOLICY_INDEX	-0.105600	0.021387	0.0000
Short Run Equation			
COINTEQ01	-0.238230	0.046057	0.0000
D(LOCAL_PRICE2(-1))	-0.025792	0.020966	0.2187
D(PRODUCTION)	0.000178	0.000167	0.2869
D(PRODUCTION (-1))	0.000176	7.97E-05	0.0278
D(ECONOMICPOLICY_INDEX)	0.016662	0.023680	0.4817
D(ECONOMICPOLICY_INDEX(-1))	-0.051328	0.032277	0.1118
C	-35.36801	8.008229	0.0000
@TREND	0.016033	0.003596	0.0000

Mean dependent var	-0.001198	S.D. dependent var	6.973186
S.E. of regression	94.03998	Akaike info criterion	6.017486
Sum squared resid	47472002	Schwarz criterion	6.164390
Log likelihood	-16396.00	Hannan-Quinn criter.	6.068730

*Note: p-values and any subsequent tests do not account for model selection.

Source: Authors using Eviews

VI. EMPIRICAL ANALYSIS AND RESULTS

A. LONG-RUN EFFECTS

Six different models were estimated to analyze the long-run effects of wind energy production on local electricity prices during COVID-19 conditions (see Table 20).

All the models except model 4 show a significant negative relationship between wind energy production and local electricity prices in the long run. This suggests that increasing wind energy production can lead to lower local electricity prices in the long run. Tables shows results for Models 2 to 6 estimated during COVID-19 conditions, highlighting negative and significant coefficients for lagged values of LOCAL_PRICE2 and dependent variables, indicating evidence of mean reversion in local electricity prices.

Models 2,5 and 6 indicate that wind energy production (PRODUCTION) has a negative and significant long-run effect on the local price of electricity, meaning that an increase in wind energy production decreases the local price of electricity. Moreover, the study also finds that a stricter government response to the COVID-19 pandemic of environmental stringency Index, containment Health Index and economics policy index has a negative and significant long-run effect on the local price of electricity, higher stringency measures, containment health and economics policy lead to a lower electricity price. Governments' implementation of higher stringency measures like lockdowns and restrictions on movement, the closure of businesses, schools, and public spaces, as well as restrictions on travel and gatherings leads to a decrease in economic activity and subsequently, reduced energy demand, this reduction in demand, combined with increased share of renewable energy due to disruptions to supply of conventional resources as coal, natural gas, and oil which can put downward pressure on prices. In other words, the decrease in demand due to the pandemic measures may shift the demand curve for electricity to the left, leading to a lower equilibrium price. Therefore, the negative long-run effect of the government's COVID-19 response on the local price of electricity is likely due to the interaction between changes in electricity supply and demand. Consequently, there is an excess supply of electricity, causing a downward impact on electricity prices. Alongside these measures, governments implement containment health policies to combat the spread of diseases during COVID-19, resulting in reduced economic activity and lower energy demand. Additionally, to spur economic growth, governments may implement economic policies that promote energy efficiency, leading to a decrease in energy demand and ultimately, lower electricity prices.

Model 3 show that the coefficient of PRODUCTION is -9.11E-05, which means that a 1% increase in wind energy production is associated with a 0.0091% decrease in the local price of electricity in the long run. The coefficient of C_CASES is 7.09E-05, which means that a 1% increase in confirmed COVID-19 cases is associated with a 0.0071% increase in the local price of electricity in the long run. The negative coefficient for wind energy production suggests that as wind energy production increases, the local price of electricity decreases. This may be because wind energy is a cheaper source of electricity compared to other sources, such as fossil fuels, and an increase in wind energy production may lead to a decrease in the cost of generating electricity, thus lowering the local price of electricity.

On the other hand, the positive coefficient for confirmed COVID-19 cases suggests that as confirmed COVID-19 cases increase, the local price of electricity also increases. This could be due to the fact that an increase in confirmed COVID-19 cases may lead to a direct impact by increasing demand for electricity specially from household actors, as more people stay at home and use more electricity for activities such as working from home and streaming entertainment. Additionally, COVID-19-related disruptions in the supply chain and workforce could also affect the production and delivery of electricity, leading to higher prices.

Model 4 indicate that the coefficient of PRODUCTION is negative but not significant, and the coefficient of DETH_COV is positive and significant at the 1% level. This indicates that in the long-run, local prices tend to be affected by the number of deaths due to COVID-19. The positive coefficient of DETH_COV suggests that higher COVID-19 mortality rates could be associated with higher local prices, possibly due to supply chain disruptions and government policies or changes in consumer behavior. It's possible that the effect of wind energy production on local prices is being dominated by the effect of COVID-19 deaths. In other words, the impact of COVID-19 deaths on local prices is stronger than the impact of wind energy production. This is supported by the fact that the coefficient of DETH_COV is significant at the 1% level, while the coefficient of PRODUCTION is not significant. It's also possible that there are other factors not included in the model that are affecting local prices, which could be contributing to the insignificant coefficient of PRODUCTION.

The results obtained indicate a negative correlation between Wind energy production and local electricity that range from -0,002% to -0,009% due to 1% increase in wind energy production, which is consistent with previous research that also shows a decrease in price resulting from a small increase in wind power production.(Jaraite et al., 2019) discovered evidence of the merit order effect in bidding area SE3, with a 1% increase in wind power production leading to a 0.083% reduction in prices, a considerably higher outcome than the findings in this study. The use of a different approach, namely an autoregressive conditional heteroskedasticity (GARCH) model, as in (J. Ketterer et al., 2012), by (Jaraite et al., 2019) may be a reason for the differences in results. The authors' model incorporates various variables, such as wind, Nordic hydro reservoirs, nuclear, demand, and biofuel price, to control for their effects. According to (J. Ketterer et al., 2012), a 1% increase in wind power caused a 0.1% price reduction in the German electricity market from 2006 to January 2012. However, (J. Ketterer et al., 2012) notes that this reduction occurs gradually over time and diminishes with time, a conclusion that is also supported by (Sensfuß et al., 2008). (Swinand & O'Mahoney, 2015) found a 0.06% price decrease in the Irish electricity market for a 1% increase in wind power. (Clò et al., 2015) also found statistically significant results demonstrating the impact of wind power production on day-ahead spot prices when controlling for factors such as demand and natural gas spot prices. (Gelabert et al., 2011) observed that a small rise in wind power caused a 4% reduction in prices between 2005 and 2009, which aligns with the predictions and results of this research. Similarly, (Würzburg et al., 2013b) detected a 20% wind power production effect in the German electricity market. (Holttinen & Valtion teknillinen tutkimuskeskus., 2004) employed a simulation model and demonstrated the production effect of wind in the Nordic electricity market, where a 10TWh increase in wind power reduced Nord Pool spot prices by €2/MWh.

In addition to the aforementioned results, it is crucial to highlight the long-run impacts of government measures and policies, as well as the influence of the COVID-19 pandemic on local electricity prices. The study reveals that during the COVID-19 period, stricter government policies and restrictions, as reflected by the stringency index, containment health index, and economic policy index, have a negative and significant impact on electricity prices. These measures, aimed at containing the spread of the virus and implementing economic policies, result in a decrease in local electricity prices by an estimated range of 151 € to 208 € across the different models employed.

Furthermore, the study uncovers a positive relationship between the increasing impact of COVID-19, as indicated by the numbers of confirmed coronavirus cases and mortality, and local electricity prices. The positive impact ranges from 0.07 € to 2.44 € across the various models used. This suggests that as the severity of the pandemic increases, local electricity prices experience an upward trend. This finding underscores the complex interactions between the pandemic and electricity pricing dynamics, highlighting the need for further analysis and investigation into the underlying mechanisms driving these relationships.

These results emphasize the role of government measures and policies in shaping the long-run dynamics of local electricity prices during the COVID-19 pandemic. Stricter measures and restrictions, combined with accommodative economic policies, contribute to a decrease in prices. Conversely, the increasing impact of COVID-19, in terms of confirmed cases and mortality, leads to an upward pressure on electricity prices. These findings have important implications for policymakers, as they highlight the significance of considering both government actions and the pandemic itself in understanding and managing electricity pricing dynamics in times of crisis.

Overall, the negative effect of government measures and the positive effect of the pandemic's severity contribute to the complex dynamics observed in electricity pricing. These findings contribute to a deeper understanding of the multifaceted factors at play in shaping electricity prices and can inform policymakers in developing effective strategies for managing electricity markets during times of crisis.

Table 20: Long run ARDL model variable measures and significance summary

Dependant Variables	Independent variables	Coefficient	Prob,*	impact in 1% increase	WEP impact of Extra 1 GW
Model 1 - ARDL(2, 2,)	PRODUCTION	-1,99E-05	0,0628*	-0,002%	-0,02 €
Model 2 - ARDL(2, 2, 2)	PRODUCTION	-5,94E-05	0,0114**	-0,006%	-0,06 €
	STRINGENCY_INDEX	-1,51E-01	0***	-15,124%	
Model 3 - ARDL (7, 2, 2)	PRODUCTION	-9,11E-05	0,0201**	-0,009%	-0,09 €
	C_CASES	7,09E-05	0,0006***	0,007%	
Model 4 - ARDL(7, 3, 3)	PRODUCTION	-6,33E-08	9,99E-01	0,000%	0,00 €
	DETH_COV	2,44E-03	0,0001***	0,244%	
Model 5 - ARDL(2, 2, 2)	PRODUCTION	-6,72E-05	0,0041***	-0,007%	-0,07 €
	CONTAINMMENT_HEALTH_INDEX	-2,08E-01	0***	-20,814%	
Model 6 - ARDL(2, 2, 2)	PRODUCTION	-5,01E-05	0,0443**	-0,005%	-0,05 €
	ECONOMICPOLICY_INDEX	-1,06E-01	0***	-10,560%	

Notes: *** ; ** and * indicate statistical significance at the levels of 1%, 5% and 10% respectively.

Models	M.1 - ARDL(2, 2)		M.2 - ARDL(2, 2, 2)		M.5 - ARDL(2, 2, 2)		M.6 - ARDL(2, 2, 2)		M.3 - ARDL (7, 2, 2)		M.4 - ARDL(7, 3, 3)	
Variable	Coefficient	Prob,*	Coefficient	Prob,*	Coefficient	Prob,*	Coefficient	Prob,*	Coefficient	Prob,*	Coefficient	Prob,*
D(PRODUCTION)	-0,0000199	0,0628*	-0,0000594	0,0114**	-0,0000672	0,0041***	-0,0000501	0,0443**	-0,0000911	0,0201**	-6,33E-08	0,9988
D(STRINGENCY_INDEX)			-0,151238	0***								
D(CONTAINMMENT_HEALTH_INDEX)					-0,208142	0***						
D(ECONOMICPOLICY_INDEX)							-0,1056					
D(C_CASES)									0,0000709	0,0006***		
D(DETH_COV)											0,002435	0,0001***

🟩 Significant
🟥 Not significant

Notes: ***; ** and * indicate statistical significance at the levels of 1%, 5% and 10% respectively.

Source: Authors suing Excel

B. SHORT-RUN EFFECTS

The PMG-ARDL estimator was used to analyze the short-run effects of wind energy production on local electricity prices during COVID-19 conditions. The results show that one-period lagged production of wind energy has a positive impact on the current local electricity prices, this impact reduced in the following days. However, current levels of wind energy production do not have a significant effect on local electricity prices in the short run, simply because wind energy production in the day-ahead market cannot be scheduled.

As an alternative, it is forecasted wind energy production that producers bid on the electricity market. Additionally, level of wind energy production in the previous period may have impacted the overall electricity supply, which could have affected the prices. When wind energy production was high, it may have increased the supply of electricity, leading to lower prices. This, in turn, could have caused an increase in current demand for electricity, resulting in a positive correlation with previous wind energy production. Conversely, when wind energy production was low in the previous period, it may have led to a reduction in the overall electricity supply, resulting in upward pressure on lagged prices. However, it could have put downward pressure on current prices due to lower electricity demand for the current period.

The five models 2 to 5 (See Table 21), shows that that there is agreement that lagged values of wind energy production have a significant impact on local electricity prices in the short run. These common results, suggest that the lagged wind energy production variable has a positive and significant effect on the current value of the dependent variable at the 5% level. This implies that wind energy production in the previous period may have affected the availability of electricity supply in the current period, which could have put upward or downward pressure on prices. However, the effect of current wind energy production on local electricity prices is mixed. an increase in current period wind energy production does not have a significant effect on the local price of electricity, indicating that there is no significant short-run relationship between the dependent variable and the current wind energy production.

In terms of the other controlled variables, Models includes environmental stringency Index, containment Health Index, economics policy index, total death by COVID-19 and total confirmed cases by COVID-19 does not have a significant effect on local electricity prices in the short run.

However, model 3 and 4 coefficients of lagged dependent variables LOCAL_PRICE2 are all negative and significant, which suggests that the local price of electricity tends to revert to its long-run equilibrium in the short run. This means that any short-term deviations from the long-run equilibrium will be corrected over time, and the local price of electricity will eventually return to its long-run equilibrium level. This means that if the current local price of electricity is above its long-run equilibrium level, it will tend to decrease in the short run to reach its equilibrium level. Conversely, if the current local price of electricity is below its long-run equilibrium level, it will tend to increase in the short run to reach its equilibrium level. This phenomenon is known as mean reversion and suggests that the local price of electricity in the short run is influenced by its previous values. The negative coefficients indicate that the local price of electricity tends to move back towards its long-run equilibrium level after a period of deviation. Both models also have different lag specifications, with Model 3 using an ARDL (7,2,2) and Model 4 using an ARDL (7,3,3). The coefficient of COINTEQ01 in Model 3 indicates a speed of adjustment of approximately 12.45% towards the long-run equilibrium value each day in response to changes in the independent variables, while the coefficient of COINTEQ01 in Model 4 indicates a speed of adjustment of approximately -0.114209, which takes around 9 days towards the long-run equilibrium value. Combining the insights from both models, we can conclude that the local price of electricity tends to revert to its long-run equilibrium in the short run and is influenced by its own past values as well as other independent variables such as confirmed COVID-19 cases and death. However, the short-run impact of wind energy production on local prices may be influenced by other factors, and there is a negative feedback effect in the short run that can lead to prices decreasing after a positive shock.

Overall, while there are some differences between the models, they all suggest that wind energy production in the previous period may have a significant impact on the current level of electricity prices. However, the effect of current wind energy production on local electricity prices is less clear as wind energy production may not have a significant effect on local electricity prices in the short run due to various reasons. One reason is that wind power production is not constant and varies based on the weather conditions thus the relationship of electricity price vs forecasted wind energy production is not always significant. Therefore, it may not have a substantial impact on electricity supply in the short run. Additionally, the electricity market operates on a merit order system, where generators with lower operating costs are given priority to supply electricity to the grid. As wind energy has relatively low operating costs, it can be supplied to the grid at a lower price, which may not significantly impact electricity prices. Furthermore, other factors such as demand, supply from other sources, and the state of the transmission and distribution network can also influence electricity prices in the short run. This claim is in line with (Mauritzen, 2012) stated that current wind energy production may not always have a significant effect on local electricity prices in the short run.

Table 21: Short run ARDL model variable measures and significance recap

Models	M.1 - ARDL(2, 2)		M.2 - ARDL(2, 2, 2)		M.5 - ARDL(2, 2, 2)		M.6 - ARDL(2, 2, 2)		M.3 - ARDL (7, 2, 2)		M.4 - ARDL(7, 3, 3)	
Variable	Coefficient	Prob,*	Coefficient	Prob,*	Coefficient	Prob,*	Coefficient	Prob,*	Coefficient	Prob,*	Coefficient	Prob,*
COINTEQ01	-0,141395	0	-0,253283	0	-0,252424	0	-0,23823	0	-0,124524	0	-0,114209	0
D(LOCAL_PRICE2(-1))	-0,128313	0	-0,01865	0,3688	-0,019212	0,3653	-0,025792	0,2187	-0,148417	0	-0,158345	0
D(LOCAL_PRICE2(-2))									-0,150052	0	-0,190569	0
D(LOCAL_PRICE2(-3))									-0,100086	0,0011	-0,1008	0,002
D(LOCAL_PRICE2(-4))									-0,100868	0	-0,099988	0
D(LOCAL_PRICE2(-5))									-0,10459	0,0178	-0,107992	0,0161
D(LOCAL_PRICE2(-6))									-0,06736	0	-0,069974	0
D(PRODUCTION)	0,000206	0,0375	0,000176	0,2856	0,000178	0,283	0,000178	0,2869	0,000143	0,3722	0,000135	0,4218
D(PRODUCTION(-1))	9,84E-05	0,0293	0,000176	0,0267	0,000177	0,0261	0,000176	0,0278	0,000153	0,0412	0,000145	0,0725
D(PRODUCTION(-2))											2,32E-06	0,9609
D(STRINGENCY_INDEX)			0,038117	0,307								
D(STRINGENCY_INDEX(-1))			-0,051398	0,3524								
D(CONTAINMMENT_HEALTH_INDEX)					0,00315	0,8702						
D(CONTAINMMENT_HEALTH_INDEX(-1))					-0,035815	0,5638						
D(ECONOMICPOLICY_INDEX)							0,016662	0,4817				
D(ECONOMICPOLICY_INDEX(-1))							-0,051328	0,1118				
D(C_CASES)									0,002029	0,0685		
D(C_CASES(-1))									-0,001071	0,262		
D(DETH_COV)											0,06454	0,1995
D(DETH_COV(-1))											-0,069117	0,219
D(DETH_COV(-2))											0,081761	0,1751
C	4,570122	0	-34,08625	0	-38,05059	0	-35,36801	0	3,705778	0	2,543353	0,0001
@TREND	0,000544	0,0004	0,015924	0	0,017584	0	0,016033	0				

🟩 Significant
🟥 Not significant

Source: Authors using Excel

We checked for short-run effects through Panel Granger Causality test using Dumiterscu-Hurlin approach which accommodates cross-sectional independence and cross-sectional dependence. For the pre-COVID-19 period, there is a statistically binary relationship between LOCAL_PRICE2 and PRODUCTION (See Table 23). During COVID-19, we observe a statistically significant binary relationships for most of the pairs of variables, except LOCAL_PRICE2 does not affect STRINGENCY_INDEX. The CONTAINMENT_HELTH_INDEX has not significant impact on LOCAL_PRICE2. The number of new COVID cases has also no effect on production. In the same vein, the number of death due to COVID-19 has no effect on ECONOMICPOLICY_INDEX (see Table 24).

We conclude that during the COVID-19 period, there was evidence of a causal relationship between wind energy production and local electricity price in the day-ahead electricity market, indicating that changes in production influenced price fluctuations and vice-versa.

Table 23: Panel Granger Causality results (During COVID-19)

Pairwise Dumitrescu Hurlin Panel Causality Tests
Sample: 1/01/2020 12/31/2020
Lags: 2

Null Hypothesis:	W-Stat.	Zbar-Stat.	Prob.
PRODUCTION does not homogeneously cause LOCAL_PRICE2	8.85455	13.1046	0.0000
LOCAL_PRICE2 does not homogeneously cause PRODUCTION	7.94355	11.3601	0.0000

Source: Authors using Eview

Table 24: Short run ARDL model variable measures and significance recap

Ho: Does not homogeneously cause

Variables	Period	LOCAL_PRICE2	PRODUCTION	STRINGENCY_INDEX	ECONOMICPOLICY_INDEX	CONTAINMENT_HEALTH_INDEX	C_CASES	DETH_COV
LOCAL_PRICE2	PCovid		0,0000					
PRODUCTION	PCovid	0,0000						
LOCAL_PRICE2	Dcovid		0,0000	0,8379	0,8345	0,5096	0,0000	0,0000
PRODUCTION	Dcovid	0,0000		0,0007	0,5346	0,0021	0,0000	0,0000
STRINGENCY_INDEX	Dcovid	0,0648	0,0000		0,0000	0,0024	0,0754	0,0000
ECONOMICPOLICY_INDEX	Dcovid	0,0120	0,0000	0,0000		0,0000	0,0088	0,0000
CONTAINMENT_HEALTH_INDEX	Dcovid	0,4089	0,0000	0,0000	0,0000		0,0727	0,0000
COV_C_CASES	Dcovid	0,0000	0,7480	0,0000	0,0001	0,0000		0,0000
Cov_ C_Deth	Dcovid	0,0000	0,0000	0,0000	0,1785	0,0038	0,0000	

Source: Authors using Excel

VII. DISCUSSION, SUMMARY AND CONCLUDING REMARKS

When comparing our research findings on the impact of wind energy production on Nord Pool electricity markets during pre- and during Covid-19 with other authors' studies, we observe both differences and similarities. (Pineau et al., 2020) examined the effects of wind power generation on electricity prices in New York and found a similar long-run relationship, indicating that an increase in wind power leads to a decline in prices. However, their study focused on the New York with Independent System Operator (NYISO) database, while our research specifically analyzed the Nord Pool market. Additionally, (Csereklyei et al., 2019) investigated the Australian market and reported an increase in electricity prices associated with wind and solar power generation, which contrasts with our findings. These differences may arise from the unique characteristics of the Australian National Electricity Market (NEM) and the time period analyzed. On the other hand, (Nieuwenhout & Brand, 2011) studied the impact of wind power on day-ahead prices in the Netherlands, and their findings align with ours in terms of a reduction in electricity prices with increased wind energy production. It is important to consider the specific methodologies, sample sizes, and regional focuses of each study when interpreting the results. Despite variations in short-run effects and specific contexts, there is a consistent pattern of long-run price reduction associated with higher wind energy production across different electricity markets.

Furthermore, other studies have employed different methodologies to examine the relationship between wind energy production and electricity prices. For instance, (Dorrell & Lee, 2021) used the Generalized Method of Moments (GMM) estimator to analyze the United States market across residential, commercial, and industrial sectors. Their findings indicated a positive and significant relationship between wind energy and electricity prices across all sectors, which contrasts with our research. The variation in results could be attributed to differences in data sources, modeling techniques, and the specific characteristics of the electricity markets studied.

In terms of the short-run effects, several studies have reported a similar pattern to our findings. (Wen et al., 2022) conducted a seasonal spatial econometric analysis in New Zealand's hydro-dominated electricity market and found that the price reduction associated with an increase in wind penetration varied across seasons. This aligns with our research, as we observed a reduction in the local electricity price during the Covid-19 period, where wind energy production played a significant role.

In terms of methodology, panel ARDL PMG approach, allows for capturing both short- and long-run dynamics while considering the panel structure of the data. The sample for our study consisted of pre-Covid-19 data from 2013 to 2019 and during Covid-19 data from 2019 to 2020, specifically focusing on the Nord Pool electricity market.

The observed reduction in the local electricity price in response to an increase in wind energy production can be attributed to the merit order effect. As wind energy has lower marginal costs compared to traditional energy sources, its increased penetration in the market displaces higher-cost generation units, leading to a downward pressure on prices. Additionally, the availability of wind energy as a renewable and sustainable source can contribute to the overall decarbonization and energy transition efforts.

In conclusion, while there are variations in the specific findings and methodologies across different studies, our research on the impact of wind energy production on Nord Pool electricity prices during pre- and during Covid-19 highlights the existence of a significant relationship and long-run price reduction. The comparisons with other authors' findings shed light on the diverse effects of wind energy on electricity prices in different markets, emphasizing the importance of considering regional factors, data sources, and modeling approaches when studying this relationship.

The findings have important policy implications, suggesting that government policies promoting renewable energy, such as wind energy, can positively impact electricity affordability in the long run. Policymakers should implement initiatives for renewable energy, energy efficiency, smart grid technology, and carbon pricing to reduce energy costs and environmental impact. The study also emphasizes the need to consider external factors, like government responses during crises, in electricity price dynamics analysis.

However, the study has some limitations, including the focus only on wind energy and the use of daily data, which restricts the number of observations. Future research can expand on this by incorporating other renewable energy sources, examining their impact on electricity demand and other economic variables. Moreover, Panel ARCH/GARCH methodology could be utilized to analyze high-frequency meteorological data. Additionally, a more comprehensive analysis of factors influencing price changes, including supply and demand dynamics and different market mechanisms, should be conducted.

References

Bai, J. (2009). Panel Data Models With Interactive Fixed Effects. *Econometrica*, *77*(4), 1229–1279. https://doi.org/10.3982/ECTA6135

Baltagi, B. H. (Badi H., & Baltagi, B. H. (Badi H. (2009). *A companion to Econometric analysis of panel data*. 295. https://www.wiley.com/en-us/A+Companion+to+Econometric+Analysis+of+Panel+Data-p-9780470744031

Belaid, F., & Elsayed, A. H. (2019). What drives renewable energy production in MENA Region? Investigating the roles of political stability, governance and financial sector. *Working Papers*. https://ideas.repec.org/p/erg/wpaper/1322.html

Brown, J., Pender, J., Wiser, R., Lantz, E., & Hoen, B. (2012). Ex Post Analysis of Economic Impacts from Wind Power Development in U.S. Counties. *Energy Economics*, *34*(6), 1743–1754. https://doi.org/10.1016/j.eneco.2012.07.010

Buttler, A., Dinkel, F., Franz, S., & Spliethoff, H. (2016). Variability of wind and solar power – An assessment of the current situation in the European Union based on the year 2014. *Energy*, *106*, 147–161. https://doi.org/10.1016/J.ENERGY.2016.03.041

Clò, S., Cataldi, A., & Zoppoli, P. (2015). The merit-order effect in the Italian power market: The impact of solar and wind generation on national wholesale electricity prices. *Energy Policy*, *77*, 79–88. https://doi.org/10.1016/J.ENPOL.2014.11.038

Csereklyei, Z., Qu, S., & Ancev, T. (2019). The effect of wind and solar power generation on wholesale electricity prices in Australia. *Energy Policy*, *131*, 358–369. https://doi.org/10.1016/J.ENPOL.2019.04.007

Dorrell, J., & Lee, K. (2021). The Price of Wind: An Empirical Analysis of the Relationship between Wind Energy and Electricity Price across the Residential, Commercial, and Industrial Sectors. *Energies*, *14*(12). https://doi.org/10.3390/EN14123363

Gelabert, L., Labandeira, X., & Linares, P. (2011). An ex-post analysis of the effect of renewables and cogeneration on Spanish electricity prices. *Energy Economics*, *33*(SUPPL. 1), S59–S65. https://doi.org/10.1016/J.ENECO.2011.07.027

Green, R., Hu, H., & Vasilakos, N. (2011). Turning the wind into hydrogen: The long-run impact on electricity prices and generating capacity. *Energy Policy*, *39*(7), 3992–3998. https://doi.org/10.1016/J.ENPOL.2010.11.007

Gürtler, M., & Paulsen, T. (2018). The effect of wind and solar power forecasts on day-ahead and intraday electricity prices in Germany. *Energy Economics*, *75*, 150–162. https://doi.org/10.1016/J.ENECO.2018.07.006

Hadri, K. (2000). Testing for stationarity in heterogeneous panel data. *The Econometrics Journal*, *3*(2), 148–161. https://doi.org/10.1111/1368-423X.00043

Holttinen, H., & Valtion teknillinen tutkimuskeskus. (2004). *The impact of large scale wind power production on the Nordic electricity system.*

Im, K. S., Pesaran, M. H., & Shin, Y. (2003). Testing for unit roots in heterogeneous panels. *Journal of Econometrics*, *115*(1), 53–74. https://ideas.repec.org/a/eee/econom/v115y2003i1p53-74.html

Jaraite, J., Kažukauskas, A., Brännlund, R., Chandra, K., & Kriström, B. (2019). Intermittency and Pricing Flexibility in Electricity Markets. *SSRN Electronic Journal*. https://doi.org/10.2139/SSRN.3389768

Jensen, C. U., Panduro, T. E., & Lundhede, T. H. (2014). The Vindication of Don Quixote: The Impact of Noise and Visual Pollution from Wind Turbines. *Land Economics*, *90*(4), 668–682. https://doi.org/10.3368/LE.90.4.668

Jónsson, T., Pinson, P., & Madsen, H. (2010). On the market impact of wind energy forecasts. *Energy Economics*, *32*(2), 313–320. https://doi.org/10.1016/J.ENECO.2009.10.018

Juergensen, J., Guimón, J., & Narula, R. (2020). European SMEs amidst the COVID-19 crisis: assessing impact and policy responses. *Journal of Industrial and Business Economics*, *47*(3), 499–510. https://doi.org/10.1007/S40812-020-00169-4

Kao, C. (1999). Spurious regression and residual-based tests for cointegration in panel data. *Journal of Econometrics*, *90*(1), 1–44. https://doi.org/10.1016/S0304-4076(98)00023-2

Katinas, V., Sankauskas, D., Markevičius, A., & Perednis, E. (2014). Investigation of the wind energy characteristics and power generation in Lithuania. *Renewable Energy*, *66*, 299–304. https://doi.org/10.1016/J.RENENE.2013.12.013

Ketterer, J. C. (2014). The impact of wind power generation on the electricity price in Germany. *Energy Economics*, *44*, 270–280. https://doi.org/10.1016/j.eneco.2014.04.003

Ketterer, J., Ketterer, & Janina. (2012). *The Impact of Wind Power Generation on the Electricity Price in Germany*. https://econpapers.repec.org/RePEc:ces:ifowps:_143

Klementavicius, A., Radziukynas, V., Radziukyniene, N., & Pukys, G. (2014). Homogeneous generation period method for the analysis of wind generation variation. *Energy Conversion and Management*, *86*, 165–174. https://doi.org/10.1016/J.ENCONMAN.2014.04.082

Maniatis, G. I., & Milonas, N. T. (2022). The impact of wind and solar power generation on the level and volatility of wholesale electricity prices in Greece. *Energy Policy*, *170*. https://doi.org/10.1016/J.ENPOL.2022.113243

Mathieu, E., Ritchie, H., Rodés-Guirao, L., Appel, C., Giattino, C., Hasell, J., Macdonald, B., Dattani, S., Beltekian, D., Ortiz-Ospina, E., & Roser, M. (2020). Coronavirus Pandemic (COVID-19). *Our World in Data*. https://ourworldindata.org/coronavirus

Mauritzen, J. (2012). What Happens When it's Windy in Denmark? An Empirical Analysis of Wind Power on Price Variability in the Nordic Electricity Market. *SSRN Electronic Journal*, *889*. https://doi.org/10.2139/ssrn.2045489

Moon, H., Perron, B., Moon, H., & Perron, B. (2004). Testing for a unit root in panels with dynamic factors. *Journal of Econometrics*, *122*(1), 81–126. https://econpapers.repec.org/RePEc:eee:econom:v:122:y:2004:i:1:p:81-126

Nicolosi, M., & Fürsch, M. (2009). The Impact of an increasing share of RES-E on the Conventional Power Market — The Example of Germany. *Zeitschrift Für Energiewirtschaft 2009 33:3*, *33*(3), 246–254. https://doi.org/10.1007/S12398-009-0030-0

Nieuwenhout, F., & Brand, A. (2011). The impact of wind power on day-ahead electricity prices in the Netherlands. *2011 8th International Conference on the European Energy Market (EEM)*, 226–230. https://doi.org/10.1109/EEM.2011.5953013

Okui, R., & Wang, W. (2021). Heterogeneous structural breaks in panel data models. *Journal of Econometrics*, *220*(2), 447–473. https://doi.org/10.1016/J.JECONOM.2020.04.009

Osman, M., Gachino, G., & Hoque, A. (2016). Electricity consumption and economic growth in the GCC countries: Panel data analysis. *Energy Policy*, *98*, 318–327. https://doi.org/10.1016/j.enpol.2016.07.050

Pedroni, P. (1999). Critical Values for Cointegration Tests in Heterogeneous Panels with Multiple Regressors. *Oxford Bulletin of Economics and Statistics*, *61*(S1), 653–670. https://doi.org/10.1111/1468-0084.0610S1653

Pedroni, P., Pedroni, & Peter. (2004). *Panel Cointegration: Asymptotic and Finite Sample Properties of Pooled Time Series Tests with an Application to the PPP Hypothesis*. https://econpapers.repec.org/RePEc:wil:wileco:2004-15

Persyn, D., Westerlund, J., Persyn, D., & Westerlund, J. (2008). Error-correction–based cointegration tests for panel data. *Stata Journal*, *8*(2), 232–241. https://econpapers.repec.org/RePEc:tsj:stataj:v:8:y:2008:i:2:p:232-241

Pesaran, M. H. (2007). A simple panel unit root test in the presence of cross-section dependence. *Journal of Applied Econometrics*, *22*(2), 265–312. https://doi.org/10.1002/JAE.951

Pesaran, M. H., Shin, Y., & Smith, R. P. (1999). Pooled Mean Group Estimation of Dynamic Heterogeneous Panels. *Journal of the American Statistical Association*, *94*(446), 621. https://doi.org/10.2307/2670182

Pineau, P.-O., Nasseri, Y., & Rafizadeh, N. (2020). The Effects of Wind Power Generation on the Electricity Price: High Frequency Evidence from New York. *Social Science Research Network*. https://doi.org/10.2139/SSRN.3639249

Sensfuß, F., Ragwitz, M., & Genoese, M. (2008a). The merit-order effect: A detailed analysis of the price effect of renewable electricity generation on spot market prices in Germany. *Energy Policy*, *36*(8). https://doi.org/10.1016/j.enpol.2008.03.035

Sensfuß, F., Ragwitz, M., & Genoese, M. (2008b). The merit-order effect: A detailed analysis of the price effect of renewable electricity generation on spot market prices in Germany. *Energy Policy*, *36*(8), 3086–3094. https://doi.org/10.1016/J.ENPOL.2008.03.035

Shen, Z., & Ritter, M. (2016). Forecasting volatility of wind power production. *Applied Energy*, *176*. https://doi.org/10.1016/j.apenergy.2016.05.071

Sohag, K., Begum, R. A., Syed Abdullah, S. M., & Jaafar, M. (2015). Dynamics of energy use, technological innovation, economic growth and trade openness in Malaysia. *Energy*, *90*, 1497–1507. https://doi.org/10.1016/J.ENERGY.2015.06.101

Swinand, G. P., & O'Mahoney, A. (2015). Estimating the impact of wind generation and wind forecast errors on energy prices and costs in Ireland. *Renewable Energy*, *75*, 468–473. https://doi.org/10.1016/J.RENENE.2014.09.060

Vincent, C. L., & Trombe, P. J. (2017). Forecasting intrahourly variability of wind generation. *Renewable Energy Forecasting: From Models to Applications*, 219–233. https://doi.org/10.1016/B978-0-08-100504-0.00008-1

Weber, J., Gotzens, F., & Witthaut, D. (2018). Impact of strong climate change on the statistics of wind power generation in Europe. *Energy Procedia*, *153*, 22–28. https://doi.org/10.1016/J.EGYPRO.2018.10.004/IMPACT_OF_STRONG_CLIMATE_CHANGE_ON_THE_STATISTICS_OF_WIND_POWER_GENERATION_IN_EUROPE.PDF

Wen, L., Suomalainen, K., Sharp, B., Yi, M., & Sheng, M. S. (2022). Impact of wind-hydro dynamics on electricity price: A seasonal spatial econometric analysis. *Energy*, *238*, 122076. https://doi.org/10.1016/J.ENERGY.2021.122076

Westerlund, J. (2007). Testing for Error Correction in Panel Data*. *Oxford Bulletin of Economics and Statistics*, *69*(6), 709–748. https://doi.org/10.1111/J.1468-0084.2007.00477.X

Westerlund, J., & Edgerton, D. L. (2008). A simple test for cointegration in dependent panels with structural breaks. *Oxford Bulletin of Economics and Statistics*, *70*(5), 665–704. https://doi.org/10.1111/J.1468-0084.2008.00513.X

Wolde-Rufael, Y., & Weldemeskel, E. M. (2020). Environmental policy stringency, renewable energy consumption and CO2 emissions: Panel cointegration analysis for BRIICTS countries. *Https://Doi.Org/10.1080/15435075.2020.1779073*, *17*(10), 568–582. https://doi.org/10.1080/15435075.2020.1779073

Würzburg, K., Labandeira, X., & Linares, P. (2013a). Renewable generation and electricity prices: Taking stock and new evidence for Germany and Austria. *Energy Economics*, *40*. https://doi.org/10.1016/J.ENECO.2013.09.011

Würzburg, K., Labandeira, X., & Linares, P. (2013b). Renewable generation and electricity prices: Taking stock and new evidence for Germany and Austria. *Energy Economics*, *40*, S159–S171. https://doi.org/10.1016/J.ENECO.2013.09.011

Impact of NPC multilevel inverter on circulating harmonic currents of double star induction machine using vector space decomposition

Khaled ben smida[1], Hajer Kouki[2]

[1,2]*Electronic industrial Department, Sousse University*
National school of engineers of Sousse. Laboratory of Advanced technology and intelligent systems-LATIS
[1]`khaled_bensmida@yahoo.fr`
[2]`hajer_kouki@yahoo.fr`

Abstract— **The fed of multiphase induction machines by a two level voltage source inverter is subject to vary extra harmonic currents of stator windings that causes losses and require larger semiconductor device ratings. In this paper, in order to eliminate these extra harmonic currents, the double star induction machine is supplied by a neutral-point-clamped (NPC) voltage inverter using the vector space decomposition concept while taking into account the stator mutual leakage between two stars. A generalized mathematical model of "N" levels inverters feeding the double star induction machine is presented.**

Keywords— **Double star induction machine (DSIM), vector space decomposition, neutral-point-clamped (NPC) voltage inverter, circulation harmonic currents**.

I. INTRODUCTION

Seeing that the polyphase machines have been developed mainly in the field of variable speed drives for high power [1] -[5] the increase in the number of phases allows to reduce the dimensioning of the components in power modulators energy and to improve functioning safety, therefore fed the polyphase machine by a voltage inverter is an essential step [6]-[9].

In the multi-phase drive systems, the electric machine has more than three phases in the stator and the same numbers of inverter legs are in the inverter side. So the current per phase in the machine and inverter is reduced. The most common multi-phase machine drive structure is the double star induction machine, which has two sets of three-phase windings, spatially phase shifted by 0°,30° and 60 electrical degrees with double neutral (Fig. 1). In this structure when a DSIM is fed by a six step voltage source inverter, large harmonic currents that do not contribute to the air gap flux have been observed. These harmonics generate additional losses in the machine and increase the size and cost of the machine drive system [10]-[12]. The researchers are focused on the suppression of these stator current harmonics. In this way, some approaches concern the machine structure design. The other approaches concern applying a proper PWM technique for reducing the harmonic voltages of the motor. In this case, without any modification on the machine and its structure, and only by proper control strategy of inverter, they try to reduce undesired current components [10], [13]-[15].

Note well that a fed of double star asynchronous machine by a two-level inverter is widely studied in the literature. Furthermore, with two level voltage inverter, the output voltage of a machine is composed of a succession of voltage pulses of amplitude equal to the DC bus voltage, while the machine is initially designed to operate in sinusoidal regime [16]- [19]. Therefore the use of the development of the NPC inverter technique was a suitable solution [20]-[24].

The aim of this paper is to present a model of the double star induction machine using the vector space decomposition concept. This technique is a way to investigate the impact of circulating harmonic currents on the double star induction machine performances, when fed by a conventional voltage source inverter. In addition, in order to reduce these extra harmonic currents, we have proposed to feed the double star induction machine by an NPC multilevel inverter. We analyse in this part, the association of the dual star asynchronous machine by a multilevel voltage inverter NPC (neutral point clamed) type. A generalized mathematical model for "N" levels

ISSN: 1737-933484

inverters feeding the double star induction machine is proposed. The considered model takes into account the stator mutual leakage with any arbitrary angle of displacement between the two three phase winding sets.

II. NATIVE MATHEMATICAL MODEL OF DOUBLE STAR INDUCTION MACHINE

As shown in figure 1, the machine has two stator windings sets (a1, b1, c1) and (a2, b2, c2) spatially shifted by γ electrical degrees with isolated neutral points and an equivalent three-phase squirrel-cage rotor. θ' is the angle shift between the rotor and the star 1, and θ' - γ is the one between the rotor and the star 2.

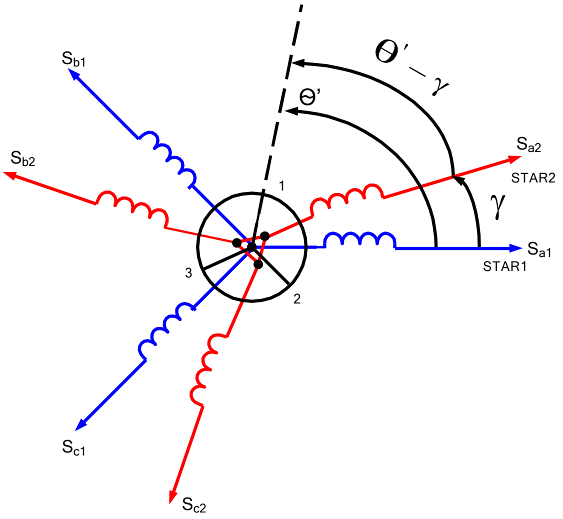

Fig. 1. Windings of double star induction machine

Whereas that the machine having six phases, the stator and rotor equations voltage can be written as follows:

$$\begin{cases} [V_s]=[R_s][I_s]+\dfrac{d}{dt}([L_{ss}][I_s]+[L_{sr}][I_r]) \\ [V_r]=[R_r][I_r]+\dfrac{d}{dt}([L_{rr}][I_r]+[L_{rs}][I_s]) \end{cases} \quad (1)$$

With:

$$[v_s]=\begin{bmatrix} v_{sa1} \\ v_{sb1} \\ v_{sc1} \\ v_{sa2} \\ v_{sb2} \\ v_{sc2} \end{bmatrix};[v_r]=\begin{bmatrix} 0 \\ 0 \\ 0 \end{bmatrix},[I_s]=\begin{bmatrix} I_{sa1} \\ I_{sb1} \\ I_{sc1} \\ I_{sa2} \\ I_{sb2} \\ I_{sc2} \end{bmatrix};[I_r]=\begin{bmatrix} I_{r1} \\ I_{r2} \\ I_{r3} \end{bmatrix}$$

$[R_s]$, $[R_r]$ are respectively the stator and rotor resistance matrix

$$[R_s]=R_s[I]_6$$

$$[R_r]=R_r[I]_3$$

Inductances of the machine are evaluated by the following matrix:

$$[L_{ss}] = \begin{bmatrix} L_{ms} & L_{ms}\cos(\frac{2\pi}{3}) & L_{ms}\cos(\frac{4\pi}{3}) & (L_{ms}+lm_{ss})\cos(\gamma) & L_{ms}\cos(\gamma+\frac{2\pi}{3}) & L_{ms}\cos(\gamma+\frac{4\pi}{3}) \\ L_{ms}\cos(-\frac{2\pi}{3}) & L_{ms} & L_{ms}\cos(\frac{2\pi}{3}) & L_{ms}\cos(\gamma-\frac{2\pi}{3}) & (L_{ms}+lm_{ss})\cos(\gamma) & L_{ms}\cos(\gamma+\frac{2\pi}{3}) \\ L_{ms}\cos(-\frac{4\pi}{3}) & L_{ms}\cos(-\frac{2\pi}{3}) & L_{ms} & L_{ms}\cos(\gamma-\frac{4\pi}{3}) & L_{ms}\cos(\gamma-\frac{2\pi}{3}) & (L_{ms}+lm_{ss})\cos(\gamma) \\ (L_{ms}+lm_{ss})\cos(\gamma) & L_{ms}\cos(\gamma-\frac{2\pi}{3}) & L_{ms}\cos(\gamma-\frac{4\pi}{3}) & L_{ms} & L_{ms}\cos(\frac{2\pi}{3}) & L_{ms}\cos(\frac{4\pi}{3}) \\ L_{ms}\cos(\gamma+\frac{2\pi}{3}) & (L_{ms}+lm_{ss})\cos(\gamma) & L_{ms}\cos(\gamma-\frac{2\pi}{3}) & L_{ms}\cos(-\frac{2\pi}{3}) & L_{ms} & L_{ms}\cos(\frac{2\pi}{3}) \\ L_{ms}\cos(\gamma+\frac{4\pi}{3}) & L_{ms}\cos(\gamma+\frac{2\pi}{3}) & (L_{ms}+lm_{ss})\cos(\gamma) & L_{ms}\cos(-\frac{4\pi}{3}) & L_{ms}\cos(-\frac{2\pi}{3}) & L_{ms} \end{bmatrix} + l_s[I_6] \tag{2}$$

$$[L_{sr}] = L_{sr}\begin{bmatrix} \cos(\theta') & \cos(\theta'+\frac{2\pi}{3}) & \cos(\theta'+\frac{4\pi}{3}) \\ \cos(\theta'-\frac{2\pi}{3}) & \cos(\theta') & \cos(\theta'+\frac{2\pi}{3}) \\ \cos(\theta'-\frac{4\pi}{3}) & \cos(\theta'-\frac{2\pi}{3}) & \cos(\theta') \\ \cos(\theta'-\gamma) & \cos(\theta'-(\gamma-\frac{2\pi}{3})) & \cos(\theta'-(\gamma-\frac{4\pi}{3})) \\ \cos(\theta'-(\gamma+\frac{2\pi}{3})) & \cos(\theta'-\gamma) & \cos(\theta'-(\gamma-\frac{2\pi}{3})) \\ \cos(\theta'-(\gamma+\frac{4\pi}{3})) & \cos(\theta'-(\gamma+\frac{2\pi}{3})) & \cos(\theta'-\gamma) \end{bmatrix} \tag{3}$$

$$[L_{rr}] = L_{mr}\begin{bmatrix} 1 & \cos\left(\frac{2\pi}{3}\right) & \cos\left(\frac{4\pi}{3}\right) \\ \cos\left(-\frac{2\pi}{3}\right) & 1 & \cos\left(\frac{2\pi}{3}\right) \\ \cos\left(-\frac{4\pi}{3}\right) & \cos\left(-\frac{2\pi}{3}\right) & 1 \end{bmatrix} + l_r[I_3] \tag{4}$$

Where :
l_s : stator leakage inductance
L_{ms} : magnetization self-inductance stator
l_{mss} : mutual inductance of stator leakage between the two stars
L_{sr} : mutual inductance between stator / rotor
l_r : rotor leakage inductance

The expression of the electromagnetic torque is obtained by deriving the following coenergie:

$$C_{em} = \frac{p}{2}[I_s]^{'}\left(\frac{\partial[L_{sr}]}{\partial\theta'}\right)[I_r] \tag{5}$$

To complete the relation (5), we add the following equations:

$$\omega_m = \frac{d\theta'}{dt} \tag{6}$$

$$\frac{d\omega_m}{dt} = \frac{P}{J}\left(C_{em} - C_r\right) \tag{7}$$

III. MODEL IN (α-β) (Z1-Z2) (Z3-Z4) SUBSPACES

As it can be seen, the DSIM is a six dimensional system. It is shown in [13-16] that it can be decomposed into three two-dimensional orthogonal subspaces, (α-β), (z1-z2), (z3-z4), by the following transformation $[T_6]$ and $[T_r]$:

$$[T_r] = \sqrt{\frac{2}{3}}\begin{bmatrix} \cos(0) & \cos(\frac{2\pi}{3}) & \cos(\frac{4\pi}{3}) \\ \sin(0) & \sin(\frac{2\pi}{3}) & \sin(\frac{4\pi}{3}) \\ \frac{1}{\sqrt{2}} & \frac{1}{\sqrt{2}} & \frac{1}{\sqrt{2}} \end{bmatrix} \tag{8}$$

$$[T_6] = k\begin{bmatrix} \cos(0) & \cos(\frac{2\pi}{3}) & \cos(\frac{4\pi}{3}) & \cos(\gamma) & \cos(\frac{2\pi}{3}+\gamma) & \cos(\frac{4\pi}{3}+\gamma) \\ \sin(0) & \sin(\frac{2\pi}{3}) & \sin(\frac{4\pi}{3}) & \sin(\gamma) & \sin(\frac{2\pi}{3}+\gamma) & \sin(\frac{4\pi}{3}+\gamma) \\ \cos(0) & \cos(\frac{4\pi}{3}) & \cos(\frac{2\pi}{3}) & \cos(\pi-\gamma) & \cos(\frac{\pi}{3}-\gamma) & \cos(\frac{5\pi}{3}-\gamma) \\ \sin(0) & \sin(\frac{4\pi}{3}) & \sin(\frac{2\pi}{3}) & \sin(\pi-\gamma) & \sin(\frac{\pi}{3}-\gamma) & \sin(\frac{5\pi}{3}-\gamma) \\ 1 & 1 & 1 & 0 & 0 & 0 \\ 0 & 0 & 0 & 1 & 1 & 1 \end{bmatrix} \tag{9}$$

In matrix (9), γ is the electrical angle between two three-phase windings. By applying the transformation (8) and (9) to ''Equation 1'', we can obtain decoupled model for SPIM.

Where:

$$[T_6][V_s] = \begin{bmatrix} v_{s\alpha} \\ v_{s\beta} \\ v_{sz1} \\ v_{sz2} \\ v_{sz3} \\ v_{sz4} \end{bmatrix}, [T_6][I_s] = \begin{bmatrix} i_{s\alpha} \\ i_{s\beta} \\ i_{sz1} \\ i_{sz2} \\ i_{sz3} \\ i_{sz4} \end{bmatrix}, [T_r][V_r] = \begin{bmatrix} 0 \\ 0 \\ 0 \end{bmatrix}, [T_r][I_r] = \begin{bmatrix} i_{r\alpha} \\ i_{r\beta} \\ i_{ro} \end{bmatrix}$$

The final model expressed in the stationary reference frame is given by:

-Machine model in α-β subspace:

The stator and rotor voltage equations are:

Copyright © 2023
ISSN: 1737-933484

$$\begin{cases} v_{s\alpha} = R_s i_{s\alpha} + L_s \dfrac{di_{s\alpha}}{dt} + M \dfrac{di_{r\alpha}}{dt} \\ v_{s\beta} = R_s i_{s\beta} + L_s \dfrac{di_{s\beta}}{dt} + M \dfrac{di_{r\beta}}{dt} \\ 0 = R_r i_{r\alpha} + L_r \dfrac{di_{r\alpha}}{dt} + M \dfrac{di_{s\alpha}}{dt} + \omega_m \lambda_{r\beta} \\ 0 = R_r i_{r\beta} + L_r \dfrac{di_{r\beta}}{dt} + M \dfrac{di_{s\beta}}{dt} - \omega_m \lambda_{r\alpha} \end{cases} \qquad (10)$$

Where:

$M = 3L_{ms} / \sqrt{2}$

$L_s = l_{s\alpha\beta} + 3L_{ms}$, $l_{s\alpha\beta} = l_s + \frac{3}{4} lm_{ss}$

$L_r = l_r + \frac{3}{2} L_{mr}$

-Machine model in z1-z2 subspace:

$$\begin{cases} v_{sz1} = R_s i_{sz1} + l_{sz1z2} \dfrac{di_{sz1}}{dt} \\ v_{sz2} = R_s i_{sz2} + l_{sz1z2} \dfrac{di_{sz2}}{dt} \end{cases} \qquad (11)$$

-Machine model in z3-z4 subspace:

$$\begin{cases} v_{sz3} = R_s i_{sz3} + l_{sz3z4} \dfrac{di_{sz3}}{dt} \\ v_{sz4} = R_s i_{sz4} + l_{sz3z4} \dfrac{di_{sz4}}{dt} \\ v_{ro} = R_r i_{ro} + l_r \dfrac{di_{ro}}{dt} \end{cases} \qquad (12)$$

With:

$l_{sz1z2} = l_{sz3z4} = l_s + \frac{3}{4} lm_{ss}$

Applying the necessary changes to ''Equation 5'', the electromagnetic torque expression becomes:

$$T_{em} = pM(i_{s\beta} i_{r\alpha} - i_{s\alpha} i_{r\beta}) \qquad (13)$$

As it can be seen from these three subsystems ''Equation 10'', ''Equation 11'' and ''Equation 12'', the electromechanical energy conversion takes place in the α-β subsystem, and the other subsystems do not contribute in the energy conversion. The (z1-z2) and (z3-z4) subsystems are only producing losses. It can be concluded that analysing DSIM is performed by help of the α-β subspace.

IV. MULTILEVEL VOLTAGES INVERTER FED DSIM

In order to more clearly define the sequences of a three-level inverter, we have established the general mathematical model of an NPC multilevel inverter at N levels. Indeed, for N levels, the number of elements per leg, such that the number of sources S, K switches, and D diodes are given by the following relationship:

$$\begin{aligned} S &= N-1 \\ K &= 2(N-1) \\ D &= 2(N-2) \end{aligned} \tag{14}$$

In the general case and since C (i, j) =1- C '(i, j), the final expression of V_{a1o}, V_{b1o} et V_{c1o} can be written as follows:

$$\begin{cases} V_{a1o} = \left(\sum_{j=1}^{N-1} C(1,j) - \sum_{j=1}^{N-1} C'(1,j)\right)\dfrac{E}{2(N-1)} = \left(2*\sum_{j=1}^{N-1} C(1,j) - (N-1)\right)\dfrac{E}{2(N-1)} \\ V_{b1o} = \left(\sum_{j=1}^{N-1} C(2,j) - \sum_{j=1}^{N-1} C'(2,j)\right)\dfrac{E}{2(N-1)} = \left(2*\sum_{j=1}^{N-1} C(2,j) - (N-1)\right)\dfrac{E}{2(N-1)} \\ V_{c1o} = \left(\sum_{j=1}^{N-1} C(3,j) - \sum_{j=1}^{N-1} C'(3,j)\right)\dfrac{E}{2(N-1)} = \left(2*\sum_{j=1}^{N-1} C(3,j) - (N-1)\right)\dfrac{E}{2(N-1)} \end{cases} \tag{15}$$

According to the system of equation (15); the output voltages of the first star can be written as follows:

$$V_{sa1} = \left(2*\sum_{j=1}^{N-1} C(1,j) - (N-1)\right)\frac{E}{2(N-1)} - \frac{E}{2(N-1)}\left[\frac{2}{3}*\sum_{j=1}^{N-1}(C(1,j)+(C(2,j)+(C(3,j)) - (N-1)\right] \tag{16}$$

$$V_{sa1} = \frac{E}{3(N-1)}\left[\sum_{j=1}^{N-1} 2*C(1,j) - \sum_{j=1}^{N-1}(C(2,j) - \sum_{j=1}^{N-1}(C(3,j)\right] \tag{17}$$

In the same way, V_{sb1} and V_{sc1}:

$$V_{sb_1} = \frac{E}{3(N-1)}\left[\sum_{j=1}^{N-1} -C(1,j) + 2*\sum_{j=1}^{N-1}(C(2,j) - \sum_{j=1}^{N-1}(C(3,j)\right] \tag{18}$$

$$V_{sc_1} = \frac{E}{3(N-1)}\left[\sum_{j=1}^{N-1} -C(1,j) - \sum_{j=1}^{N-1}(C(2,j) + 2*\sum_{j=1}^{N-1}(C(3,j)\right] \tag{19}$$

Application of above equations to a DSIM supplied by an NPC multilevel voltage inverter for N levels is given by the following matrix relation:

ISSN: 1737-933484

$$\begin{pmatrix} V_{sa_1} \\ V_{sb_1} \\ V_{sc_1} \\ V_{sa_2} \\ V_{sb_2} \\ V_{sc_2} \end{pmatrix} = \frac{E}{3(N-1)} \begin{bmatrix} 2 & -1 & -1 & 0 & 0 & 0 \\ -1 & 2 & -1 & 0 & 0 & 0 \\ -1 & -1 & 2 & 0 & 0 & 0 \\ 0 & 0 & 0 & 2 & -1 & -1 \\ 0 & 0 & 0 & -1 & 2 & -1 \\ 0 & 0 & 0 & -1 & -1 & 2 \end{bmatrix} \begin{pmatrix} \sum_{j=1}^{N-1} C(1,j) \\ \sum_{j=1}^{N-1} C(2,j) \\ \sum_{j=1}^{N-1} C(3,j) \\ \sum_{j=1}^{N-1} C(4,j) \\ \sum_{j=1}^{N-1} C(5,j) \\ \sum_{j=1}^{N-1} C(6,j) \end{pmatrix} \tag{20}$$

The transformation (9) applied in the preceding section gives the voltage vectors components in the (α-β), (z_1-z_2,) and (z_3-z_4) subspace. The (z_3-z_4) components are always (for the three angle shift) all equal to zero because the neutrals of the two windings sets are isolated.

In order to reduce the size of the program and the simulation time, a connection matrix between DSIM and NPC voltage inverter association , with any arbitrary angle of displacement between the two three phase winding sets γ and whatever the level N, was proposed. The transformation matrix [T_6] projecting the output voltages vectors of the inverter on the (α-β), (z_1-z_2,) and (z_3-z_4) bases, components of voltage vectors as well transformed and are obtained from the following relationship:

$$\begin{bmatrix} V_{s\alpha} \\ V_{s\beta} \\ V_{sz1} \\ V_{sz2} \\ V_{sz3} \\ V_{sz4} \end{bmatrix} = E\,k \begin{bmatrix} 1 & \cos(\frac{2\pi}{3}) & \cos(\frac{4\pi}{3}) & \cos(\gamma) & \cos(\frac{2\pi}{3}+\gamma) & \cos(\frac{4\pi}{3}+\gamma) \\ 0 & \sin(\frac{2\pi}{3}) & \sin(\frac{4\pi}{3}) & \sin(\gamma) & \sin(\frac{2\pi}{3}+\gamma) & \sin(\frac{4\pi}{3}+\gamma) \\ 1 & \cos(\frac{4\pi}{3}) & \cos(\frac{2\pi}{3}) & -\cos(\gamma) & \cos(\frac{\pi}{3}-\gamma) & \cos(\frac{5\pi}{3}-\gamma) \\ 0 & \sin(\frac{4\pi}{3}) & \sin(\frac{2\pi}{3}) & \sin(\gamma) & \sin(\frac{\pi}{3}-\gamma) & \sin(\frac{5\pi}{3}-\gamma) \\ 0 & 0 & 0 & 0 & 0 & 0 \\ 0 & 0 & 0 & 0 & 0 & 0 \end{bmatrix} \begin{pmatrix} \sum_{j=1}^{N-1} C(1,j) \\ \sum_{j=1}^{N-1} C(2,j) \\ \sum_{j=1}^{N-1} C(3,j) \\ \sum_{j=1}^{N-1} C(4,j) \\ \sum_{j=1}^{N-1} C(5,j) \\ \sum_{j=1}^{N-1} C(6,j) \end{pmatrix} \tag{21}$$

Where
E: dc bus
k=1/3

V. SIMULATION RESULTS

The simulations results of the DSIM-NPC multi-level inverter association are carried out with the following parameters: N=3 then N=7, f_p = 4650 Hz, fs=50Hz, Cr = 2N.m.

In order to show the influence of the supply of the DSIM by NPC multi-level voltage inverters on the circulation harmonics currents, we will study and analyze the waveforms components of isz_1, torque and phase current for the three different angle shifts and for two types of levels 3 and 7.

Figure 2 illustrate the temporal evolution of i_{sz1} currents, electromagnetic torque and phase currents.

ISSN: 1737-933484

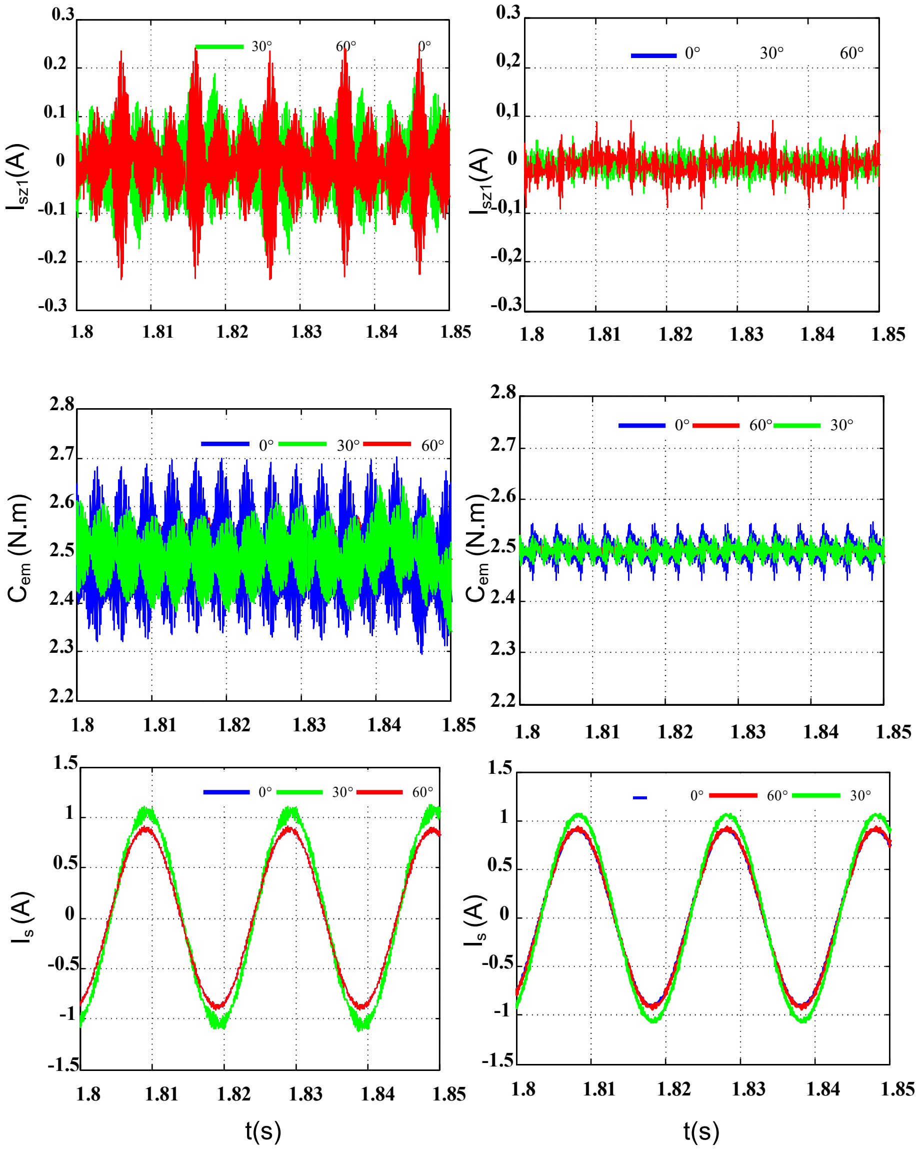

(a) (b)

Fig. 2. (a) NPC 3 levels, (b) NPC 7 levels

As shown in figure 2, the increase of the level number reduces significantly the torque ripple and circulation harmonic currents for various angle shifts between the two stars.

Table 1: Impact of the levels number on the circulation harmonic current and the DSIM performances.

	3 Levels			7 Levels		
	ΔC_{em} %	**THD % of isa1**	**Maximum amplitude of isz1 (A)**	**ΔC_{em} %**	**THD % of isa1**	**Maximum amplitude of isz1 (A)**
0°	18.4%	2.03%	0	4.48%	0.56%	0

30°	16.28%	4.49%	0.27	2.24%	1.74%	0.046
60°	11.8%	4.18%	0.22	0.92%	1.22%	0.061

Table 1 shows that in the case of 30° between two stars, the harmonic currents decrease from 0.27 A to 0.046. For 60 °, the amplitude has decreased from 0.22 A to 0.061 A. The torque ripple for 7 levels is much lower than for 3 levels. The obtained results are full of promise and show the interest of the feeding of the DSIM by NPC multi-level inverters in reducing harmonic currents.

VI. CONCLUSION

The modeling of a double star induction machine (DSIM) fed by a neutral-point-clamped (NPC) voltage inverter using the vector space decomposition concept was presented and analyzed. A generalized mathematical model for "N" levels inverters, including stator mutual leakage with any arbitrary angle of displacement between the two three phase winding sets was proposed. The obtained results are full of promise and show the interest of the feeding of the DSIM by NPC multi-level inverters in reducing harmonic currents and torque ripple.

REFERENCES

[1] J. Paredes, B. Prieto, M. Satrústegui, I. Elósegui and P. González, "Improving the Performance of a 1-MW Induction Machine by Optimally Shifting From a Three-Phase to a Six-Phase Machine Design by Rearranging the Coil Connections," in IEEE Transactions on Industrial Electronics, vol. 68, no. 2, pp. 1035-1045, Feb. 2021.

[2] Farag K. Abo-Elyousr1, G. H. Rim, "Performance Evaluation of AC/DC PWM Converter for 12-phase Stand-Alone PMSG with Maximum Power Extraction, " International Conference on Electrical Machines and Systems (ICEMS), Incheon, pp. 82 – 87, December 2010.

[3] M. Bagheri, E. Farjah and T. Ghanbari, "Selective Utilized Phase Number of Multiphase Induction Motors Strategy to Enhance Electric Vehicles' Drive Range," 2021 12th Power Electronics, Drive Systems, and Technologies Conference (PEDSTC), Tabriz, Iran, 2021, pp. 1-5

[4] J.M. Apsley, , S. Williamson, A.C. Smith and M. Barnes, " Induction motor performance as a function of phase number, in Proc. of the IEE Electric Power Applications, vol. 153, no. 6, pp.1350-2352, 2006.

[5] L. Parsa," On Advantages of Multi-Phase Machines, " Industrial Electronics Society, IECON, 31 Annual Conference of IEEE, 2005, pp. 1574-1579.

[6] A. Bughneda, M. Salem, A. Richelli, D. Ishak and S Alatai, "Review of multilevel inverters for PV energy system applications", Energies, vol. 14, no. 6, pp. 1585, 2021

[7] A. M. L. Baltatanu, " Multiphase machines used in electric vehicles propulsion," International Conference on Electronics, Computers and Artificial Intelligence (ECAI),2013, *pp. 1-6.*

[8] A. Tessarolo, "Benefits of increasing the number of stator phases in terms of winding construction technology in high-power electric machines, "5th IET Int. Conf. on Power Electronics, Machines and Drives (PEMD), 2010, pp. 1-6

[9] K. Marouani, K. Nounou, and M. B. Tabbache, " Power factor correction of an electrical drive system based on multiphase machines, " International Conference on Green Energy, 2014, pp. 152 – 157.

[10] Hajer Kouki, Mouldi Ben Fredj, Habib Rehaoulia, "Harmonic analysis of SVPWM control strategy on VSI-fed double-star induction machine performances",Electr Eng vol. 98, pp.133–143, 2016.

[11] Hu Yashan, Zi. Zhu, and K. Liu , " Current Control for Dual Three-Phase Permanent Magnet Synchronous Motors Accounting for Current Unbalance and Harmonics", IEEE Journal Emerging and Selected Topics in Power Electronics, vol. 2, no. 2, pp. 272 – 284, 2014.

[12] K. Marouani, F. Khoucha, L. Baghli, D. Hadiouche, and A. Kheloui, " Study and harmonic analysis of SVPWM techniques for VSI-Fed double-star induction motor drive, "Mediterranean Conference on Control & Automation, 2007, pp. 1 –6.

[13] Zhao; Y. and T. A. Lipo, "Space Vector PWM Control of Dual Three Phase Induction Machine Using Vector Space Decomposition, " IEEE Transactions on Industry Applications, vol. 31, no. 5, pp. 1100-1109, 1995.

[14] Kamari, M. Keramatzadeh, and R. Kianinezhad, “Space Vector Double Frame Field Oriented Control of Six Phase Induction Motors, “ WSEAS Transactions on Systems and Control, vol. 4, no. 3, pp.129-139, 2009.

[15] Hadiouche, D., L. Baghli and A. Rezzoug, “Space vector PWM techniques for dual three-phase AC machines: analysis, performance evaluation and DSP implementation, “ IEEE Industry Applications Conference, vol. 42, no. 4, pp. 1112 – 1122, 2006.

[16] Khoudir Marouani, Farid Khouchal, Abdelaziz Khelouil, Lotfi Baghli and Djafar Hadiouche, “Study and Simulation of Direct Torque Control of Double-Star Induction Motor Drive“, EPEPEMC 2006,

[17] PWM Inverters and Double Star Asynchronous Machine drive- Sliding mode solution, IEEE Industrial Electronics, IECON 2006- 32nd Annual Conference on 6-10 Nov. 2006.

[18] D. Yazdani, S.A. Khajehoddin, A. Bakhshai, and G. Joos, “Full Utilization of the Inverter in Split-Phase Drives by Means of a Dual Three-Phase Space Vector Classification Algorithm, “ IEEE Transactions on Industry Electronics, vol. 56, no. 1, pp. 120-129, 2009.

[19] Vilas Bugade1, Pradeep K. Katti2,” Multiphase Induction Motor Drive for Energy and Electrical Transportation Applications”, International Journal for Research in Applied Science & Engineering Technology (IJRASET) ISSN: 2321-9653; IC Value: 45.98; Volume 6 Issue IV, April 2018.

[20] U. -M. Choi and J. -S. Lee, "Single-Phase Five-Level IT-Type NPC Inverter With Improved Efficiency and Reliability in Photovoltaic Systems," in IEEE Journal of Emerging and Selected Topics in Power Electronics, vol. 10, no. 5, pp. 5226-5239, Oct. 2022.

[21] A. K. Gopi, M. A. Kumar, J. Biswas and M. Barai, "An Optimized Hybrid PWM Strategy for Five Level NPC VSI With Unequal DC-Links in a PV System," in IEEE Journal of Emerging and Selected Topics in Industrial Electronics, vol. 3, no. 3, pp. 766-776, July 2022.

[22] Abdelkrim, T.; Berkouk, E. M.; Benamrane, K.; Benslimane, T., “Study and Control of Three-Level PWM Rectifier-Five-Level NPC Active Power Filter Cascade by Using Feedback Control and Redundant Vectors“, IREE, vol. 5, issue 3, part B, pp820830, May-Jun 2010.

[23] Z. Oudjebour ; E. M. Berkouk ; M. O. Mahmoudi, “Stabilization by New control technique of the input DC voltages of five-level diode - Clamped inverters. Application to double star induction machine“, 2nd International Symposium on Environment Friendly Energies and Applications (EFEA), 2012.

[24] Beriber, D ; Berkouk, E.M. ; Talha, A. ; Mahmoudi, M.O. “ Study and control of two two-level PWM rectifiers-clamping bridge-two three-level NPC VSI cascade. application to double stator induction machine“,IEEE 35th Annual power Electronics Specialists Conference, 2004. PESC 04.